UNIVERSITÉ DE MONTRÉAL

SEISMIC PROPERTIES OF POLYPHASE ROCKS

QIN WANG
DÉPARTEMENT DES GÉNIES CIVIL, GÉOLOGIQUE ET DES MINES
ÉCOLE POLYTECHNIQUE DE MONTRÉAL

THÈSE PRÉSENTÉE EN VUE DE L'OBTENTION
DU DIPLÔME DE PHILOSOPHIAE DOCTOR (Ph.D.)
(GÉNIE MINÉRAL)
SEPTEMBRE 2004

© Qin Wang, 2004

UNIVERSITÉ DE MONTRÉAL

ÉCOLE POLYTECHNIQUE DE MONTRÉAL

Cette thèse intitulée

SEISMIC PROPERTIES OF POLYPHASE ROCKS

présentée par: WANG Qin

en vue de l'obtention du diplôme de: Philosophiae Doctor

a été dûment accepte par le jury d'examen constitué de:

M. CHOUTEAU Michel, Ph.D., président

M. JI Shaocheng, Ph.D., membre et directeur de recherche

M. MARTIGNOLE Jacques G., Ph.D., membre

M. MARESCHAL Jean C., Ph.D., membre

To my father Funan Wang 王扶南, *my mother Shuizhen Guo* 郭水珍,

and my husband Jilin Zhou 周济林

Acknowledgements

I would like to express my sincere gratitude to my supervisor Prof. Shaocheng Ji for his constant guidance, encouragement and help during my Ph.D period. Without his initiation of the project and financial support, I could not come to Canada to complete my thesis and explore a different culture. His enthusiasm, insights and dedication to science helped me to begin a research career and will inspire me in the future.

I am grateful to Prof. Matthew H. Salisbury for his support and kindness during the velocity measurements and during the preparation of thesis, and to Mr Robert Iuliucci for his generous technical assistance and patience in the GSC/Dalhousie High Pressure Laboratory. I would also like to thank Prof. Jacques Martignole for his constructive reading of my manuscripts and invaluable friendship, Prof. Denis Marcotte for his course Statistics that is useful to my research, and Dr. Mingbao Pan for his field assistance in the Sulu terrane, east China.

I would like to thank Département des Génies Civil, Géologique et des Mines of École Polytechnique de Montréal. It is such a friendly place for studying. Many thanks to Ms Manon Latour, Ms Huguette Perron and Mr André Lacombe for their efficient support and warm smile. And I gratefully acknowledge the China/Canada Educational Exchange Programs and École Polytechnique de Montréal for the exemption of my foreign student tuition fees.

Many thanks to Prof. Huafu Lu, Prof. Liangshu Wang and Prof. Dong Jia for encouraging me to study abroad and continuous help in these years, to all my friends in Canada and in China for shearing wonderful time together.

Finally, and most of all, I would like to thank my father Funan Wang, my mother Shuizhen Guo and my husband Jilin Zhou for their unconditional love, support and trust.

Résumé

La connaissance des propriétés sismiques des roches polyphasées est essentielle pour l'interprétation des profils sismiques réfraction et réflexion et pour l'établissement des modèles lithologiques et structuraux de la lithosphère. Le but de ce travail est d'améliorer notre compréhension des corrélations entre les propriétés sismiques des roches et les facteurs de contrôle (par exemple, la pression, la température, la présence de fluides, la composition chimique, la minéralogie, les orientation préférentielles des réseaux cristallins). Ces renseignments seront très utiles pour extrapoler les propriétés sismiques calculées et mesurées en laboratoire aux profondeurs voulues et pour expliquer les données sismiques en termes de composition lithologique et de processus géodynamiques.

Tout d'abord, nous avons établi une banque de données des propriétés sismiques des roches (DPSR: http://texture.civil.polymtl.ca:8080/seismic-properties/index.jsp) et publié un manuel des propriétés sismiques des minéraux, des roches et des minerais. Cette banque et ce manuel comportent presque toutes les données publiées depuis quarante ans et devraient être facilement utilisables pour les géophysiciens et les géologues. Le traitement statistique des données de la DPSR permet d'étudier les corrélations entre les propriétés sismiques d'une part et d'autre part la densité, la porosité, la teneur en eau, et les compositions minéralogiques et chimiques.

Dans la deuxième partie de ce travail, nous avons examiné les lois de mélange pour calculer des vitesses sismiques des ondes P (*Vp*). Nous avons calculé les *Vp* pour 696 échantillons à sec en tenant compte des proportions volumiques et des constantes élastiques de chacune des phases minérales et en utilisant 16 différentes lois de mélange. Bien que seulement 22 minéraux communs aient été pris en considération dans notre calcul, les vitesses obtenues coïncident avec les valeurs mesurées à ~300 MPa, pression à laquelle la plupart des microfractures sont fermées et la moyenne *Vp* d'une roche

polyphasée est exclusivement contrôlée par sa composition modale. Cependant, aucune des lois de mélange ne peut décrire toutes les *Vp* mesurées pour tous les types de roche et à toutes les pressions. Le choix d'une loi de mélange pour le calcul des vitesses sismiques demande donc une certaine prudence.

Dans la partie principale de ce travail, nous avons mesuré les vitesses sismiques de compression et de cisaillement (*Vp* et *Vs*) sous les pressions de confinement allant jusqu'à 800 MPa et suivant trois directions orthogonales, sur une trentaine d'écologites et de roches encaissantes. Les échantillons de roche métamorphiques de ultra-haute pression (UHP) ont été prélevés dans la ceinture orogénique Dabie-Sulu en Chine, soit le plus grand terrain UHP connu à ce jour. Les mesures réalisées permettent de déduire les propriétés sismiques et la composition lithologique en dessous des zones de subduction, et plus particulièrement le rôle des éclogites sur la réflectivité et sur le déphasage des ondes S dans la croûte inférieure et dans le manteau supérieur.

Nous avons distingué trois types d'éclogite suivant la taille du grain, le degré de métamorphisme rétrograde et les propriétés pétrophysiques. Les éclogites de Type-1 sont à grain grossier et représentent des éclogites aux conditions métamorphiques maximales (domaine de stabilité du diamant). Les éclogites de Type-2 sont à grain fin et formées pendant la première exhumation des eclogites de Type-1 depuis le manteau supérieur jusqu'à la croûte inférieure. Les éclogites de Type-3 sont rétrogradées dans les conditions du faciés des amphibolites pendant l'exhumation dans la croûte. La densité et les vitesses moyennes diminuent, depuis les éclogites de Type-1 jusqu'aux éclogites de Type-2 et aux éclogites de Type-3, ceci en raison d'une diminution du contenu en grenat et d'une augmentation des minéraux rétrogrades tels que l'amphibole, l'épidote, le mica et le plagioclase. L'anisotropie des éclogites de Type-1 et de Type-2 est généralement inférieure à 5% tandis que le métamorphisme rétrograde et le litage compositionnel peuvent augmenter l'anisotropie sismique et la biréfringence des ondes S dans les éclogites. Ceci nous permet donc de réévaluer la contribution des écologites à

l'anisotropie sismique du manteau supérieur, aussi bien dans les zones de subduction anciennes que dans les plus récentes.

Pour fournir plus de renseignements sur les propriétés pétrophysiques des roches communes, nous avons synthétisé toutes les données mesurées en laboratoire. À 600 MPa et 25 °C, les propriétés des éclogites sont: Vp = 7.991±0.489 km/s; Vs = 4.552±0.279 km/s; Vp/Vs = 1.756±0.044; le coefficient de Poisson (σ) = 0.259±0.018; la masse volumique (ρ) = 3.449±0.134 g/cm^3 et la teneur en SiO_2 = 46.9±3.9%. Les rapports Vp/Vs et les coefficients de Poisson des éclogites des trois types ci-dessus montrent les valeurs moyennes semblables mais les éclogites de Type-3 exhibent une plus grande variance.

En règle générale, les éclogites et les péridotites sont indétectables par leurs vitesses sismiques. Parce que les péridotites ont la dérivée de Vs par la température plus grande que les écologites, aux profondeurs du manteau supérieur, le coefficient de Poisson atteindra 0.24-0.25 pour les écologites de Type-1 et de Type-2, 0.28-0.29 pour les péridotites et 0.30-0.31 pour les péridotites serpentinisées, ce qui suggère une façon potentielle de les distinguer en utilisant des méthodes sismiques.

Nous avons proposé l'équation empirique suivante : $V = a(\ln P)^2 + b\ln P + c$ $(P \leq P_c)$ en régressant les données expérimentales et nous l'avons employée pour modéliser les vitesses sismiques à faible profondeur. Les paramètres a et b sont des constantes décrivant la fermeture des microfissures au-dessous d'une pression critique (P_c). Au-dessus de cette pression, toutes les microfractures sont fermées. Le paramètre c est la vitesse pour une pression (P) égale à l'unité (1 MPa). Au-dessus de la P_c, l'augmentation linéaire de vitesse est représentée par l'équation suivante : $V = V_0 + DP$, où V_0 est la vitesse théorique d'un échantillon élastique à la pression de 0.1 MPa, et D est la dérivée intrinsèque de la vitesse par rapport à la pression. Les élasticités linéaires des éclogites de Dabie-Sulu sont: Vp = 8.42+1.41×10^{-4}P et Vs = 4.76+1.46×10^{-4}P pour le Type-1, Vp =

$7.80+1.58\times10^{-4}P$ et $Vs = 4.44+1.67\times10^{-4}P$ pour le Type-2, et $Vp = 7.33+2.04\times10^{-4}P$ et $Vs = 4.21+2.02\times10^{-4}P$ pour le Type-3, où Vp et Vs sont en km/s et P en MPa.

Grâce à leur forte densité et leur grande vitesse de propagation, les éclogites et les péridotites non altérées peuvent produire des réflexions sismiques fortes aux contacts avec les gneiss granitiques, les paragneiss, les marbres, les amphibolites, les granulites et les péridotites serpentinisées. Nous pouvons interpréter la couche de Vp élevée (8.72 km/s à une profondeur de 71 kilomètres, Xu et al., 2001) sous la région de Dabie-Sulu comme une couche dominée par des éclogites de Type-1 et enfoncée dans le manteau supérieur depuis 200-220 Ma. Si un tel assemblage des matériaux continentaux a été « subducté » et est préservé dans le manteau supérieur aujourd'hui, comme les éclogites intercalées dans les gneiss felsiques, les quartzites à grenat et jadéite, les marbres et les péridotites serpentinisées, il peut générer des réflexions sur les profils sismiques des chaînes orogéniques.

En intégrant les données des vitesses sismiques mesurées en laboratoire et sur le terrain et en considérant les observations géologiques, nous avons employé les moyennes géométriques comme loi de mélange pour inverser les compositions lithologiques et chimiques de la croûte profonde dans la région des montagnes de Dabie et dans celle du terrain de Sulu. Les résultats indiquent que la plupart des éclogites seraient concentrées dans la croûte supérieure. Bien que la croûte inférieure de Dabie-Sulu montre une composition intermédiaire, les montagnes de Dabie pouraient contenir plus de granulites mafiques et avoir une croûte inférieure plus froide et plus dense que le terrain de Sulu. La lithosphère de Sulu a été fortement modifiée par l'extension tectonique de la croûte et par l'amincissement lithosphérique pendant le Cénozoïque. La rareté des éclogites dans la croûte profonde d'aujourd'hui suggère que la zone UHP de Dabie-Sulu représente des écailles tectoniques relativement minces du craton Yangtsé. Ce derniere a été « subducté » dans le manteau supérieur et ensuite exhumé rapidement. Les éclogites et les roches encaissantes ont été juxtaposées au-dessus d'une croûte moyenne à inférieure,

par chevauchement le long d'une série de zones de cisaillement dans la zone de collision entre le craton Yangtsé et le craton de Sino-Coréen.

Abstract

Knowledge about the seismic properties of polyphase rocks is fundamental for interpreting seismic refraction and reflection data and for establishing lithospheric structure and composition models. This study aims to obtain more precise relationships between seismic properties of rocks and controlling factors (e.g., pressure, temperature, mineralogical and chemical compositions, microstructure of rocks), particularly for those rocks imprinted by ultrahigh-pressure (UHP) metamorphism. These relationships will be very helpful to extrapolate calculated and measured seismic properties of rocks to depths of interest and to engender interpretations relevant to petrological composition and tectonic process.

An Internet Database of Rock Seismic Properties (DRSP) was set up and a *Handbook of Seismic Properties of Minerals, Rocks and Ores* was published. They comprise almost all data available in the literature during the past 4 decades and can serve as a convenient, comprehensive and concise information source on physical properties of rocks to the earth sciences and geotechnical communities. Statistical results of the DRSP reveal the dependence of seismic properties on density, porosity, humidity, and mineralogical and chemical compositions.

Using 16 different averaging methods, we calculated P-wave velocities of 696 dry samples according to the volume fraction and elastic constants of each constituent mineral. Although only 22 common minerals were taken into account in the computation, the calculated P-wave velocities agree well with laboratory values measured at about 300 MPa, where most microcracks are closed and the mean Vp of a polymineralic rock is exclusively controlled by its modal composition. However, none of these mixture rules can simultaneously fit measured P-wave velocities for all lithologies or at all pressures. Therefore, more prudence is required in selecting an appropriate mixture rule for calculation of seismic velocities of different rock types.

Widely exposed diamond- and/or coesite-bearing rocks in the Dabie-Sulu orogenic belt in eastern central China, the largest known UHP metamorphic belt up to now, provide an ideal opportunity to study seismic properties of UHP rocks. We measured P- and S-wave velocities (*Vp* and *Vs*), anisotropy and shear wave splitting of eclogites and their country rocks from the Dabie-Sulu UHP belt under confining pressure up to 800 MPa. Three types of eclogites were distinguished according to their grain size, degree of retrograde metamorphism and petrophysical properties. Type-1 eclogites are coarse-grained and almost unaffected by retrograde metamorphism, representing eclogites at peak metamorphic conditions (in the diamond stability field). Type-2 eclogites are fine-grained, reworked Type-1 eclogites under quartz/coesite boundary conditions during exhumation from the upper mantle to lower crust. Type-3 eclogites are overprinted by amphibolite facies metamorphism during exhumation within the crust. From Type-1 to Type-2 and to Type-3 eclogites, seismic velocities and density successively decrease due to a decrease in garnet content and an increase in retrograde minerals such as amphibole, epidote, mica and plagioclase. Seismic anisotropy of Type-1 and Type-2 eclogites is generally less than 5% while the retrograde metamorphism and compositional layering can result in significant anisotropy and shear wave splitting in eclogites, implying a detectable contribution of eclogites to seismic anisotropy of the upper mantle.

In order to provide constraints on lithological interpretation of seismic profiles, we summarized petrophysical properties of common rock types by integrating previous experimental data with results of this study. The average properties of 57 eclogite samples at 600 MPa and 25 °C are: Vp = 7.991±0.489 km/s, Vs = 4.552±0.279 km/s, Vp/Vs = 1.756±0.044, σ = 0.259±0.018, ρ = 3.449±0.134 g/cm^3 and SiO_2 = 46.9±3.9%. From Type-1 to Type-2 to Type-3 eclogites, Vp/Vs ratios and Poisson's ratios display similar mean values but wider variations.

The similarities in P- and S-wave velocities of eclogites and peridotites lead to an ambiguity in interpretation of seismic profiles. However, because peridotites have larger

temperature derivatives of *Vs* than eclogites, Poisson's ratios, at depths of upper mantle, will reach 0.24-0.25 for Type-1 and Type-2 eclogites, 0.28-0.29 for peridotites and 0.30-0.31 for serpentinized peridotites, implying a way to distinguish them by seismic methods.

In order to curve-fit experimental data points, an empirical equation $V = a(\ln P)^2 + b\ln P + c$ ($P \leq P_c$) was proposed to describe the nonlinear velocity increase below a critical pressure (P_c), at which all microcracks are closed and rocks behave as purely elastic aggregates. Parameters a and b are constants describing the closure of microcracks below P_c; c is the velocity when pressure (P) is equal to unity (1 MPa). This equation is used to predict seismic velocities at shallow depth, which provides satisfying agreement with reflection profile passing through the Chinese Continental Scientific Drilling borehole. Above P_c, the linear velocity increase follows $V = V_0 + DP$, where V_0 is the projected velocity of a crack-free sample at room pressure, and D is the intrinsic pressure derivative of velocitiy. Average linear velocity-pressure relationships of eclogites from the Dabie-Sulu UHP belt are: $Vp = 8.42+1.41\times10^{-4}P$ and $Vs = 4.76+1.46\times10^{-4}P$ for Type-1, $Vp = 7.80+1.58\times10^{-4}P$ and $Vs = 4.44+1.67\times10^{-4}P$ for Type-2, and $Vp = 7.33+2.04\times10^{-4}P$ and $Vs = 4.21+2.02\times10^{-4}P$ for Type-3, where Vp and Vs are in km/s and P in MPa.

Due to high density and velocity, eclogites and peridotites can produce strong seismic reflections at contacts with granitic gneisses, paragneisses, marbles, amphibolites, granulites and serpentinized peridotites in the complex of the UHP rocks. The high Vp layer (8.72 km/s at a depth of 71 km) beneath the Dabie-Sulu region can be interpreted as the remnant of a subducted slab, which is dominated by Type-1 eclogites and has frozen in the upper mantle since about 200-220 Ma. Such relic crustal materials, subducted and preserved as eclogites interlayered with felsic gneisses, garnet-jadeite quartzites, marbles and serpentinized peridotites, could be responsible for observed mantle reflections beneath orogenic belts.

Combining laboratory-derived in situ seismic velocities of rocks with seismic refraction data and geological observations, we used the geometric mean as a mixture rule to invert lithological and chemical compositions of the crust beneath the Dabie-Sulu UHP belt. The results indicate that most eclogites are concentrated in the uppermost crust. Although both the Dabie Mountains and the Sulu terrane display a bulk intermediate lower crust, the Dabie Mountains may contain more mafic granulites and have a colder, denser lower crust than the Sulu terrane that experienced crustal extension and lithospheric thinning during the Cenozoic. The scarcity of eclogites in the today's deep crust suggests that the Dabie-Sulu UHP belt consists of tectonic slices of deeply exhumed continental crust of the Yangtze craton. These eclogite-bearing UHP rocks were juxtaposed over an UHP-free middle-lower crust by syncollisional exhumation along a series of shear zones between the Sino-Korean and Yangtze cratons.

Condensé en français

L'étude des propriétés sismiques des roches polyphasées permet d'obtenir des informations essentielles pour interpréter les profils sismiques réfraction et réflexion en termes de composition lithologique, de structure et de déformation. Beaucoup de facteurs tels que l'hétérogénéité latérale, l'anisotropie, la porosité, la température et la pression affectent les vitesses mesurées. Le but de ce travail est de mettre en lumière les questions suivantes :

- Comment peut-on décrire, d'une manière quantitative et précise, la variation de vitesse sismique et d'anisotropie des roches en fonction de la pression hydrostatique, et comment peut-on interpréter les observations sismiques à partir des propriétés sismiques des échantillons de petite taille?
- Quelle est l'influence des lois de mélange sur le calcul des vitesses sismiques des roches polyphasées?
- Comment peut-on expliquer la réflectivité et les couches à vitesse élevée dans la croûte continentale et dans le manteau supérieur? Quels renseignements géodynamiques la réflectivité et les vitesses sismiques peuvent-elles fournir, particulièrement pour les zones de subduction?

Pour aborder les problèmes mentionnés ci-dessus, deux méthodes ont été utilisées : le calcul des propriétés élastiques des agrégats cristallins et la mesure directe des vitesses sismiques en laboratoire. La comparaison des données théoriques et expérimentales permet d'évaluer les facteurs de contrôle et d'extrapoler les propriétés sismiques calculées et mesurées en laboratoire aux conditions correspondant aux profondeurs voulues, et d'interpréter les observations sismiques en termes de composition lithologique et de processus géodynamique. Afin de relier les propriétés sismiques des roches et l'interprétation des profils sismiques, nous avons choisi la ceinture orogénique Dabie-Sulu en Chine, soit le plus grand terrain de ultra-haute pression (UHP) connu à ce jour. L'étude pétrophysique de roches prélevées dans cette région, principalement

d'éclogites, sert à déduire la contribution des roches UHP à l'anisotropie et à la réflectivité dans les zones de subduction, et à examiner les modèles tectoniques d'exhumation des roches UHP dans la croûte inférieure et dans le manteau supérieur.

Le premier chapitre est consacré à développer ces deux méthodes et les informations qu'elles apportent à notre connaissance des propriétés sismiques de la croûte continentale. Le calcul des vitesses de propagation des ondes P et S (*Vp* et *Vs*) dans les roches est fondé sur la théorie de l'élasticité des matériaux. En combinant les coefficients d'élasticité des minéraux, les orientations préférentielles de réseau des minéraux et les compositions modales des roches, nous pouvons calculer les propriétés sismiques des agrégats cristallins (Cross et Lin, 1971; Ji et Mainprice, 1988; Mainprice, 1990, par exemple). Les vitesses de propagation des ondes sismiques sur des échantillons sont principalement contrôlées par deux facteurs : la microfracturation et l'orientation préférentielle de réseaux. À relativement basse pression de confinement, les vitesses sismiques augmentent très rapidement et après ~300 MPa la croissance des vitesses devient linéaire à pression de confinement élevée. Par contre, l'augmentation de température va diminuer les vitesses sismiques.

Dans le deuxième chapitre nous introduisons rapidement une base de données sur les propriétés sismiques des roches (DPSR). Il y a de nombreux articles qui contiennent la mesure des vitesses sismiques des roches à pression élevée et à température élevée depuis que Birch (1960, 1961) a publié ses mesures expérimentales de *Vp* jusqu'à 1000 MPa. Afin de fournir une source informatisée et complète pour les géophysiciens et les géologues, nous avons établi DPSR (http://texture.civil.polymtl.ca :8080/seismic-properties/index.jsp) et nous avons publié un manuel des propriétés sismiques des minéraux, des roches et des minerais (Ji et al., 2002). Cette banque et ce manuel comportent presque toutes les données publiées depuis quarante ans. Le traitement statistique des données de la DPSR permet de faire les corrélations entre les propriétés

sismiques d'une part et d'autre part la densité, la porosité, la teneur en eau, et les compositions minéralogiques et chimiques.

Dans le troisième chapitre, ayant accès aux propriétés sismiques de nombreux échantillons, nous avons calculé les vitesses sismiques des ondes P de 696 échantillons à sec à partir des données de la DPSR, en tenant compte des proportions volumiques et des constantes élastiques de chaque phase minérale et en utilisant 16 lois de mélange. En comparant les vitesses calculées et les vitesses mesurées, nous pouvons juger qu'elle est la méthode la plus appropriée pour le calcul des vitesses sismiques des roches polyphasées.

En raison du manque d'information sur l'orientation et la distribution géométrique de chaque phase, nous assumons que nos échantillons de roches sont isotropes. Les vitesses sismiques d'un agrégat isotrope peuvent être déterminées en deux étapes. La première étape consiste à calculer les modules élastiques (le module d'élasticité volumique K_i, et le module de cisaillement G_i) de l'agrégat monominéral polycristallin à partir de tous les minéraux constitutifs. La deuxième étape consiste à calculer le module élastique M_c (K ou G) de la roche polyminéral de la façon suivante : $M_c = \left[\sum_{i=1}^{N}(f_i M_i^J)\right]^{1/J}$, où f_i est la fraction volumique du i^e minéral et J est un paramètre de microstructure. Le cas $J = 1$ correspond à la moyenne arithmétique ou moyenne de Voigt (M_V), et le cas $J = -1$ est la moyenne harmonique ou moyenne de Reuss (M_R). La moyenne de Hill (M_H) est indiquée par : $M_H = (M_V + M_R)/2$. Comme J approche 0, la limite de M_c est la moyenne géométrique (M_G). Ensuite, les vitesses de propagation des ondes P des roches sont calculées à partir des valeurs de M_c et de la densité (ρ) : $Vp = \sqrt{\frac{K + 4G/3}{\rho}}$. Il y a en tout 16 possibilités pour prévoir les propriétés élastiques d'une roche polyphasée. Elle sont désignées par les termes VV, VR, VH, VG, RV, RR, RH, RG, HV, HR, HH, HG, GV, GR, GH, et GG, où V, R, H et G dénotent les moyennes de Voigt, Reuss, Hill et

géométrique, respectivement. La première lettre représente la méthode employée dans la première étape et la deuxième, la loi de mélange dans la deuxième étape.

Les 696 échantillons sont classés suivants 15 lithologies communes. Nous avons examiné les erreurs absolues et les erreurs relatives entre les vitesses mesurées et calculées par les 16 méthodes pour quantifier les effets des lois de mélange sur le calcul. Bien que seulement 22 minéraux communs aient été pris en considération dans notre calcul, les vitesses obtenues coïncident avec les valeurs mesurées à ~300 MPa, pression à laquelle la plupart des microfractures sont fermées et à laquelle la moyenne *Vp* d'une roche polyphasée est exclusivement contrôlée par sa composition modale. Quand une loi de mélange appropriée est employée et quand la composition modale est correctement déterminée, les *Vp* calculées peuvent caractériser les propriétés séismiques moyennes des roches et se comparer avec les données obtenues dans les profils sismiques.

Cependant, aucune des lois de mélange ne peut décrire toutes les *Vp* mesurées pour tous les types de roche et à toutes les pressions. Par exemple, sous une pression de 200 à 500 MPa, la loi VR permet d'obtenir une meilleure prédiction de *Vp* pour l'amphibolite, l'anorthosite, la diorite, le granite-granodiorite, le gneiss quartz-feldspathique et le marbre; mais la loi RH est plus appropriée pour les *Vp* de l'éclogite et de la peridotite. Les *Vp* calculées par la loi HH s'accordent bien avec les vitesses mesurées sur les gneiss intermédiaires et sur le quartzite. Le choix d'une loi de mélange pour le calcul des vitesses sismiques demande donc une certaine prudence.

Pour étudier les propriétés sismiques de la croûte inférieure et du manteau supérieur, et plus particulièrement le rôle que peut y jouer l'anisotropie et la réflectivité dans les zones de subduction, nous avons mesuré les vitesses de propagation des ondes P et S sous des pressions de confinement allant jusqu'à 800 MPa et suivant trois directions orthogonales, et ce sur une trentaine d'écologites et de roches encaissantes prélevées dans la ceinture orogénique Dabie-Sulu en Chine. Les résultats et la discussion sont exposés en

deux parties qui font l'objet chacune d'un article, sur les vitesses de propagation des ondes P et S, respectivement. Nous consacrerons les chapitres 4 et 5 à deux articles qui constituent la partie principale de cette thèse.

La ceinture orogénique Dabie-Sulu en Chine est un des rares objets géologiques où l'on peut effectivement observer des roches métamorphiques de ultra-haute pression. Les roches UHP représentent les matériaux de la croûte du craton Yangtsé qui ont été « subductés » à plus de 100 km et rapidement exhumés pendant la collision entre le craton Yangtsé et le craton de Sino-Coréen. Parce que l'éclogitisation des roches gabbroïques ou basaltiques est la clé de l'évolution des zones de subduction, l'écologite a déjà fait l'objet de nombreux travaux pétrographiques et géochimiques et, en moindre mesure, des travaux de sismique et de géodynamiques. En juillet 2001 le programme de forage scientifique continental chinois (FSCC) a commencé près du village de Maobei, au sud de la zone UHP de Sulu terrane. Le forage de FSCC doit atteindre une profondeur de 5000 m au printemps de 2005, et traverser toutes les couches à vitesse élevée et tous les réflecteurs. Les nouveaux profils sismiques dans cette région donnent une chance de vérifier les propriétés sismiques des roches UHP obtenues en laboratoire. Par ailleurs, nous avons déterminé la composition de la croûte de Dabie-Sulu. Cela permet d'évauler les différents modèles d'exhumation des matériaux continentaux.

Grâce à l'étude détaillée des propriétés sismiques des éclogites et grâce à l'observation directe des roches, nous avons distingué trois types d'éclogites dans le Dabie-Sulu, et ce, suivant la taille du grain, le degré de métamorphisme rétrograde et les propriétés pétrophysiques. Les éclogites de Type-1 sont à grain grossier et correspondent à des conditions maximales de métamorphism (domaine de stabilité du diamant). Elles se composent principalement de grenat et d'omphacite, avec des quantités mineures de rutile (~1-2%), de coesite et/ou de quartz. Les éclogites de Type-2, à grain fin, ont été formées pendant la remonté initiale des eclogites de Type-1 depuis le manteau supérieur jusqu'à la croûte inférieure. La foliation est définie principalement par le litage compositionnel et

la linéation d'étirement est définie par le grenat et l'omphacite allongés. Les éclogites de Type-3 ont subi le métamorphisme rétrograde dans les conditions du faciès des amphibolites pendant le processus d'exhumation. Elles contiennent du grenat et de l'omphacite qui ont été remplacés par les assemblages symplectiques d'amphibole, de quartz et de plagioclase, avec une quantité variable de phengite, de rutile et d'épidote.

Bien que les éclogites aient généralement des densités et des vitesses élevées et une anisotropie faible, les différences de proprietés sismiques parmi les trois types d'éclogites sont remarquables. Les éclogites de Type 1 ont les plus fortes densités (ρ = 3.57±0.05 g/cm^3) et les plus hautes vitesses sismiques (Vp = 8.51±0.11 km/s et Vs = 4.85±0.06 km/s à 600 MPa); les éclogites de Type-2 ont des densités modérées (ρ = 3.44±0.07 g/cm^3) et des vitesses intermédiaires (Vp = 7.89±0.16 km/s et Vs = 4.53±0.04 km/s à 600 MPa); et les éclogites Type-3 ont les densités relativement faibles (ρ = 3.44±0.03 g/cm^3) et les plus basses vitesses sismiques (Vp = 7.46±0.26 km/s et Vs = 4.33±0.09 km/s à 600 MPa). La diminution des densités et des vitesses sismiques depuis les éclogites de Type-1 jusqu'aux éclogites de Type-2 et aux éclogites de Type-3 correspond à la diminution du contenu en grenat et à l'augmentation des minéraux rétrogrades. L'anisotropie des éclogites de Type-1 et de Type-2 est généralement inférieure à 5% tandis que le métamorphisme rétrograde et le litage compositionnel peuvent augmenter l'anisotropie sismique et la biréfringence des ondes S dans les éclogites, suggérant leur contribution possible à l'anisotropie sismique dans la croûte inférieure, le manteau supérieur, en particulier dans les zones de subduction.

Pour fournir plus de renseignements sur les propriétés pétrophysiques des roches, nous avons synthétisé toutes les données mesurées en laboratoire et nous avons estimé les dérivées de Vp et Vs par rapport à la température et par rapport à la pression pour des roches communes. Les propriétés des éclogites à 600 MPa et 25 °C sont: Vp = 7.991±0.489 km/s; Vs = 4.552±0.279 km/s; Vp/Vs = 1.756±0.044; le coefficient de Poisson (σ) = 0.259±0.018; la densité = 3.449±0.134 g/cm^3 et la teneur en SiO_2 =

46.9±3.9%. Les rapports Vp/Vs et les coeffieients de Poisson des éclogites des trois types ci-dessus montrent des valeurs moyennes semblables mais les éclogites de Type-3 ont une plus grande variance.

Généralement, les éclogites et les péridotites sont indétectables par leurs vitesses sismiques. Vu que les péridotites ont la dérivée de Vs par rapport à la température plus grande que les écologites, aux profondeurs du manteau supérieur, le coefficient de Poisson atteindra 0.24-0.25 pour les écologites de Type-1 et de Type-2, 0.28-0.29 pour les péridotites et 0.30-0.31 pour les péridotites serpentinisées, ce qui suggère une façon potentielle de les distinguer en utilisant des méthodes sismiques.

Nous avons proposé l'équation empirique suivante : $V = a(\ln P)^2 + b\ln P + c \ (P \leq P_c)$ en régressant les données expérimentales. Les paramètres a et b sont des constantes décrivant la fermeture des microfissures au-dessous d'une pression critique (P_c). Au-dessus de cette pression, toutes les microfractures sont fermées. Le paramètre c est la vitesse pour une pression (P) égale à l'unité (1 MPa). Au-dessus de la P_c, l'augmentation linéaire de vitesse est représentée par l'équation suivante : $V = V_0 + DP$, où V_0 est la vitesse théorique d'un échantillon élastique à la pression de 0.1 MPa, et D est la dérivée intrinsèque de la vitesse par rapport à la pression. Les élasticités linéaires des éclogites de Dabie-Sulu sont: $Vp = 8.42+1.41\times10^{-4}P$ et $Vs = 4.76+1.46\times10^{-4}P$ pour le Type-1, $Vp = 7.80+1.58\times10^{-4}P$ et $Vs = 4.44+1.67\times10^{-4}P$ pour le Type-2, et $Vp = 7.33+2.04\times10^{-4}P$ et $Vs = 4.21+2.02\times10^{-4}P$ pour le Type-3, où Vp et Vs sont en km/s et P en MPa.

Nous avons employé l'équation nonlinéaire pour modéliser les vitesses sismiques dans le forage de FSCC et pour calculer les coefficients de réflexion aux contacts entre des lithologies. Les coefficients de réflexion calculés s'accordent bien avec les réflexions observées. Grâce à leur forte densité et leur grande vitesse de propagation, les éclogites et les péridotites non altérées peuvent produire des réflexions sismiques fortes aux contacts avec les gneiss granitiques, les paragneiss, les marbres, les amphibolites, les granulites et

les péridotites serpentinisées. Nous pouvons interpréter la couche de *Vp* élevée (8.72 km/s à une profondeur de 71 kilomètres, Xu et al., 2001) sous la région de Dabie-Sulu comme une couche dominée par les éclogites de Type-1 et enfouie dans le manteau supérieur depuis 200-220 Ma. Si un tel assemblage de matériaux continentaux a été « subducté » et est préservé dans le manteau supérieur aujourd'hui, comme les éclogites intercalées dans les gneiss felsiques, les quartzites à grenat et jadéite, les marbres et les péridotites serpentinisées, il peut générer des réflexions sur les profils sismiques des chaînes orogéniques. Des exemples de cette situation peuvent retrouver dans la Province Supérieure du Canada (Calvert et al., 1995; Bostock, 1997) et dans les Territories Nord-oust (Cook et al., 1999).

En intégrant les données des vitesses sismiques mesurées en laboratoire et sur le terrain et en considérant les observations géologiques, nous avons employé les moyennes géométriques comme loi de mélange pour inverser les compositions lithologiques et chimiques de la croûte profonde dans la région des montagnes de Dabie et dans celle du terrain de Sulu. Les résultats indiquent que la plupart des éclogites seraient concentrées dans la croûte supérieure. Bien que la croûte inférieure de Dabie-Sulu montre une composition intermédiaire, les montagnes de Dabie pouraient contenir plus de granulites mafiques et avoir une croûte inférieure plus froide et plus dense que le terrain de Sulu. La lithosphère de Sulu a été fortement modifiée par l'extension tectonique de la croûte et par l'amincissement lithosphérique pendant le Cénozoïque. La rareté des éclogites dans la croûte profonde d'aujourd'hui suggère que la zone UHP de Dabie-Sulu représente des écailles tectoniques relativement minces du craton Yangtsé. Ce dernier a été « subducté » dans le manteau supérieur et exhumé rapidement. Les éclogites et les roches encaissantes ont été juxtaposées au-dessus d'une croûte moyenne à inférieure, par chevauchement le long d'une série de zones de cisaillement dans la zone de collision entre le craton Yangtsé et le craton de Sino-Coréen.

Table of contents

DEDICATION ..... **IV**

ACKNOWLEDGEMENTS ..... **V**

RÉSUMÉ ..... **VI**

ABSTRACT ..... **XI**

CONDENSÉ EN FRANÇAIS ..... **XV**

TABLE OF CONTENTS ..... **XXIII**

LIST OF TABLES ..... **XXVI**

LIST OF FIGURES ..... **XXVII**

LIST OF INITIALS AND ABBREVIATIONS ..... **XXXIII**

LIST OF APPENDICES ..... **XXXV**

INTRODUCTION **1**

CHAPTER 1 LITERATURE REVIEW **4**

1.1 Calculation of seismic properties of polyphase rocks 4

1.1.1 Theory of elasticity 4

1.1.2 Seismic properties of rock-forming minerals 9

1.1.3 Seismic properties of polyphase rocks 23

1.2 Laboratory sample studies 25

1.3 Seismic properties of the continental crust and upper mantle 31

1.3.1 Velocity structures 31

1.3.2 Seismic anisotropy 35

CHAPTER 2 DATABASE OF ROCK SEISMIC PROPERTIES (DRSP) **39**

2.1 Database design 40

2.2 Statistic results of the DRSP 42
2.2.1 Velocity – density relationship 46
2.2.2 Velocity – porosity relationship 50
2.2.3 Seismic properties of different lithologies 51
2.3. Summary 61

CHAPTER 3 P-WAVE VELOCITIES OF POLYMINERALIC ROCKS: COMPARISION OF THEORY AND EXPERIMENT AND TEST OF ELASTIC MIXTURE RULES 62

3.1 Introduction 62
3.2 Procedure of *Vp* calculation 64
3.3 Comparison of theory and experiment 65
3.3.1 Measured Vp data 65
3.3.2 Absolute error 68
3.3.3. Relative error 72
3.4 Discussion 82
3.5 Conclusions 88

CHAPTER 4 PRESSURE DEPENDENCE AND ANISOTROPY OF P-WAVE VELOCITIES IN ULTRAHIGH-PRESSURE METAMORPHIC ROCKS FROM THE DABIE-SULU OROGENIC BELT (CHINA): IMPLICATIONS FOR SEISMIC PROPERTIES OF SUBDUCTED SLABS AND ORIGIN OF MANTLE REFLECTIONS 90

4.1 Abstract 91
4.2 Introduction 92
4.3 Geological setting 96
4.4 Samples and experimental technique 100
4.5 Experimental results 111
4.5.1 Vp data 111
4.5.2 Vp anisotropy 115

4.6 Discussion 117
4.6.1 Pressure dependence of P-wave velocities 117
4.6.2 Seismic anisotropy 126
4.6.3 Implications for the upper mantle structure beneath the orogenic belt 130
4.6.4 Origin of seismic reflections in the upper mantle 132
4.7 Conclusions 138

CHAPTER 5 SHEAR WAVE PROPERTIES AND POISSON'S RATIOS OF ULTRAHIGH-PRESSURE METAMORPHIC ROCKS FROM THE DABIE-SULU OROGENIC BELT, CHINA: IMPLICATIONS FOR CRUSTAL COMPOSITION 141

5.1 Abstract 142
5.2 Introduction 143
5.3 Geological setting 146
5.4 Samples and experimental technique 147
5.5 Experimental results 149
5.5.1 Shear wave velocities 149
5.5.2 Shear wave anisotropy 161
5.5.3 Shear wave splitting 162
5.6 Discussion 164
5.6.1 Pressure dependence of shear wave velocity 164
5.6.2 Velocity-depth behavior of Dabie-Sulu lithologies 168
5.6.3 Poisson's ratio 177
5.6.4 Implications for crustal composition and exhumation of UHP rocks 179
5.7 Conclusions 189

CHAPTER 6 GENERAL DISCUSSION AND CONCLUSIONS 192

REFERENCES 199

APPENDICES 227

List of tables

Table 1.1 Stress-strain relations for orthorhombic, hexagonal, cubic and isotropic systems 6

Table 1.2 Independent single-crystal stiffness coefficients at room conditions 7

Table 1.3 Anisotropic seismic properties of single crystals 12

Table 3.1 Bulk (*K*) and shear (*G*) moduli (in GPa) of 22 monomineralic aggregates calculated with the Voigt (V), Reuss (R), Hill (H) and geometric (G) averages. 66

Table 3.2 Mean absolute errors and seismic anisotropy for 15 common lithologic categories (the seismic velocities and anisotropy were measured at 300 MPa) 86

Table 4.1 Sample number, locality, lithology and modal composition (vol. %) 97

Table 4.2 Chemical composition (wt.%) and mean atomic weight of samples 105

Table 4.3 *Vp* (km/s), anisotropy (%) and densities at various confining pressures of UHP rocks from the Dabie-Sulu belt 108

Table 4.4 Least square solutions of *Vp*-pressure relationships for UHP rocks from the Dabie-Sulu belt 123

Table 4.5 Average values of parameters for *Vp*-pressure relationship and pressure derivatives at various confining pressures 124

Table 4.6 Reflection coefficients (Rc) at possible lithological interfaces in the Dabie-Sulu UHP belt at 50 MPa and 600 MPa 136

Table 5.1 S-wave velocities (km/s) and anisotropy (%) at various confining pressures for UHP rocks from the Dabie-Sulu belt 150

Table 5.3 Average parameters describing variations of P- and S-wave velocities with pressure and temperature 172

Table 5.4 Shear wave reflection coefficients (Rc) at possible lithological interfaces in the Dabie-Sulu UHP belt at 50 MPa and 600 MPa 176

Table 5.5 Average densities, *Vp*, *Vs* and Poisson's ratios of 22 common rock types at confining pressures of 200, 400 and 600 MPa 180

Table 5.6 Characteristics of three types of eclogites from the Dabie-Sulu UHP belt, China 190

Table A1.1 *J*-value as functions of the phase shape and distribution 257

List of figures

Figure 1.1 Stress components acting on the faces of a unit cube. 5

Figure 1.2 Shear wave splitting and direction setting in an anisotropic body. 10

Figure 1.3 P- and S-wave properties of 16 common rock-forming minerals. 12

Figure 1.4 Seismic properties of an amphibolite from Ivrea Zone as a function of pressure at 20 °C and as a function of temperature at 600 MPa (original data from Barruol, 1993). (a) *Vp*-pressure, (b) *Vs*-pressure, (c) *Vp*-temperature, (d) *Vs*-temperature, (e) anisotropy-pressure, and (f) anisotropy-temperature. 28

Figure 1.5 Comparison of (a) measured Poisson's ratio and Vp (200 MPa, 25 °C) of common rock types with (b) theoretical values of monomineralic aggregates 29

Figure 1.6 Variations of seismic properties at 600 MPa in a quartzite due to the α-β quartz transition with changing temperature. (a) P-wave velocities in the X, Y and Z directions, (b) S-wave velocities propagating and vibrating in the X, Y, and Z directions, and (c) the mean P- and S-wave velocities..... 30

Figure 1.7 Contour map of global crustal thickness, Northern Polar Regions are not shown 31

Figure 1.8 Travel time anomalies from 400 to 40 km to an average Earth. Dark areas are fast relative to the Earth, while light areas are slow 32

Figure 1.9 Average crustal columns for seven geologic provinces, showing variations in crustal thickness 33

Figure 2.1 Structure of the database of rock seismic properties (DRSP). 41

Figure 2.2 (a) Histogram of P-wave velocities for 3259 samples, and (b) histogram of S-wave velocities for 1206 samples at 600 MPa and 25 °C. 42

Figure 2.3 (a) Histogram of P-wave velocities for 235 samples, and (b) histogram of S-wave velocities for 209 samples at 600 MPa and 600 °C. 43

Figure 2.4 Histogram of P-wave velocities at 200 MPa and 25 °C of wet basalt samples from (a) Atlantic Ocean and (b) Pacific Ocean..... 44

Figure 2.5 Histograms of mean P- and S-wave velocities at 600 MPa and 25 °C for igneous and metamorphic rocks from (a-b) Canada and (c-d) USA..... 45

Figure 2.6 (a) *Vp*-density and (b) *Vs*-density relations at 600 MPa and 25 °C..... 47

Figure 2.7 (a) *Vp*-density and (b) *Vs*-density relations for typical lower crustal rocks measured at 600 MPa and 25 °C. N – Sample number..... 48

Figure 2.8 Variations of the mean *Vs* as a function of density. 49

Figure 2.9 Dependence of P- and S-wave velocities on porosity (ϕ) for dry clastic rocks. (a) *Vp* at 50 MPa versus porosity and (b) *Vs* at 50 MPa versus porosity. 50

Figure 2.10 Dependence of P- and S-wave velocities on porosity (ϕ) of water-saturated basalts at confining pressure of (a) 200 MPa and (b) 600 MPa.. 52

Figure 2.11 P-wave velocities at 600 MPa of quartzofeldspathic rocks versus (a) quartz content and (b) feldspar content. 53

Figure 2.12 (a) *Vp* versus SiO_2 content at 600 MPa and 25°C for 499 samples, and (b) *Vp* versus content of Fe_2O_3+FeO+MgO at 600 MPa and 25°C for 416 samples.. 54

Figure 2.13 (a) *Vs* versus SiO_2 content at 600 MPa and 25°C for 255 samples, and (b) *Vs* versus content of Fe_2O_3+FeO+MgO at 600 MPa and 25°C for 234 samples.. 55

Figure 2.14 (a-b) P-wave velocities (c-d) S-wave velocities at 200 MPa versus silica content and density of coarse-grained igneous rocks, respectively. 56

Figure 2.15 Average anisotropy of P-wave velocity for common lithologies at 600 MPa. 58

Figure 2.16 Split shear wave velocities of peridotites along Z-direction at (a) 100 MPa and (b) 600 MPa. 59

Figure 2.17 Average seismic velocities and Poisson's ratios at 600 MPa of common rock types. (a) *Vp*, (b) *Vs* and (c) Poisson's ratio. 60

Figure 3.1 Comparison of the theoretical P-wave velocities (zero porosity, 25 °C and 0.1 MPa) with those measured at different pressure.. 69

Figure 3.2 Elastic wave velocity versus pressure. 71

Figure 3.3 Comparison of the theoretical P-wave velocities (zero porosity, 25 °C and 0.1 MPa) with those measured at different pressure for 15 common categories of rocks. 73

Figure 3.4 Relative errors of the VV (a), RR (b), HH (c) and VR (d) models for 696 samples. 76

Figure 3.5 Relative errors of the HH model for 15 common lithologic categories. 78

Figure 3.6 Relative errors of the VR model for 15 common lithologic categories. 80

Figure 3.7 Relative errors of the RH model for eclogite (a) and peridotite (b). 82

Figure 3.8 Seismic anisotropy versus absolute error plots for each sample. (a) HH model, (b) VR model, and (c) VH model. 85

Figure 4.1 Simplified geological map of the Sulu metamorphic terrane, eastern China.. 93

Figure 4.2 Elastic wave velocity (V) versus pressure (P). 95

Figure 4.3 (a) Eclogite blocks in serpentinized garnet peridotite, (b) Contact between foliated, fine-grained eclogite and felsic gneiss, (c) Interlayered garnetite and omphacitite, and (d) Coarse-grained eclogite.. 99

Figure 4.4 P-T-t paths of three types of Dabie-Sulu eclogites..... 102

Figure 4.5 Typical microstructures of eclogites from the Sulu terrane, China. (a) Type-1 eclogite with flattened and stretched garnet and omphacite grains. (b) Radiating cracks surrounding polycrystalline quartz aggregate after a coesite inclusion in omphacite from Type-1 eclogite. (c-d) SEM orientation contrast images of Type-2 eclogites with fine-grained recrystallized garnet and omphacite neoblasts. (e-f) Type-3 retrograded eclogites with fibrous symplectites of fine-grained hornblende, quartz and magnetite along grain boundary cracks. 103

Figure 4.6 Relationships between major oxides (weight percent) of the Dabie-Sulu eclogites. (a) Al_2O_3 versus SiO_2 and (b) MgO versus Na_2O..... 106

Figure 4.7 P-wave velocities versus pressure in the X, Y and Z directions for three typical eclogite samples (MB27: Type-1 eclogite; DG1: Type-2 eclogite; QL2: Type-3 eclogite) from the Sulu UHP zone. 112

Figure 4.8 Mean P-wave velocities versus densities at 50 MPa (a) and 600 MPa (b) for Dabie-Sulu samples. 113

Figure 4.9 Variations of eclogite P-wave velocity at 600 MPa as a function of (a) garnet (Grt) content and (b) the volume fraction of pyroxene (Pyx), amphibole (Amp) and symplectite (Symp). 114

Figure 4.10 Mean P-wave velocities of eclogites at 600 MPa versus silica content. 115

Figure 4.11 Vp anisotropy as a function of pressure for Dabie-Sulu UHP rocks. (a) Type-1 eclogites, (b) Type-2 eclogites, (c) Type-3 eclogites, and (d) Country rocks..... 116

Figure 4.12 Experimental data points are best fit by the expressions $V = a(\ln P)^2 + b\ln P + c$ and $V = DP + V_0$ at pressures below and above P_c, respectively. (a) Core X from MB23 (Type-1 eclogite), (b) Core X from DG1 (Type-2 eclogite), (c) Core Z from JC1 (Type-3 eclogite), and (d) Core Y from TF1 (granitic gneiss). 120

Figure 4.13 Pressure derivative (Vp') as a function of pressure for Sulu eclogite MB27X.. 121

Figure 4.14 Intrinsic pressure derivatives (D) and reference velocities (V_0) of eclogites from (a-b) low-pressure (300-600 MPa) and (c-d) high-pressure (600-1000 MPa) measurements. 125

Figure 4.15 Normalized pressure derivative (δ_λ) as a function of pressure in the nonlinear regime for (a) Pattern 1, (b) Pattern 2, and (c) Pattern 3 anisotropy 129

Figure 4.16 Calculated velocity-depth profiles for major lithologies from the Dabie Mountains..... 131

Figure 4.17 Lithologic column of drill hole ZK703 at Maobei (34°25′N, 118°40′E), Donghai County, China..... 134

Figure 4.18 (a) A simplified lithological profile of 0-2000 m in the CCSD main hole (simplified from Xu, 2004), (b) calculated velocity-depth profile, (c) inferred P-wave reflection coefficients (Rc), and (d) reflection profile of the study area (after Zhao et al., 2004). 135

Figure 5.1 Simplified geological map of the Dabie-Sulu UHP metamorphic belt, eastern-central China.. 145

Figure 5.2 Plot of shear wave velocity (*Vs*) versus confining pressure for three typical types of eclogites: (a) Type-1 eclogite MB27, (b) Type-2 eclogite SB1, (c) Type-3 eclogite 98501, and (d) mean shear wave velocities of these three samples. 156

Figure 5.3 Mean shear wave velocities ($\overline{Vs}$) versus densities at (a) 50 MPa and (b) 600 MPa of Dabie-Sulu UHP rocks. 158

Figure 5.4 Mean shear wave velocities (*Vs*) of eclogites at 600 MPa versus volume fraction of (a) garnet (Grt) and (b) pyroxene (Pyx), amphibole (Amp), phengite (Phn) and symplectite (Symp)..... 159

Figure 5.5 Chemical dependence of shear wave velocities at 600 MPa of eclogites: (a) $\overline{Vs}$ -SiO_2 content, (b) $\overline{Vs}$ -Na_2O content. 160

Figure 5.6 Pressure dependence of shear wave anisotropy (*As*). 162

Figure 5.7 Pressure dependence of shear wave splitting (ΔVs), splitting-produced anisotropy (A_λ) along a given propagation direction λ (X, Y or Z) and bulk anisotropy (*As*) for (a-b) Type-1 eclogite MB27, (c-d) Type-2 eclogite SB1 and (e-f) Type-3 eclogite 98501, respectively..... 165

Figure 5.8 Split shear wave velocities along X-, Y- and Z-directions at (a-c) 50 MPa and (d-f) 600 MPa.. 166

Figure 5.9 (a) Laboratory Vs_{ZX} data and regression results for Type-1 eclogite MB26 and (b) its pressure derivative (Vs_{ZX}'). 167

Figure 5.10 Histograms of (a) reference shear wave velocities (V_0) and (b) intrinsic pressure derivatives (*D*) of eclogites from this study and the literature. 170

Figure 5.11 (a) Three-layered crustal models of the Sulu UHP terrane (Yang et al., 2004), the Dabie Mountains and the Lower Yangtze region (Wang et al., 2000), North Jiangsu basin and Western Shandong block (Ma et al., 1991), Yangtze craton and North China craton (Gao et al., 1998). (b) Calculated geotherms for the tectonic regions shown in (a).. 173

Figure 5.12 Calculated in situ (a) S-wave velocities and (b) P-wave velocities with depth for the Sulu crust. 175

Figure 5.13 Histograms of petrophysical properties of eclogites: (a) P-wave velocity (*Vp*), (b) S-wave velocity (*Vs*), (c) *Vp*/*Vs* ratio, (d) Poisson's ratio, (e) density and (f) SiO_2 content.. 178

Figure 5.14 (a) Seismic profile AA′ in the Sulu terrane (see Figure 5.1) with *Vp* and Poisson's ratios in parentheses (after Yang et al., 2004). (b) Inferred crustal composition beneath the CCSD main hole assuming an eclogite-bearing model (Model 1) and an eclogite-free model (Model 2). Lithology symbols are: Amp: amphibolite; Ec: a mixture of 30% Type-1, 30% Type-2 and 40% Type-3 eclogites; Fel: felsic gneiss; Par: paragneiss; Int: intermediate gneiss; Pel: metapelite; Mar: marble; Maf: mafic granulite; Ultra: ultramafic rocks. (c) SiO_2 content with depth, calculated using Model 1 and Model 2. 181

Figure 5.15 Schematic representation of different exhumation models. (a) Subduction flow and return flow in a narrowing channel (e.g., Cloos, 1982; Gerya and Stöckhert, 2002); (b) Buoyancy-driven exhumation of upper crustal slices (e.g., Chemenda et al., 1995; Ernst and Peacock, 1996); (c) New subduction-triggered exhumation; (d) Lower crustal delamination (Kay and Kay, 1991). 186

Figure 5.16 (a) Seismic refraction profile BB′ across the Dabie Mountains (see Figure 5.1) with *Vp* and Poisson's ratios in parentheses (after Wang et al., 2000); (b) Inferred crustal composition beneath the Dabie UHP unit. Lithology symbols are defined in Figure 14b; (c) Density and SiO_2 content with depth, calculated using Model 1 and Model 2. 187

Figure A1.1 Experimental and theoretical results for relative Young's modulus of porous Al_2O_3 (a and b) and MgO (c) as a function of the volume fraction of solid component. 236

Figure A1.2 Comparison between experimental and theoretical results for relative bulk modulus (Kc-Kw)/(Ks-Kw) for glass foams..... 237

Figure A1.3 Comparison between experimental and theoretical results for relative Young's modulus (a), shear modulus (b) and bulk modulus (c) for sandstone analogs made from fused glass beads. 238

Figure A1.4 P-wave (a) and S-wave (b) velocities for sandstone analogs made from fused glass beads plotted against volume fraction of solid glass. 239

Figure A1.5 Relative Young's modulus (a), shear modulus (b) and bulk modulus (c) for WC-Co alloys plotted against volume fraction of WC. 240

Figure A1.6 Relative Young's modulus for WC-Co alloys plotted against volume fraction of WC. 241

Figure A1.7 Theoretical curves on relative Young's modulus $(E_c-E_m)/(E_s-E_m)$ for aluminium-matrix composites plotted against volume fraction of reinforcement. Al-SiC composites (a and b) and Al-boron composites (c). 242

Figure A1.8 Relative Young's modulus (a), shear modulus (b) and bulk modulus (c) for Al-spinel composite plotted against volume fraction of spinel. 243

Figure A1.9 Comparison of the predictions of the present approach, the Hashin-Shtrikman upper (HS^+) and lower (HS^-) bounds, Paul's (1960) calculations (P) with

experimental data on relative elastic Young's moduli of epoxy resin-based composites. Epoxy-Silica composites (a and b) and epoxy-glass composites (c-d). 245

Figure A1.10 Comparison of the predictions of the present approach, the Hashin-Shtrikman upper (HS^+) and (HS^-) bounds with experimental data on relative Young's modulus (a), shear modulus (b) and bulk modulus (c) of epoxy-glass composites. . 246

Figure A1.11 Relative Young's modulus (a), shear modulus (b) and bulk modulus (c) for epoxy-Al composite plotted against volume fraction of Al. 248

Figure A1.12 P-wave (a) and S-wave (b) velocities for epoxy-Al composites plotted against volume fraction of Al. 249

Figure A1.13 Theoretical curves on relative Young's modulus $(E_c-E_w)/(E_s-E_w)$ for glass-matrix composites plotted against volume fraction of reinforcement. Glass-Al_2O_3 composites (a) and glass-tungsten composites (b).. 250

Figure A1.14 Comparison between the predictions of the present approach and the Einstein equation for the relative viscosity of a suspension as a function of identically spherical, solid inclusions. 252

Figure A1.15 Variation of P-wave (a) and S-wave (b) impedances for olivine-wadsleyite system with its composition for three typical structure: curve ABCD, discontinuous weak phase (olivine) grains in continuous strong framework of wadsleyite; curve DEFA, discontinuous strong phase (wadsleyite) embedded in a continuous weak matrix; curve EB, calculated from Equation (A1.8) with $J = 0.5$ and $k = 1.1$, both phases are either discontinuous or continuous and there is a transition from an olivine-dominant configuration to a wadsleyite-dominant configuration with increasing the volume fraction of wadsleyite (from E to B). 255

Figure A3.1 Regression results of experimental data points of amphibolite YM4Y (a) Regression equations of YM4Y. (b) Distribution of relative errors versus pressure; (c) Histogram of relative errors of spline interpolation; (d) Histogram of relative errors of regression results. 270

List of initials and abbreviations

Symbol	Notation
Acc	accessories
Act	actinolite
Alt	alteration
Amp	amphibole
And	Andalusite
Anh	anhydrite
Ap	apatite
Aug	augite
Bt	biotite
Cal	calcite
Can	carnallite
Car	carbonate
Ccp	chalcopyrite
Chl	chlorite
Chr	chromite
Clast	clasts in sedimentary rocks
Clay	clay in sedimentary rocks
Cld	chloritoid
Cpx	clinopyroxene
Crd	cordierite
Czo	clinozoisite
Di	diopside
Dol	dolomite
Ep	epidote
Fl	fluorite
Fsp	feldspar
Glass	volcanic glass
Gp	gypsum
Gr	graphite
Grt	garnet
Hbl	hornblende
Hl	halite
Hy	hypersthene
Idd	iddingsite
Ilm	ilmenite
Kfs	K-feldspar
Kie	kieserite
Ky	kyanite
LOI	Loss on ignition

Symbol	Notation
Mag	magnetite
Mc	microcline
Mica	mica
Ms	muscovite
Mym	myrmekite
Ne	nepheline
Oam	orthoamphibole
Ol	olivine
Omp	omphacite
Opq	opaque oxides
Opx	orthopyroxene
Phl	phlogopite
Pl	plagioclase
Pmp	pumpellyite
Pn	pentlandite
Po	pyrrhotite
Prh	prehnite
Py	pyrite
Pyx	pyroxene
Qtz	quartz
Rt	rutile
Sa	sanidine
Scp	scapolite
Ser	sericite
Sil	sillimanite
Sme	smectite
Sp	sphalerite
Spl	spinel
Spn	sphene
Srp	serpentine
St	staurolite
Sul	sulfide
Symp	symplectite
Tlc	talc
Tr	tremolite
Vesicle	pores in volcanic rocks
Zeo	zeolite
Zo	zoisite
Zrn	zircon

Symbol	Notation
ρ	Density in g/cm^3
Φ	Porosity (%)
λ	Direction of wave propagation and polarization
A	Velocity anisotropy
K	Bulk modules
G	Shear modules
$\boldsymbol{C}$	Stiffness tensor
$\boldsymbol{S}$	Compliance tensor
P	pressure
T	temperature
M	Mean velocity
LPO	Lattice-preferred orientation
Vp	Compressional wave velocity
Vs	Shear wave velocity
Vs1	Fast shear wave velocity in shear wave splitting
Vs2	Slow shear wave velocity in shear wave splitting
X	Direction parallel to the stretching lineation
Y	Direction perpendicular to the lineation and in the foliation
Z	Direction normal to the foliation

List of appendices

APPENDIX 1 MECHANICAL PROPERTIES OF MULTIPHASE MATERIALS AND ROCKS: A PHENOMENOLOGICAL APPROACH USING GENERALIZED MEANS 227

A1.1 Abstract 228
A1.2 Introduction 229
A1.3 Mechanical properties of multiphase aggregates 229
A1.4 Comparison with experiments 233
A1.4.1 SPSS composites 234
A1.4.2 WPSS composites 244
A1.5 Application to the interpretation of 410-km seismic discontinuity 251
A1.6 Discussion and conclusions 256

APPENDIX 2 CLASSIFICATION OF ROCK CATEGORY 261

APPENDIX 3 REGRESSION ANALYSIS OF VELOCITY-PRESSURE RELATIONSHIP 265

A3.1 Least-squares method 265
A3.2 MATLAB program VPPLOT 267
A3.2.1 Interpolate data 267
A3.2.2 Find the critical point and regression functions 268
A3.2.3 Study residuals 269

Introduction

Whereas the upper crust is accessible to geological sampling and mapping, the deeper portions of the crust and the upper mantle are relatively inaccessible. Much of our knowledge on the composition, structure and evolution of the deep crust and upper mantle has been derived from various seismic refraction and reflection measurements. Interpretation of these seismic data in terms of lithology, mineralogical and chemical compositions is largely constrained by comparing in situ observed seismic velocities with those of relevant rocks or mineral assemblages thought to exist in the ranges of temperature and pressure of interest. In addition, seismic properties of rocks have significant practical applications in the mining industry and geotechnical engineering (e.g., construction of buildings, dams, tunnels, bridges and nuclear waste storage). Therefore, this study is of more than academic interest.

The aim of this study is to improve our understanding of the following questions:

- What are the control parameters of P- and S-wave velocities (*Vp* and *Vs*), anisotropy and shear wave splitting of rocks? Can we determine rock types from average seismic velocities, anisotropy and Poisson's ratio in a more precise way?
- What are the effects of different averaging methods on calculated velocities of polyphase rocks?
- How can we describe, in a quantitative and precise way, the variation of seismic velocity as a function of confining pressure?
- What are the seismic properties of ultrahigh-pressure (UHP) metamorphic rocks, e.g., diamond- and coesite-bearing eclogites and their host rocks from the Dabie-Sulu orogenic belt of China, the world's largest UHP terrane? And if these deeply exhumed rocks exit in the deep crust and upper mantle, how can we detect them by seismic investigations?

- How were these UHP rocks exhumed from depths of 100-150 km? And how many eclogites could be preserved in today's deep crust beneath the Dabie-Sulu UHP units?
- For modern and ancient subduction zones, what is the origin of high velocity layers and seismic reflectors in the lower crust and upper mantle?

This thesis focuses on theoretical and laboratory studies of seismic properties of polyphase rocks. Chapter 1 gives indispensable background on elastic and seismic properties of rocks and their implications for the composition and structures of the continental crust and upper mantle. In Chapter 2, a concise introduction is given to an Internet Database of Rock Seismic Properties (DRSP: http://texture.civil.polymtl.ca:8080/seismic-properties/index.jsp). The DRSP comprises almost all data available in the literature published in English and French during the last 4 decades and is more complete than any previous compilations. Compared with a traditional compilation in the form of tables, the DRSP can perform much more complex tasks with much higher efficiency, and permit enormous volumes of data to be studied in a far more comprehensive fashion than has hitherto been attempted. Some statistic results on relationships between seismic properties and density, porosity, petrology and chemical composition are presented as examples of DRSP applications.

In Chapter 3, P-wave velocities of 696 dry samples are compared with theoretical values calculated using 16 different averaging schemes. It is found that the mean *Vp* of a polymineralic rock is exclusively controlled by the volume fractions of its constituent minerals while grain shape and crystallographic orientations, anisotropy and other perturbations have minimum effects. The mean *Vp* can be fairly well predicted as long as a relevant mixture rule is used and the volume fraction is accurately determined for each mineral. Applications of an inappropriate mixture rule will potentially cause the misinterpretation of the crust and mantle *Vp* data in terms of mineralogical compositions and structures. I was also involved in a study on the generalized mixture rules and their

application to the prediction of mechanical and physical properties of multiphase materials with various microstructures (Appendix 1).

As the most important part of this thesis, results of high-pressure laboratory measurements of P-wave and S-wave properties for UHP metamorphic rocks from the Dabie-Sulu orogenic belt (China), are presented, respectively, in Chapter 4 and Chapter 5. Chapter 4 is a research article to be accepted by Tectonophysics, and Chapter 5 is a manuscript submitted to Journal of Geophysical Research. The experimental results are used to interpret field seismic reflection and refraction data and construct crustal composition models of the Sulu terrane and the Dabie Mountains. The inferred crustal composition suggests that the eclogite-bearing UHP rocks are tectonic slices thrust, along a series of shear zones during the continental collision between the North China and Yangtze cratons, over a normal UHP-free middle-lower crust with overall intermediate composition. Compositional layering and retrograde metamorphism of eclogites can result in significant anisotropy and shear wave splitting, implying a plausible contribution of eclogites to seismic anisotropy in the lower crust, upper mantle and especially subducted slabs. Our results also indicate that subducted crustal materials such as eclogite layers intercalated with felsic gneiss, garnet-jadeite quartzite, marble and serpentinized peridotite, if they are preserved in the present-day upper mantle, could be responsible for regionally observed seismic reflectors in the upper mantle. Finally, Chapter 6 summarizes our main conclusions.

Chapter 1
Literature review

In this chapter, concepts and problems related to seismic properties of polyphase rocks are reviewed. Section 1.1 presents general principles of elasticity theory and calculation methods of seismic properties of rock-forming minerals and polymineralic rocks. Section 1.2 overviews laboratory measurements of seismic velocities of rock samples. Section 1.3 illustrates seismic properties of the continental crust and upper mantle.

1.1 Calculation of seismic properties of polyphase rocks

1.1.1 Theory of elasticity

Many substances including rocks can be approximately considered perfectly elastic without appreciable error when the deformations are small, as is the case for seismic waves except near a seismic source. The theory of elasticity deals with the relations between the stress (σ_{ij}) and the resulting strain (ε_{ij}) on a body, where i, j may take the values 1, 2, or 3, parallel to the coordinate axes x_1, x_2, x_3, respectively, the first suffix denotes the direction of the stress component and the second indicates the direction of the normal to the plane under consideration (Nye, 1957, Figure 1.1). Stresses of the type σ_{11} are normal stresses, and of the type σ_{12}, shear stresses. A perfect elastic body deforms as linear elasticity, which is stated by Hooke's law:

$$\sigma_{ij} = C_{ijkl}\varepsilon_{kl} \tag{1.1}$$

or

$$\varepsilon_{kl} = S_{ijkl}\sigma_{kl} \tag{1.2}$$

where C_{ijkl} and S_{ijkl} are the elastic stiffness and compliance, respectively, and i, j, k, l =1, 2, or 3. Because the conditions for zero rotation of the body are $\sigma_{12} = \sigma_{21}$, $\sigma_{13} = \sigma_{31}$ and $\sigma_{23} = \sigma_{32}$, σ_{ij} contains only 6 independent components and the stiffness C_{ijkl} can be expressed by a 6×6 tensor:

$$C_{qr} = \begin{pmatrix} C_{11} & C_{12} & C_{13} & C_{14} & C_{15} & C_{16} \\ C_{21} & C_{22} & C_{23} & C_{24} & C_{25} & C_{26} \\ C_{31} & C_{32} & C_{33} & C_{34} & C_{35} & C_{36} \\ C_{41} & C_{42} & C_{43} & C_{44} & C_{45} & C_{46} \\ C_{51} & C_{52} & C_{53} & C_{54} & C_{55} & C_{56} \\ C_{61} & C_{62} & C_{63} & C_{64} & C_{65} & C_{66} \end{pmatrix} \tag{1.3}$$

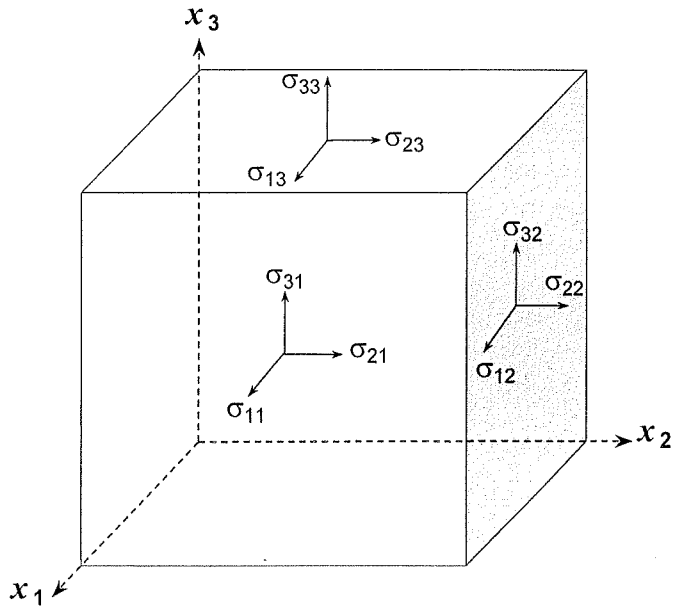


Figure 1.1 Stress components acting on the faces of a unit cube.

The stresses C_{qr} can be further simplified into 21 independent elements due to the reciprocal relations $C_{qr} = C_{rq}$ imposed by thermodynamic requirements. The components

of compliance S_{ijkl} can be specified in a similar way to the stresses. And the compatibility between C_{qr} and S_{qr} requires

$$C_{qr} \bullet S_{q_r} = I \qquad (1.4)$$

where $\boldsymbol{I}$ is the unit tensor. The 21 stiffnesses (or compliances) of the generalized Hooke's law describe the elastic behavior of a material belonging to the triclinic crystal system. The existence of symmetry will reduce the number of independent elastic constants to 13 for monoclinic, 9 for orthorhombic, 7 or 6 for tetragonal and trigonal, 5 for hexagonal, and 3 for cubic crystal systems (Table 1.1 and Table 1.2). For isotropic material, its elastic behavior can be completely described by two independent stiffnesses (or compliances).

Table 1.1 Stress-strain relations for orthorhombic, hexagonal, cubic and isotropic systems

Stress	Strain			
	Orthorhombic	Hexagonal	Cubic	Isotropic
σ_{11} =	$C_{11}\varepsilon_{11} + C_{12}\,\varepsilon_{22} + C_{13}\,\varepsilon_{33}$	$C_{11}\,\varepsilon_{11} + C_{12}\,\varepsilon_{22} + C_{13}\,\varepsilon_{33}$	$C_{11}\,\varepsilon_{11} + C_{12}\,\varepsilon_{22} + C_{12}\,\varepsilon_{33}$	$C_{11}\,\varepsilon_{11} + C_{12}\,\varepsilon_{22} + C_{12}\,\varepsilon_{33}$
σ_{22} =	$C_{12}\,\varepsilon_{11} + C_{22}\,\varepsilon_{22} + C_{23}\,\varepsilon_{33}$	$C_{12}\,\varepsilon_{11} + C_{11}\varepsilon_{22} + C_{13}\,\varepsilon_{33}$	$C_{12}\,\varepsilon_{11} + C_{11}\,\varepsilon_{22} + C_{12}\,\varepsilon_{33}$	$C_{12}\,\varepsilon_{11} + C_{11}\,\varepsilon_{22} + C_{12}\,\varepsilon_{33}$
σ_{33} =	$C_{13}\,\varepsilon_{11} + C_{23}\,\varepsilon_{22} + C_{33}\,\varepsilon_{33}$	$C_{13}\,\varepsilon_{11} + C_{13}\,\varepsilon_{22} + C_{33}\,\varepsilon_{33}$	$C_{12}\,\varepsilon_{11} + C_{12}\,\varepsilon_{22} + C_{11}\,\varepsilon_{33}$	$C_{12}\,\varepsilon_{11} + C_{12}\,\varepsilon_{22} + C_{11}\,\varepsilon_{33}$
σ_{23} =	$C_{44}\,\varepsilon_{23}$	$C_{44}\,\varepsilon_{23}$	$C_{44}\,\varepsilon_{23}$	$(C_{11} - C_{12})\,\varepsilon_{23}/2$
σ_{13} =	$C_{55}\,\varepsilon_{13}$	$C_{44}\,\varepsilon_{13}$	$C_{44}\,\varepsilon_{13}$	$(C_{11} - C_{12})\,\varepsilon_{13}/2$
σ_{12} =	$C_{66}\,\varepsilon_{12}$	$(C_{11} - C_{12})\,\varepsilon_{12}/2$	$C_{44}\,\varepsilon_{12}$	$(C_{11} - C_{12})\,\varepsilon_{12}/2$

Table 1.2 Independent single-crystal stiffness coefficients at room conditions

Symmetry	Monoclinic	Orthorhombic	Tetragonal		Trigonal		Hexagonal	Cubic
Crystal	Diopside[1]	Olivine (Fo93Fa7)[2]	Scheelite $CaWO_4$[3]	Rutile[4]	Dolomite[4]	α-Quartz[4]	Graphite[5]	Pyrope[6]
N	13	9	7	6	7	6	5	3
C_{11}	204	323.7	141	269	205	86.6	1060	296.2
C_{22}	175	197.6						
C_{33}	238	235.1	125	480	113	106.1	36.5	
C_{44}	67.5	64.6	33.7	124	39.8	57.8	0.3	91.6
C_{55}	58.8	78.1						
C_{66}	70.5	79	40.7	192				
C_{12}	84.4	66.4	61	177	71	6.7	180	111.1
C_{13}	88.3	71.6	41	146	57.4	12.6	15	
C_{14}					-19.5	-17.8		
C_{15}					13.7			
C_{16}			-17					
C_{23}	48.2	75.6						
C_{15}	-19.3							
C_{25}	-19.6							
C_{35}	-33.6							
C_{46}	-11.3							

N is the number of independent elastic constants of each crystal symmetry. 1. Alexandrov et al., 1964; 2. Kumazawa and Anderson, 1969; 3, Hearmon, 1979; 4. Hearmon, 1984; 5, Blakslee et al., 1970; 6, O'Neil et al., 1991.

According to Equation (1.1) and Table 1.1, several elastic constants are widely used to describe the elasticity of an **isotropic** body. Young's modulus E is the ratio of tensional stress to the resultant longitudinal strain for a small cylinder under tension at both ends:

$$E = \frac{\sigma_{11}}{\varepsilon_{11}} \tag{1.5}$$

Poisson's ratio σ is the negative of the ratio of the fractional lateral contraction to the fractional longitudinal extension of the same cylinder under extension at both ends:

$$\sigma = -\frac{\varepsilon_{33}}{\varepsilon_{11}} \tag{1.6}$$

The resistance of a body to shearing strain is defined by shear modulus G as follows:

$$G = \frac{\sigma_{12}}{2\varepsilon_{12}} \tag{1.7}$$

And the ratio of a hydrostatic pressure to the resulting compression of a small body is called bulk modulus or incompressibility K:

$$K = \frac{E}{3(1-2\sigma)} = G\frac{1+\sigma}{3\sigma} = \frac{EG}{3(3G-E)} \tag{1.8}$$

The P- and S-wave velocities (Vp and Vs) depend on physical properties of the material though which the wave travels:

$$Vp = \sqrt{\frac{K+4G/3}{\rho}} \tag{1.9}$$

$$Vs = \sqrt{\frac{G}{\rho}} \tag{1.10}$$

And the relationship between Poisson's ratio and Vp/Vs ratio is as follows:

$$\sigma = \frac{0.5(V_p/V_s)^2 - 1}{(V_p/V_s)^2 - 1} \qquad (1.11)$$

The values of Poisson's ratio range from 0.05 for very hard, rigid rocks to about 0.45 for soft, poorly consolidated materials. Liquids have no resistance to shear but are incompressible and hence σ = 0.5. For most rocks, Poisson's ratio is about 0.25-0.26. A negative value of Poisson's ratio implies that a cylinder undergoing compression along its axis would contract simultaneously in all directions, which has been observed for certain directions in single crystals (Svetlov et al., 1988).

1.1.2 Seismic properties of rock-forming minerals

In isotropic elastic solid, linear P-wave particle motion is parallel to the propagation direction and S-wave particle motion is perpendicular to propagation, with two components arbitrarily defined as oriented horizontally and in the vertical plane. While for anisotropic media, waves are neither purely longitudinal nor transverse except in certain directions. The particle displacement has components both along and transverse to the direction of propagation. Since particle motions are no longer simply related to ray directions, the waves are called quasi-P wave with linear particle motion that is not quite parallel to the propagation direction, and two quasi-S waves (*Vs*1 and *Vs*2, *Vs*1 > *Vs*2) with polarization parallel and perpendicular to the fast direction for the propagation direction in question (Figure 1.2a).

Calculation of seismic properties of rock-forming minerals is very important for understanding the relationship between the lattice preferred orientation (LPO) and volume fraction of each constituent mineral, and the overall seismic velocities and anisotropy of polycrystalline rocks (e.g., Crosson and Lin, 1971; Baker and Carter, 1972; Peselnick et al., 1974; Ji and Mainprice, 1988). For each propagation direction, the P-wave velocity, the two shear wave velocities and shear wave splitting (*Vs1-Vs2*) can be

computed according to the elastic constants (the 6×6 symmetric matrix) and density of each mineral, the Christoffel equation and the Hill averaging scheme. The *Vp* anisotropy, $A(Vp)$, is defined as $(V_{\max} - V_{\min})/V_m \times 100\%$, where $V_m = (V_X + V_Y + V_Z)/3$, X is parallel to the stretching lineation, Y perpendicular to the lineation and in the foliation, and Z normal to the foliation (Figure 1.2b). Thus, $A(Vp)$ is direction-independent and only reflects the relative difference between the maximum and minimum *Vp* values. The *Vs* anisotropy along the propagation direction in question, $A(Vs)$, is defined as $(Vs1 - Vs2)/Vs_m \times 100\%$, where $Vs_m = (Vs1 + Vs2)/2$. So $A(Vs)$ is a directional parameter.

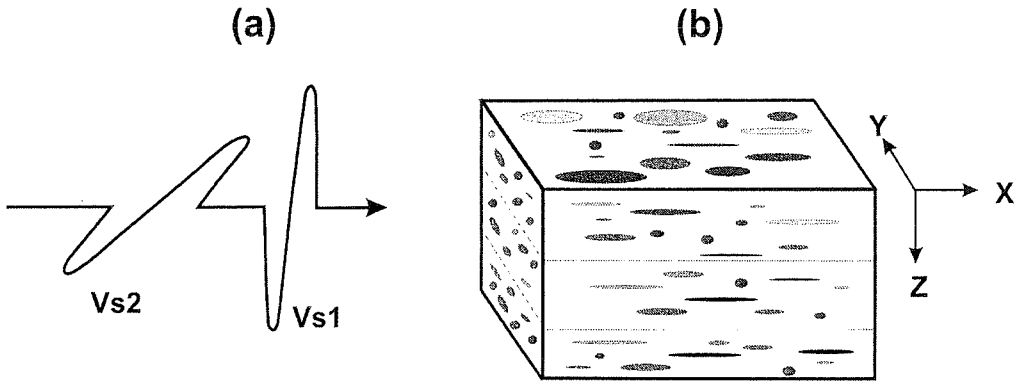


Figure 1.2 Shear wave splitting and direction setting in an anisotropic body.

Ji et al. (2002) presented single crystal 3D seismic properties of 53 common rock-forming minerals. Figure 1.3 illustrates spatial representation of P- and S-wave velocities and shear wave splitting of 16 important minerals (Ji et al., 2002). Anisotropic properties of these 16 minerals are summarized in Table 1.3.

The single-crystal symmetry of plagioclase is actually triclinic, however, due to the lack of adequate single-crystal elastic constants, it has been treated as monoclinic so far. Except albite (Figure 1.3a), the maximum *Vp* of anorthite (Figure 1.3b), plagioclase (Figure 1.3c) and K-feldspar (Figure 1.3d) occur parallel to the **b***-axis [the direction

perpendicular to the (010) plane] and their maximum shear wave splitting concentrates around [011] direction.

Quartz, calcite and dolomite exhibit trigonal symmetry, with the maximum shear wave splitting parallel to the **a**-axis (Figures 1.3e-g). For hornblende the symmetry plane is defined by the **a***-[the direction perpendicular to the (100) plane] and **c**-axes. The maximum of *Vp* is observed parallel to the **c**-axis and a pronounced shear wave splitting occurs in the plane marked by the **b***- and **c**-axes with a maximum parallel to the **c**-axis (Figure 1.3h). Muscovite can be treated as hexagonal since the velocity difference in the directions of the **a**- and **b**-axes are vanishing small. A maximum of *Vp* and shear wave splitting occurs in the (001) plane, and the minimum parallel to the **c**-axis (Figure 1.3i). Seismic properties of muscovite can approximate those of biotite, whose single crystal elastic data are not available up to now.

The fastest *Vp* and the maximum shear wave splitting of epidote lie parallel to the **b***-axis (Figure 1.3j). For pyroxene, omphacite (Di 30 mol%, Jd 58 mol%) displays the maximum *Vp* around [101] and pronounced shear wave splitting in the plane defined by the **b***- and **c**-axes (Figure 1.3k); while the fastest *Vp* of enstatite distributes sub-parallel to the **a**-axis and the maximum shear wave splitting lies around [111] (Figure 1.3*l*). For olivine that is dominant in the upper mantle, the maximum shear wave splitting is observed along [101] direction. Parallel to the **a**-axis, which is the fastest *Vp* direction, the shear wave splitting vanishes (Figure1.3m). The fastest *Vp* of tetragonal rutile occurs parallel to **c**-axis and the maximum shear wave splitting perpenticular to **c**-axis (Figure 1.3n). Finally, cubic spinel and garnet display extremely high velocities, and the later shows very weak elastic anisotropy although it is optically isotropic (Figures 1.3o-p).

Table 1.3 Anisotropic seismic properties of single crystals

Mineral	Symmetry	Vp (km/s)		Vs1 (km/s)		Vs2 (km/s)		Vs1-Vs2	Anisotropy (%)		
		max	min	max	min	max	min	(km/s)	Vp	Vs1	Vs2
Albite	Triclinic	7.4	5.2	4.4	3.0	3.5	2.5	1.4	30.9	31.2	27.2
Anorthite	Triclinic	8.6	5.9	5.0	3.6	3.8	2.9	1.2	31.8	27.5	23.2
Plagioclase (An_{53})	Triclinic	7.8	5.7	4.7	3.4	3.6	2.7	1.3	27.4	27.4	24.4
K-feldspar	Triclinic	8.1	5.1	4.8	2.8	3.6	2.3	1.9	37.4	42.6	35.3
Quartz	Trigonal	7.0	5.3	5.1	3.7	4.7	3.3	1.8	24.3	26.8	29.5
Calcite	Trigonal	7.7	5.6	4.7	2.9	3.8	2.5	2.2	27.6	38.0	33.8
Dolomite	Trigonal	8.7	6.3	5.3	3.6	4.3	3.0	2.3	27.9	32.7	29.5
Hornblende	Monoclic	7.9	6.0	4.3	3.4	3.8	3.2	1.1	23.8	22.3	16.2
Muscovite	Monoclic	8.1	4.5	5.0	2.5	3.5	2.4	2.7	44.2	50.7	32.9
Epidote	Monoclic	8.4	6.7	5.0	3.5	4.6	3.4	1.4	19.9	30.7	25.9
Diopside	Monoclic	9.4	7.0	5.0	4.3	4.8	4.0	0.9	25.8	13.7	16.2
Jadeite	Monoclic	9.5	7.9	5.7	4.9	5.6	4.3	1.0	16.8	12.7	23.9
Omphacite	Monoclic	9.4	7.6	5.4	4.8	5.3	4.3	0.8	18.6	12.0	18.3
Enstatite	Orthorhombic	8.4	7.5	5.1	4.9	5.0	4.4	0.5	11.3	4.1	11.4
Olivine	Orthorhombic	10.0	7.7	5.6	4.9	4.9	4.4	1.0	22.9	12.7	9.4
Rutile	Tetragonal	10.6	7.9	6.7	5.4	5.4	3.3	2.1	25.1	19.5	38.5
Spinel	Cubic	10.6	8.9	6.6	5.2	6.6	4.2	2.3	16.3	20.4	35.5
Garnet	Cubic	8.6	8.5	4.8	4.7	4.8	4.7	0.1	0.9	2.1	1.5

Figure 1.3 P- and S-wave properties of 16 common rock-forming minerals.
(a) albite, (b) anorthite, (c) plagioclase (An_{53}), (d) K-feldspar, (e) quartz, (f) calcite, (g) dolomite, (h) hornblende, (i) muscovite, (j) epidote, (k) omphacite, (l) enstatite, (m) olivine, (n) rutile, (o) spinel and (p) almandine. The P-wave phase velocities (Vp, up-left), the fast S-wave velocities (Vs1, up-right), the slow S-wave velocities (Vs2, low-left), and the shear wave splitting (Vs1-Vs2, low-right) are shown in equal area stereographic projection with respect to the crystallographic orientations of a, b, c, a* and b*, where a* and b* are the directions normal to (100) and (010) planes, respectively. The maximum velocity (in km/s) is marked by a solid square and the minimum by an open circle. The anisotropy is in percent. Notice that the contour intervals are not the same for every diagram. Shaded areas correspond to directions of high P- or S-wave velocities.

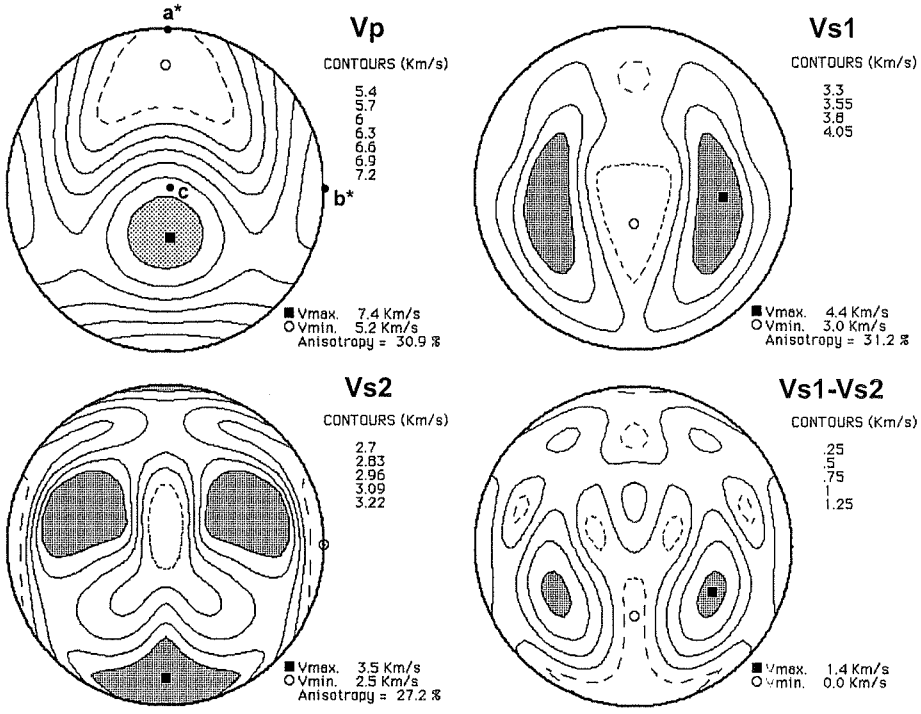


Figure 1.3 (a) Albite $NaAlSi_3O_8$

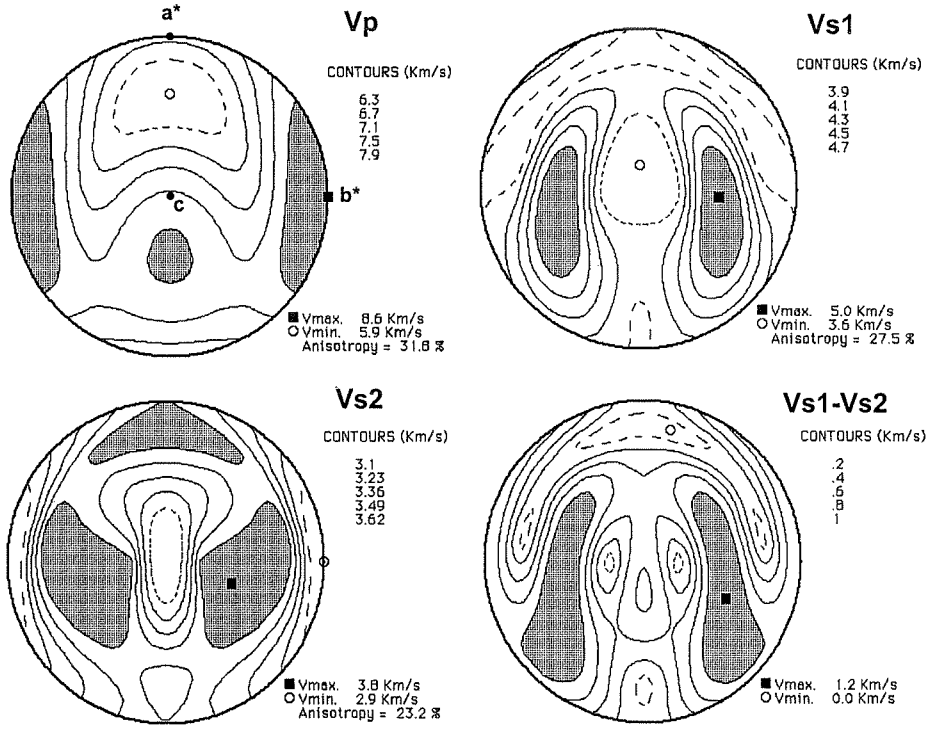


Figure 1.3 (b) Anorthite $CaAl_2Si_2O_8$

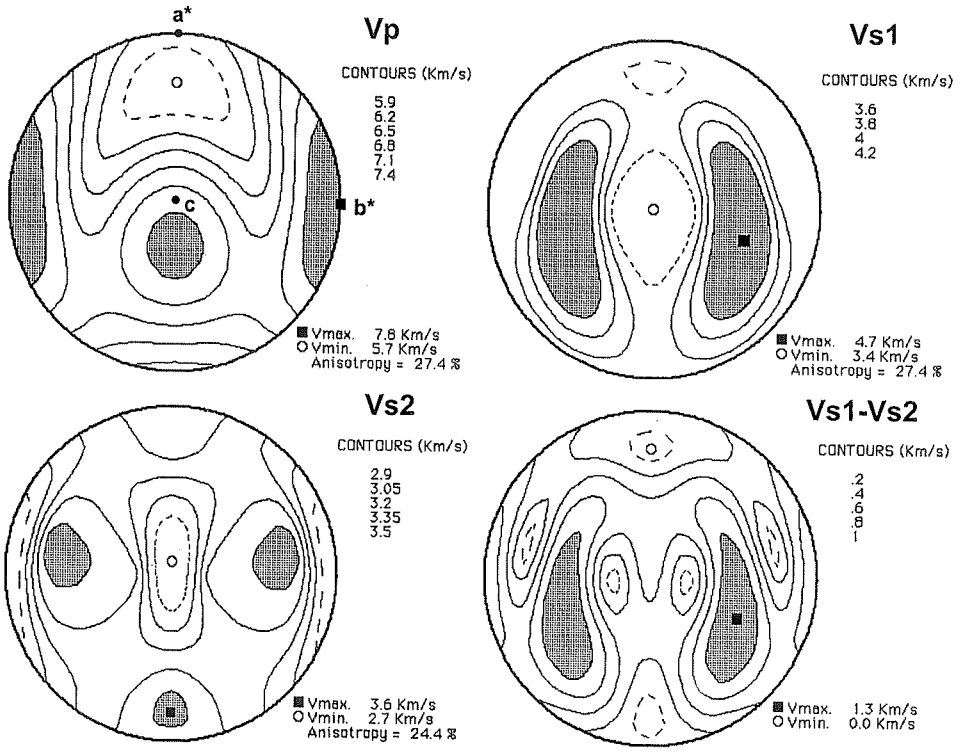


Figure 1.3 (c) Plagioclase An_{53}

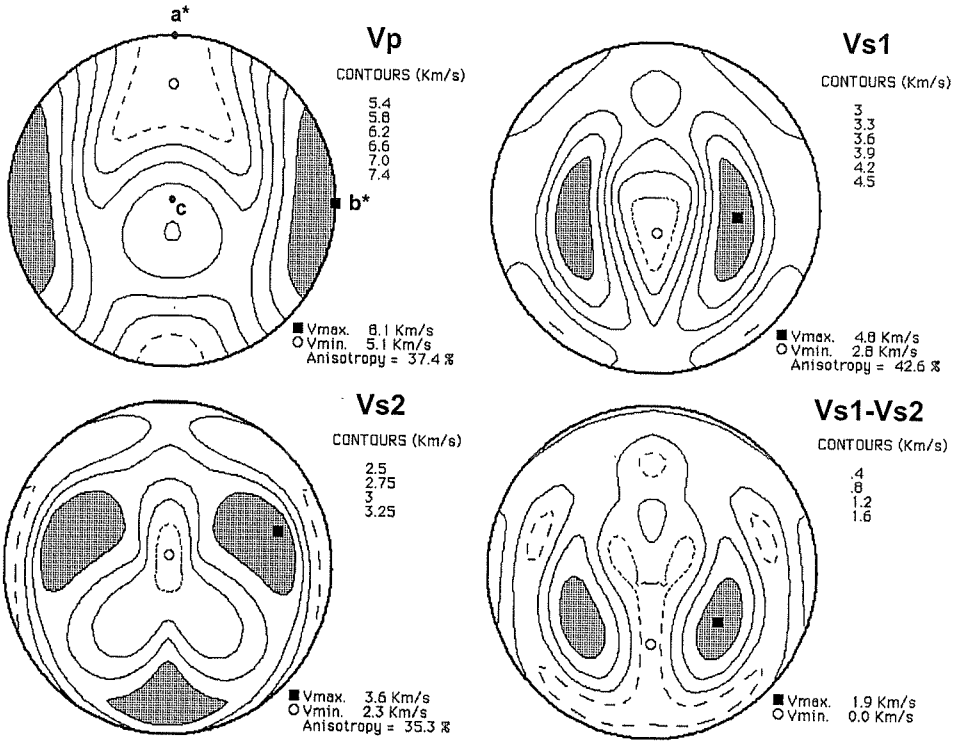


Figure 1.3 (d) K-feldspar $KAlSi_3O_8$

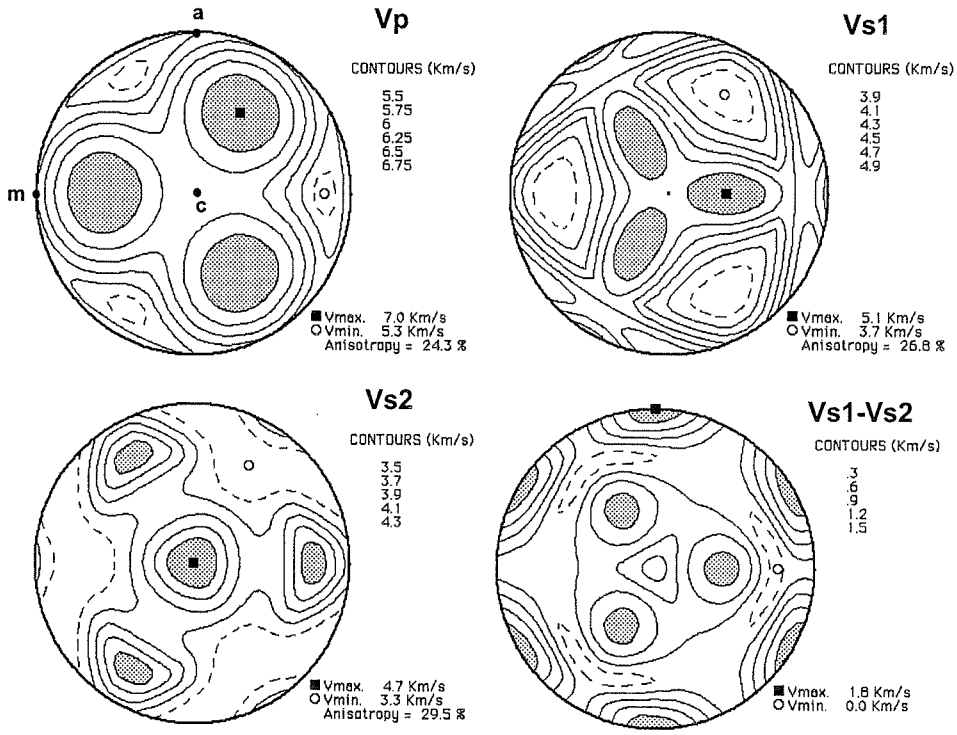


Figure 1.3 (e) Quartz SiO_2

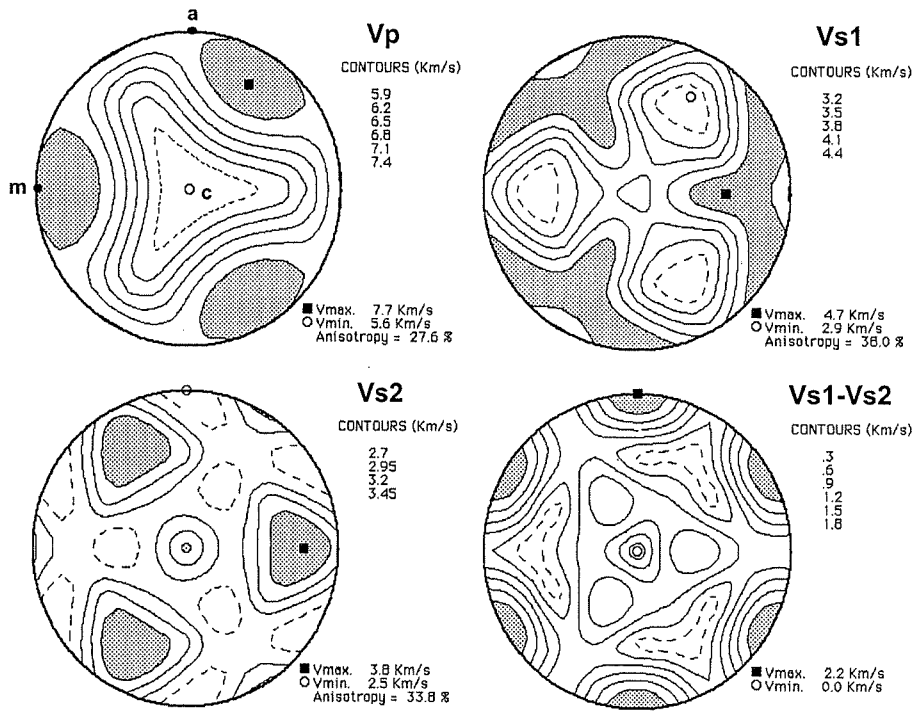


Figure 1.3 (f) Calcite $CaCO_3$

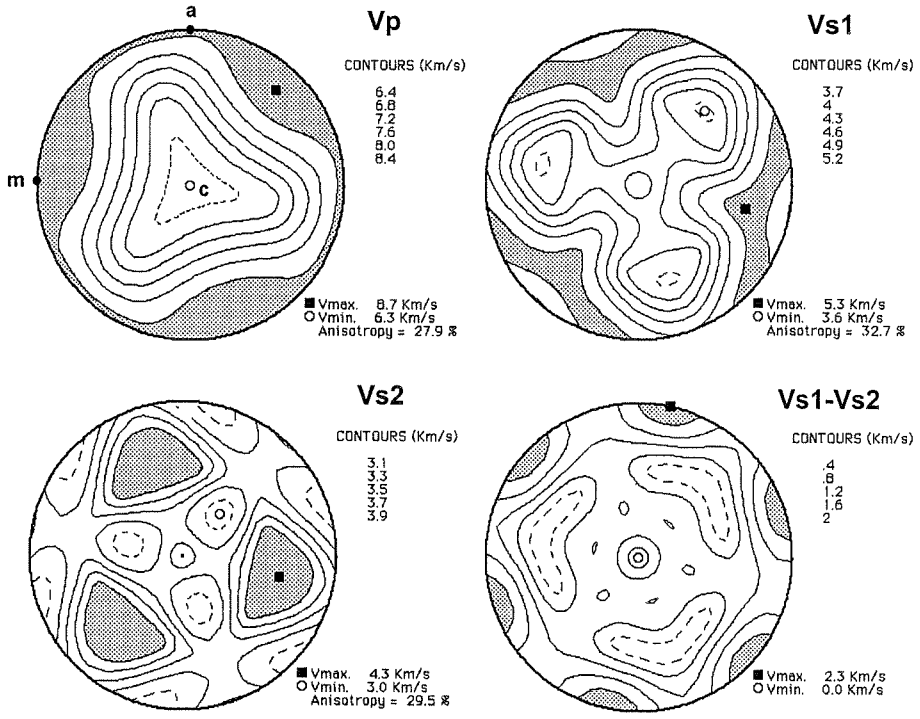


Figure 1.3 (g) Dolomite $CaMg(CO_3)_2$

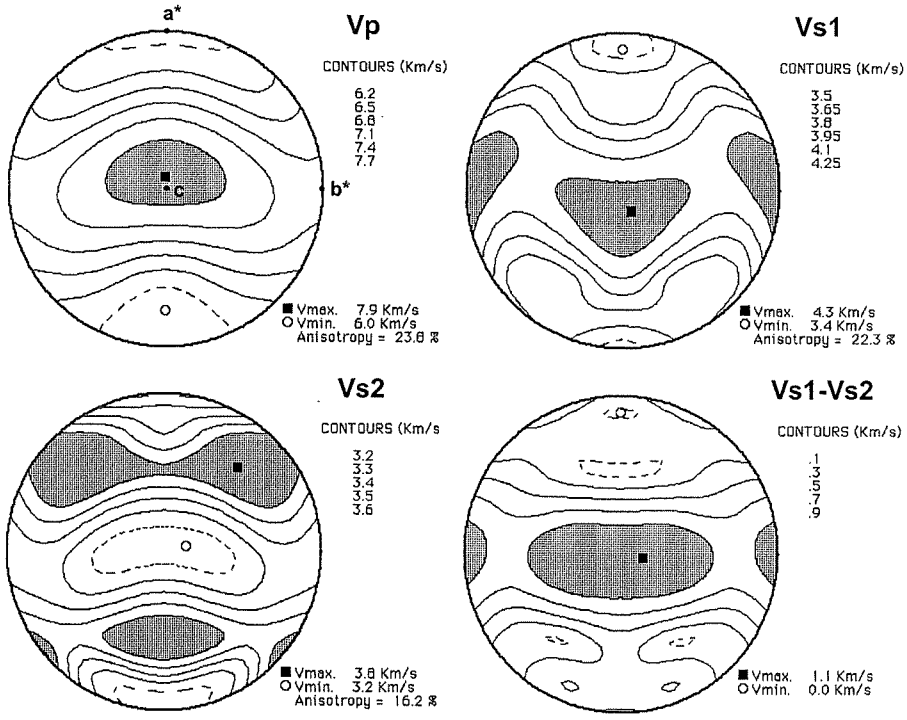


Figure 1.3 (h) Hornblende $(Ca,Na)_{2\text{-}3}(Mg,Fe,Al)_5(Al,Si)_8O_{22}(OH)_2$

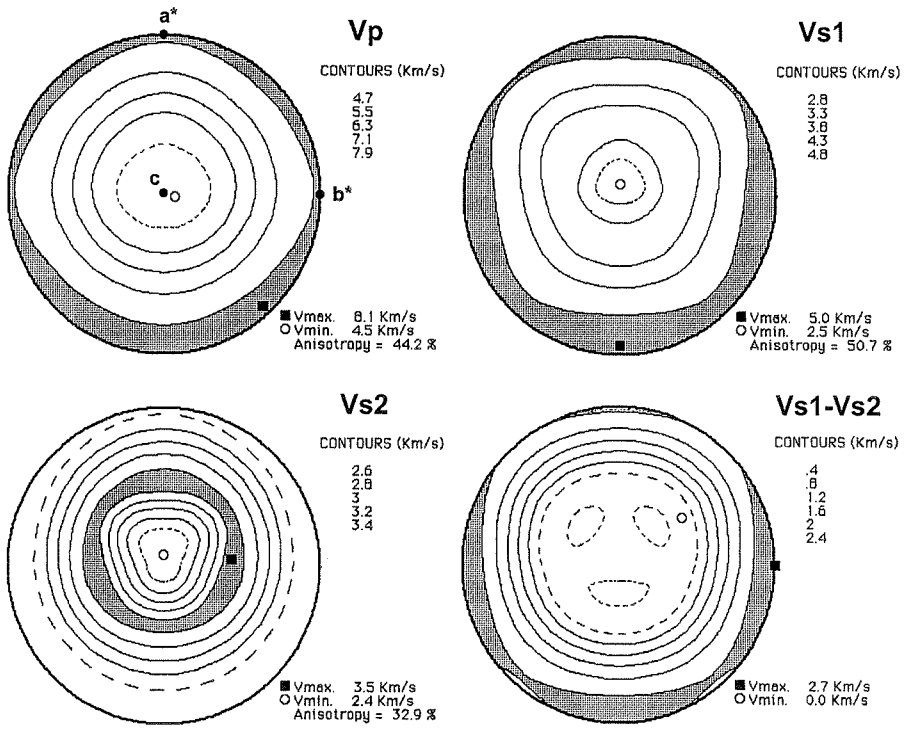


Figure 1.3 (i) Muscovite $KAl_3Si_3O_{10}(OH)_2$

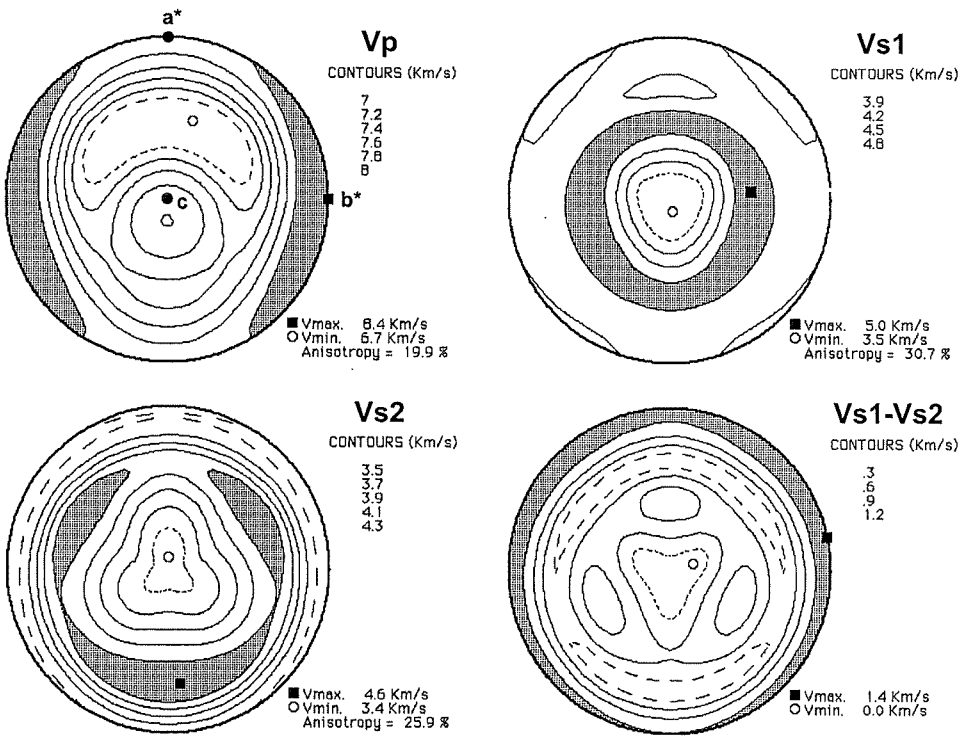


Figure 1.3 (j) Epidote $Ca_2(Al,Fe)_3Si_3O_{12}(OH)$

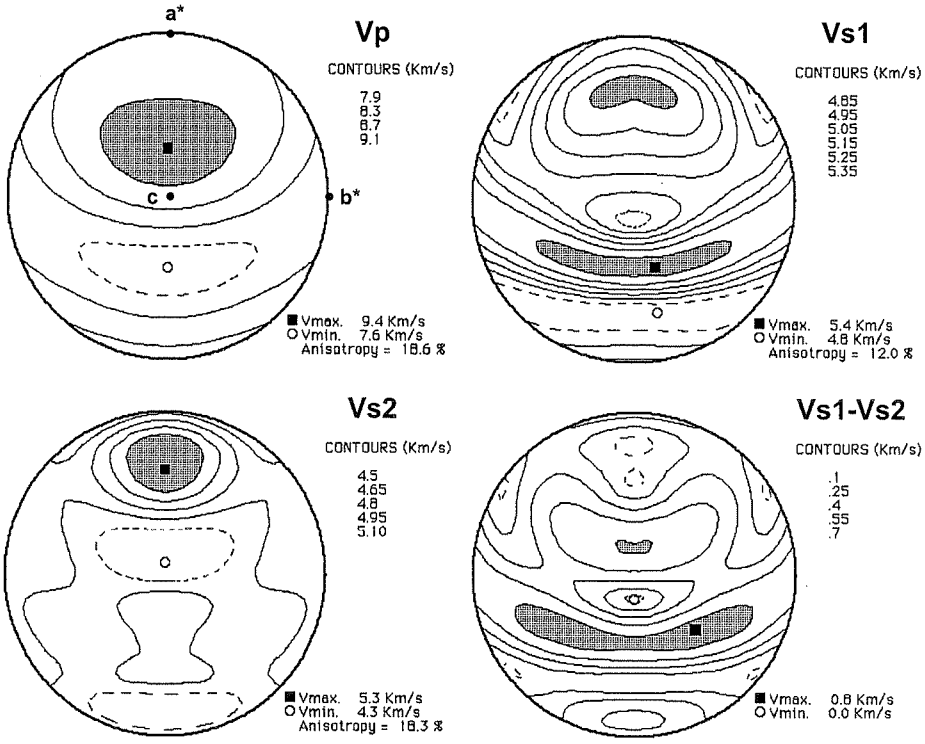


Figure 1.3 (k) Omphacite Di 30 mol%, Jd 58 mol%

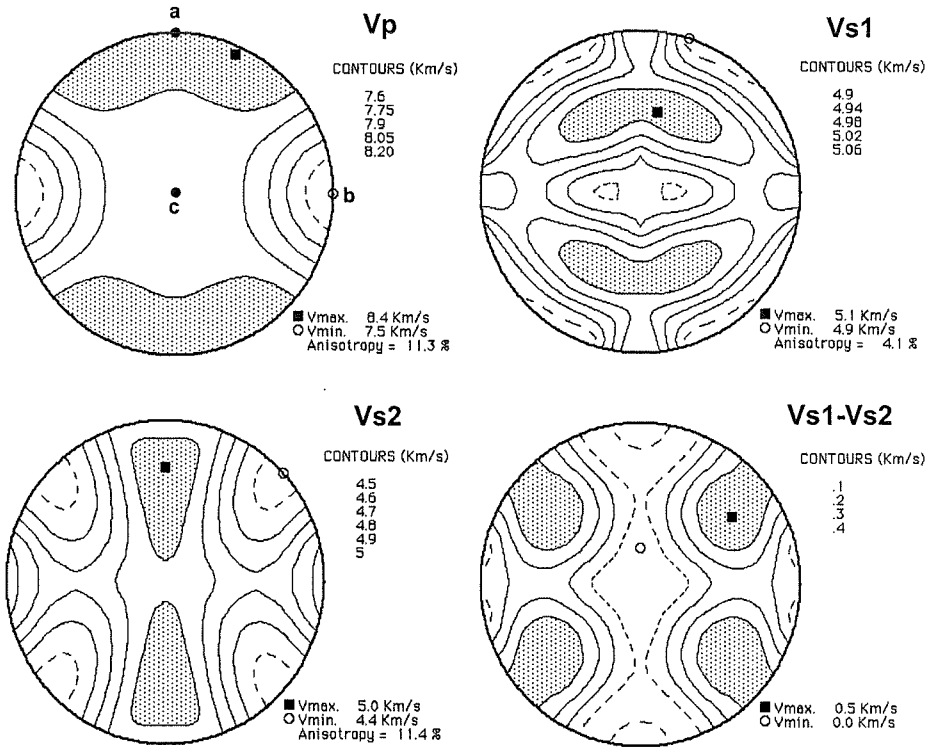


Figure 1.3 (l) Enstatite ($MgSiO_3$)

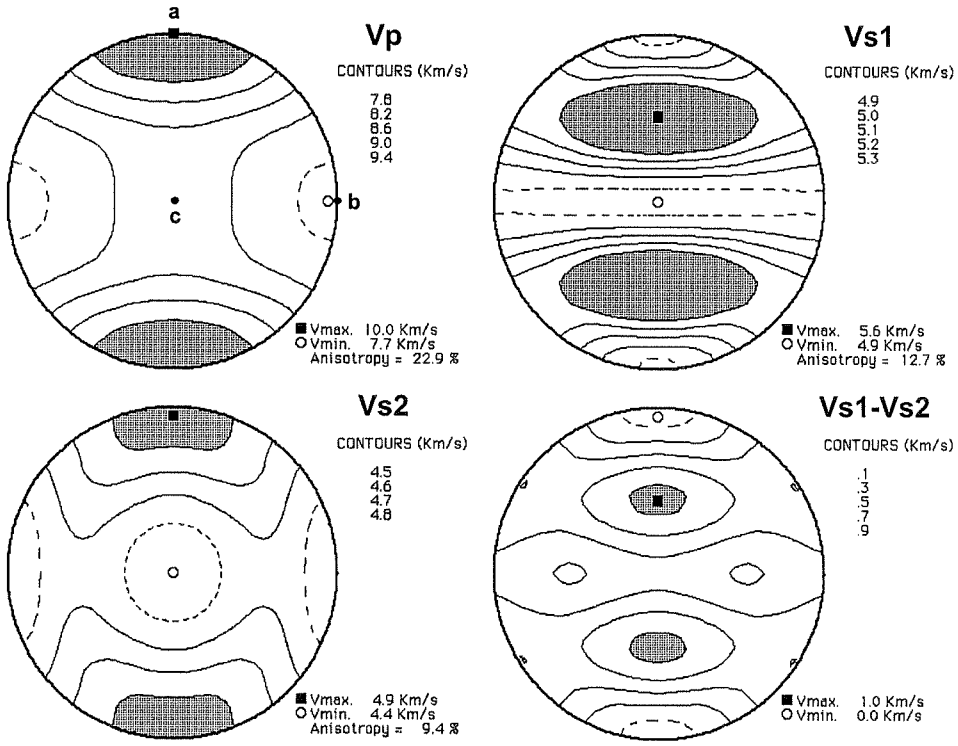


Figure 1.3 (m) Olivine $Fo_{93}Fa_7$

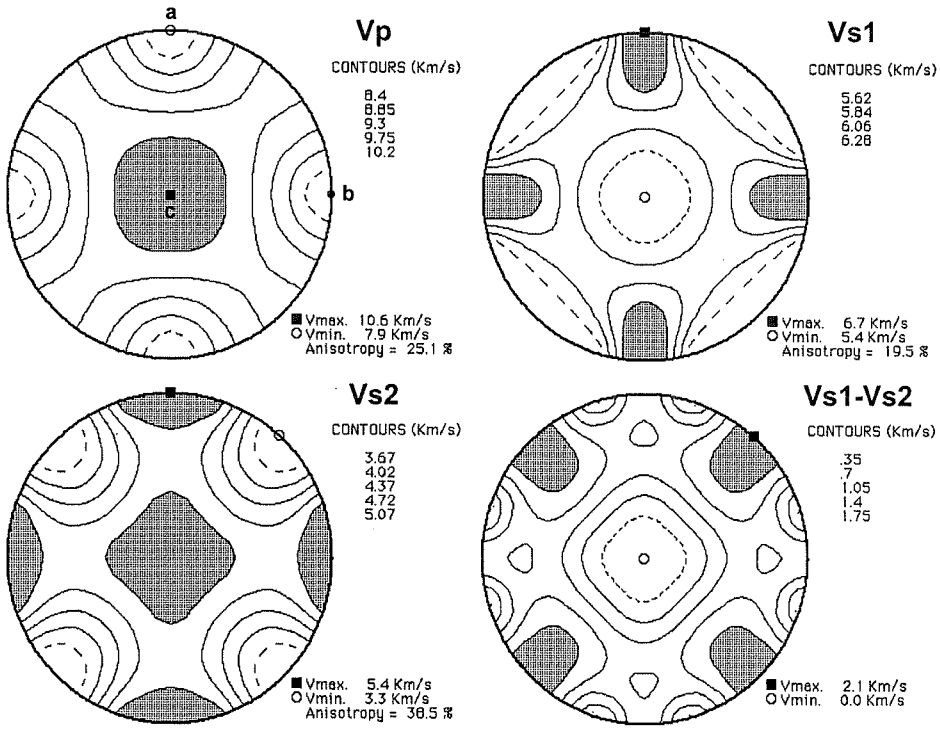


Figure 1.3 (n) Rutile TiO_2

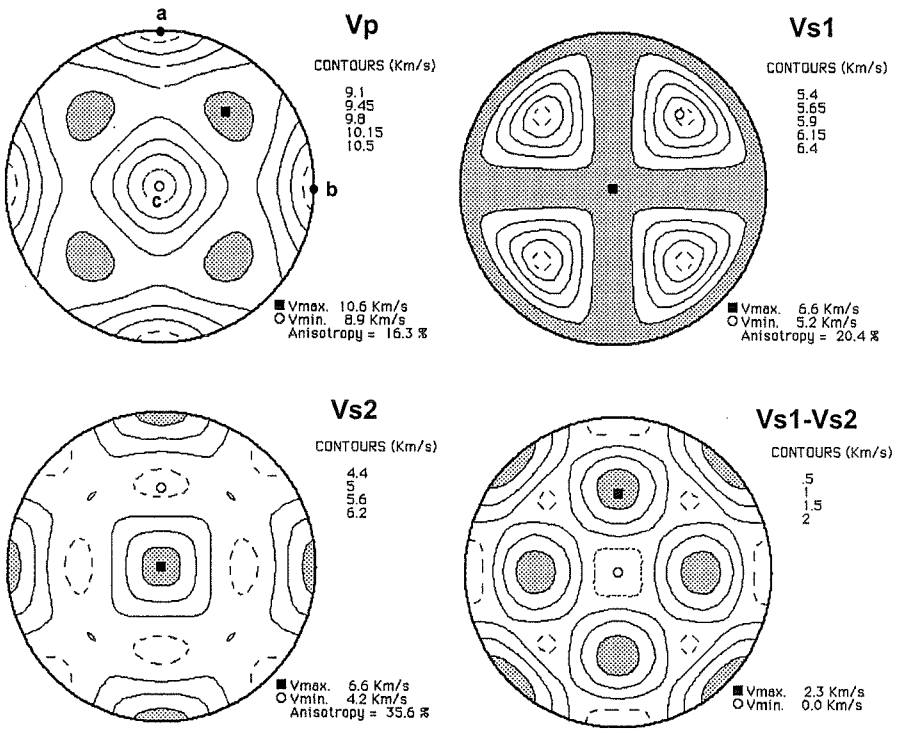


Figure 1.3 (o) Spinel $MgAl_2O_4$

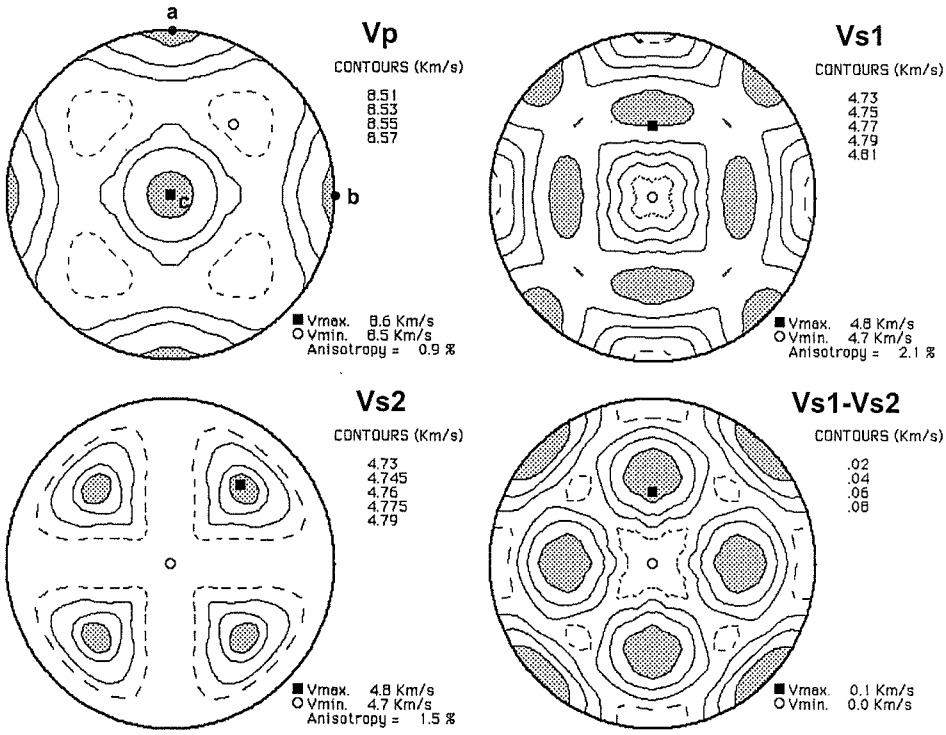


Figure 1.3 (p) Almandine $Alm_{74}Py_{20}Gr_3Sp_3$

A composite is statistically isotropic when its effective stress-strain relation is independent of the choice of coordinate system (Hashin, 1983). By neglecting its detailed microstructure, a polycrystalline monophase or multiphase rock can be assumed to be macroscopically homogenous and isotropic with equiaxed grains and randomly oriented crystals. Such isotropic aggregates can be characterized by only two independent elastic constants, for example, the bulk modulus K and the shear modulus G. The approaches most frequently used for calculation average K and G values for polycrystals are those of Voigt (1928) and Reuss (1929), which assume uniform strain and stress, respectively, in an isotropic aggregate. Hill (1952) demonstrated that the Voigt and Reuss averages represent upper and lower bounds of apparent elastic moduli of an isotropic aggregate, and the arithmetic mean of the upper and lower bounds, termed the Hill or the Voigt-Reuss-Hill average, would be a convenient approximation.

For a monomineralic aggregate, its averaging elastic moduli can be calculated according to the following equations:

$$K_V = [C_{11} + C_{22} + C_{33} + 2(C_{12} + C_{13} + C_{23})]/9 \tag{1.12}$$

$$G_V = [C_{11} + C_{22} + C_{33} - (C_{12} + C_{13} + C_{23}) + 3(C_{44} + C_{55} + C_{66})]/15 \tag{1.13}$$

$$K_R = [S_{11} + S_{22} + S_{33} + 2(S_{12} + S_{13} + S_{23})]^{-1} \tag{1.14}$$

$$G_R = 15[4(S_{11} + S_{22} + S_{33}) - 4(S_{12} + S_{13} + S_{23}) + 3(S_{44} + S_{55} + S_{66})]^{-1} \tag{1.15}$$

$$K_H = (K_V + K_R)/2 \tag{1.16}$$

$$G_H = (G_V + G_R)/2 \tag{1.17}$$

$$K_G = \sqrt{K_V K_R} \tag{1.18}$$

$$G_G = \sqrt{G_V G_R} \tag{1.19}$$

where the subscripts V, R, H, G denote Voigt, Reuss, Hill and geometric averages, respectively. The component C_{qr} and S_{qr} are the 6×6 single-crystal elastic stiffness and compliance tensors defined in Equations (1.3) and (1.4). It is worth emphasizing that although the Hill average has been widely used as the best representation of the overall elastic properties of polycrystalline aggregates (e.g., Watt, 1988; Zhao and Anderson, 1994), it does not give compatible stiffness (C_{qr}) and compliance (S_{qr}) tensors described by Equation (1.4). In contrast, a geometric mean of the Voigt and Reuss bounds fulfills the compatibility and it is very close to the much more complicated iterative, self-consistent, micromechanical models (e.g., Matthies and Humbert, 1993; Mainprice and Humbert, 1994).

In addition, the Voigt and Reuss bounds often spread about 5% or more on either side of the Hill average. With increased precision in the measurement of elastic stiffnesses, this theoretical uncertainty becomes more significant than the experimental uncertainty. Hashin and Shtrikman (1962a, 1962b, 1963) proposed a more sophisticated variational approach for polycrystals with cubic symmetry, which considerable reduced the Voigt and Reuss bounds. Subsequently, the Hashin-Shtrikman bounds were derived for materials of all crystal symmetries and classes, except triclinic (Peselnick and Meister, 1965; Meister and Peselnick, 1966; Watt and Peselnick, 1980). Watt (1987) presented a FORTRAN program, POLYXSTAL, to calculate Voigt, Reuss and Hashin-Shtrikman bounds on the average bulk and shear moduli of isotropic polycrystals with any symmetry, except triclinic.

1.1.3 Seismic properties of polyphase rocks

Elastic moduli of an isotropic polymineralic rock can be calculated according to its modal composition and elastic moduli of constituent minerals as follows:

$$M_c = \left[\sum_{i=1}^{N}(f_i M_i^J)\right]^{1/J} \tag{1.20}$$

where M_c and M_i are an elastic modulus (either K or G) of the polymineralic rock consisting of N minerals and of ith monomineralic aggregate obtained from Equations (1.12)-(1.19), respectively, f_i is the volume fraction of ith mineral, and J is a scaling parameter. Equation (1.20) is the generalized means widely used in statistics. The case J = 1 yields the arithmetic mean or Voigt average (M_V), and the case J = -1 yields the harmonic mean or Reuss average (M_R). As J approaches 0, the limit of M_c is the geometric mean (M_G). Finally, the Hill average (M_H) is given by $M_H = (M_V + M_R)/2$. Then according to Equations (1.9) and (1.10), P- and S-wave velocities of the isotropic polymineralic rock can be calculated from values of M_c and density. Thus, polyphase rocks can be characterized by "effective" or "equivalent" density and elastic moduli if the dimensions of the constituents (e.g., grains, pores, fractures, layering) are small compared with the shortest wavelengths of significance.

Ji et al. (2004, see Appendix 1) found that the generalized means can provide a phenomenological approach for the prediction of mechanical properties of multiphase materials and rocks. The parameter J can be regarded as a microstructure coefficient that is mainly controlled by the shape and distribution (continuity and connectivity) of the phases, and consequently, phase volume fractions. The means with J = 0.5 or J = -0.5 provides good agreement with the experimental data of Young's modulus for two-phase composites in which spherical strong or weak inclusions are continuous support medium. For most composite materials in which the inclusions are shaped somewhat randomly, the

means with $J = 0.25$ and $J = -0.25$ fit well the measured values of Young's modulus for those with strong-phase continuous (the volume fraction of strong phase $f_s \geq 0.7$) and weak-phase continuous ($f_s \leq 0.5$), respectively. In the intermediate compositional range ($0.4-0.5 \leq f_s \leq 0.6-0.7$), J may vary progressively from -0.5 to 0.5 or from -0.25 to 0.25 due to the transition in microstructure. Therefore, a systematic study on different average schemes will bring new information on interpretation of seismic data.

The LPO of minerals can be measured by using an optical microscope equipped with a five-axis universal stage (i.e., U-stage), a X-ray or neutron texture goniometry, or a SEM equipped with an electron backscatter diffraction (EBSD) system. When the LPO data of constituent minerals are available, 3D seismic properties of an anisotropic, polymineralic rock can be calculated (e.g., Crosson and Lin, 1971; Ji and Mainprice, 1988; Mainprice, 1990; Ji et al., 1994). Furthermore, if we know pressure and temperature derivatives of the single crystal elastic constants, the LPO-derived seismic properties can be extrapolated to any pressure (P) and temperature (T):

$$C_{qr}(P,T) = (C_{qr})_0 + \left(\frac{dC_{qr}}{dP}\right)(P-P_0) + \left(\frac{dC_{qr}}{dT}\right)(T-T_0) \qquad (1.21)$$

$$\rho(P,T) = \rho_0 + \left(\frac{\rho_0}{K}\right)(P-P_0) - \alpha\rho_0(T-T_0) \qquad (1.22)$$

where K is the bulk modulus; $(C_{qr})_0$ and ρ_0 are the elastic stiffness coefficient and density at room temperature (T_0) and room pressure (P_0); dC_{qr}/dP and dC_{qr}/dT are the pressure and temperature derivatives, respectively; and α is the thermal expansion coefficient.

1.2 Laboratory sample studies

Laboratory measurements of elastic constants and elastic wave velocities are interesting practice for geophysicists since 1960's, with focus on natural rocks (e.g., Birch, 1960; Christensen, 1965; Kern, 1993; Ji et al., 1993; Ji and Salisbury, 1993), hot-pressed polycrystalline aggregates (e.g., Watt, 1988; Wang and Ji, 2001) and single crystals (e.g., Wang, 1966, Bhagat et al., 1992). The accuracies of laboratory velocities depend on the techniques employed, varying from 0.5% to 3% for the pulse-transmission method commonly used for rocks (e.g., Birch, 1960; Kern, 1982a) to approximately 0.01% with interferometric method for single crystal and polycrystalline specimens (e.g., McSkimin, 1950; Liu et al., 2000). Recently, Li et al. (2004) reported combined ultrasonic interferometry, X-ray diffraction and X-radiography in multi-anvil apparatus for measuring elasticity of polycrystalline Mg_2SiO_4 at pressure to 6.7 GPa and temperature to 1273 K. Moreover, they used dual-mode transducers to produce P-and S-wave data at same conditions in a single acoustic experiment. Their new techniques enable simultaneous measurements on P- and S-wave velocities, sample lengths and X-radiographic images.

Generally, seismic velocities of natural rocks are measured by the ultrasonic transmission method using piezoelectric transducers with frequencies of 1-2 MHz. Reported velocities are derived from curves during decompression runs because these measurements can be reproduced whereas velocities determined during pressurization are not reproducible. Although the frequencies used in the laboratory experiments are much higher than those in field studies, laboratory-derived seismic velocities can be directly compared with field data due to negligible dispersion in the frequency range of 10^{-1} to 10^7 Hz (Christensen, 1989). Two groups of experimental techniques can be distinguished according to the method of pressure generation, the preparation of specimen and the position of transducers relative to specimen.

(1) Measurements on jacketed cylindrical samples in internally heated fluid or gas apparatuses with the transducers placed directly onto the sealed specimen (e.g., Birch, 1960; Christensen, 1965; Ji and Salisbury, 1993). Confining pressure is generated by advance of a piston over the pressure medium. Transmitting and receiving transducers are exposed to pressure and temperature during the experiment, which limits the working temperatures up to 450-500 °C because of the Curie temperature of the transducer material. The advantage of this technique is that truly hydrostatic pressure is obtained and the sealing of the specimen allows the study of the effects of pores on velocities. Errors mainly result from inaccuracies in core length measurements, travel time determination, and sample length change at high pressures. The accuracy of *Vp* and *Vs* are estimated roughly to be 0.5% and 1%, respectively.

(2) Experiments on unjacketed, cube-shaped specimens in a cubic anvil pressure apparatus (e.g., Kern, 1982a; Kern et al., 2001). A state of near-hydrostatic stress is achieved by pressing six pyramidal pistons in the three mutually orthogonal directions onto a cube-shaped specimen. A furnace surrounds one end of each piston next to the specimen and heat is transmitted from pistons to the specimen. Transducers are placed on the low-temperature side of the pistons, which allows measurements to be carried out at temperatures as high as 700 °C. This technique can simultaneously measure P- and S- wave velocities on the three perpendicular directions, and directly determine length changes (density change) of the sample with increasing pressure and temperature. The cumulative error in *Vp* and *Vs* is estimated to be less than 1%. However, because the pressure is not exactly hydrostatic, the values of pressure derivative and seismic anisotropy could be potentially overestimated.

Relationships between seismic velocities and pressure, temperature, density or chemical and mineralogical compositions have been carefully investigated (for summary see Christensen, 1989; Schön, 1996; Ji et al., 2002). For most crustal rocks, positive

pressure derivatives and negative temperature derivatives of seismic velocities essentially counteract each other. To prevent thermal cracking, the minimum pressure increment is generally needed to be 1 MPa/°C, but in quartz-rich rocks the pressure increment should be higher because of the very large thermal expansion of quartz (Kern, 1982b). Figure 1.4 illustrates a whole data set of laboratory measurements on seismic properties of an amphibolite. The rapid increase of *Vp* (Figure 1.4a) and *Vs* (Figure 1.4b) at low pressure is attributed to the closure of microcracks with increasing pressures. Above a crack-closing pressure, the linear parts of velocity-pressure and velocity-temperature curves allow the calculations of pressure and temperature derivatives of velocities (Figure 1.4a-d). No matter how P- and S-wave anisotropy varies at low pressure, at high pressure the values of anisotropy will approach a constant (Figure 1.4e) and apparently are not much affected by temperature (Figure 1.4f), which is explained by the closure of microcracks and the contribution of the LPO of minerals at high pressure. Therefore velocities and anisotropy measured at low pressure cannot represent the state of seismic properties in deeper levels of the crust. In deep crust where confining pressures are high, the change of anisotropy and velocities with depth will be very small for most rock types.

Besides pressure, temperature and rock fabric, one of the most significant parameter controlling seismic properties of rocks is mineralogy, which is a function of chemical composition and petrologic evolution. P-wave velocities of coarse-grained igneous rocks and metamorphic rocks (Figure 1.5a) increase from felsic to ultramafic composition, which is consistent with *Vp* values of their constituent minerals (Figure 1.5b). A triangular distribution of Poisson's ratio versus *Vp* is observed, which is bounded by quartzite with low velocity and low Poisson's ratio, serpentinite with low velocity and high Poisson's ratio, peridotite and eclogite with high velocity and intermediate Poisson's ratio (Figure 1.5a). Poisson's ratios increase as composition changes from granite and felsic gneiss (~0.24) to gabbro and mafic granulite (~0.27) by decreasing quartz and increasing anorthite content of plagioclase feldspar, and then decreases to 0.26 in peridotite with decreasing plagioclase and increasing olivine contents.

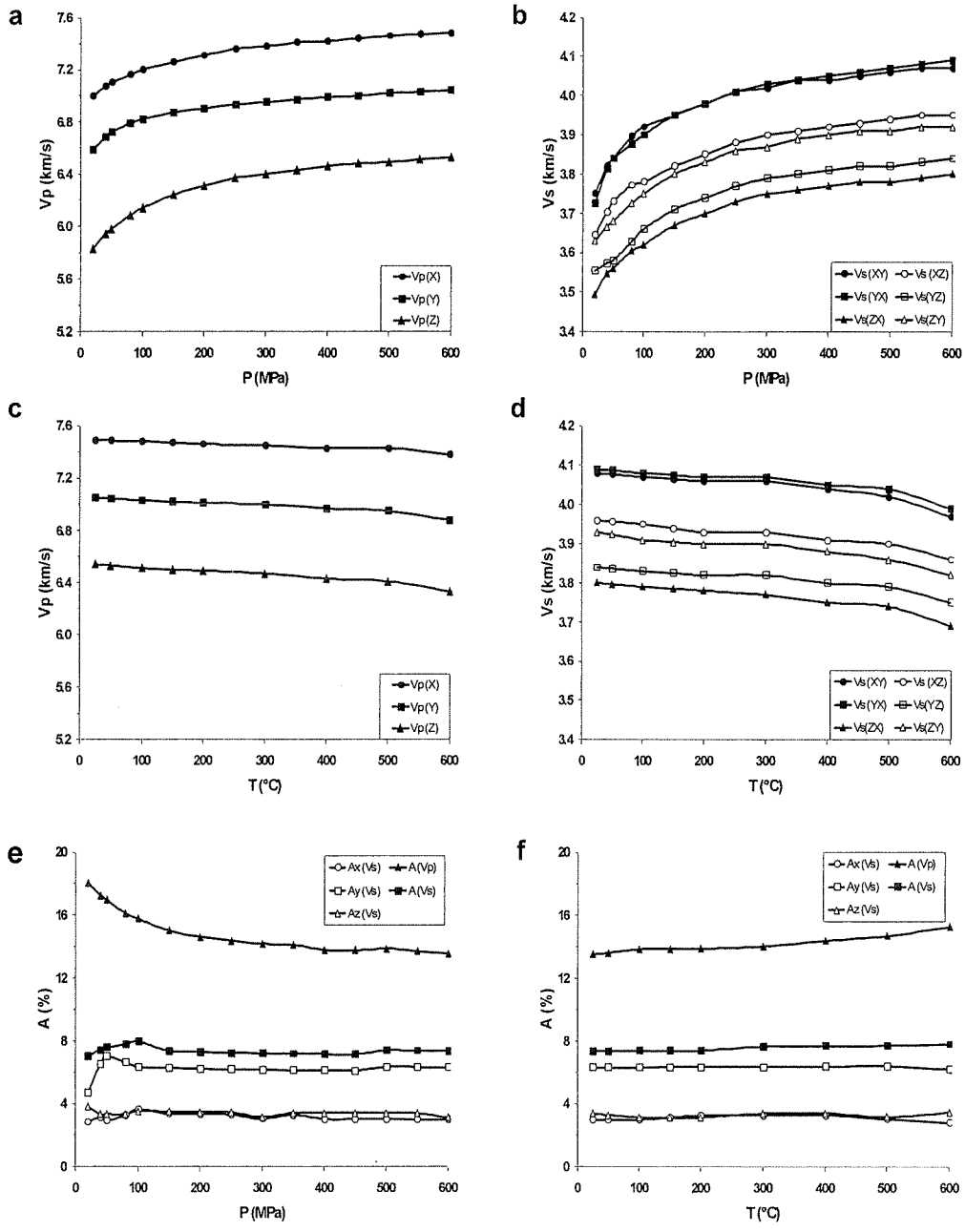


Figure 1.4 Seismic properties of an amphibolite from Ivrea Zone as a function of pressure at 20 °C and as a function of temperature at 600 MPa (original data from Barruol, 1993). (a) *Vp*-pressure, (b) *Vs*-pressure, (c) *Vp*-temperature, (d) *Vs*-temperature, (e) anisotropy-pressure, and (f) anisotropy-temperature.

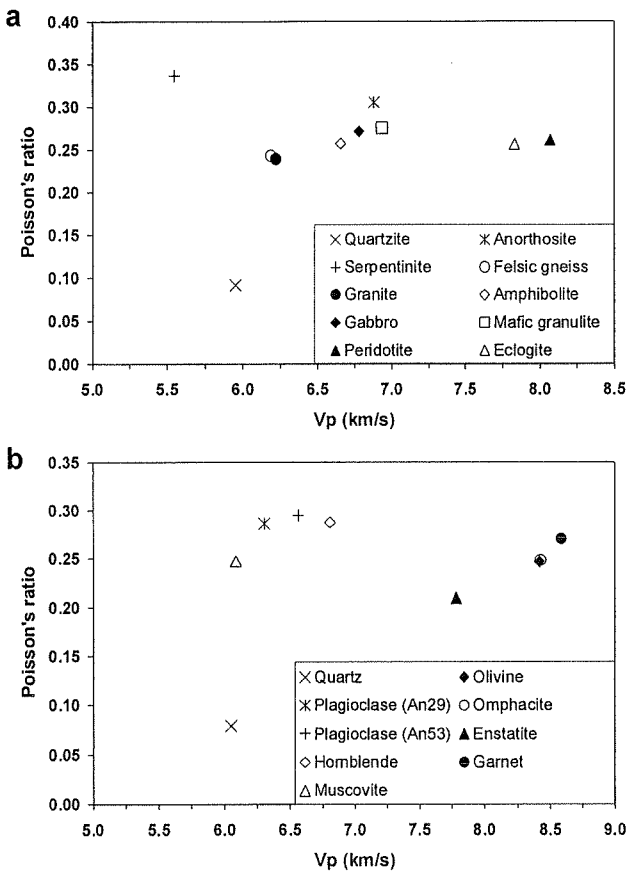


Figure 1.5 Comparison of (a) measured Poisson's ratio and Vp (200 MPa, 25 °C) of common rock types with (b) theoretical values of monomineralic aggregates (zero porosity, 0.1 MPa and 25 °C).

Moreover, mineral phase transition can significantly affect seismic velocities and Poisson's ratio of rocks. As shown in Figure 1.6, the quartz α-β phase transition will result in a decrease in *Vp* and Poisson's ratio in the temperature range 500-650 °C, which has been used as a temperature estimator for the upper and middle continental crust composed of quartz-rich felsic rocks (e.g., Mechie et al., 2004). The drop of *Vp* is explained by the elastic softening of quartz structure near α-β phase transition and the opening of grain-boundary cracks, caused by the very high volumetric thermal expansion of quartz. The subsequent velocity increase in the β-field may be attributed to an elastic hardening of the quartz structure (Kern, 1979, 1982b; Meister et al., 1980).

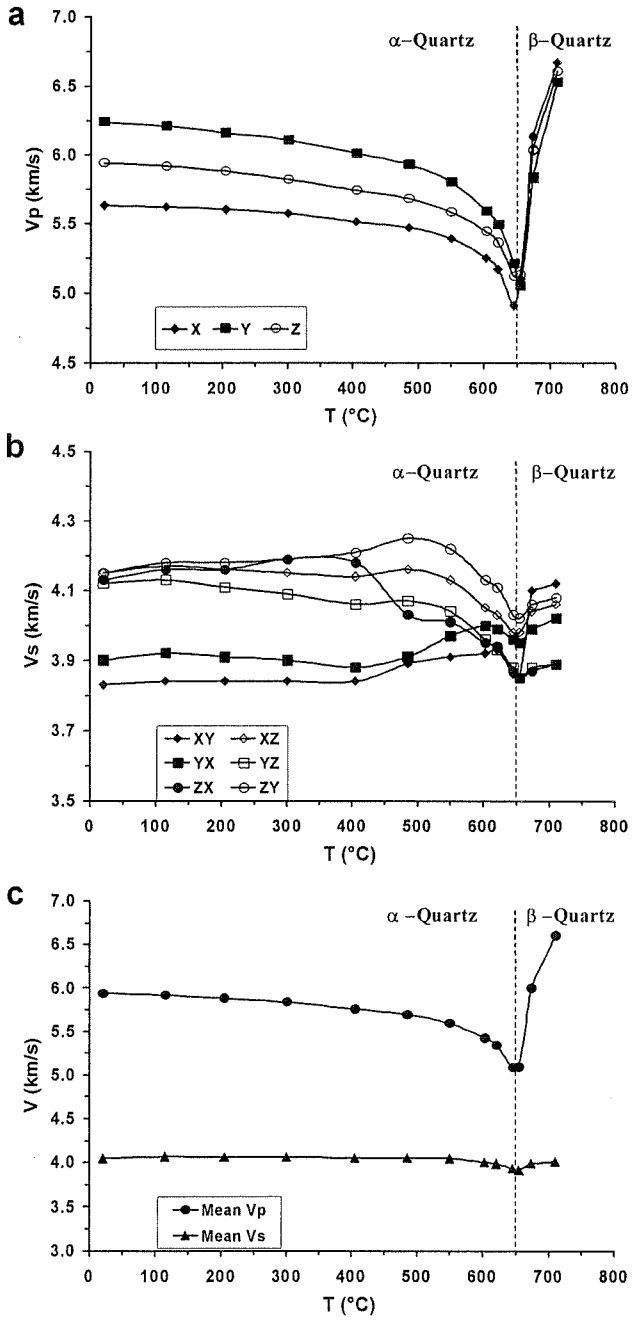


Figure 1.6 Variations of seismic properties at 600 MPa in a quartzite due to the α-β quartz transition with changing temperature. (a) P-wave velocities in the X, Y and Z directions, (b) S-wave velocities propagating and vibrating in the X, Y, and Z directions, and (c) the mean P- and S-wave velocities. After Ji et al. (2002) and original experimental data from Barruol (1993).

1.3 Seismic properties of the continental crust and upper mantle

1.3.1 Velocity structures

The crust is the low-density outermost layer of the Earth above the Mohorovicic discontinuity (the Moho), which is a global boundary where *Vp* increases rapidly to a value in excess of 7.8 km/s (the upper mantle). The average *Vp* of the crust is 6.45 km/s, and that of the uppermost mantle (Pn velocity) is 8.09 km/s. Perhaps the most basic parameter regarding the crust is total thickness (Figure 1.7). Christensen and Mooney (1995) gave the weighted average continental crustal thickness of 41.1 km. More than 95% of all continental crust has a thickness between 22 km and 57 km. The thinnest continental crust (the Afar Triangle, northeast Africa) is about 16 km thick, and the thickest crust (the Himalayan Mountains) is about 72 km thick.

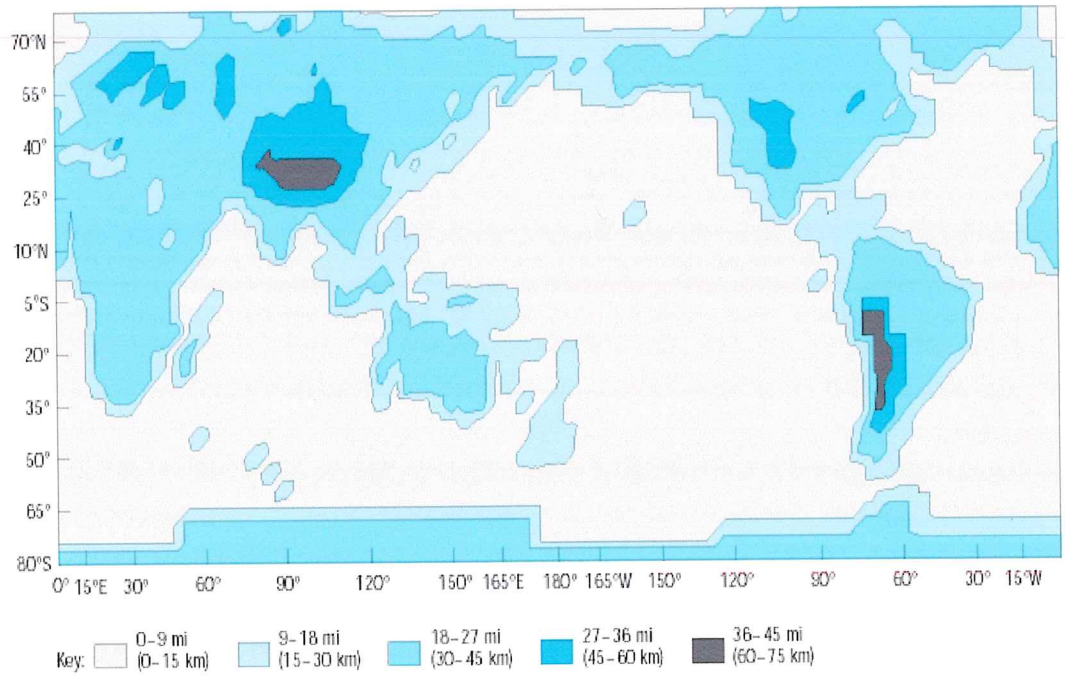


Figure 1.7 Contour map of global crustal thickness, Northern Polar Regions are not shown (after Mooney and Natland, 2001).

The thickness difference will affect the travel time of seismic wave passing through the Earth. Figure 1.8 gives the deviation away from vertical S-wave travel time of an average Earth, which is derived by vertically integrating a three-dimensional model of shear-velocity variation. The darkest regions correspond to the oldest continental crust with faster *Vs*, known as cratons, while the lightest areas correspond to regions of active rifting with slower *Vs*, either at mid-ocean ridges or incipient oceans such as the Red Sea.

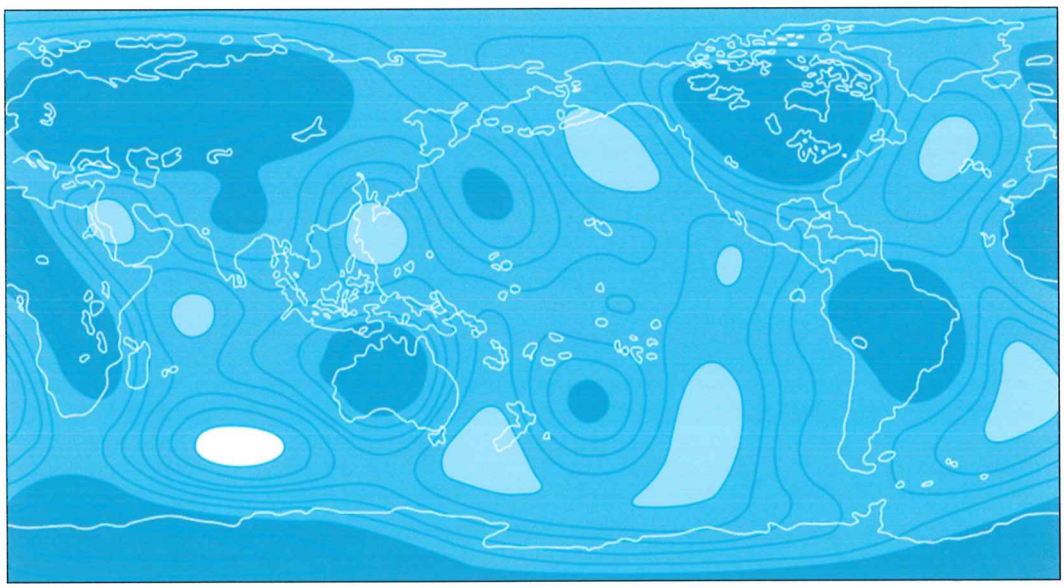


Figure 1.8 Travel time anomalies from 400 to 40 km to an average Earth. Dark areas are fast relative to the Earth, while light areas are slow (after Mutter and Lerner-Lam, 2002).

Despite its geologic complexity, the continental crust is generally divided into four layers according to progressive increasing *Vp* values: an uppermost sedimentary layer, and an upper, middle, and lower crust composed of crystalline rocks. As shown in Figure 1.9, crustal seismic properties vary systematically in various tectonic environments (e.g., Holbrook et al., 1992; Rudnick and Fountain, 1995; Christensen and Mooney, 1995). Because positive pressure derivatives and negative temperature derivatives usually counteract each other for common crustal rocks, in a crust with no compositional or

metamorphic variations and no fracture porosity, seismic velocity would increase with depth very slightly in stable continental areas with modest geothermal gradients (10-15 °C/km), and would in fact decrease in tectonically active areas with high geothermal gradients (20-25 °C/km). The observation that seismic velocities increase with depth supports the common model of a continental crust that is increasingly mafic with depth, featuring an upper crust dominated by felsic and intermediate rocks and a lower crust dominated by mafic rocks.

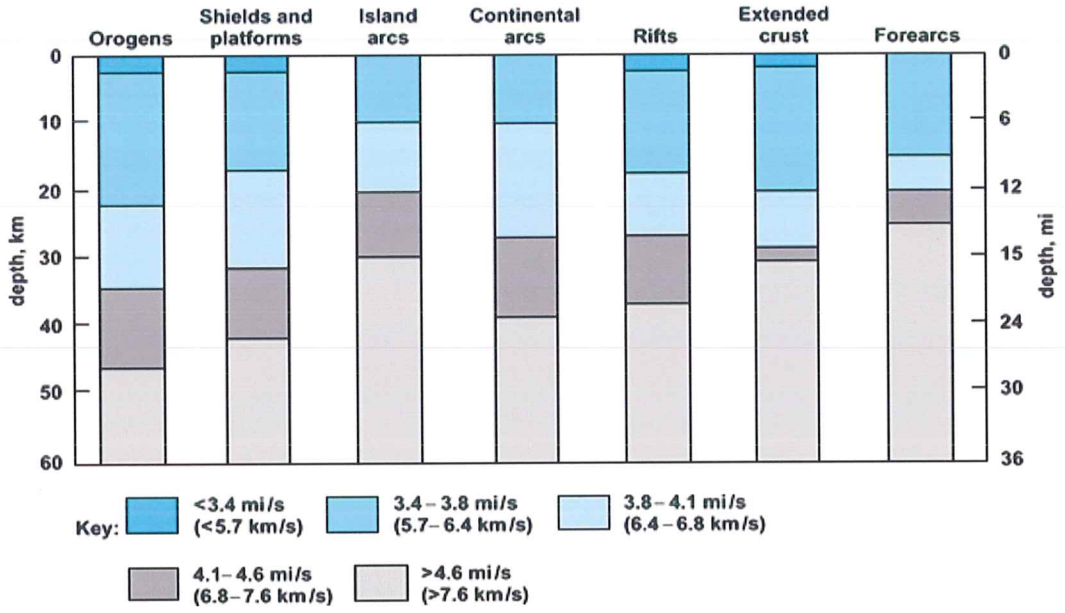


Figure 1.9 Average crustal columns for seven geologic provinces, showing variations in crustal thickness (after Mooney and Natland, 2001).

The sedimentary cover of the continental crust averages 1 km in thickness, and varies in thickness from zero (e.g., on shields) to more than 10 km in deep basins. In stable continental crust of average thickness, the crystalline upper crust is commonly 10-15 km thick and has an average composition equivalent to granite. The "Conrad discontinuity", a relatively abrupt increase in the velocity from 6.1 to 6.4-6.7 km/s, occurs at various depths and marks contact of granitic and basaltic layers, separating the upper crust from middle crust (or in some cases lower crust) in many crustal sections. The 5-15 km thick

middle crust consists of amphibolite facies rocks and is intermediate in bulk composition. The thickness of lower continental crust is generally about 10 km except in extended crust that has extremely thin lower crust and in orogens that may exceed 20 km. There is large variation in average P- and S-wave velocities of the lower crust between different geologic settings (Holbrook et al., 1992). The composition of lower continental crust is equivalent to primitive mantle derived basalt, but it may range to intermediate bulk composition in some regions (e.g., Rudnick and Fountain, 1995; Gao et al., 1998).

However, because many rocks display similar seismic velocities, there are unavoidable ambiguities in estimating petrological composition of the deep crust from the comparison of field- and laboratory-derived P- or S-wave velocities. For example, the span of the lower crustal P-wave velocities, from 6.4 km/s to 7.5 km/s, covers the velocity ranges of schist, intermediate and mafic granulites, anorthosite, amphibolite and metapelites, which implies that the lower continental crust must be composed of a diversity of lithologies in different tectonic environments (Holbrook et al., 1992). Poisson's ratio or *Vp/Vs* ratio can provide valuable constraints on interpretation of seismic field data. Poisson's ratio of quartz is extremely low (0.06-0.1) while that of feldspars is quite high (0.28-0.30). In general, Poisson's ratio appears very little dependent on both pressure and temperature for most rocks (Christensen, 1996). Thus Poisson's ratio generally increase from the upper crust to lower crust because the quartz content decreases while feldspar content increases in rocks. The average Poisson's ratio for continental and oceanic crusts are estimated to be 0.265 and 0.30, respectively (Christensen, 1996).

Because of the similar velocities of granite, diorite, paragneiss, felsic gneiss and intermediate gneiss, the continental upper crust is often non-reflective although complex structures and compositional changes may exit in this level. In many regions, particularly in extended crust, the lower crust contains numerous horizontal reflections that terminate at the depth of the Moho. As a possibility, these reflections result from igneous intrusions

in the lower crust, combined with the horizontal stretching of the warm and ductile lower crust (Mooney and Meissner, 1992).

1.3.2 Seismic anisotropy

For mathematical convenience, the Earth is usually assumed to be isotropic to the propagation of seismic waves. However, seismic anisotropy of rocks can produce a large variation in velocities, sometimes even overwhelms effects of petrological change. Since 1960's, study of seismic anisotropy has become an important subject in seismology of first oceans and then continents and has provided valuable insights into geodynamic process in plate tectonics (for review, see Savage, 1999; Park and Levin, 2002). The most obvious manifestations of anisotropy are:

- Shear wave splitting – the polarization of the fast wave (Φ) and of the delay time (δt) between fast and slow waves;
- Azimuthal anisotropy – the arrival times, or apparent velocities of seismic waves at a given distance from an event, depend on azimuth;
- An apparent discrepancy between Love waves and Rayleigh waves.

As shown in Figure 1.3 and Table 1.3, most minerals are strongly anisotropic. The directional dependence of P- and S-wave velocities and shear wave splitting can be correlated with the LPO of constituent minerals and be analyzed in the same terms used to describe crystal symmetry (e.g., Barruol and Mainprice, 1993). Hexagonal symmetry, although a special case of anisotropy, has quite general applicability within the Earth. This kind of anisotropy is exhibited by laminated or finely stratified media, solids containing oriented cracks or melt zones, and floating ice sheets. For simplicity, peridotite massifs, harzburgite bodies and the oceanic upper mantle have also been approximated by a hexagonal symmetry. The symmetry axis can be fast, as for strained olivine-rich rocks (e.g., Christensen, 1978; Ji et al., 1994; Ben Ismaïl and Mainprice, 1998), or slow, as for mica-rich rocks (e.g., Siegesmund et al., 1989; Weiss et al., 1999; Ji et al., 2002). If the symmetry axis is vertical, anisotropy mainly affects wave speeds,

while horizontal and plunging symmetry axes will result the polarization birefringence and amplify scattering between different waves (Savage, 1999).

In the upper crust, crack-reduced seismic anisotropy is well related with the distribution of regional stress, e.g., in fault zones (Mizuno et al., 2001), in mountain belts (Lokmer and Herak, 1999), and in fracturing reservoirs for gas and oil exploration (MacBeth et al., 1998). Fluids trapped in cracks and pores increase seismic velocity and play an important role in the special and temporal variations of seismic anisotropy. For example, at 9 km of KTB borehole, seismic events caused by the fluid injection could result in the tectonic stress release and consequently, the temporal anisotropy variation (Bokelmann and Harjes, 2000). As an application, changes in shear wave splitting can be observed before and after large earthquakes.

In contrast, seismic anisotropy of deep crust is mainly controlled by the LPO of minerals such as biotite and amphibole. The amphibolitic mylonite and mica-rich mylonite often possess a seismic anisotropy greater than 8% (e.g., Ji et al., 1993). At high pressure, the igneous rocks are quasi-isotropic and high-grade granulite and eclogite facies rocks display relatively low anisotropy. Thus seismic anisotropy is more significant for the upper and middle crust than for the lower crust, and can be used as an indicator of shear zones or thrust faults in the deep crust (e.g., Jones and Nur, 1984; Fountain et al., 1984; Ji et al., 1993). For example, low-angle mylonitic zones can be distinguished by fabric-related velocity anisotropy because mylonites appear as low-velocity layers when seismic waves propagate perpendicular to the foliation (Ji et al., 1993; Zorin et al., 2002). For those large-scale strike-slip fault zones (e.g., the Red River fault), the steeply dipping foliation and horizontal extension lineation will be transversely anisotropic in middle crust with the slowest seismic velocity perpendicular to the foliation (Ji and Salisbury, 1993). At deeper lever, however, the fault lies in the granulite facies and may be quasi-isotropic (Ji and Salisbury, 1993). Hence the special change of anisotropy for a shear zone implies different metamorphic facies in a given level of crust.

The anisotropy of the upper mantle is mainly attributed to the orthorhombic mineral olivine. Like velocity structures of the crust, characteristic seismic anisotropy in the upper mantle can be related with different tectonic processes. These include, but are not limited to, cratonization, terrane accretion and collision, continental rifting (both passive and active), subduction, and lithospheric basal erosion due to a relative motion of cratonic keels and the convective mantle. For example, the fast axis of strained olivine-rich mantle rocks will align with the extension direction in simple shear, which occurs at the base of a moving plate and produces anisotropy with a plunging axis of symmetry (e.g., at the base of the North American plate, Barruol et al., 1997). At convergent margins, pure shear in the shallow mantle can explain orogen-parallel fast polarization in the Pyrenees (Barruol et al., 1998) and in South Island, New Zealand (Little et al., 2002). In tectonically active continental regions, although seismic anisotropy often agree well with localized lithospheric flows during the most recent thermotectonic events, the pre-existing mantle fabric may control the deformation regime and impose a strong strike-slip shear component. As for instance, the NW-SE trending fast shear wave in the southern Massif Central, France, appears to be uncorrelated to Hercynian structures or to the present-day motion of the plate, but is correlated to the Tertiary extension direction (Barruol and Granet, 2002). In stable continental shields, a relict anisotropy can be preserved as long as one billion years or more and indicate fossil mantle textures since the initial rifting, collision and accretion events (e.g., Canadian Shield, Ji et al., 1996; North America, Silver and Chan, 1991; southern Africa, Silver et al., 2001).

Although there has been significant advance in measurements and interpretation of seismic anisotropy, some questions are still open.

- With the change of pressure and temperature, it seems impossible to distinguish the petrology heterogeneity from structural anisotropy within the resolution of seismic profiles. Moreover, the dipping of foliation may be neither horizontal nor vertical, thus the observations of anisotropy cannot be explained by the maximum

experiment results on the specimen or crystals (Ji et al., 1994). The credit of xenoliths for interpretation of anisotropy is under challenge too (Christensen, 2002).

- In tectonic zones with long history, seismic anisotropy may reflect the degree of the crust and upper mantle involved: from the crack-induced anisotropy in the upper crust to the LPO-dominant anisotropy in the lower crust and upper mantle, the discrepancy of direction and quantity can be a parameter to trace its tectonic evolution (Babuska and Cara, 1991). But the believable comparison example is lack up to now.
- Olivine is regarded as the main mineral to induce anisotropy in the upper mantle, however, its percentage in rocks may substantially affect the anisotropy observed but the exact relationship has not been set up (e.g., Saruwatari et al., 2001; Blackman et al, 2002).
- The influence of fluids is still not very clear in the lower crust and upper mantle, especially in subduction zone, where fluids can take part into the phase transition and change the effective pressure totally.

In conclusion, crack- and fine layering-induced anisotropy is prevalent in the upper and lower crust, respectively, while fabric-related anisotropy is more important in the upper mantle. To have a better understanding of the interior of the Earth, we need more detailed laboratory and field experiments and more prudence in interpretation.

Chapter 2
Database of rock seismic properties (DRSP)

The past 4 decades have been a virtual explosion in the amount of data on seismic velocities and anisotropy of rocks from around the world. The latest compilation of seismic velocities of rocks was done by N.I. Christensen as a chapter in *Practical Handbook of Physical Properties of Rocks and Minerals* (edited by R.S. Carmichael, 1989). Christensen's compilation is a straight listing of data published before 1980, without additional information such as mineralogical and chemical compositions, metamorphic grade and microstructural information. His compilation included few data of seismic velocities as a function of temperature and none of shear wave splitting of rocks. However, enormous volumes of data have been accumulated since 1980. Thus a new compilation of seismic properties of minerals, rocks and ores is urgently needed to provide a convenient, compact and comprehensive source for geotechnical engineers and geoscientists.

We have collected almost all data available in the literature published in English and French during last 4 decades and established an Internet Database of Rock Seismic Properties (DRSP: http://texture.civil.polymtl.ca:8080/seismic-properties/index.jsp), which is more complete than any previous compilations (e.g., Christensen, 1989; Schön, 1996) and permit enormous volumes of data to be studied in a far more comprehensive fashion than has hitherto been attempted. We also published *Handbook of Seismic Properties of Minerals, Rocks and Ores* (Ji, Wang and Xia, 2002; Polytechnic International Press, Montreal, pp. 630). Statistics analysis on these data will provide helpful information on exploration laboratory data to seismic field observations.

2.1 Database design

We collected 245 references on laboratory measurements of P- and S-wave velocities of minerals, rocks and ores, including original contributions, LITHOPROBE reports, previous compilations in books and review papers, unpublished M.Sc. and Ph.D. theses from major laboratories. All seismic data (about 1000 rock samples) measured in the GSC/Dalhousie High Pressure Laboratory of M.H. Salisbury over last 15 years are also merged into the DRSP. Furthermore, the users of the DRSP are invited to submit their data as well as related information so that the DRSP can be updated at regular intervals.

To facilitate the finding of related records, a relational database is required to link all entities involved such as P- and S- wave velocities (*Vp* and *Vs*) along propagation and vibration directions (X - parallel to the stretching lineation, Y - perpendicular to the lineation and parallel to the foliation, and Z - normal to the foliation) at various pressures and temperatures, mean *Vp* and *Vs*, seismic anisotropy (A), density, mineralogical and chemical compositions of rock samples, etc. A unique sample identity number is given to each sample by combining author name, publication year and original sample number, e.g., "Kern2001-LS98-09". The sample information contains source literature, lithology (granite, basalt, eclogite, mylonite, sandstone, and many others), rock category (igneous, metamorphic, sedimentary rocks or ores), geographic location (country, province, region, longitude and latitude), strain (deformed or undeformed), humidity (dry or wet) and porosity. As shown in Figure 2.1, the unique sample identity number links six tables (relations) describing the *Vp*-pressure, *Vs*-pressure, *Vp*-temperature, *Vs*-temperature, modal composition and chemical composition of rock samples.

The primary controls on seismic velocities, such as mineral composition, preferred mineral orientation, temperature, confining pressure and porosity, could be investigated by using the ample data. Lithology is one of the most important sorting parameters of the DRSP. The mineralogy and texture are used to describe names of igneous and

sedimentary rocks, while many metamorphic rock names are based entirely on rock texture. In some cases, the chemistry alone is the criterion for classification (Raymond, 1995). It is confusing to see so many different rock names just due to different classification standards and personal preferences. To simplify the database and provide more representative data for a lithology of interest, we classified all samples according to the original rock name, mineralogy, texture and chemical composition (Appendix 2).

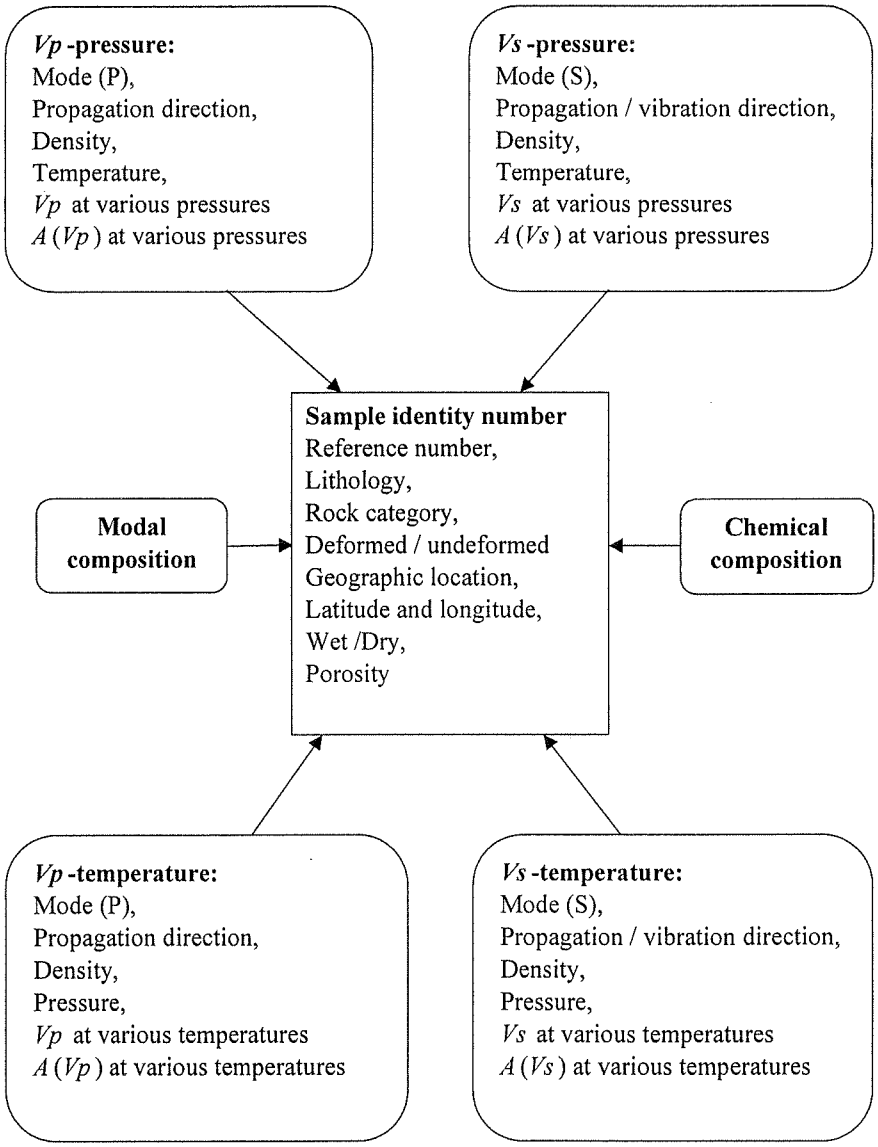


Figure 2.1 Structure of the database of rock seismic properties (DRSP).

2.2 Statistic results of the DRSP

Users of the DRSP can retrieve *Vp* and *Vs* of rocks according to propagation and vibration directions and the characteristic items of samples. Mean velocities and anisotropy of samples were also calculated and included in the DRSP. Up to now, most experiments were focused on the magmatic and metamorphic rocks (Figure 2.2), especially for high temperature measurements (Figure 2.3).

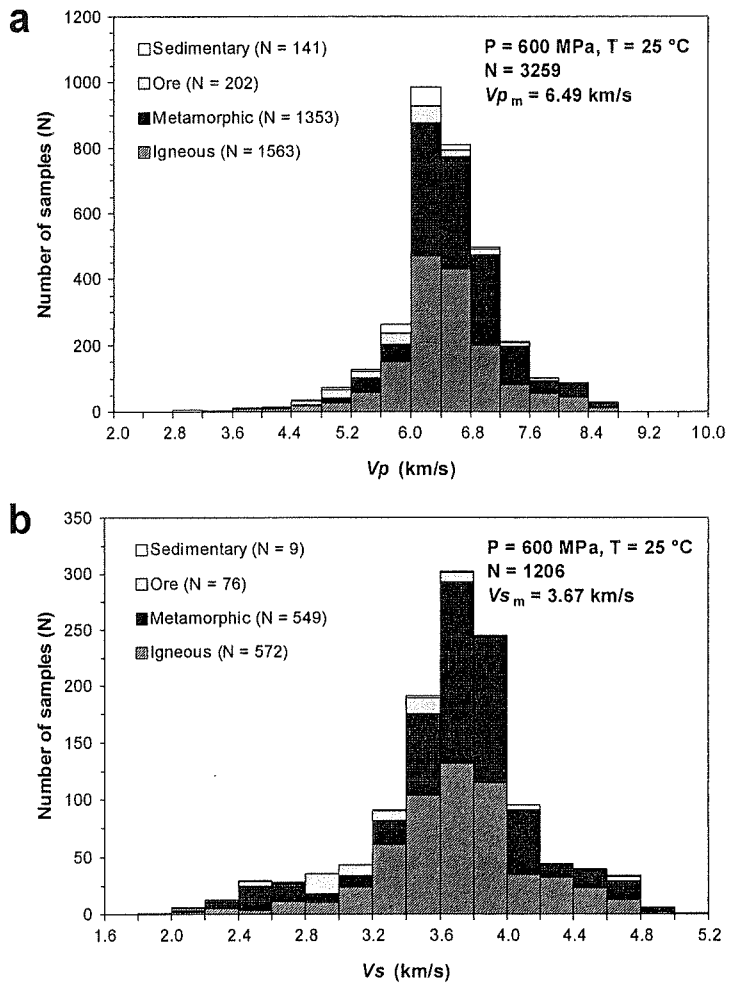


Figure 2.2 (a) Histogram of P-wave velocities for 3259 samples, and (b) histogram of S-wave velocities for 1206 samples at 600 MPa and 25 °C.

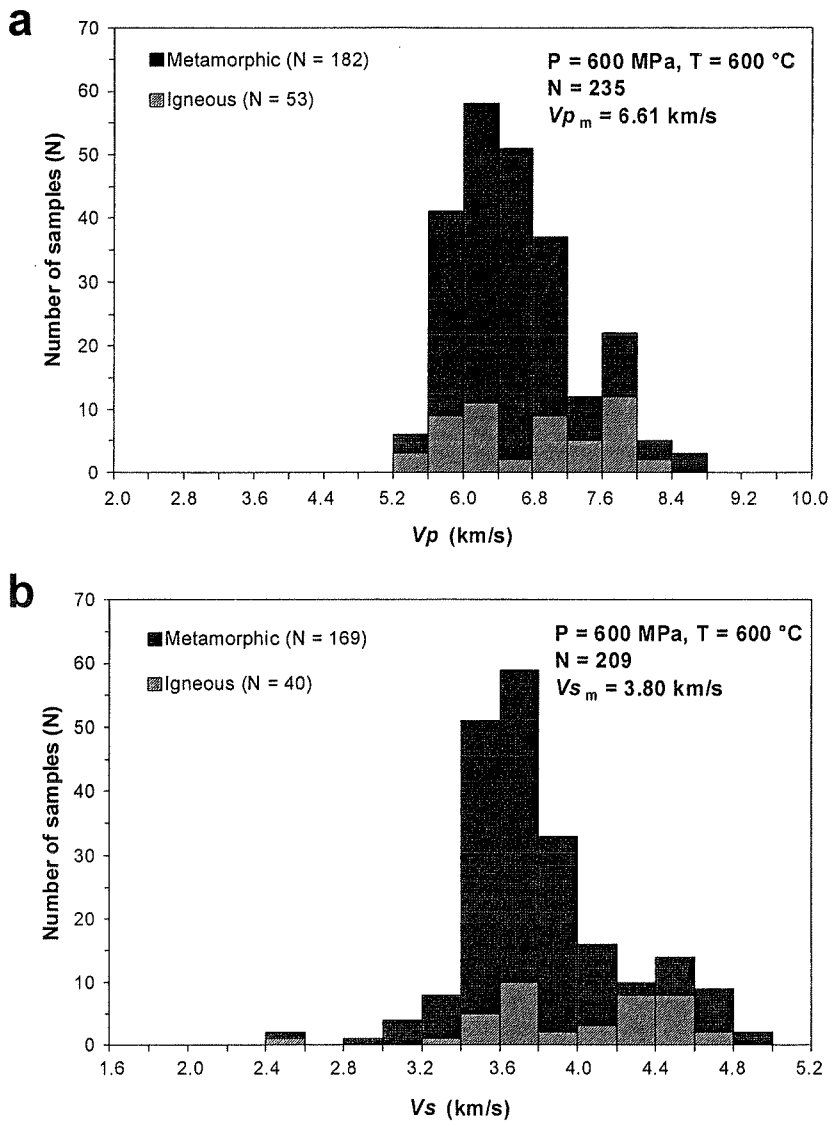


Figure 2.3 (a) Histogram of P-wave velocities for 235 samples, and (b) histogram of S-wave velocities for 209 samples at 600 MPa and 600 °C.

It should emphasize that rock sampling is very uneven around the world. For example, among 3259 samples in Figure 2.2a, there are 1250 samples from Canada, 515 samples from United States, 394 samples from Atlantic Ocean, 270 samples from Pacific Ocean, 181 samples from Italy, 96 samples from China and 95 samples from Japan. In Figure 2.3a, among 235 samples measured up to 600 MPa and 600 °C, except 8 samples

from Atlantic Ocean, all samples were collected from continents including 94 samples from China, 65 from Italy and 20 from Russia. Therefore rock samples from the above 8 regions comprise more than 80% data of the DRSP.

The DRSP is able to provide a statistical investigation on:

- Histogram distribution of seismic velocities (Figures 2.4) and anisotropy for each lithology or rock category as well as for all the rocks from a given region (Figure 2.5);

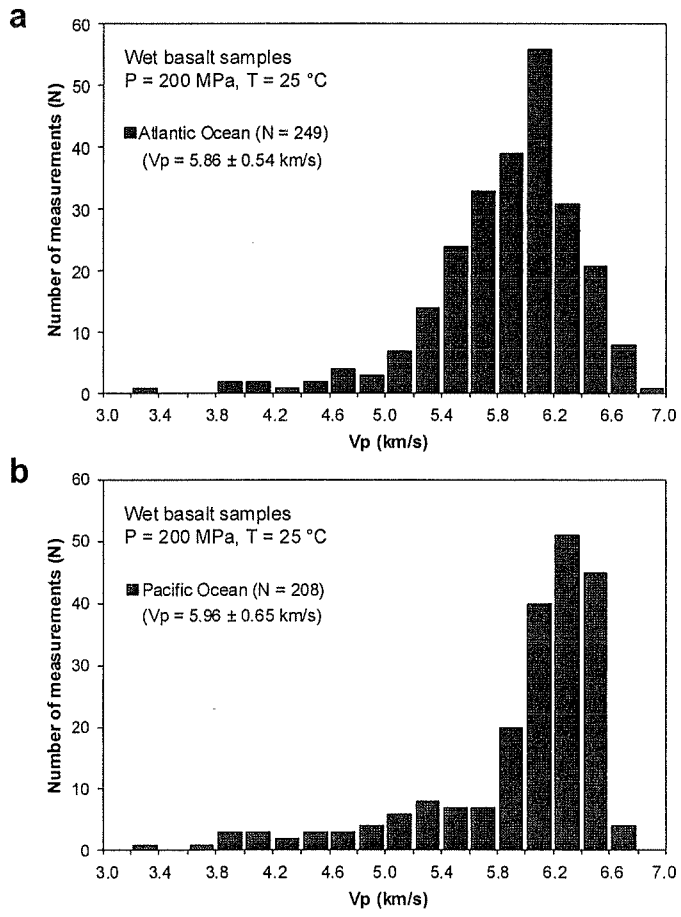


Figure 2.4 Histogram of P-wave velocities at 200 MPa and 25 °C of wet basalt samples from (a) Atlantic Ocean and (b) Pacific Ocean.

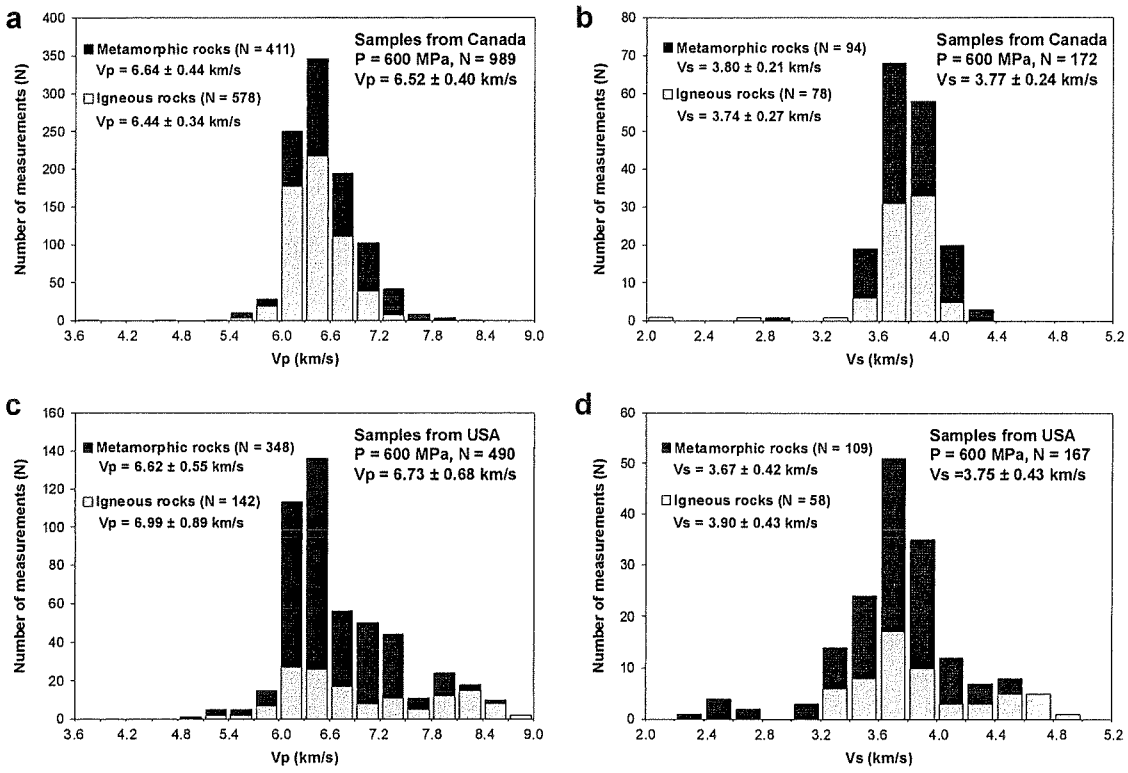


Figure 2.5 Histograms of mean P- and S-wave velocities at 600 MPa and 25 °C for igneous and metamorphic rocks from (a-b) Canada and (c-d) USA.

- Relationship between rock density and velocity (average velocity, or velocity for each given propagation direction) at given pressure and temperature (Figures 2.6-2.8);
- Relationship between sedimentary rock porosity and seismic velocities (Figure 2.9);
- Effects of pore-fluid on seismic properties and anisotropy (Figure 2.10);
- Quantitative correlation between seismic properties and mineralogical (Figure 2.11) and chemical composition (Figures 2.12 and 2.13);
- Correlation between seismic properties and finite strain axes, providing a valuable tool to constrain the interpretation of seismic and teleseismic data (e.g., SKS- or SKKS-splitting) from various tectonic provinces (Figure 2.16);

- Average *Vp* and *Vs* data for calculating the *Vp/Vs* ratio and Poisson's ratio (σ), with a special attention paid to the possibility of using these ratios to determine lithologic composition (Figure 2.17).

2.2.1 Velocity – density relationship

Birch (1961) noted that the mean atomic weight ($\overline{m}$) is a significant physical parameter for common rocks in the crust and upper mantle. The $\overline{m}$ value of a rock is calculated from the data of chemical analysis according to the following equation:

$$\overline{m} = \left(\sum \frac{x_i}{m_i} \right)^{-1} \qquad (2.1)$$

where m_i is the mean atomic weight of oxide i, and x_i is the proportion by weight of this oxide in the rock. The $\overline{m}$ values of most common rocks in the crust and upper mantle range from 20 to 22 and arise with increasing iron content. For example, the $\overline{m}$ value is about 21 for granite and about 22 for mafic rocks. The linear relationship between seismic velocities (V) and density (ρ) of rocks, known as Birch's law, is described as

$$V = a + b\rho \qquad (2.2)$$

where $a = f(\overline{m})$ and b is a constant. This relationship means that at high pressure, the principal factors determining velocity are density and mean atomic weight, details of symmetry or crystal structure appear to be of secondary importance. Birch's law fits measurements from many crustal and mantle rocks fairly reasonably and has been used to determine the density profiles from measured velocities, especially in the lithosphere that consists of chemically heterogeneous crust and a part of upper mantle. However, Birch's law does not satisfy the velocity changes related to phase transition, which can be rationalized in terms of an interatomic potential model (Campbell and Heinz, 1992).

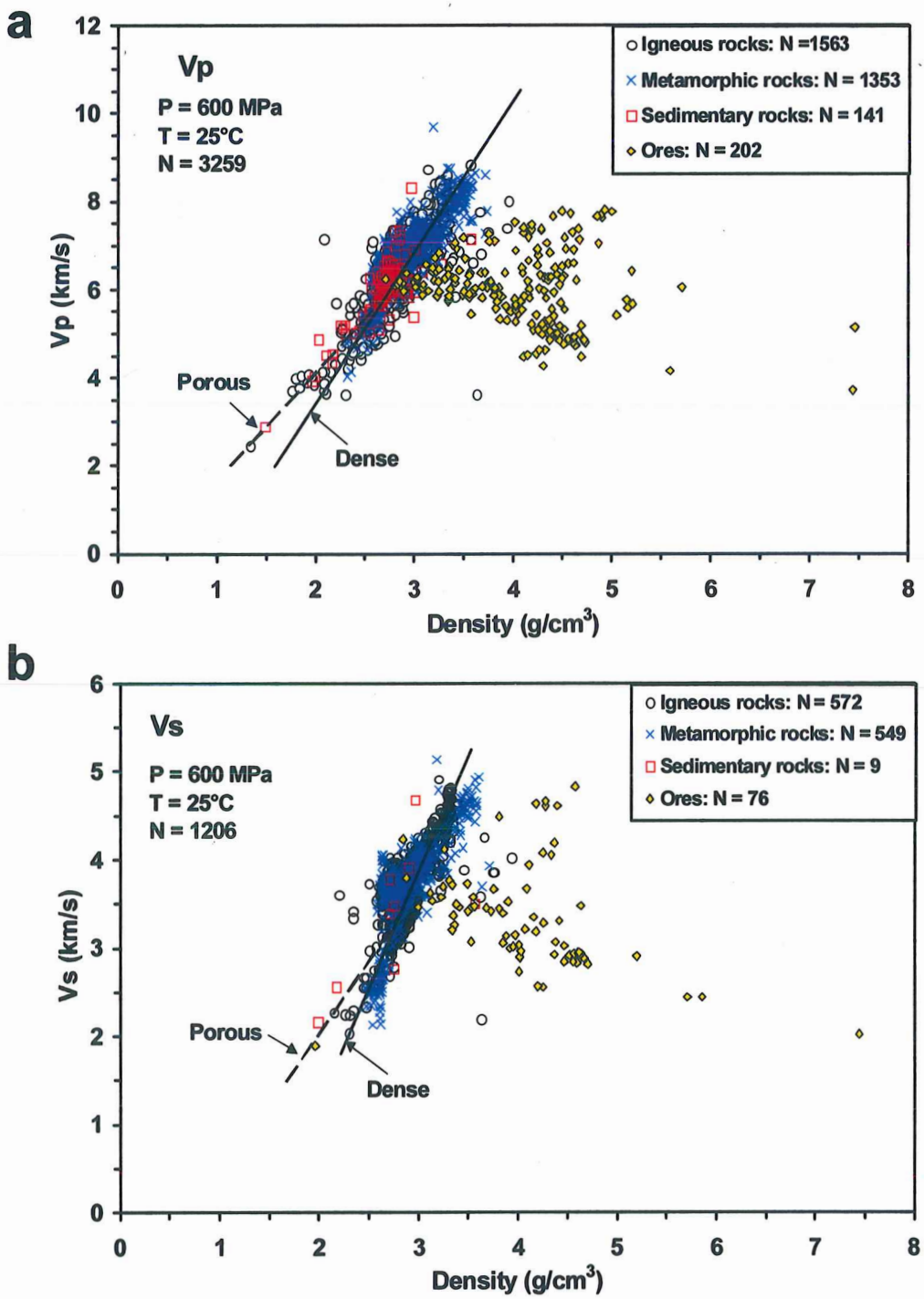


Figure 2.6 (a) *Vp*-density and (b) *Vs*-density relations at 600 MPa and 25 °C.

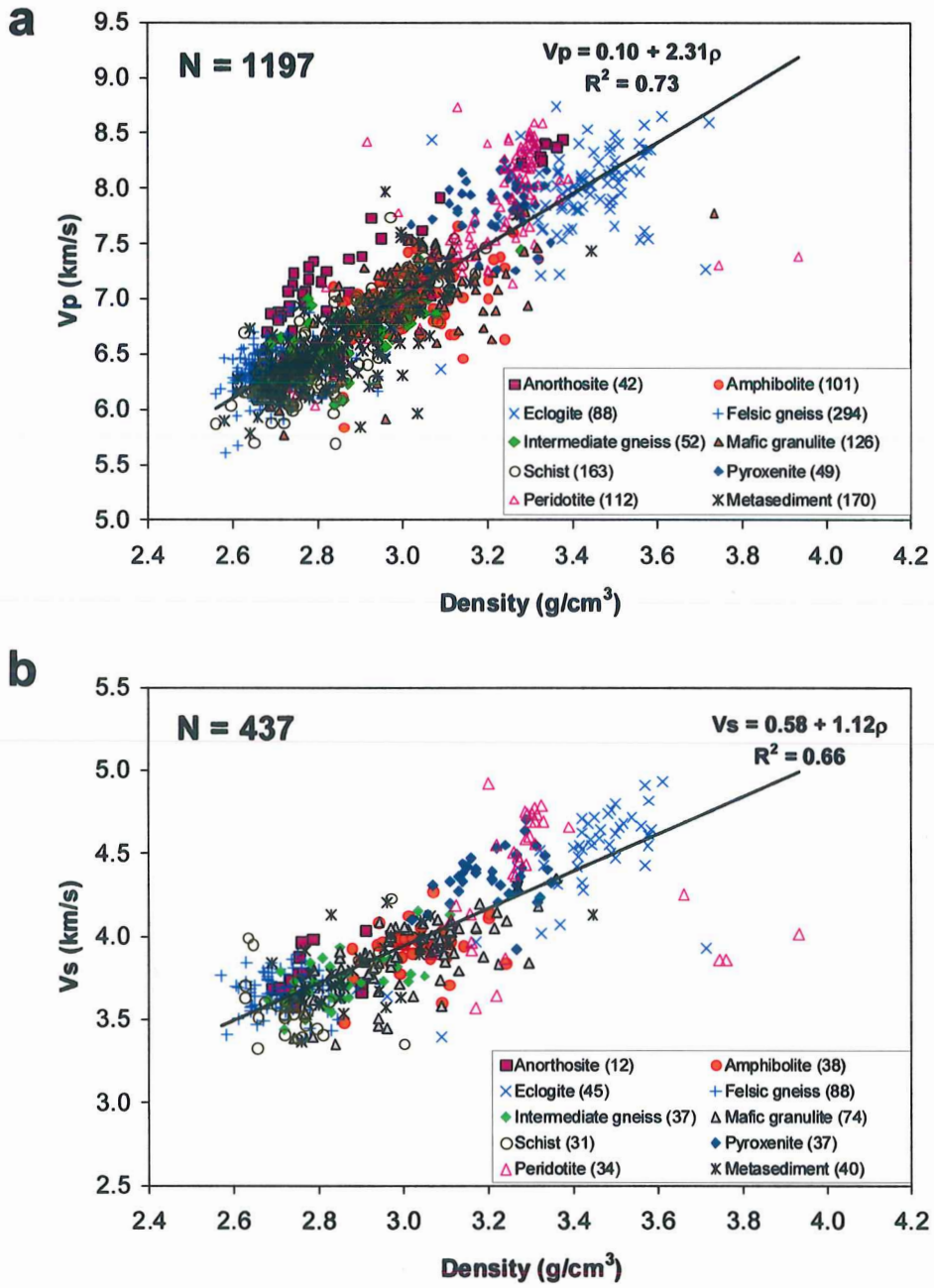


Figure 2.7 (a) *Vp*-density and (b) *Vs*-density relations for typical lower crustal rocks measured at 600 MPa and 25 °C. N – Sample number. The number in parentheses is the sample number of each lithology.

Figure 2.6 illustrates a correlation between densities and P- and S-wave velocities at 600 MPa for all samples from the DRSP. The linear relationship between velocities and densities is more evident in dense rocks. As shown in Figure 2.7, for the lower crustal rocks, the velocity-density relationships are: $Vp = 0.10 + 2.31\rho$ and $Vs = 0.58 + 1.12\rho$, where Vp and Vs in km/s, ρ is density in g/cm^3. Anorthosite, pyroxenite and most peridotite fall above the velocity-density trend, but serpentinized peridotite samples display relatively lower velocities. Felsic gneiss and eclogite can be easily distinguished according to their extremely low or high velocities and densities, respectively, meanwhile intermediate gneiss, amphibolite, schist and metasediments show overlapping velocities and densities. The deviation from the general velocity-density relationship is found in some monomineralic rocks (e.g., marble, quartzite, serpentinite) and sulfides, and in rocks with high porosity, such as basalt and tuff even at 600 MPa (Figure 2.8).

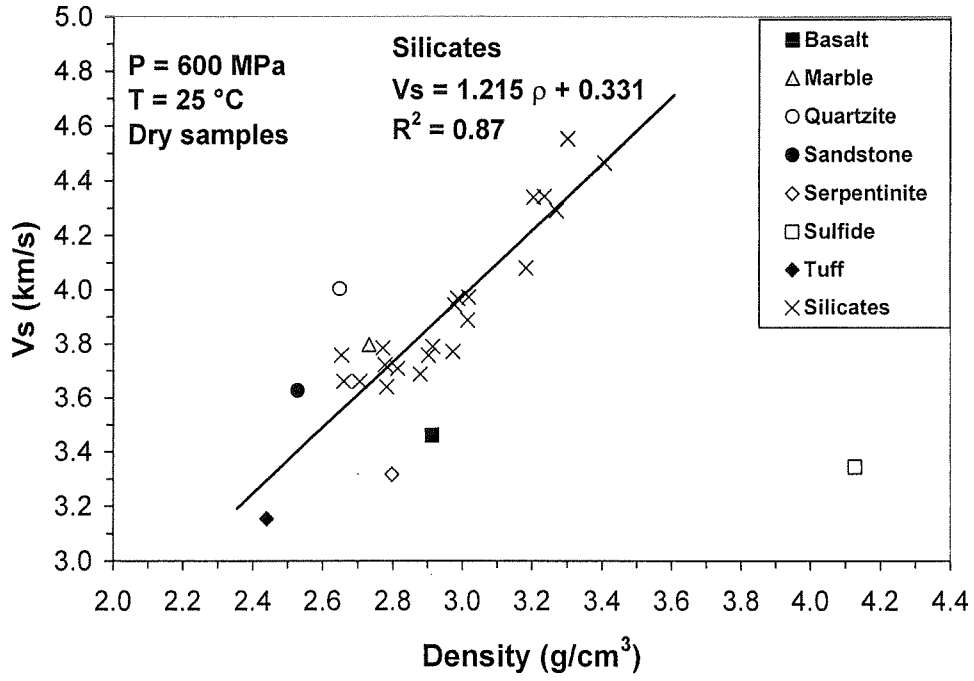


Figure 2.8 Variations of the mean Vs as a function of density. Note that the deviation from the general trend is caused by either porosity or specific mineralogy.

2.2.2 Velocity – porosity relationship

Porosity and fluids contained in the pore space are key factors controlling seismic velocities and anisotropy of rocks, especially for sedimentary and volcanic rocks at low pressures (e.g., Popp and Kern, 1994). As shown in Figure 2.9, *Vp* and *Vs* at 50 MPa of dry sandstones systematically decrease with increasing porosity. For clay-rich rocks (e.g., shale, claystone and siltstone), however, the velocity also depends on the content of clay minerals that have much lower velocities than quartz (Freund, 1992).

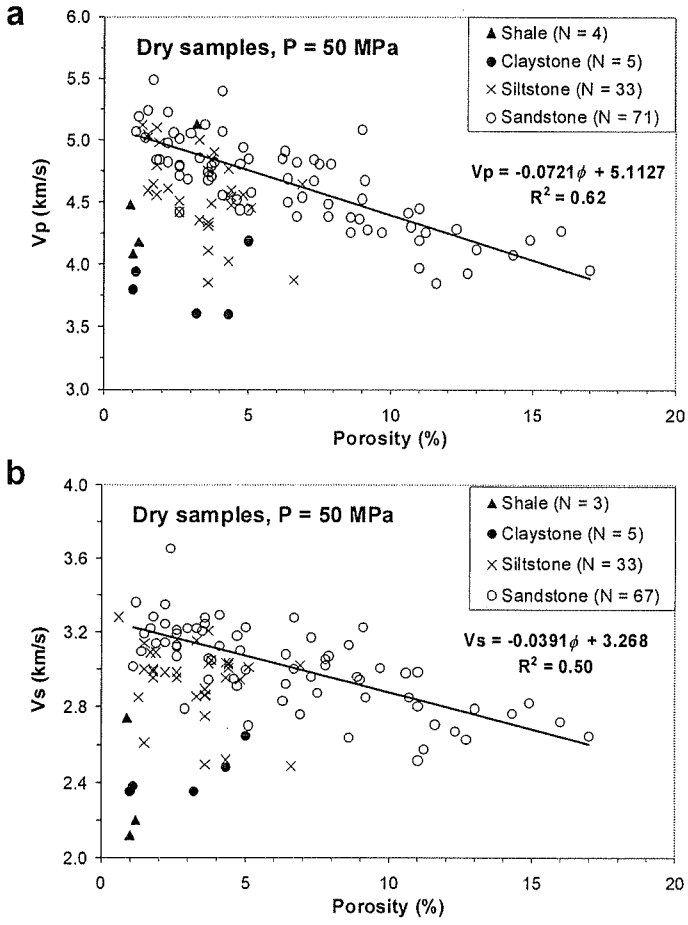


Figure 2.9 Dependence of P- and S-wave velocities on porosity (ϕ) for dry clastic rocks. (a) *Vp* at 50 MPa versus porosity and (b) *Vs* at 50 MPa versus porosity. N is the sample number; solid line is the least squares fit to the data of dry sandstones.

Effects of pore fluids on seismic velocities are two-faced. First, because $V_{water} > V_{gas}$, increasing water saturation will generally increase velocities of rocks. Second, high pore-fluid pressure will reduce effective pressure P_{eff} ($P_{eff} = P_c - P_f$, where P_c is the confining pressure and P_f is the pore-fluid pressure) and consequently, decrease seismic velocities. Therefore, the difference between the velocities of dry and water-saturated samples increases with increasing porosity and decreases with increasing pressure. Figure 2.10 displays a linear decrease of *Vp* and *Vs* with increasing porosity of water-saturated basalt samples. The influence of fluids is stronger to *Vp* than to *Vs*, especially at high confining pressures (Figure 2.10b) because fluids are incompressible.

2.2.3 Seismic properties of different lithologies

No obvious linear relationship is observed between seismic velocity and mineralogy of quartzofeldspathic rocks because quartz, potassium feldspar and sodic plagioclase have similar seismic velocity (Figure 2.11). Except eclogite and serpentinite, the decrease in P- and S-wave velocities of rocks with increasing SiO_2 content and decreasing Fe_2O_3+FeO+MgO content can be primarily due to increasing amount of quartz and decreasing content of mafic minerals (Figures 2.12 and 2.13). Unfortunately, this trend is not very clear for S-wave velocities because quartz displays relatively high *Vs* values (Figure 1.3e).

For dry, coarse-grained igneous rocks, a relationship between P- and S- wave velocities, silica content and density can be well established. As shown in Figure 2.14, both P- and S-wave velocities decrease with increasing silica content and increase with increasing densities, which can be attributed to the increasing content of mafic minerals that generally have higher velocities and densities than felsic minerals. Due to extremely low *Vp/Vs* ratio of quartz, the *Vs* difference between gabbro, diorite and granite is not as much as in *Vp* values.

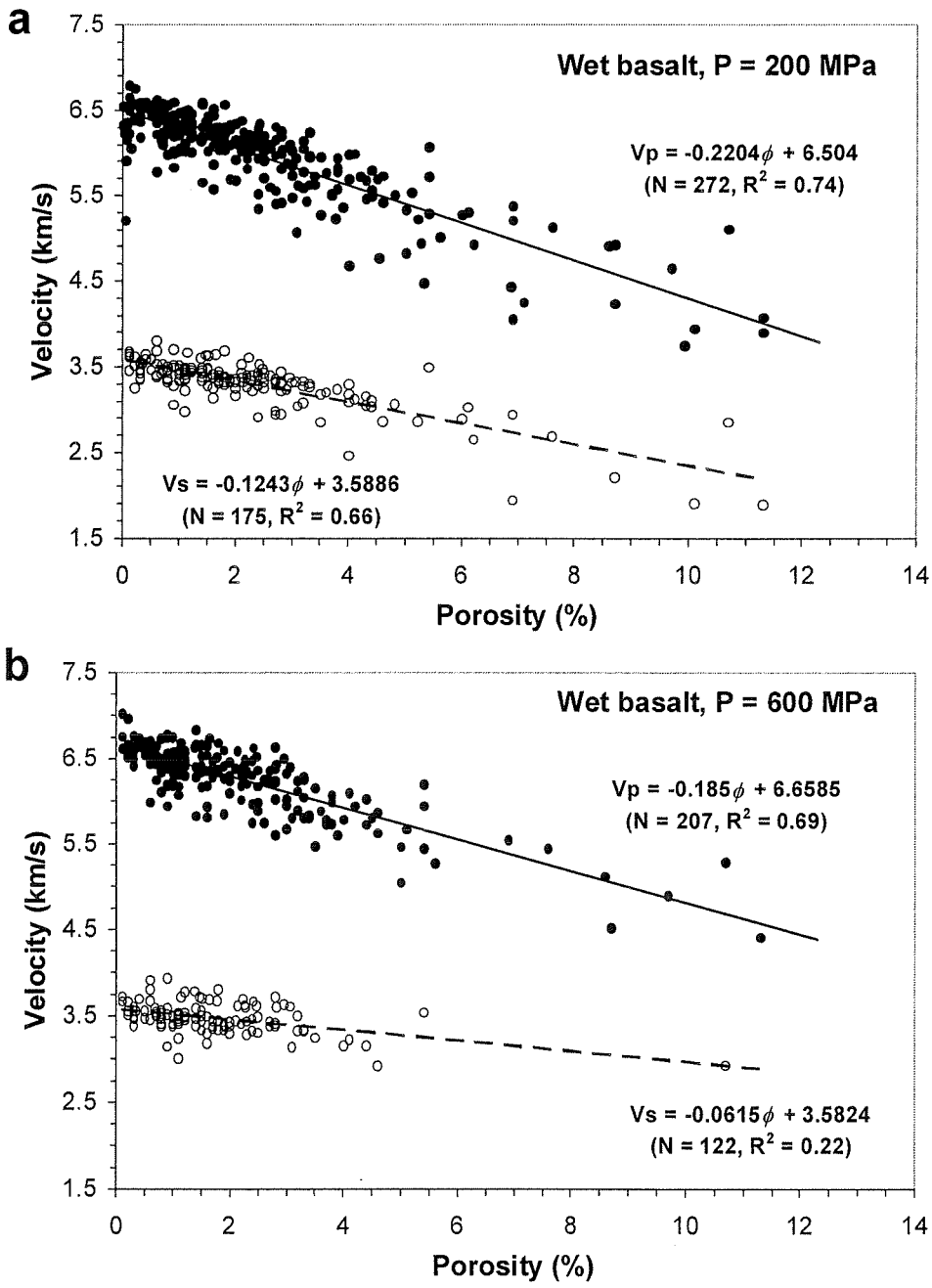


Figure 2.10 Dependence of P- and S-wave velocities on porosity (ϕ) of water-saturated basalts at confining pressure of (a) 200 MPa and (b) 600 MPa. N is the sample number; solid line and dashed line are the least squares fit to *Vp* data (solid circle) and *Vs* data (open circle), respectively.

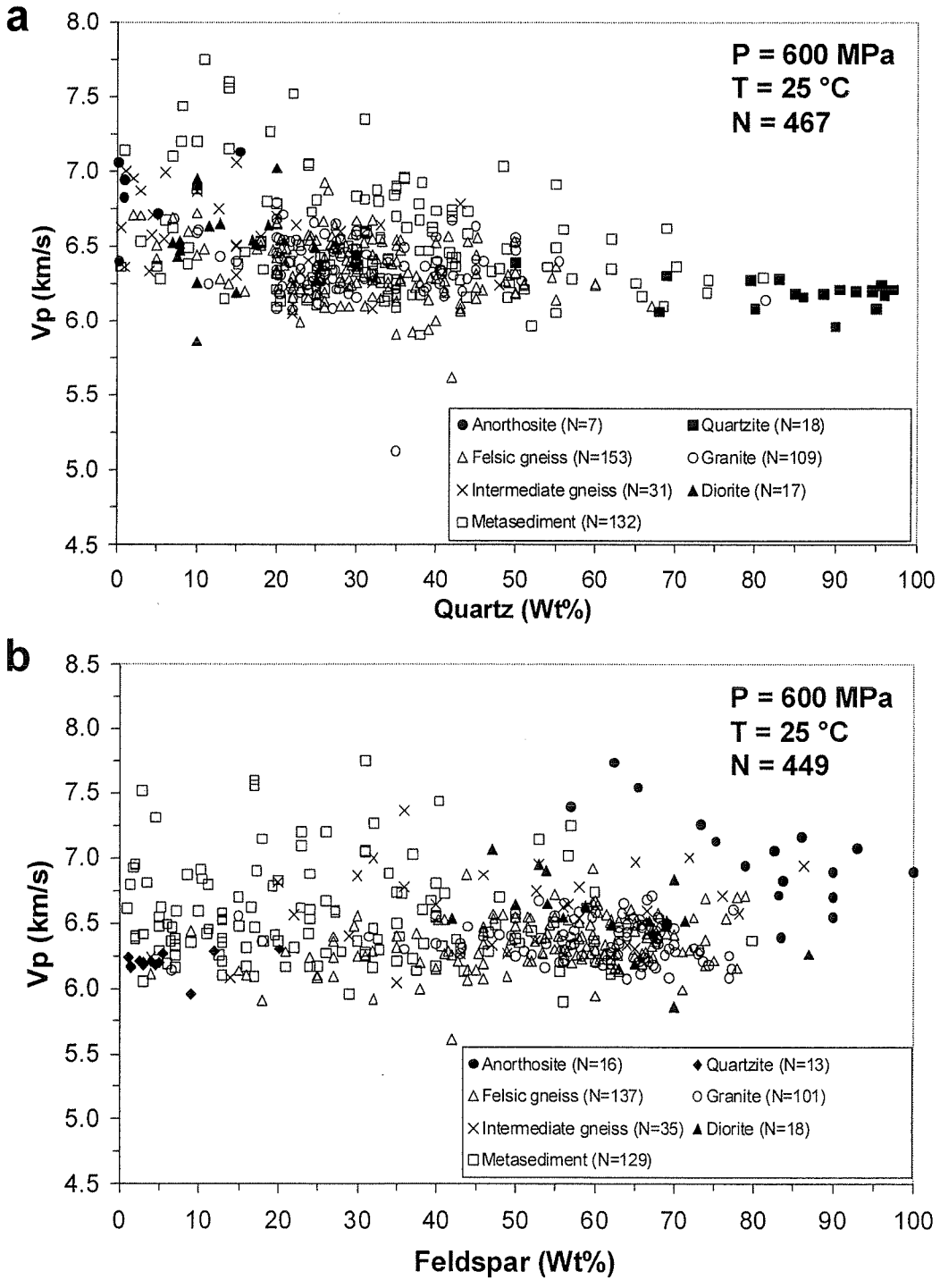


Figure 2.11 P-wave velocities at 600 MPa of quartzofeldspathic rocks versus (a) quartz content and (b) feldspar content. N- Sample number.

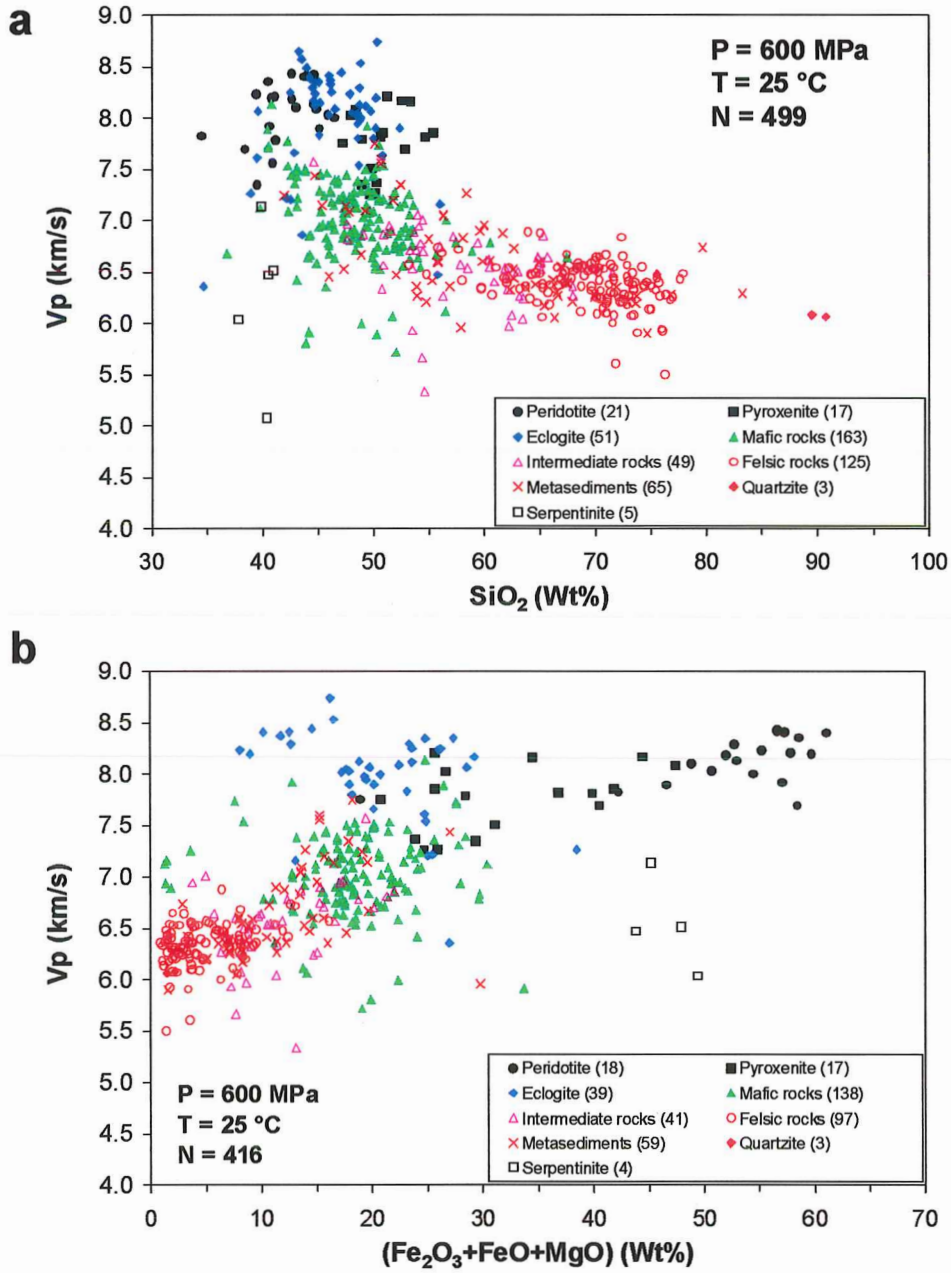


Figure 2.12 (a) *Vp* versus SiO_2 content at 600 MPa and 25°C for 499 samples, and (b) *Vp* versus content of Fe_2O_3+FeO+MgO at 600 MPa and 25°C for 416 samples. The sample number of each rock type is given in parentheses.

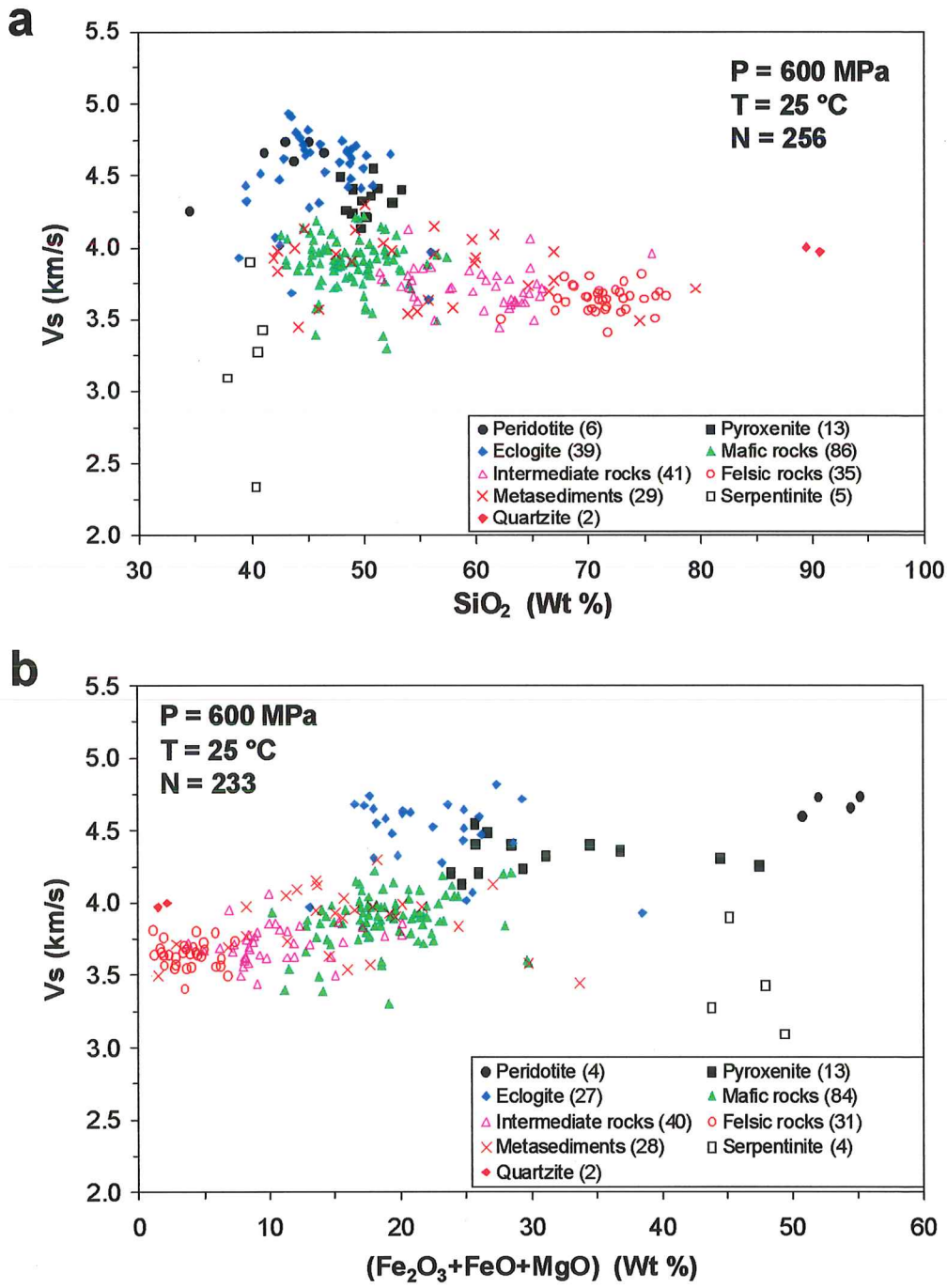


Figure 2.13 (a) *Vs* versus SiO_2 content at 600 MPa and 25°C for 255 samples, and (b) *Vs* versus content of Fe_2O_3+FeO+MgO at 600 MPa and 25°C for 234 samples. The sample number of each rock type is given in parentheses.

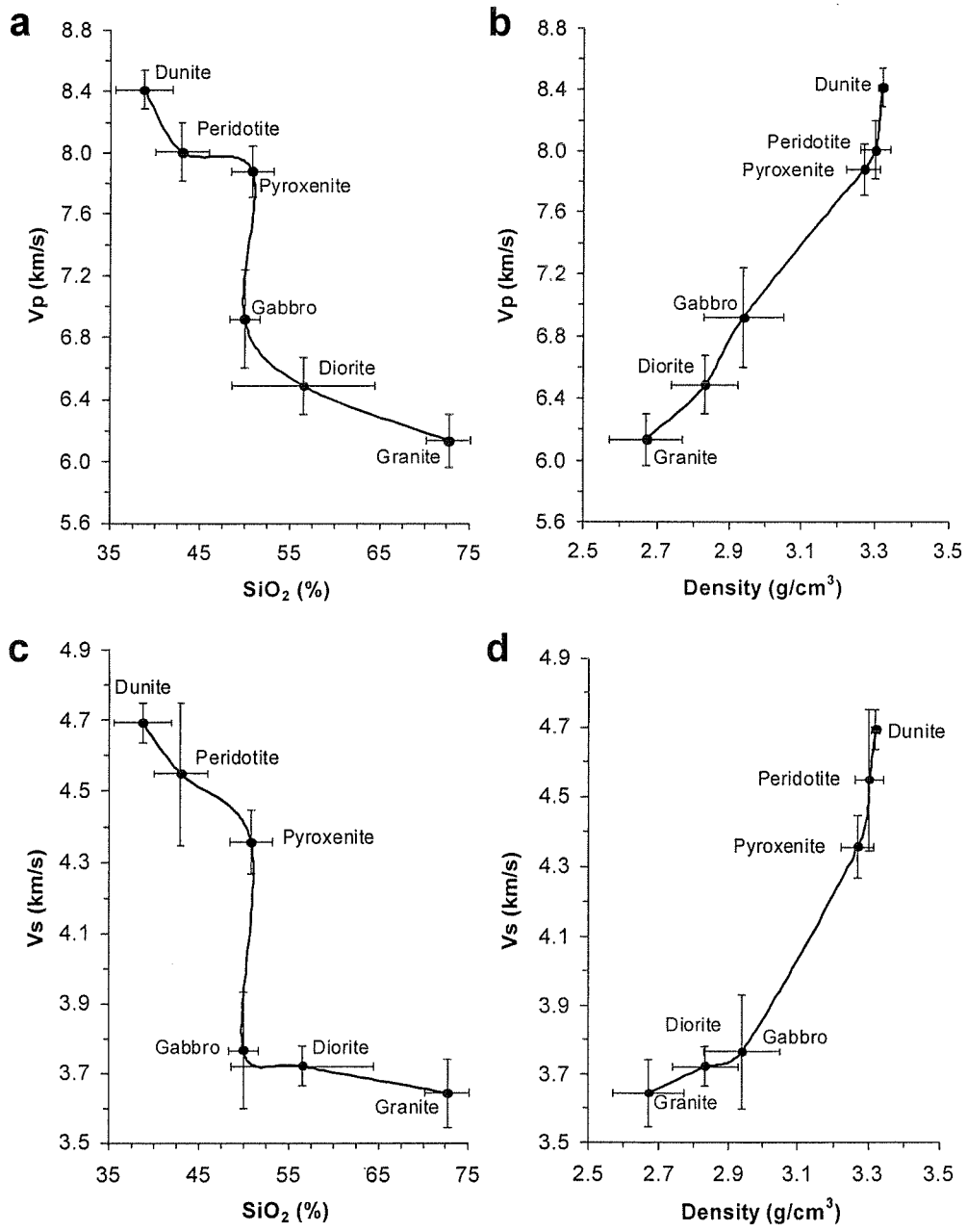


Figure 2.14 (a-b) P-wave velocities (c-d) S-wave velocities at 200 MPa versus silica content and density of coarse-grained igneous rocks, respectively. The numbers of samples with both velocities and densities measured: granite – 17; diorite – 12; gabbro – 16; pyroxenite – 11; peridotite – 8; dunite – 4. The numbers of samples with silica contents reported: granite – 16; diorite – 8; gabbro – 6; pyroxenite – 14; peridotie – 16; dunite – 9.

As shown in Figure 2.15, many of the metamorphic rocks display significant anisotropy while igneous rocks are quasi-isotropic. Anisotropy is a particularly important characteristic in the low-grade pelitic rocks, reaching average values of 11.9% in phyllite and 10.4% in slate. In general, the medium-grade metamorphic rocks are highly anisotropic, especially in mica-rich rocks such as amphibolite, paragneiss and schist (A > 9%). The high-grade metamorphic rocks are weakly anisotropic except stronalite. The average anisotropy of peridotite is about 6%, while the mantle dunite can have stronger anisotropy (> 8%) due to a high volume fraction of olivine.

At low pressure, the effect of microcracks often obliterates the fabric-related anisotropy. For example, comparison of Vs_{ZX} and Vs_{ZY} at 100 MPa of peridotites does not show any correlation of the fast shear wave (Vs1) polarization with the LPO of olivine (Figure 2.16a). However, at 600 MPa, the polarization of Vs1 is apparently parallel to the lineation direction X, especially for dunite (Figure 2.16b), which has been used to explain observed SKS delay time (e.g., Ji et al., 1994; Long and Christensen, 2000; Saruwatari et al., 2001).

Poisson's ratio appears independent on both pressure and temperature for most rocks, except that quartzites display much smaller Poisson's ratios associated with the quartz α-β phase transition (Figure 1.6). Figure 2.17 shows average Poisson's ratios of common rocks in the crust and upper mantle, which can be divided into three groups: low values (< 0.15) for quartz-rich rocks, medium values for most rocks (0.2-0.3), and high value for serpentinite. Water saturation can increase the Poisson's ratio of rocks, for instance, the average Poisson's ratio of wet basalt samples (0.294) is significantly higher than dry ones (0.266), so does for gabbro-diabase (0.282 of wet samples and 0.273 of dry ones). This suggests a possible way to estimate the water content of oceanic rocks but more detailed laboratory experiments are needed to set up a more exact correlation.

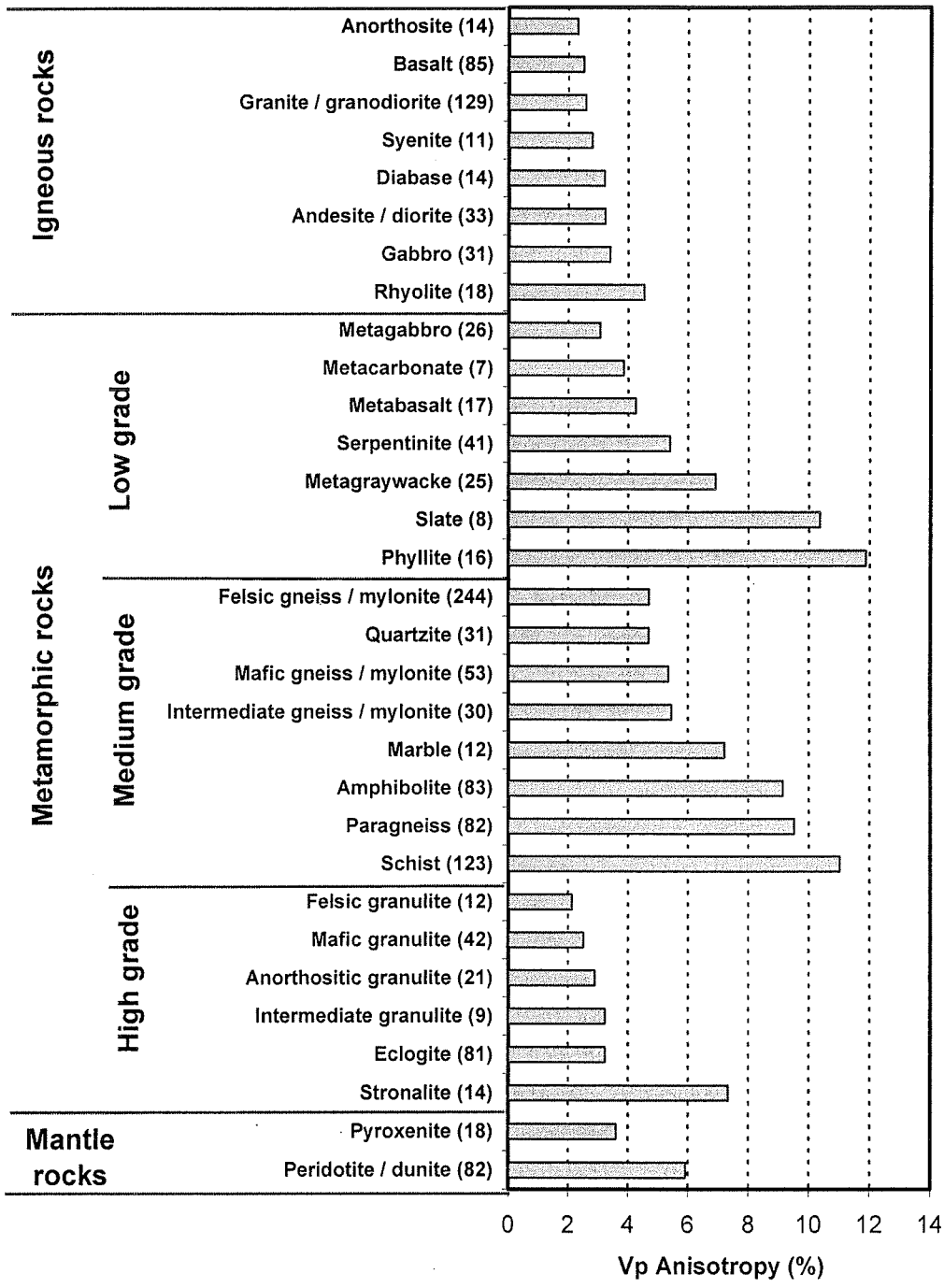


Figure 2.15 Average anisotropy of P-wave velocity for common lithologies at 600 MPa. The sample number of each lithology is given in parentheses.

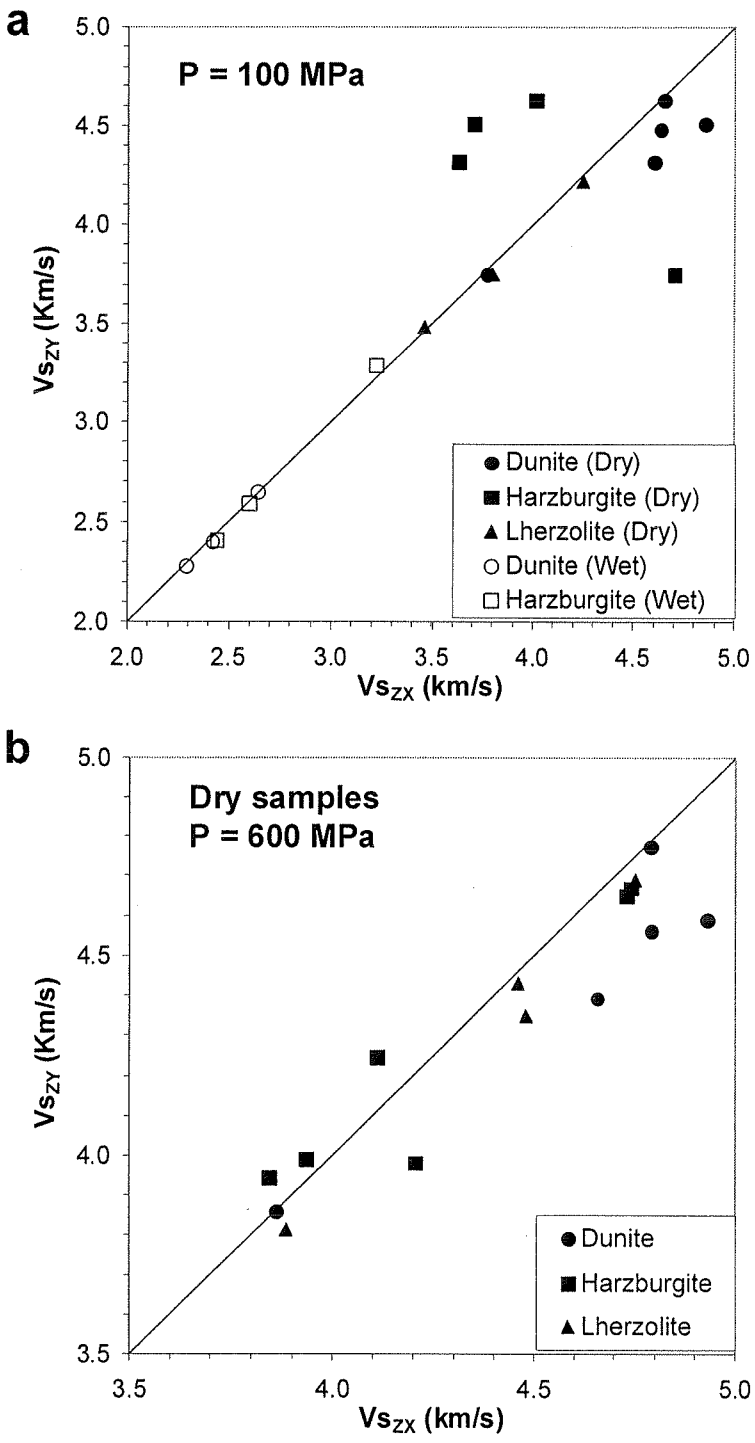


Figure 2.16 Split shear wave velocities of peridotites along Z-direction at (a) 100 MPa and (b) 600 MPa. The diagonal indicates zero shear wave splitting.

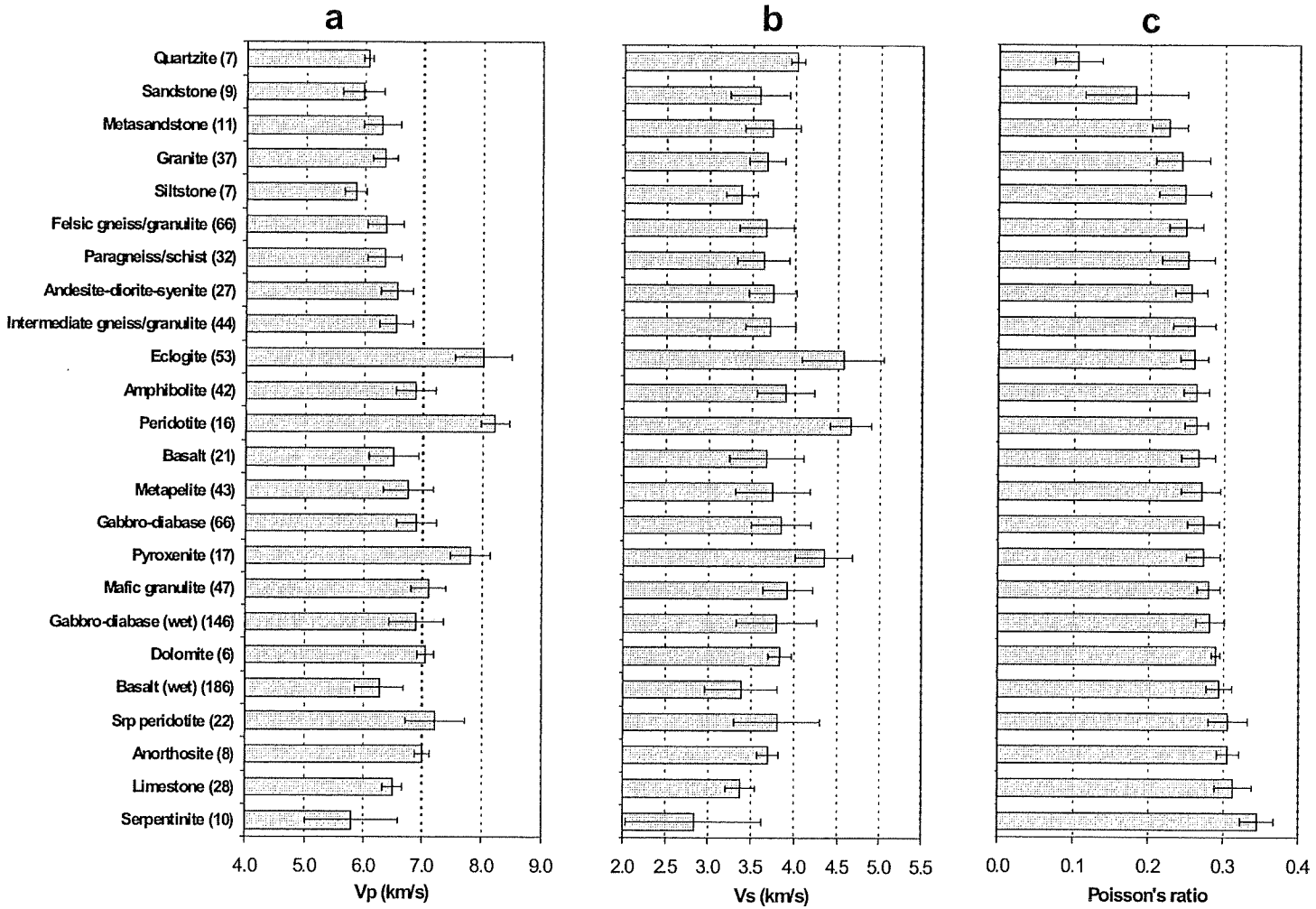


Figure 2.17 Average seismic velocities and Poisson's ratios at 600 MPa of common rock types. (a) *Vp*, (b) *Vs* and (c) Poisson's ratio. Error bars represent 2σ standard deviations of the datasets. The sample number of each rock type is given in parentheses.

2.3. Summary

Thanks to a funding support from the Canadian national LITHOPROBE, we have established an Internet Database of Rock Seismic Properties (DRSP) and published a handbook (Ji et al., 2002), which comprise almost all data available in the literature published in English and French and are more complete than any previous compilations.

The DRSP allows its users to retrieve data according to geographic location, tectonic province, rock category, lithology, propagation and vibration directions, mean P- or S-wave velocity, seismic anisotropy, strain, humidity and source literature. The DRSP also provides its users a statistical display on: (a) Histogram distribution of seismic velocities and anisotropy for each lithology or rock category as well as for all the rocks from a given region; (b) Relationship between rock density and seismic velocity at given pressure and temperature; (c) Relationship between sedimentary rock porosity and seismic velocities; (d) Effects of pore-fluid on seismic properties and anisotropy; (e) Quantitative correlation between seismic properties and mineralogical and chemical composition; (f) Correlation between seismic properties and finite strain axes, providing a valuable tool to constrain the interpretation of seismic and teleseismic data from various tectonic provinces; (g) Average *Vp* and *Vs* data for calculating the *Vp/Vs* ratio and Poisson's ratio, with a special attention paid to the possibility of using these ratios to determine lithological composition.

Obviously, such a computerized database can perform much more complex tasks with higher efficiency. The DRSP will serve as a convenient, compact, yet comprehensive source of basic information and will keep the world earth science and geotechnical communities informed about the growing body of rock physical property data. Moreover, it will provide a set of statistical analyses of rock seismic properties for research, engineering, and educational purposes.

Chapter 3

P-wave velocities of polymineralic rocks: comparison of theory and experiment and test of elastic mixture rules

3.1 Introduction

In Chapter 2, we briefly introduced our Database of Rock Seismic Properties (DRSP). Chapter 3 presents an example of its applications. We compare the measured *Vp* data of 696 dry samples from the DRSP with the theoretical values calculated using 16 different averaging methods in order to search the best mixture rule in estimation of overall seismic properties for polymineralic rocks. We also try to verify if an averaging approach is good for a lithology but poor for other lithology and if the theoretical velocities calculated from the room pressure single crystal elastic constants and the volume fraction of the constituent minerals should be compared with the values measured at different pressure for different lithology in order to obtain the closest agreement. The results of this study were published in a Tectonophysics paper (Shaocheng Ji, Qin Wang, Bin Xia, 2003).

Interpretation of seismic refraction and reflection data in terms of lithology, mineralogy and chemical composition is largely constrained by comparing in situ observed seismic velocities with those of relevant rocks or mineral assemblages thought to exist in the ranges of temperature and pressure of interest. As reviewed in Chapter 1, seismic velocities of rocks can be determined using two methods. The first method is a calculation of the overall magnitude of seismic velocities based on high-precision single crystal elastic constants, modal composition of the rock and appropriate mixture rules. Seismic anisotropy of a rock can also be computed if the petrofabric data of its constituent minerals are available (e.g., Crosson and Lin, 1971; Baker and Carter, 1972; Mainprice, 1990). Calculated seismic properties are particularly useful in modeling the

deep crust and mantle velocities obtained from seismic inversion. The second is a direct laboratory measurement of rock samples at high pressures (usually up to 600-1000 MPa) and high temperatures (usually up to 600-900 °C). The measured velocities are generally influenced by porosity, crack shape and distribution, compositional layering, anisotropy, alteration and secondary minerals. The alteration and secondary minerals, which formed during exhumation, might not exist in the in situ rocks within the deep crust or upper mantle.

The reliable calculations of seismic velocities depend on not only accurate knowledge of the elastic properties of the proposed minerals but also the adequacy of the mixture rule used (Crosson and Lin, 1971; Ji and Wang, 1999). Although the approaches most frequently used for the calculations of elasticity are the Voigt, Reuss, Hill and geometric means, it has not been clear which mixture rule is best to predict the average elastic properties of a given polymineralic rock. Crosson and Lin (1971) observed that the Voigt average from the room pressure elastic constants offers better predictions of *Vp* for the quasi-monomineralic Twin Sisters dunite (94.1% olivine, 4.9% orthopyroxene and 1% chromite and magnetite) than the other averages at pressures above 200 MPa. Seront et al. (1993) found that the Voigt average gives the closest approximation (within 0.1 km/s) to the high pressure (800 MPa) experimental *Vp* values of anorthosite (90% plagioclase and 10% olivine), while the Reuss and Hill schemes are significantly lower. The closest agreement between calculated and measured seismic velocities at 500-600 MPa has been reported for high-grade mylonites (Siegesmund et al., 1989; Ji and Salisbury, 1993; Ji et al., 1993; Barruol and Kern, 1996). Thus the Voigt average has been widely used in numerical modeling of rock seismic properties (e.g., Mainprice and Casey, 1990; Ji et al., 1994; Kern et al., 1996; Kern et al., 2001; Saruwatari et al., 2001).

However, Christensen and Ramananantoandro (1971) and Babuska (1972) observed that the Hill average from the room pressure elastic constants provided the best prediction for the elastic wave velocities of dunite and bronzitite measured at 1.0 GPa. The Hill

scheme was employed for calculating seismic properties of ultramafic rocks (Baker and Carter, 1972; Long and Christensen, 2000). Ji and Wang's (1999) experiments suggested that the shear-lag model, which gives lower P- and S-wave velocities even than the Reuss bound, should be more appropriate for hot-pressed olivine-orthopyroxene composites. Recently, Hurich et al. (2001) claimed that the Voigt average results in the least error between measured and calculated velocities at 400 MPa for granitic rocks while the Reuss average produces the best fit for gabbroic rocks.

3.2 Procedure of *Vp* calculation

By neglecting its detailed microstructure (geometric orientation and distribution of each phase), a multiphase rock can be assumed to be macroscopically homogenous and isotropic, that is, their grains are equiaxed and have random crystal orientations. Such isotropic aggregates can be characterized by only two independent elastic constants (the bulk modulus, K, and the shear modulus, G). Owing to lack of information on the orientation of each individual grain, the study rock samples are assumed to be isotropic. Seismic velocities of such a polymineralic composite can be simply modeled according to a two-step procedure. The first step involves calculating the elastic moduli (K_i and G_i) of the polycrystalline monomineralic aggregate of ith constituent mineral from its elastic stiffness (C_{ij}) and compliance (S_{ij}) tensors, using Equations (1.12)-(1.19). The second step is to calculate, using Equations (1.16), (1.17) and (1.20), the overall elastic moduli (K and G) of the sample according to its modal mineralogy (V_i) and the results of the first step (K_i and G_i). The resultant overall elastic moduli are then used to calculate P- and S-wave velocities of the sample. Both steps involve Voigt, Reuss, Hill and geometric averaging approaches. Unlike the complicated self-consistent method that needs to assume a specific microstructure of the aggregate (e.g., Hill, 1965; Mainprice and Humbert, 1994), these simple averaging schemes are possible to predict the effective elastic properties of an isotropic polymineralic rock when only information on phase volume fraction is available. There are in total 16 different approaches to calculate the overall elastic

properties of a multiphase rock. They are inferred as VV, VR, VH, VG, RV, RR, RH, RG, HV, HR, HH, HG, GV, GR, GH, and GG, where V, R, H and G denote the Voigt, Reuss, Hill and geometric averaging methods, respectively. The first letter signifies the averaging method used in the first step, and the second indicates the averaging method used in the second step.

In Table 3.1, we present the Voigt, Reuss, Hill and geometric averaging elastic properties of 22 common rock-forming minerals for texture-free monomineralic aggregates at standard pressure and temperature (0.1 MPa and 25 °C), calculated from the elastic stiffness coefficients of these minerals using the methods described by Watt (1987).

3.3 Comparison of theory and experiment

3.3.1 Measured Vp data

The measured *Vp* data of 696 dry samples, which are compared with the calculated results, were carefully chosen from our database of rock seismic properties (DRSP; Ji et al., 2002; also see Chapter 2). Almost all the experimental data used in this study are from credible laboratories such as those of N.I. Christensen, D.M. Fountain, H. Kern and M.H. Salisbury. Measurements in the laboratories of Christensen, Fountain, and Salisbury were made on jacketed cylindrical samples in hydrostatic fluid-medium apparatus with transducers placed directly onto the sealed specimens (Christensen, 1985). Measurements in Kern's laboratory were performed on unjacketed, cube-shaped specimens in a cubic pressure apparatus. A state of nearly hydrostatic stress was achieved by pressing six pyramidal pistons in the three orthogonal directions onto the cubic samples (Kern, 1982). The velocities measured using both kinds of apparatus were calibrated to be accurate to 0.5-1.0 % (Kern, 1982; Christensen, 1985).

Table 3.1 Bulk (K) and shear (G) moduli (in GPa) of 22 monomineralic aggregates calculated with the Voigt (V), Reuss (R), Hill (H) and geometric (G) averages.

Mineral	ρ	K_V	G_V	K_R	G_R	K_H	G_H	K_G	G_G
Apatite[1]	3.200	84.60	63.80	83.90	57.50	84.25	60.70	84.25	60.57
Calcite[1]	2.712	76.02	36.80	70.60	27.13	73.31	31.97	73.26	31.60
Clinopyroxene (Diopside)[2]	3.289	117.67	69.00	108.19	65.19	112.93	67.09	112.83	67.07
Epidote[3]	3.400	107.41	64.99	104.90	57.42	106.15	61.20	106.15	61.09
Garnet (Alm64Py22Gr1 Sp11And2)[4]	4.131	176.83	95.90	176.83	95.88	176.83	95.89	176.83	95.89
Hornblende[1]	3.120	90.10	44.90	84.17	41.41	87.14	43.15	87.08	43.12
Ilmenite[5]	3.795	215.78	140.67	208.79	123.87	212.28	132.27	212.26	132.00
K-Feldspar[1]	2.560	62.66	31.85	44.80	22.61	53.73	27.23	52.98	26.83
Magnetite[1]	5.206	161.00	91.50	161.00	91.23	161.00	91.37	161.00	91.37
Mica (Muscovite)[6]	2.844	67.69	43.09	48.68	27.62	58.18	35.36	57.40	34.50
Olivine (Fo93Fa7)[7]	3.311	131.51	80.53	127.24	77.41	129.38	78.97	129.36	78.95
Omphacite[8]	3.327	133.50	80.64	127.96	77.69	130.73	79.16	130.70	79.15
Orthopyroxene (En80Fs20)[9]	3.354	104.79	75.51	102.13	73.92	103.46	74.72	103.45	74.71
Plagioclase (An29)[1]	2.640	66.42	33.71	59.58	29.09	63.00	31.40	62.91	31.32
Plagioclase (An53)[1]	2.680	73.83	35.82	67.52	31.31	70.68	33.56	70.60	33.49
Plagioclase (An9)[1]	2.610	57.53	32.70	44.07	25.79	50.80	29.25	50.35	29.04
Quartz[1]	2.648	38.12	47.60	37.56	40.98	37.84	44.29	37.84	44.17
Rutile[1]	4.260	217.33	124.60	208.57	98.65	212.95	111.63	212.91	110.87
Silimanite[10]	3.241	175.67	96.54	173.36	84.15	174.51	90.34	174.51	90.13
Spinel[11]	3.578	197.90	118.38	197.90	98.52	197.90	108.45	197.90	107.99
Zeolite (Natrolite)[1]	2.250	51.12	29.23	46.65	25.58	48.89	27.41	48.84	27.35
Zircon[1]	4.649	230.41	119.31	225.12	98.14	227.77	108.72	227.75	108.21

References: 1. Hearmon (1984); 2. Levien et al. (1979); 3. Ryzhova et al. (1966); 4. Babuska et al. (1978); 5. Weidner and Ito (1985); 6. Vaughan and Guggenheim (1986); 7. Kumazawa and Anderson (1969); 8. Bhagat et al. (1992); 9. Frisillo and Barsch (1972); 10. Vaughan and Weidner (1978); 11. Chang and Barsch (1973).

The P-wave velocity used for the comparison with the calculated value of each sample is the arithmetic mean of the velocities measured from three mutually perpendicular directions. According to Christensen and Ramananantoandro (1971), the mean velocity calculated in this way gives a value very close to true isotropic elastic properties even in highly anisotropic rocks. For the rocks in which both foliation and lineation are developed, these directions are parallel to the X-, Y- and Z-axis of the tectonic framework (Figure 1.2b). If the sample is foliated but not lineated, both X- and Y-directions are arbitrarily aligned in the foliation plane. For samples that displayed neither foliation nor lineation, all the three directions are aligned in an arbitrary direction or only one direction is taken because such rocks are generally isotropic. All the *Vp* data selected for this study were measured on dry and low porosity (< 1%) samples at room temperature and confining pressures up to 0.6-1.0 GPa using the ultrasonic pulse transmission technique with frequencies of about 1-2 MHz (e.g., Birch, 1960; Kern et al., 1982; Christensen, 1985). As noted by many investigators, the velocity measured at low pressures during initial pressurization is commonly lower than the velocity measured during depressurization, due to the closing of microcracks at high pressures (Birch, 1960). Thus, only velocities obtained during depressurization are compared with the calculated values. Furthermore, the samples containing more than 5% minerals (e.g., serpentine, chlorite, sericite and talc), whose elastic stiffness coefficients are not available, were not used in the comparison. This kind of samples includes mainly serpentinized peridotite and altered rocks.

The modal composition of each sample [f_i in Equation (1.20)] was determined by microscopic image analysis (e.g., Barruol and Kern, 1996; Burlini et al., 1998) or standard point counting (e.g., Christensen, 1965; Ji et al., 1993; Fountain et al., 1994) on petrographic thin sections, or mass balance calculations from the chemical compositions of bulk rock and its constitutive minerals (e.g., Kern et al., 1996). The modal composition data, which are critical for the accuracy of the *Vp* calculation (see Discussion), were obtained mainly from the point counting that is regarded to be accurate as long as the thin

section can represent the bulk sample (Underwood, 1970). Either the Vp or modal composition data of the 696 samples studied are not tabulated here; they are available upon request from the authors.

3.3.2 Absolute error

The absolute error (Ae) between the calculated and measured velocities is defined as:

$$Ae(\%) = \frac{|V_c - V_m|}{V_m} \times 100\% \qquad (3.1)$$

where V_c is the velocity calculated for the polymineralic rock at standard conditions (zero porosity, 0.1 MPa and 25 °C) using a given averaging approach, and V_m is the mean velocity measured at room temperature and a given pressure. The Ae value is taken as a statistic measure of the goodness of the prediction. The smaller the Ae, the better the agreement between the predicted and observed velocities.

Figure 3.1, which was computed using data of all the 696 samples, illustrates the mean absolute error ($\overline{Ae}$) versus pressure for each model. It is interesting to note:

(1) The Hill averaging differs very little from the geometric mean. The Hill scheme is always slightly better than the geometric mean although the latter is more rigorous in the physical implication given in Equation (1.4). The discrepancy of the VG from the VH, RG from RH, GV from HV, GH from HG, GR from HR, as well as GG from HH is in fact so small that it can be negligible (Figure 3.1a).

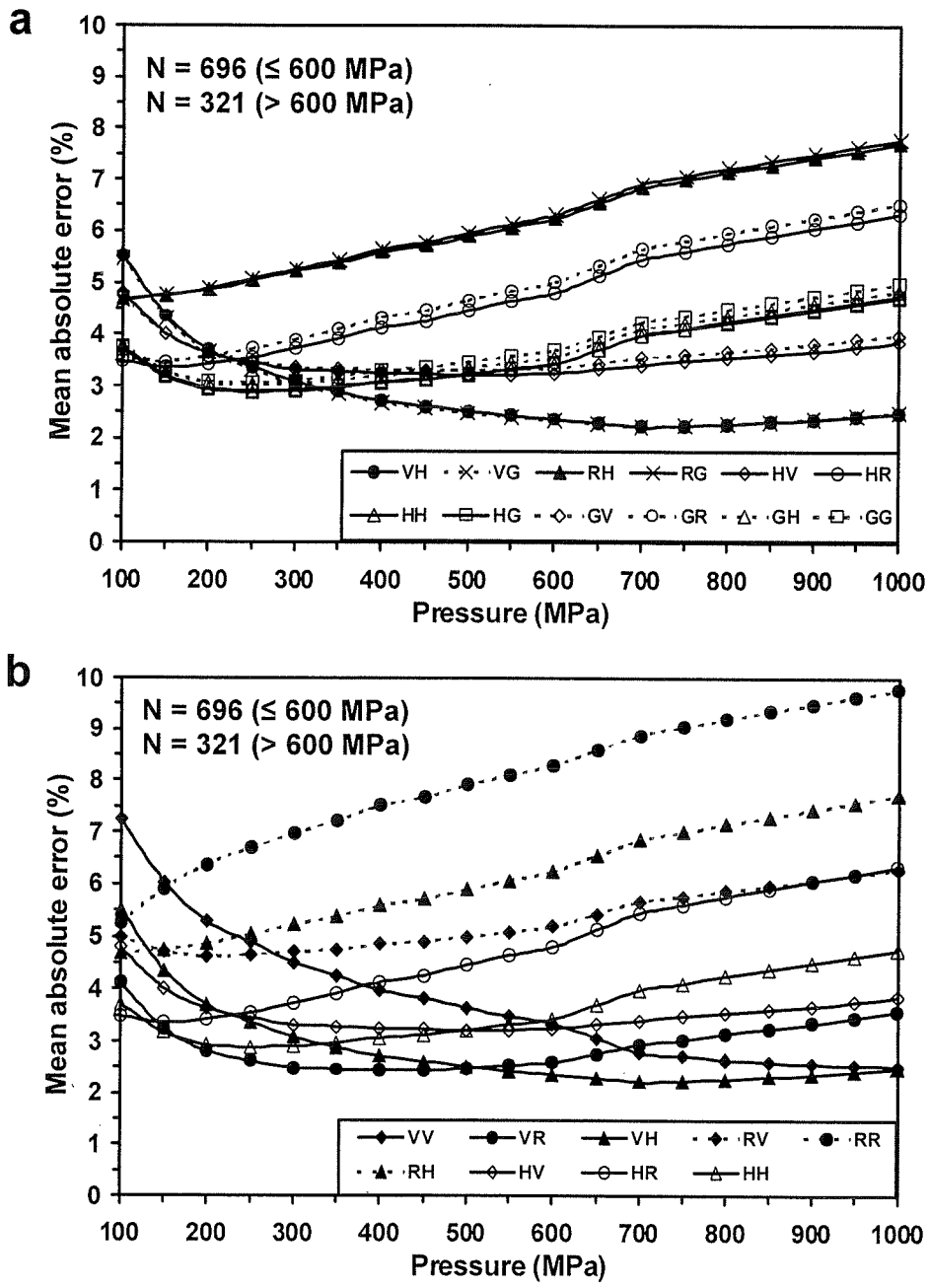


Figure 3.1 Comparison of the theoretical P-wave velocities (zero porosity, 25 °C and 0.1 MPa) with those measured at different pressure. Mean absolute error ($\overline{Ae}$, %) is taken as a statistic measure of the goodness of each averaging model. N – Sample number.

(2) The deviation of the *Vp* calculated according to the VV model from the measured value decreases with increasing pressure (Figure 3.1b). The VV model gives a better estimate of *Vp* ($\overline{Ae}$ < 3%) at pressures above 600-700 MPa. This is not surprising because seismic velocities almost always increase with increasing pressure and the VV represents theoretically the upper bound. A tendency is expected to decrease the deviation of the measured values at higher pressure from the VV bound calculated for an ideal, porosity-free aggregate from the room pressure single crystal elastic constants (Figure 3.2). This may be the reason for the common observation that the Voigt average exhibits a fairly good match to velocities measured at high pressures (Crosson and Lin, 1971; Seront et al., 1989; Ji et al., 1993; Ji and Salisbury, 1993; Kern et al., 1996). In contrast, the RR model (lower bound) gives generally a poor prediction for the measured *Vp* value. The $\overline{Ae}$ value of the RR model increases when the calculated *Vp* results are compared with the measurements at higher pressure.

(3) The VR and VH approximations yield the best estimate of *Vp* at pressures below and above 500 MPa, respectively (Figure 3.1b). These two models thus offer a greater improvement over the HH, HV, HR, RV, RH, VV and RR models. The accuracy of these two models is within the current certainty of most in situ seismic measurements.

(4) The calculated *Vp* values of 696 samples according to the VR scheme at standard conditions display the best agreement with the measured data at about 300 MPa (Figure 3.1b). It is well known that the *Vp*-pressure curves for rock samples (Figure 3.2) are characterized by an initial quick, non-linear rise in velocity below a critical confining pressure (P_c), followed by a more gradual linear increase above this critical pressure (e.g., Christensen, 1965; Kern et al., 1982; Fountain et al., 1990; Ji et al., 1993). The linear rise indicates an elastic volume deformation of the compacted aggregates while the non-linear rise marks a combination of the progressive closing of cracks and pore spaces (Birch, 1960; Christensen, 1965) and lattice compression within the sample. As shown in Figure 3.2, V_B and V_A are, respectively, the velocities

measured at room pressure and at P_c, and V_0 is the room pressure velocity, which is obtained from the extrapolation of the observed linear velocity-pressure relationship to room pressure. V_0-V_B reflects the increase in velocity due to the closing of cracks and pore spaces while V_A-V_0 corresponds the velocity rise from the lattice compression. The present results suggest that the velocity measured at around 300 MPa (P_0) statistically corresponds to the V_0. Because V_0 is lower than V_A but higher than V_B, the P_c should be significantly higher than 300 MPa for most polymineralic rocks.

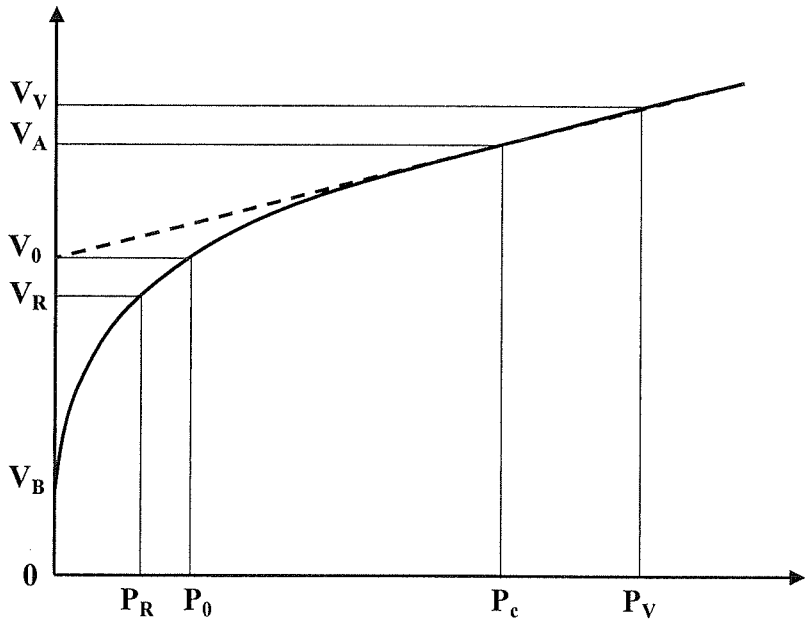


Figure 3.2 Elastic wave velocity versus pressure. V_0 is the projected 0.1 MPa pressure velocity; V_V and V_R are the theoretical velocities calculated using the Voigt and Reuss averages, respectively. Calculated V_V, V_0 and V_R should be compared with measured values at pressures P_V, P_0 and P_R, respectively, in order to obtain the best agreement. P_c is the critical pressure above which the rock can be considered as a compacted aggregate.

The 696 samples have been classified into 15 lithologic types according to their chemical and mineralogic compositions and textures. Figure 3.3 was built to verify if the

general trend shown in Figure 3.1b is applicable to each specific lithology. It is found that none of these averaging methods can simultaneously produce the best fit between the calculated and measured P-wave velocities for all the lithologic types. One method may work well for one lithology but poor for other lithology. In the range of 200-500 MPa, for example, the RH scheme gives the closest agreement with the measured *Vp* data for peridotite and eclogite (Figures 3.3a-b) while the HH average is the best estimation for the *Vp* data for schist and intermediate gneiss/mylonite (Figures 3.3c-d). For metasediment, gabbro-diabase, and mafic gneiss/mylonite, both the HH and VR schemes fit almost equally well to the measured *Vp* data at 200-500 MPa (Figures 3.3e-g). Even for a given lithology, an averaging method may yield good agreement at moderate pressure but poor agreement at high pressure. For pyroxenite, for example, the HV model is closest to the *Vp* data at 150-300 MPa while the VV model is better at >350 MPa (Figure 3.3h). Granite-granodiorite (Figure 3.3i), diorite (Figure 3.3j), felsic gneiss/mylonite (Figure 3.3k), anorthosite (Figure 3.3*l*), amphibolite (Figure 3.3m), marble (Figure 3.3n) and quartzite (Figure 3.3o) also fall into this category. The VR model is closest to the measured *Vp* data of granite-granodiorite below 400 MPa while the VH model does better above this pressure (Figure 3.3i). For anorthosite, the best model is the VR, VH, and VV models in the ranges of about 150-350, 350-500 and >500 MPa, respectively (Figure 3.3*l*). For marble and quartzite, the VR does the best job of predicting the *Vp* values above 300 MPa while the HH does better below this pressure (Figure 3.3n-o).

3.3.3. Relative error

The relative error (*Re*) between the calculated and measured velocities of each sample is defined as:

$$\mathrm{Re}(\%) = \frac{V_c - V_m}{V_m} \times 100\% \qquad (3.2)$$

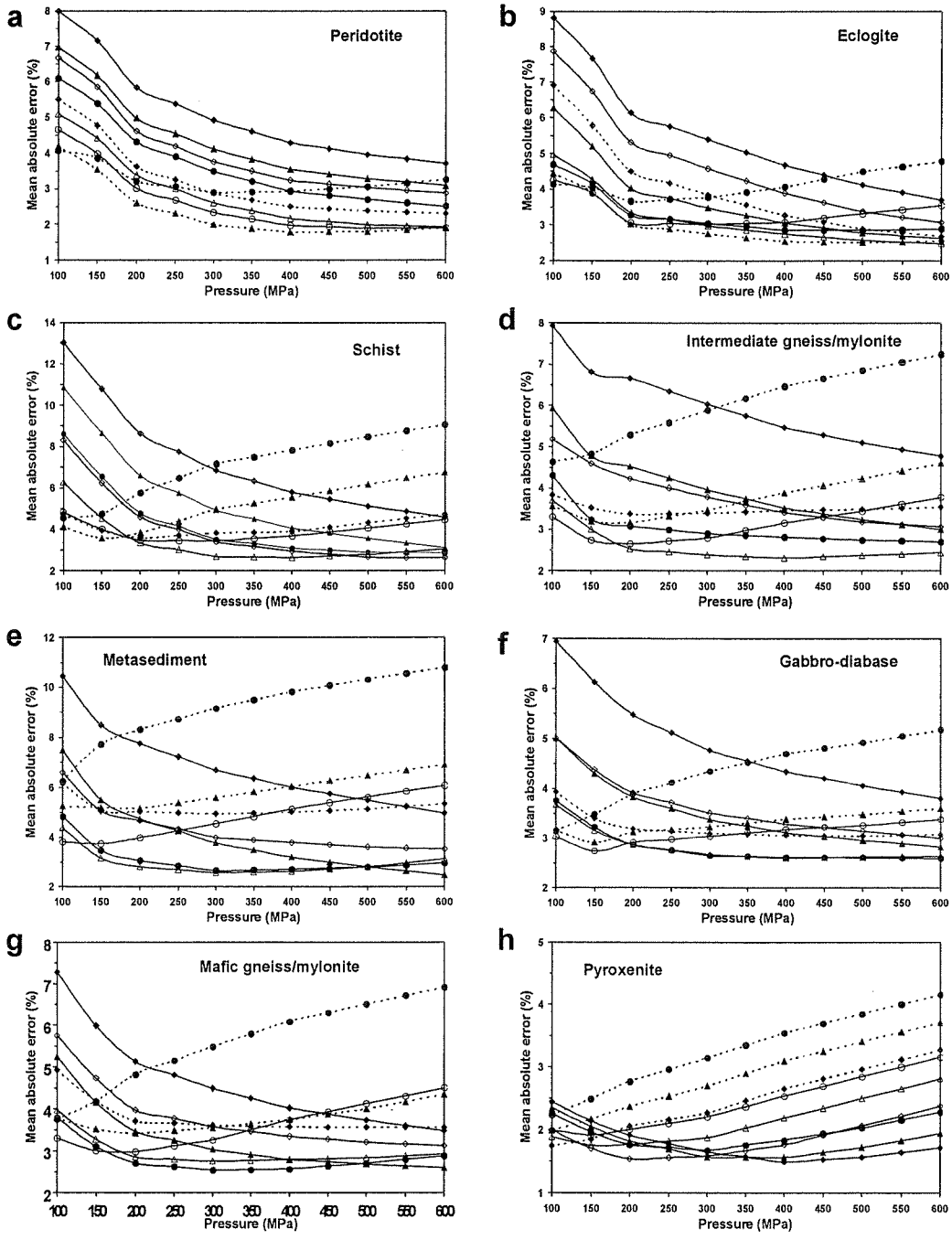


Figure 3.3 Comparison of the theoretical P-wave velocities (zero porosity, 25 °C and 0.1 MPa) with those measured at different pressure for 15 common categories of rocks. Mean absolute error ($\overline{Ae}$, %) is taken as a statistic measure of the goodness of each averaging model.

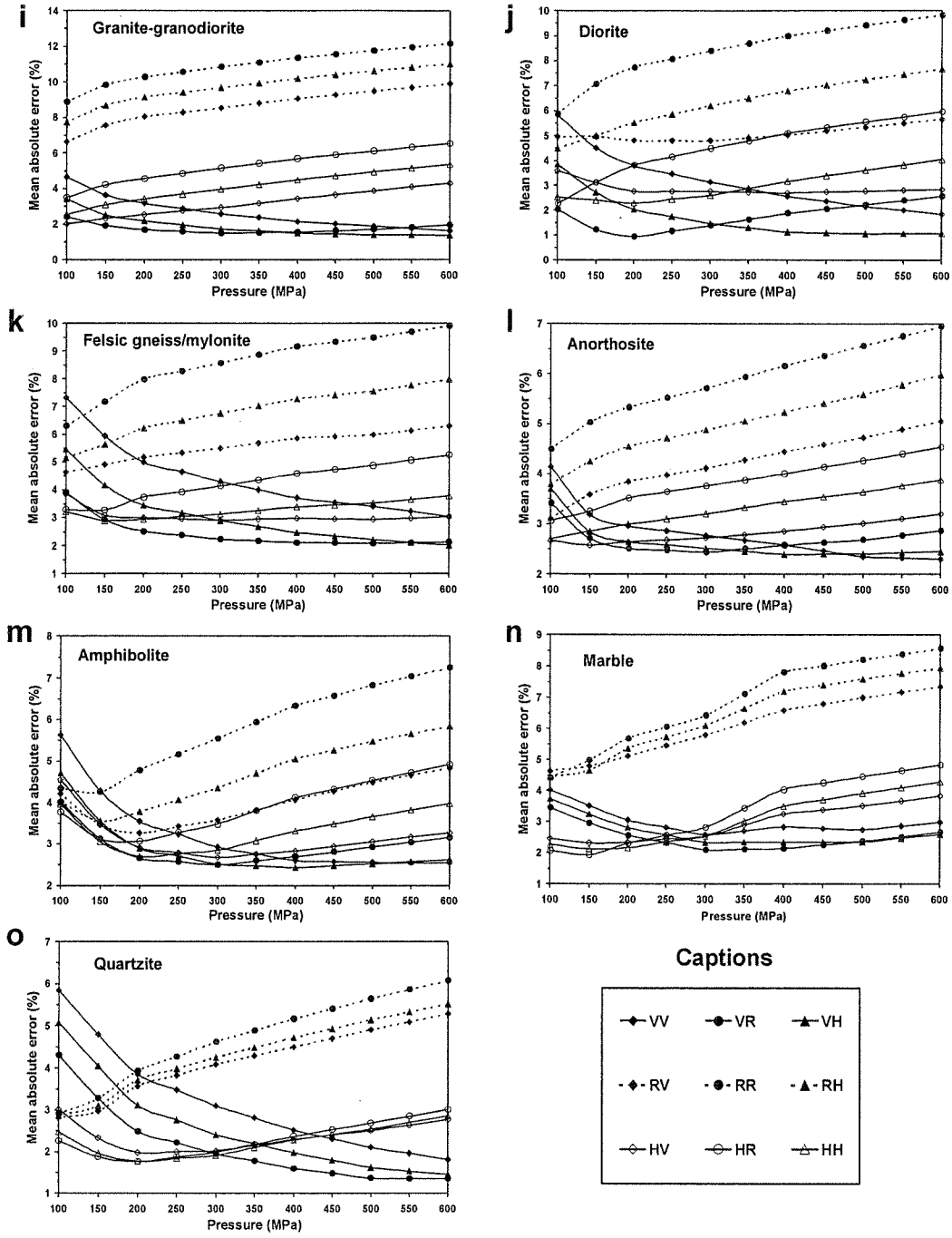


Figure 3.3 (continued)

Figure 3.4 shows the distribution of *Re* for the VV, RR, HH and VR models at 300 MPa. The measured P-wave velocities of 574 samples among a total of 696 samples lie in the range given by the VV upper and RR lower bounds. 80 samples show their measured *Vp* slightly higher (mainly <2%) than the VV bounds (Figure 3.4a). This phenomenon is observed in about 37% of amphibolites, 36% anorthosite, 25% pyroxenite, 25% marble, 21% diorite, 17% mafic gneiss/mylonite, 8% granite-granodiorite, felsic and intermediate gneiss/mylonite samples.

As shown in Figure 3.4b, the RR average produces a systematic underestimation of the *Vp* values for common crustal igneous rocks (e.g., granite, granodiorite, anorthosite, and gabbro-diabase) and metamorphic rocks (e.g., amphibolite, felsic, intermediate and mafic gneiss/mylonite, marble, quartzite, schist and metasediment). 42 samples among a total number of 696 have their *Vp* measured at 300 MPa lower than the RR bounds (Figure 3.4b) and the "anomaly" occurs in 43% of peridotite, 30% eclogite, 25% pyroxenite, and 14% gabbro-diabase samples. For those rocks from the upper mantle, the measured velocities are lower than calculated values probably due to cracks that cannot completely closed during experimental measurements at 300 MPa. These openings are believed to be the result of rapid tectonic exhumation from the upper mantle depth to the surface, and can be fully closed only at high temperature and high pressure (e.g., >1.0 GPa, Christensen, 1965; Kern et al., 2001). In addition, the presence of a few percent of alteration such as serpentine in peridotite and chlorite in eclogite and pyroxenite should tend to lower the measured velocities. A quantitative evaluation of the contribution of these impurities is difficult because their elastic stiffness coefficients have not been experimentally determined. Furthermore, recent high-pressure experiments on hot-pressed olivine-orthopyroxene mixtures (Ji and Wang, 1999) demonstrated that the measured velocity values are lower than the RR values, but can be better described by the shear-lag model that takes into account the mechanical interaction between phases.

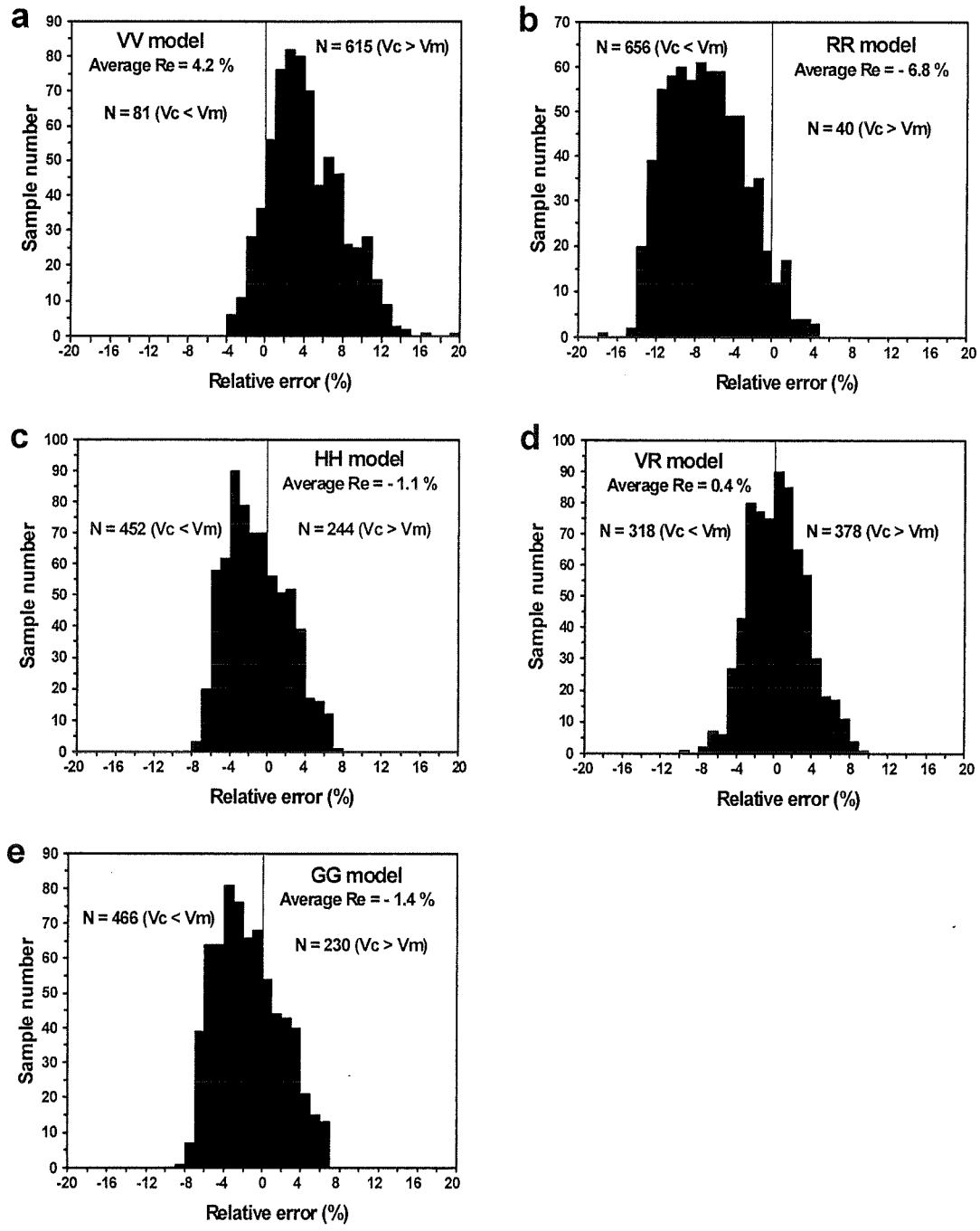


Figure 3.4 Relative errors of the VV (a), RR (b), HH (c) and VR (d) models for 696 samples. Calculated Vp data (V_c) are compared with measured values (V_m) at 300 MPa. N – Sample number. The relative error is defined by Equation (3.2).

It is interesting to note that the *Re* value of the HH model shows an asymmetric distribution with respect to zero where the calculated *Vp* is exactly equal to the measured value (Figure 3.4c), with the maximum in the domain of $Re<0$ or $V_c<V_m$. This indicates that the HH model tends to underestimate the *Vp* for the great majority of the samples (Figure 3.5). The VR model, however, displays a nearly normal distribution of *Re* with the maximum at zero (Figure 3.4d). Such characteristic suggests that the VR model produces the best fit between the calculated and measured velocities at 300 MPa over all the 696 dry samples.

As demonstrated by the *Re* histograms in Figure 3.5, the HH model tends to underestimate the *Vp* values of granite-granodiorite, diorite, felsic gneiss/mylonite, amphibolite, anorthosite, and marble, and to overestimate those of peridotite and eclogite. Contrary to the suggestion of Hurich et al. (2001) that the HH average overestimates the velocity of gabbroic rocks, we observed that this averaging method produces statistically good agreement between the calculated and measured *Vp* values for gabbro-diabase and mafic gneiss/mylonite at 300 MPa (Figure 3.5c-d). Moreover, it is also found that the HH model provides a fairly good match to *Vp* measured at 300 MPa for quartzite (Figure 3.5*l*), pyroxenite (Figure 3.5j), schist (Figure 3.5n), metasediment (Figure 3.5o), and intermediate metamorphic rocks (Figure 3.5f).

Figure 3.6 shows the *Re* histograms for the VR model at 300 MPa. This model offers obviously an improvement over the other models for amphibolite, anorthosite, diorite, granite-granodiorite, felsic gneiss/mylonite, and marble. For peridotite and eclogite, however, the RH gives the closest agreement to the measured *Vp* data (Figures 3.4a-b and 3.7).

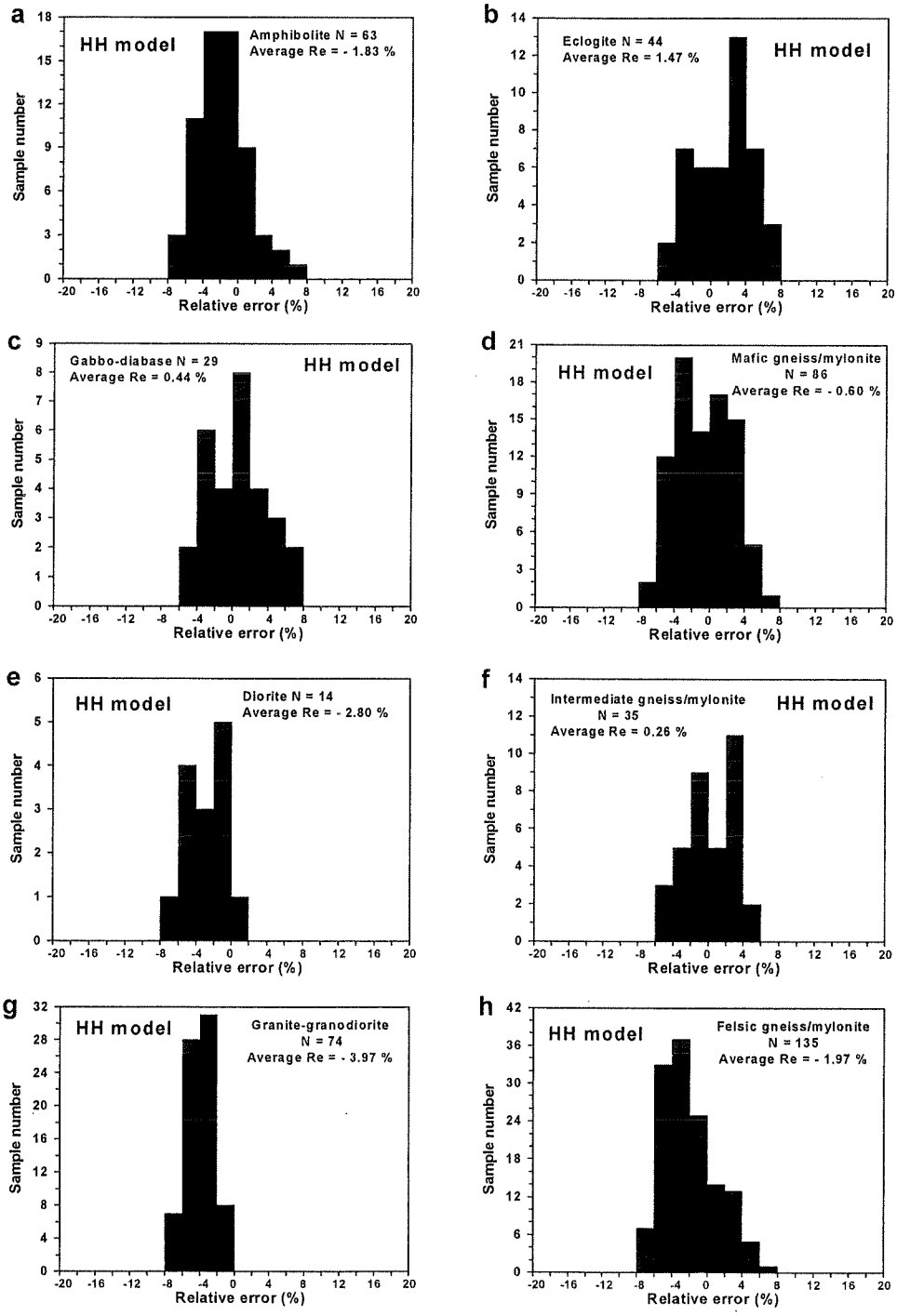


Figure 3.5 Relative errors of the HH model for 15 common lithologic categories. Calculated *Vp* data are compared with measured values at 300 MPa. N – Sample number. The relative error is defined by Equation (3.2).

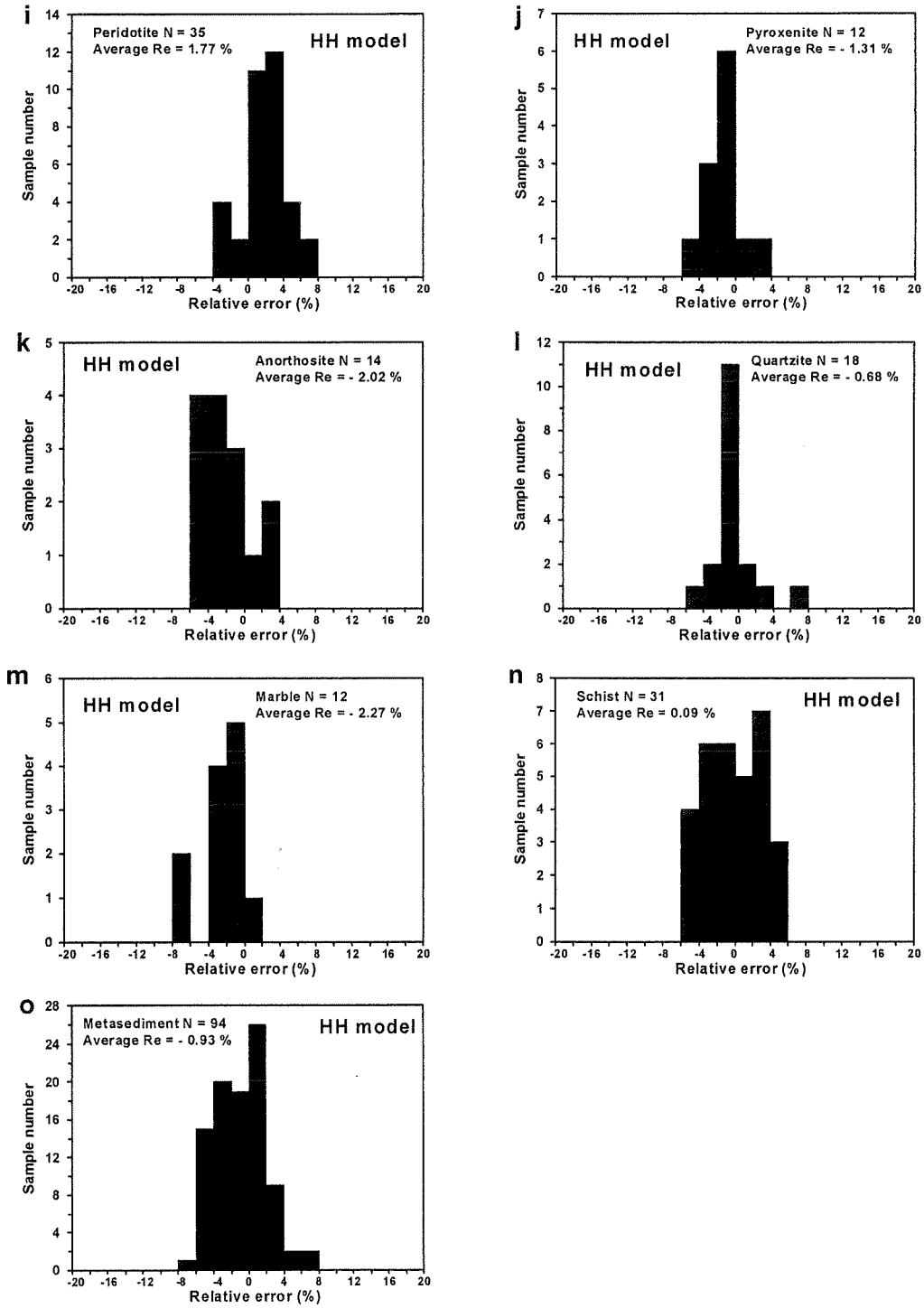


Figure 3.5 (continued)

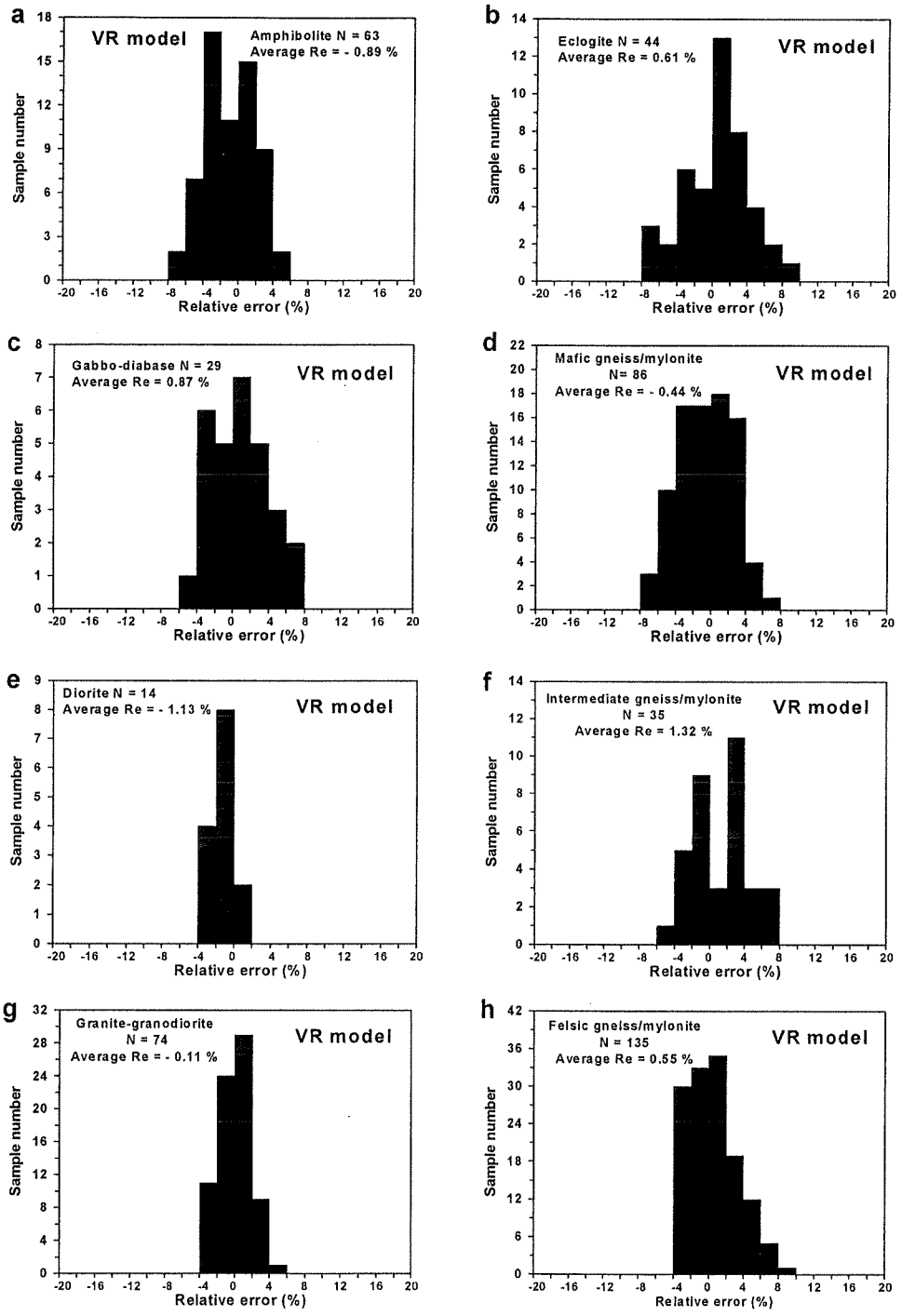


Figure 3.6 Relative errors of the VR model for 15 common lithologic categories. Calculated *Vp* data are compared with measured values at 300 MPa. N – Sample number. The relative error is defined by Equation (3.2).

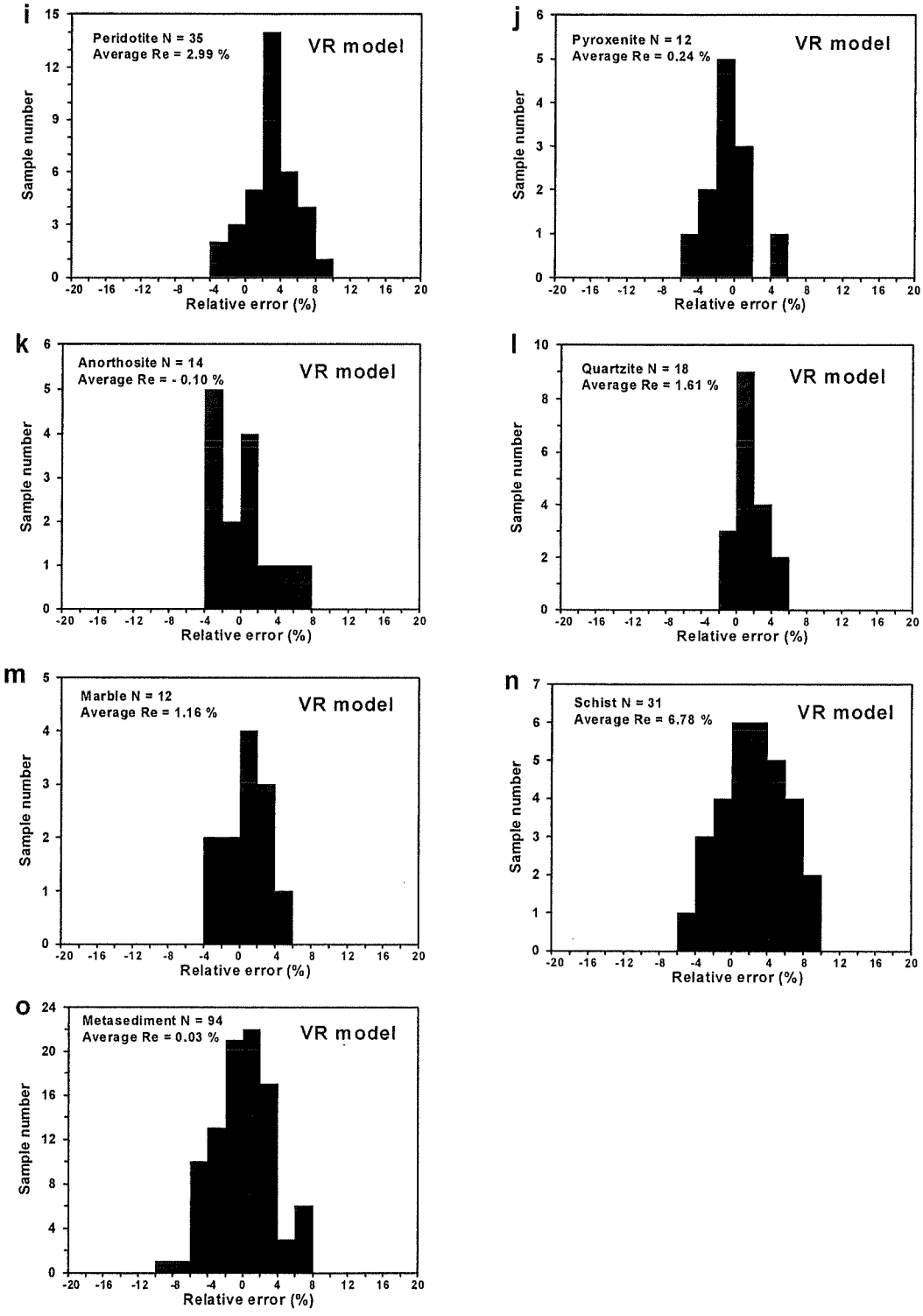


Figure 3.6 (continued)

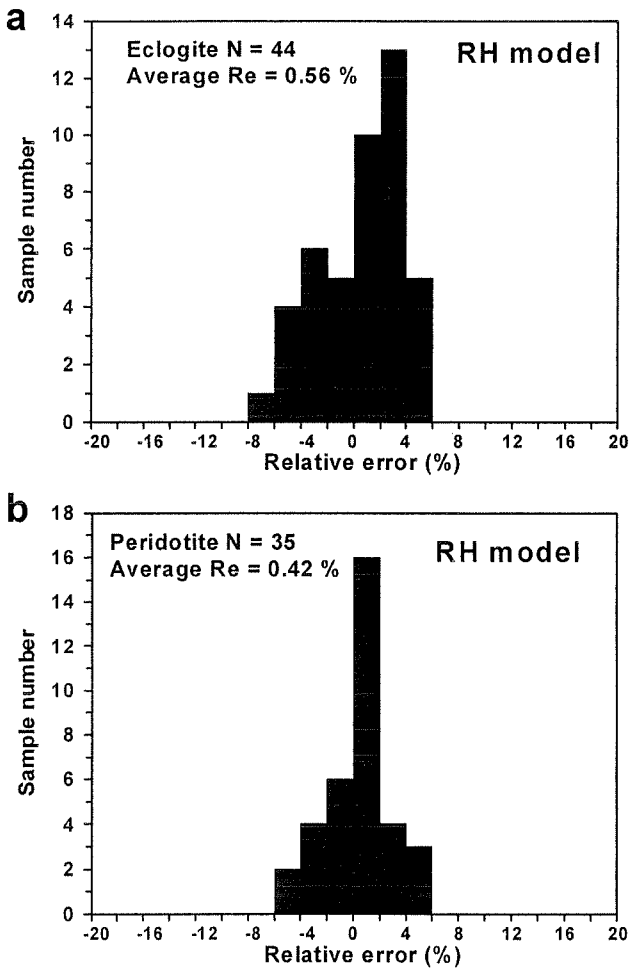


Figure 3.7 Relative errors of the RH model for eclogite (a) and peridotite (b). Calculated *Vp* data are compared with measured values at 300 MPa. N – Sample number. The relative error is defined by Equation (3.2).

3.4 Discussion

It is evident that the absolute errors of the calculated P-wave velocities are much larger than those arising from experimental errors in the measured values. The latter is estimated to be < 0.5-1.0% (Kern, 1982; Christensen, 1985). We cannot discount the possibility that some errors in the input data for the calculations influence the

comparison; however, the source of such errors is undoubtedly difficult to avoid at this moment. Several possible causes are briefly analyzed below:

(1) A constituent mineral with a complex chemical composition (e.g., amphibole, pyroxene, plagioclase and garnet) may not have exactly same elastic constants as the single crystal on which the published elastic constants were determined. It is likely that there are some minerals whose elastic constants are very similar to the rocks investigated while others not. It is unrealistic, if not impossible, to have elastic constants determined for each mineral of specific composition. Moreover, the single crystal elastic constants are determined on small crystals of gem quality, free of cracks or inclusions, which may be rare in natural rocks. In addition, grain boundaries are somewhat dirty and usually contain retrograde products. Effects of alteration and accessory minerals are difficult to evaluate because elastic constants of many alteration minerals (e.g., serpentine, sericite and chlorite) and accessory minerals are not available. We suggest, for want of accurate experimental data on single crystal elasticity of more minerals, that to use the elastic constants measured from a mineral having the closest composition to the component of the sample of interest should offer a significant improvement to the prediction of rock elastic properties.

(2) The modal content data are obtained, using the standard point counting or image analysis techniques on a thin section, from a very small volume of each sample, as compared with the volumes of core or cubic samples in which velocities are measured. As long as compositional heterogeneity exists, the thin section may not be an accurate representation of the rock sample. It is interesting to note that errors in the modal content has less pronounced influence on *Vp* variations of felsic rocks than mafic rocks. This difference reflects the fact that *Vp* in potassium feldspar, plagioclase and quartz are very similar in felsic rocks while *Vp* in plagioclase, amphibole, garnet, clinopyroxene and orthopyroxene are considerably different in mafic rocks. Consequently, variations in the proportions of these minerals lead to

very disparate *Vp* variations in mafic rocks and metasediments while only a minor influence on seismic velocity of felsic rocks (e.g., Fountain et al., 1990).

(3) Theoretically speaking, all the averaging approaches we use are applicable only to texture-free rocks in which neither shape preferred orientation (SPO) nor lattice preferred orientation (LPO) occurs. The developed SPO such as foliation and lineation generally result in a higher *Vp* parallel to the lineation while a lower *Vp* normal to the lineation (Seront, 1993; Ji et al., 1997). A LPO, if produced by a simple shear, is often of monoclinic symmetry with respect to the tectonic framework (X-Y-Z) and may cause the fastest, intermediate and slowest P-wave velocities not exactly parallel to the X, Y and Z directions (Ji et al., 1993). In order to check the potential effects of anisotropy on the comparison between the calculated and measured P-wave velocities, we plot the absolute error (*Ae*) against the seismic anisotropy for each sample (Figure 3.8). The anisotropy is defined as $100\%(V_{max} - V_{min})/V_m$ (Birch, 1960). Table 3.2 lists the mean absolute error and mean anisotropy for the 15 main lithologic categories investigated. The absolute error, which is a statistic measure of the goodness of the comparison, shows no remarkable correlation with the seismic anisotropy. This indicates that the mean velocity calculated from the measurements in the X, Y and Z directions does give a good approximation to true isotropic elastic properties even in highly anisotropic rocks.

(4) Actually most of the observed departure of the calculated values from the measured values can be accounted for by the errors discussed above, although there are some systematic deviations are likely caused by small but real differences between the ideal composites and measured samples. These systematic deviations are believed to relate to effects of mechanical interaction between phases (Ji and Wang, 1999) and those of grain boundaries and interfaces that have a typical thickness of 0.1-1 μm in natural rock samples. In a rock the grains themselves act as perfectly elastic units while the

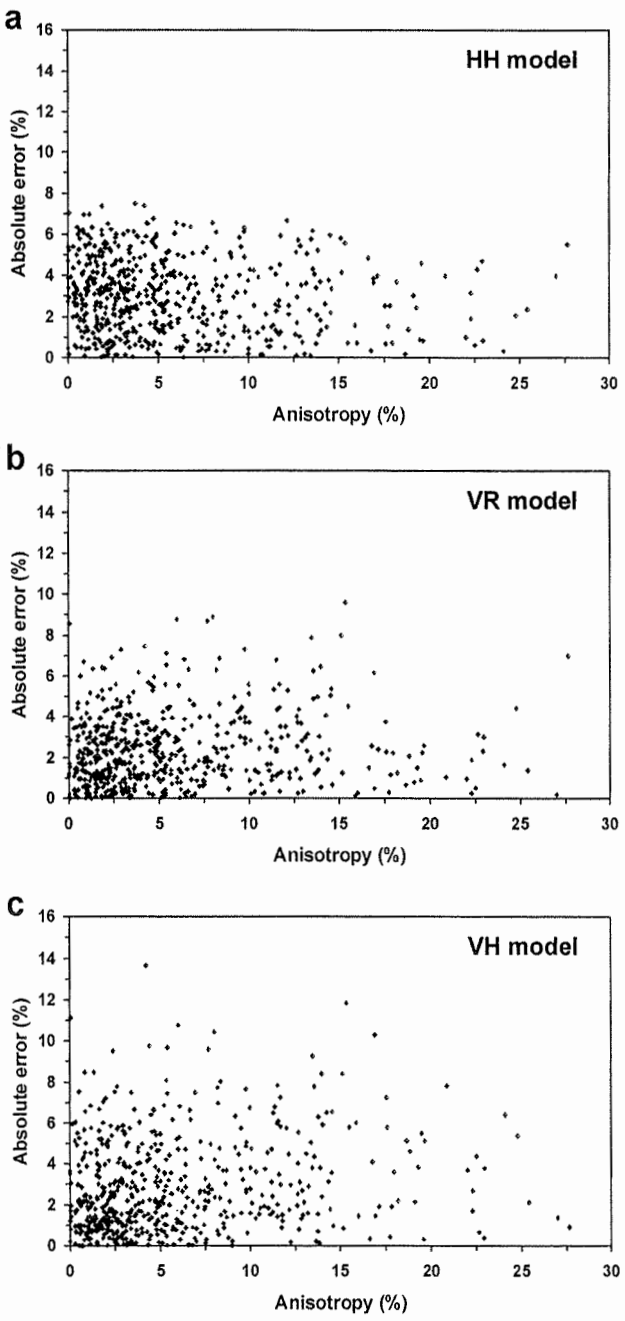


Figure 3.8 Seismic anisotropy versus absolute error plots for each sample. (a) HH model, (b) VR model, and (c) VH model. The absolute error is defined by Equation (3.1). P-wave velocities and anisotropy were measured at 300 MPa.

contacts between grains — grain boundaries and interfaces — often display non-linear elastic behaviour. As a result, the rock may be elastically non-linear and hysteretic. The traditional theory of linear elasticity and resultant averaging methods thus may not do an accurate job of describing the overall elastic properties of these so-called non-linear mesoscopic elastic materials (Guyer and Johnson, 1999).

Table 3.2 Mean absolute errors and seismic anisotropy for 15 common lithologic categories (the seismic velocities and anisotropy were measured at 300 MPa)

Lithology	Mean anisotropy (%)	Mean absolute error (%)		
		HH model	VR model	VH model
Anorthosite	2.2	3.1	2.7	2.7
Granite-granodiorite	2.3	4.1	1.5	1.6
Diorite	2.9	2.7	1.4	1.5
Gabbro-diabase	2.9	2.6	2.5	2.8
Eclogite	3.3	3.4	3.6	3.8
Pyroxenite	3.4	1.9	1.7	1.6
Mafic gneiss	3.9	2.7	2.5	2.8
Felsic gneiss	3.9	3.2	2.0	2.6
Intermediate gneiss / mylonite	5.7	2.5	2.7	3.3
Peridotite	6.1	2.5	3.5	4.3
Marble	6.3	2.7	2.0	2.2
Quartzite	6.6	1.9	1.8	2.3
Amphibolite	9.2	2.8	2.5	2.4
Metasediment	10.8	2.6	2.5	3.6
Schist	13.6	2.7	3.7	4.9

In spite of the errors discussed above, the modal composition data generally lead to remarkably good prediction of the average *Vp* values in the studied 696 samples from quasi-isotropic (e.g., granite, granodiorite and diorite) to highly anisotropic (e.g., amphibolite, metasediment, and schist) rocks. This seems to justify the assumption made,

that a polymineralic rock could be regarded as an isotropic aggregate for analysis of its mean elastic properties and seismic wave velocities. It furthermore appears that the P-wave velocity of a polymineralic rock at above 300 MPa can be fairly well predicted as long as the volume fractions and single crystal elastic constants of its constituent minerals are available and a relevant mixture rule is used. Therefore, the volume fractions of the rock-forming minerals are the critical factor in controlling the mean P-wave velocity of a polymineralic rock while grain shape and preferred orientation, anisotropy, and other perturbations appear to have minimum effect on it. In other words, the deviation of the predicted values from the measured values is mainly due to errors in the determination of mineral volume fractions and to compositional heterogeneity of the rocks.

Similar to the Hill scheme, physical implications of the mixed averaging schemes such as VR, VH and RH remain unclear yet. However, we do find that the VR and VH schemes yield better agreements with experimental data than the VV, RR, HH and GG models below and above 500 MPa, respectively (Figure 3.1). This may indicate that the Voigt average is relevant for monomineralic aggregates while the Reuss or Hill average is good for polymineralic composites. In fact, the mechanic processes in monomineralic aggregates (like-phase mixing) and in polymineralic composites (unlike-phase mixing) are generally different. For example, the stress transfer across a grain boundary between two like-phase grains is distinct from an interface between two unlike-phases (Clyne and Withers, 1993). Thus, the detailed physical implication of each averaging scheme should be an important topic for future investigation.

As the uncertainties discussed above are difficult to avoid in the case of natural samples, comparisons between calculated and observed values of hot-pressed, isotropic multiphase composites with well controlled chemical composition, volume fraction and geometric configuration of each phase are clearly preferable to better test the mixture rules (Watt et al., 1976; Zhang et al., 1996; Ji and Wang, 1998). Much work remains to

be done in this area because it can yield better constraints on the interpretation of seismic data.

3.5 Conclusions

The following conclusions have been reached from the present study:

(1) Application of the averaging methods to 696 dry samples for which both P-wave velocity and modal composition were measured produced somewhat surprising results. The exceptional large number of samples covers almost all common lithologic types of igneous and metamorphic rocks. The seismic velocities calculated from the room pressure single crystal elastic constants are in good agreement with laboratory values measured at about 300 MPa, even though elastic constants of only 22 common minerals (Table 3.1) were taken in account in the computation. As long as a relevant averaging scheme is used and the volume fraction is correctly determined for each mineral, the calculated seismic velocities of most crustal and upper mantle crusts are certainly of quality high enough to characterize the average seismic properties of rocks, for example, for interpretation of seismic reflection and refraction profiles.

(2) In the moderate pressure range (200-500 MPa), the RH average produced the best fit between the calculated and measured velocities for eclogite and peridotite. The HH average is the best estimation for the *Vp* data for schist and intermediate gneiss/mylonite. Either VR or HH is closest to the measured *Vp* data for metasediment, gabbro-diabase and mafic gneiss/mylonite at 200-500 MPa. The VV scheme fits best for pyroxenite at pressures above 350 MPa. For granite-granodiorite, diorite, amphibolite, anorthosite and felsic gneiss/mylonite, the VR average generally produces the best fit between the calculated and measured P-wave velocities at 200-300 MPa. At higher pressures, the VH or VG average is the best approximation of the measured values. For quartzite and marble, the VR scheme does the best job of

predicting *Vp* values at above 250-300 MPa while the HH average does better at lower pressures. Hence none of these averaging methods can simultaneously produce the best fit between the calculated and measured P-wave velocities for all the lithologic types or for the data of all the pressures. Applications of an inappropriate mixture rule should result in either under- or over-estimations for the mean *Vp* of a polymineralic rock in a given pressure range, depending on its lithology. Therefore, selection of relevant mixture rule plays a critical role in the interpretation of the crust and mantle seismic velocity data in terms of the mineralogic compositions and structures.

(3) It is generally accepted that the geometric mean is satisfied with the rigorous physical condition that the aggregate mean is equal to the mean of the inverse property (i.e., mean elastic stiffness and compliance) while the Hill average lacks physical justification. The geometric mean, which was shown to be almost identical to the much more complicated iterative self-consistent method (Mathies and Humbert, 1993; Mainprice and Humbert, 1994), is actually very close to the Hill averaging at least for most of polymineralic rocks.

(4) The goodness of the comparison between the calculated and measured *Vp* data shows no remarkable correlation with the seismic anisotropy, implying that the mean velocity calculated from the measurements in the X, Y and Z directions represents a good approximation to bulk elastic properties of samples from quasi-isotropic (e.g., granite, granodiorite and diorite) to highly anisotropic (e.g., amphibolite, metasediment, and schist) rocks.

Chapter 4

Pressure dependence and anisotropy of P-wave velocities in ultrahigh-pressure metamorphic rocks from the Dabie-Sulu orogenic belt (China): implications for seismic properties of subducted slabs and origin of mantle reflections

Qin Wang[a], Shaocheng Ji[a,c], Matthew H. Salisbury[b], Bin Xia[c], Mingbao Pan[a,d], Zhiqin Xu[e]

[a]*Département des Génies Civil, Géologique et des Mines, École Polytechnique de Montréal, Montréal, Québec, Canada H3C 3A7*

[b]*Geological Survey of Canada-Atlantic, Bedford Institute of Oceanography, P.O Box 1006, Dartmouth, Nova Scotia, Canada B2Y 4A2*

[c]*Laboratory of Marginal Sea Geology, Guangzhou Institute of Geochemistry, Chinese Academy of Sciences, Guangzhou 510640, China*

[d]*Geological Survey of Jiangsu Province, Nanjing 210018, China*

[e]*Chinese Continental Scientific Drilling, Institute of Geology, Chinese Academy of Geological Sciences, Beijing 100037, China*

Acknowledgements

We thank NSERC, LITHOPROBE and the Chinese Academy of Sciences (KZCXZ-SW-117) for research grants. We are grateful to R. Iuliucci for his generous technical support in the laboratory, J. Martignole for helpful discussion and to S.T. Xu for providing the Bixiling eclogite samples. And we appreciate the constructive comments of Dr. K. Furlong and two anonymous reviewers. This is LITHOPROBE contribution No. 1384.

This paper was submitted to Tectonophysics in February 2004.

4.1 Abstract

The compressional wave velocities (*Vp*), pressure derivatives (*Vp'*) and anisotropy (*A*) of three types of eclogites and country rocks from the Dabie-Sulu ultrahigh-pressure (UHP) metamorphic belt, China, have been measured under confining pressures up to 800 MPa. Type-1 eclogites, which are coarse-grained and subjected to almost no retrograde metamorphism, experienced recovery-accommodated dislocation creep at peak metamorphic conditions (in the diamond stability field). Type-2 eclogites are fine-grained reworked Type-1 materials that experienced recrystallization-accommodated dislocation creep under quartz/coesite boundary conditions during the early stage of exhumation. Type-3 eclogites are retrograde samples that were overprinted by significant amphibolite facies metamorphism during a late stage of exhumation within the crust. Type-1 eclogites are richer in Al_2O_3 and MgO but poorer in SiO_2 and NaO_2 than Type-2 and Type-3 eclogites. Anisotropy of Type-1 and Type-2 eclogites is generally low (<4%) because volumetrically important garnet is elastically quasi-isotropic, while Type-3 eclogites can exhibit high anisotropy (>10%) due to the presence of strongly anisotropic retrograde minerals such as amphibole, plagioclase and mica. The transition of the pressure dependence of velocity from the poroelastic to elastic regimes occurs at a critical pressure (P_c), which depends mainly on the density and distribution of microcracks and in turn on the exhumation history of rocks. The *Vp*-pressure relationship can be expressed by $Vp = a(\ln P)^2 + b\ln P + c$ $(P \le P_c)$ and $Vp = V_0 + DP$ $(P \ge P_c)$, where P is the confining pressure, a and b are constants describing the closure of microcracks below P_c, c is the velocity when P is equal to one (MPa), V_0 is the projected velocity of a crack-free sample at room pressure, and D is the intrinsic pressure derivative above P_c. When data are curve-fit, pressure derivatives and anisotropy as functions of pressure are determined. The average *Vp* of the eclogites in the linear regime is $8.42 + 1.41\times10^{-4}P$ for Type-1, $7.80 + 1.58\times10^{-4}P$ for Type-2, and $7.33 + 2.04\times10^{-4}P$ for Type-3, where *Vp* is in km/s and P in MPa. The decrease in V_0 and increase in D from Type-1 to Type-3 eclogites are attributed to a decrease in garnet content and an increase in retrograde minerals. The NE-

SW trending, NW-dipping, slab-like high *Vp* anomaly (8.72 km/s at a depth of 71 km) which extends from the Moho to at least 110 km beneath the Dabie-Sulu region, can be interpreted as the remnant of a subducted slab which is dominated by Type-1 eclogites and has frozen in the upper mantle since about 200-220 Ma. Such relic crustal materials, subducted and preserved as eclogite layers intercalated with felsic gneiss, garnet-jadeite quartzite, marble and serpentinized peridotite, could be responsible for regionally observed seismic reflectors in the upper mantle.

Keywords: UHP metamorphic rocks; Eclogite; Compressional wave velocity and anisotropy; Pressure derivatives; Mantle reflections; Dabie-Sulu orogenic belt

4.2 Introduction

The seismic velocity and anisotropy structures of the crust and upper mantle are increasingly well-resolved by seismic techniques, but the structural and petrologic interpretation of seismic data depends critically on our understanding of the seismic properties of candidate rocks and the variation of these properties with pressure and temperature. Knowledge of the seismic properties of eclogites and their host rocks is of particular importance for the interpretation of seismic data from ancient and modern subducted slabs (e.g., Wang et al., 2000; Xu et al., 2001; Yang, 2002, 2003), and for understanding the mechanism of subduction and exhumation of ultrahigh-pressure (UHP) metamorphic rocks. For this purpose, Kern et al. (1999, 2002) measured the P- and S-wave velocities of a set of rock samples from the Dabie-Sulu UHP metamorphic belt at confining pressures up to 600 MPa. The Dabie-Sulu orogenic belt in east-central China (Figure 4.1) is the largest UHP metamorphic belt recognized in the world. Extensive studies have shown that both eclogites and country rocks such as felsic gneisses, quartzites and marbles from this belt contain inclusions of UHP minerals (e.g., diamond and coesite), indicating that the continental crust has been subducted to a depth of at least 100 km before being rapidly exhumed up to the surface (e.g., Wang and Liou, 1991;

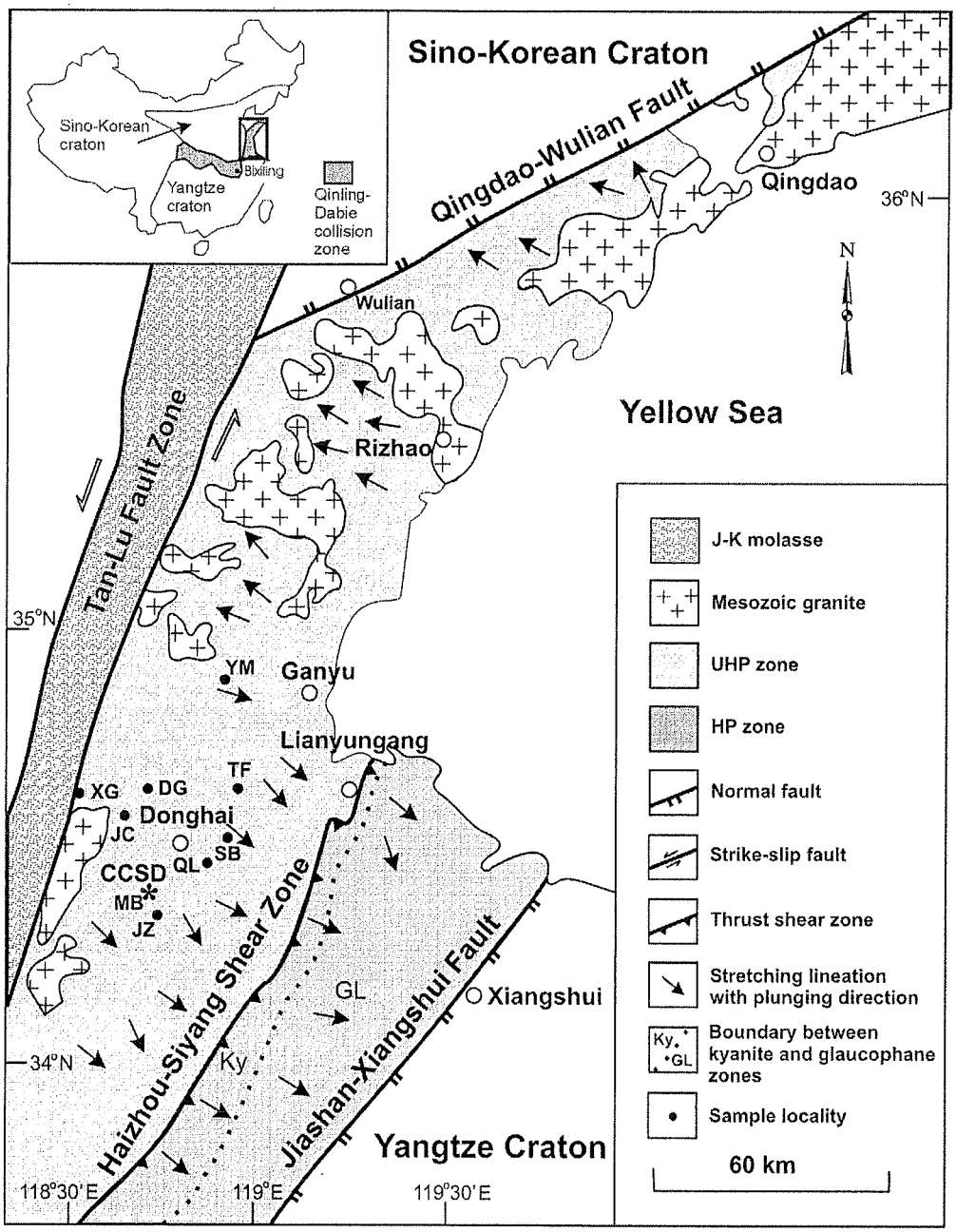


Figure 4.1 Simplified geological map of the Sulu metamorphic terrane, eastern China. Star shows location of drill site (Maobei, Donghai County, Jiangsu Province) of the Chinese Continental Scientific Drilling (CCSD) program. Sample localities are: DG, Dugou; JC, Jianchang; JZ, Jiangzhuang; MB, Maobei; SB, Shanbeitou; TF, Tuofeng; XG, Xugou; YM, Yanmachang. Bixiling sample site is shown in the sketch map of China.

Zhang et al., 1994; Hacker et al., 2000; Liou et al., 2000b). While the eclogites studied by Kern et al. (1999, 2002) displayed high velocities, their measurements were performed on unjacketed, cube-shaped specimens using an apparatus in which the confining pressure was achieved by pressing six pyramidal pistons in three orthogonal directions on the specimen. As stated by these authors, the pressure probably was not perfectly hydrostatic, and 600 MPa is not high enough to fully close all cracks. Such tests may potentially cause an overestimation of both pressure derivatives and seismic anisotropy, making the extrapolation of seismic velocities and anisotropy to higher pressures questionable. Thus, it is necessary to calibrate the seismic properties and anisotropy of the UHP rocks under higher, purely hydrostatic pressures. To this end, we measured the P- and S-wave velocities, derivatives and anisotropy of a suite of 29 eclogites and host rocks from the Dabie-Sulu orogenic belt under hydrostatic pressures ranging from 10-800 MPa.

In making such measurements, it is commonly observed that the experimental velocity-pressure curves for rocks display a rapid, nonlinear rise in velocity at low pressures, followed by a slow linear increase at high pressures (Figure 2.1). The nonlinear rise is attributed to a combination of the gradual closure of cracks and pore spaces and lattice compression within the sample while the linear increase marks an elastic volume deformation of the compacted aggregate (e.g., Birch, 1960; Christensen, 1974; Ji et al., 1993; Kern et al., 2002). Although there exist a few empirical equations (Eberhart-Phillips et al., 1989; Wepfer and Christensen, 1991; Freund, 1992; Shapiro, 2003) for describing the pressure dependence of seismic velocity, some questions remain open. What is the significance of the critical pressure (P_c) marking the transition from nonlinear to linear behaviour, and does P_c depend on lithology, tectonic setting or exhumation history? Is there a simpler equation which can better describe the velocity-pressure variation in the nonlinear regime and if such an equation exists, what are the physical implications of its parameters? Answers to these questions are critically important for calibrating the effects of cracks and pores, crystallographic preferred orientation (CPO) and compositional layering on seismic properties and for justifying the extrapolation of

velocity-pressure functions obtained over a limited range of pressure to either lower or higher pressures.

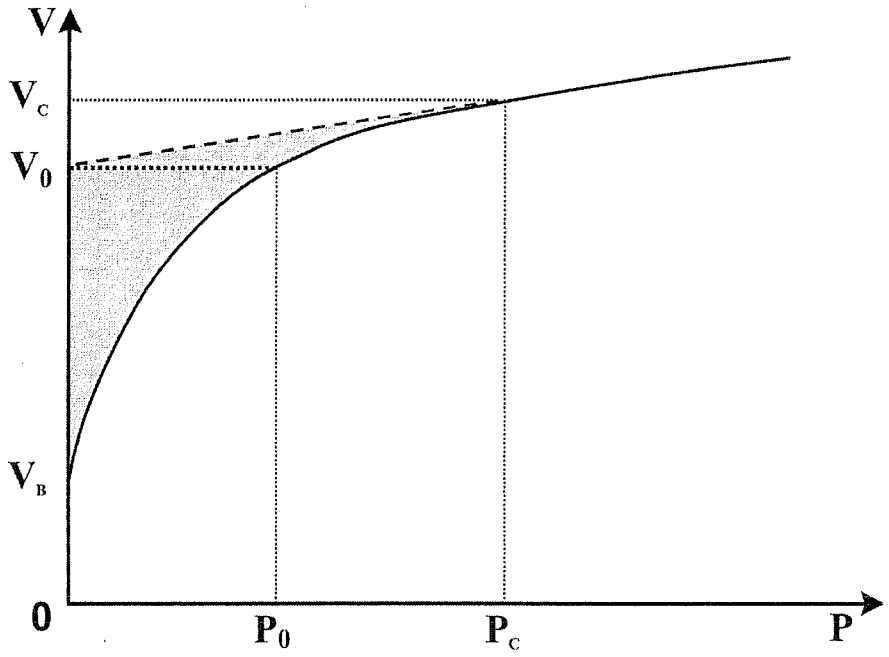


Figure 4.2 Elastic wave velocity (V) versus pressure (P). V_0 is the projected velocity of a crack-free sample at atmospheric pressure (0.1 MPa) and corresponds to the measured velocity at P_0 in the velocity-pressure curve; P_c is the critical pressure above which the rock can be considered as a compacted aggregate. V_c and V_B are the measured velocities at P_c and 0.1 MPa, respectively. Effects of microcracks and pores on the velocity are illustrated by the shadowed area.

The present paper is thus threefold. First, we measure the P-wave velocities (*Vp*), pressure derivatives (*Vp'*) and anisotropy (*A*) of eclogites and country rocks from the Dabie-Sulu UHP belt, China. Second, we establish standard expressions for *Vp*, *Vp'* and anisotropy (*A*) as a function of confining pressure for such rocks for both the nonlinear and linear regimes. Finally the results are used to provide a new, plausible interpretation for the origin of seismic reflections in the upper mantle. The results of S-wave velocities and anisotropy will be reported in a separate paper.

4.3 Geological setting

All of the study samples were collected from the Sulu region except for two from the Dabie Mountains (Table 4.1, Figure 4.1). The Sulu terrane, which has been displaced about 530 km by the sinistral Tan-Lu fault zone, is an eastern extension of the Qinling-Dabie collision zone between the Sino-Korean and Yangtze cratons (e.g., Liou et al., 1998; Hacker et al., 2000). The Yangtze craton subducted northward and first collided with the Sino-Korean craton at the eastern end during the Late Permian. As the collision proceeded from east to west, the triangular ocean basin between the Sino-Korean and Yangtze cratons closed progressively, causing the Yangtze craton to rotate clockwise about 60° during the Triassic (Zhu et al., 1998). After the basin completely disappeared, the two cratons continued to converge by continental subduction and shortening during the Jurassic.

The Dabie-Sulu UHP metamorphic belt consists of interlayered pelitic and granitic gneisses, phengite-quartz schist, quartzite, marble, eclogite and garnet peridotite (Figures 4.3a-b). These rocks commonly contain coesite and occasionally microdiamond as inclusions in garnet, omphacite, jadeite and zoisite and their peak metamorphic P-T conditions were 3.2-4.7 GPa and 750-900 °C (e.g., Zhang et al., 1994; Zhang et al., 1995a,b; Liou et al., 1998; Zhang et al., 2000). This indicates that the eclogites are not exotic in origin and that all of the rocks used to be part of the Yangtze craton were subducted to levels deep within the upper mantle where they suffered in situ UHP metamorphism.

Stable isotopic geochemical data (e.g., Rumble et al., 2000) indicate that the protoliths of these UHP metamorphic rocks were most likely continental shelf limestone, quartzo-feldspathic sandstone (greywacke) and mafic volcanoclastic sediments. The protoliths are Early Proterozoic (~1700-1900 Ma, Jahn et al., 1996; Yang et al., 2003) or

Table 4.1 Sample number, locality, lithology and modal composition (vol. %)

Sample	Locality	Coordinates	Lithology	Modal composition
86351	Maobei	N34.40, E118.67	Coarse-grained eclogite	Grt 63.0, Cpx 35.0, Rt 1.5, Qtz 0.5
MB22	Maobei	N34.40, E118.67	Coarse-grained eclogite	Grt 63.0, Cpx 35.0, Rt 1.5, Qtz 0.5
MB23	Maobei	N34.40, E118.67	Coarse-grained eclogite	Grt 70.0, Cpx 26.0, Phn 2.0, Rt 1.0, Qtz 1.0
MB25	Maobei	N34.40, E118.67	Coarse-grained eclogite	Grt 65.0, Cpx 33.0, Rt 1.5, Qtz 0.5
MB26	Maobei	N34.40, E118.67	Coarse-grained eclogite	Grt 70.0, Cpx 29.0, Rt 0.8, Qtz 0.2
MB27	Maobei	N34.40, E118.67	Coarse-grained eclogite	Grt 68.0, Cpx 31.0, Rt 1.0
MB30	Maobei	N34.40, E118.67	Coarse-grained eclogite	Grt 70.0, Cpx 29.0, Rt 0.5, Qtz 0.5
MB2B	Maobei	N34.40, E118.67	Coarse-grained garnetite	Grt 88.0, Cpx 10.0, Phn 1.5, Rt 0.5
MB34	Maobei	N34.40, E118.67	Coarse-grained garnetite	Grt 75.0, Cpx 23.0, Rt 1.0, Qtz 1.0
MB62	Maobei	N34.40, E118.67	Coarse-grained garnetite	Grt 84.0, Cpx 15.0, Rt 0.5, Qtz 0.5
DG1	Dugou	N34.64, E118.64	Fine-grained eclogite	Grt 45.0, Cpx 50.0, Symp 2.5, Hbl 1.0, Rt 1.0, Qtz 0.5
JC2	Jianchang	N34.62, E118.65	Fine-grained eclogite	Grt 15.0, Cpx 75.0, Rt 2.5, Qtz 3.0, Hbl 1.0, Phn 1.0, Opq 0.5, Symp 3.0
JZ1	Jiangzhuang	N34.39, E118.67	Fine-grained eclogite	Grt 25.0, Cpx 63.0, Hbl 5.0, Rt 2.0, Qtz 2.0, Phn 1.0, Symp 2.0
SB1	Shanbeitou	N34.52, E118.90	Fine-grained eclogite	Grt 33.0, Cpx 60.0, Hbl 2.0, Rt 2.0, Qtz 1.0, Symp 2.0
98401	Bixiling	N30.73, E116.29	Retrograded eclogite	Grt 30.0, Cpx 45.0. Hbl 15.0, Rt 2.0, Qtz 1.0, Opq 1.0, Symp 6.0
98501	Bixiling	N30.73, E116.29	Retrograded eclogite	Grt 25.0, Cpx 20.0, Hbl 37.0, Bt 2.0, Phn 2.0, Opq 2.0, Rt 1.0, Qtz 1.0, Symp 20.0
JC1	Jianchang	N34.62, E118.65	Retrograded eclogite	Grt 20.0, Cpx 60.0, Hbl 7.0, Qtz 3.0, Rt 1.0, Opq 1.0, Symp 8.0
QL2	Qinglongshan	N34.51, E118.89	Retrograded eclogite	Grt 10.0, Cpx 50.0, Hbl 8.0, Phn 10.0, Ep 5.0, Chl 3.0, Qtz 5.0, Rt 2.0, Opq 1.0, Symp 6.0
QL3	Qinglongshan	N34.51, E118.89	Retrograded eclogite	Grt 22.0, Cpx 55.0, Hbl 5.0, Phn 5.0, Ep 5.0, Qtz 2.0, Rt 2.0, Opq 1.0, Symp 3.0
QL4	Qinglongshan	N34.51, E118.89	Amphibolite	Hbl 50.0, Chl 12.0, Grt 3.0, Cpx 15.0, Pl 10.0, Qtz 5.0, Ep 2.0, Rt 2.0, Opq 1.0
QL5	Qinglongshan	N34.51, E118.89	Amphibolite	Hbl 45.0, Chl 30.0, Cpx 12.0, Ep 3.0, Rt 2.0, Opq 3.0, Qtz 2.0, Symp 3.0
YM4	Yanmachang	N34.87, E118.88	Amphibolite	Hbl 80.0, Qtz 8.0, Pl 5.0, Opx 5.0, Opq 2.0
TF1	Tuofeng	N34.58, E118.85	Granitic gneiss	Qtz 35, Pl 40, Kfs 15, Opx 7.0, Grt 1.5, Opq 1.0, Rt 0.5
TF2	Tuofeng	N34.58, E118.85	Granitic gneiss	Qtz 24, Pl 40, Kfs 25, Opx 3.0, Grt 2.0, Bt 3.0, Opq 2.0, Rt 1.0
TF3	Tuofeng	N34.58, E118.85	Granitic gneiss	Qtz 20, Pl 30, Kfs 42, Opx 4.0, Opq 1.5, Rt 0.5
XG1	Xugou	N34.63, N118.50	Serpentinite	Srp 83.0, Ol 10.0, Opq 7.0
XG3	Xugou	N34.63, N118.50	Serpentinite	Srp 80.0, Ol 15.0, Opq 5.0
YM1	Yanmachang	N34.87, E118.88	Marble	Dol 87, Cal 7.0, Qtz 4.0, Grt 1.0, Cpx 1.0
YM2	Yanmachang	N34.87, E118.88	Marble	Dol 86.0, Cal 7.0, Qtz 5.0, Grt 1.5, Rt 0.5

Abbreviations: Grt, garnet; Cpx, clinopyroxene; Opx, orthopyroxene; Hbl, hornblende; Bt, biotite; Phn, phengite; Chl, chlorite; Ol, olivine; Ep, epidote; Rt, rutile; Opq, opaques; Symp, symplectite; Qtz, quartz; Pl, plagioclase; Kfs, K-feldspar; Srp, serpentine; Cal, calcite; Dol, dolomite

Late Proterozoic (~650-800 Ma, Rowley et al., 1997; Hacker et al., 1998) in age. The peak UHP metamorphism, which is interpreted to correspond to the final collision between the Sino-Korean and Yangtze cratons, occurred about 220-240 Ma (e.g., Liu et al., 2003; Yang et al., 2003). The amphibolite facies overprinted the earlier UHP metamorphism during late exhumation within the crust at 180-210 Ma (e.g., Hacker et al., 1998; Liu et al., 2003).

The Sulu terrane is bounded by the Qingdao-Wulian fault on the north and the Jiashan-Xiangshui fault on the south, and can be further subdivided into a northern UHP zone and a southern high-pressure (HP) zone by the Haizhou-Siyang shear zone (Figure 4.1). The terrane is characterized by dominant SE-SSE dipping foliation and SE-plunging lineation in the south, and NW-NWW dipping foliation and NW-plunging lineation in the north, indicating regional top-to-NW thrusting along a major dome-shaped shear zone under amphibolite facies conditions (Faure and Lin, 2001; Xu et al., 2004). A similar tectonic pattern was also documented in the Dabie Mountains (Hacker et al., 1998, 2000; Faure et al., 2003b). The eclogites occur as lenses, pods and layers ranging from tens of centimetres to a few kilometers in size within foliated ultramafic blocks (e.g., at Xugou, Figure 4.1), biotite paragneisses and felsic gneisses (e.g., at Maobei, Qinglongshan and Jianchang), granulites, kyanite quartzites, and marbles (e.g., at Yanmachang). The eclogite blocks, which are interpreted as tectonic boudins (Figure 4.3a), often display strong, flattened foliations and stretching lineations (Figures 4.3b-d) that are generally consistent with those of the country rocks (Figure 4.3b). Locally, the early UHP foliation is crosscut by late amphibolite facies shear zones. A granulite facies overprint on coesite-bearing eclogites was also found in the northern part of the Sulu UHP zone (Banno et al., 2000; Yao et al., 2000), while in our sampling area there is no clear evidence for the transition from eclogite to granulite facies before regional amphibolite facies metamorphism took place.

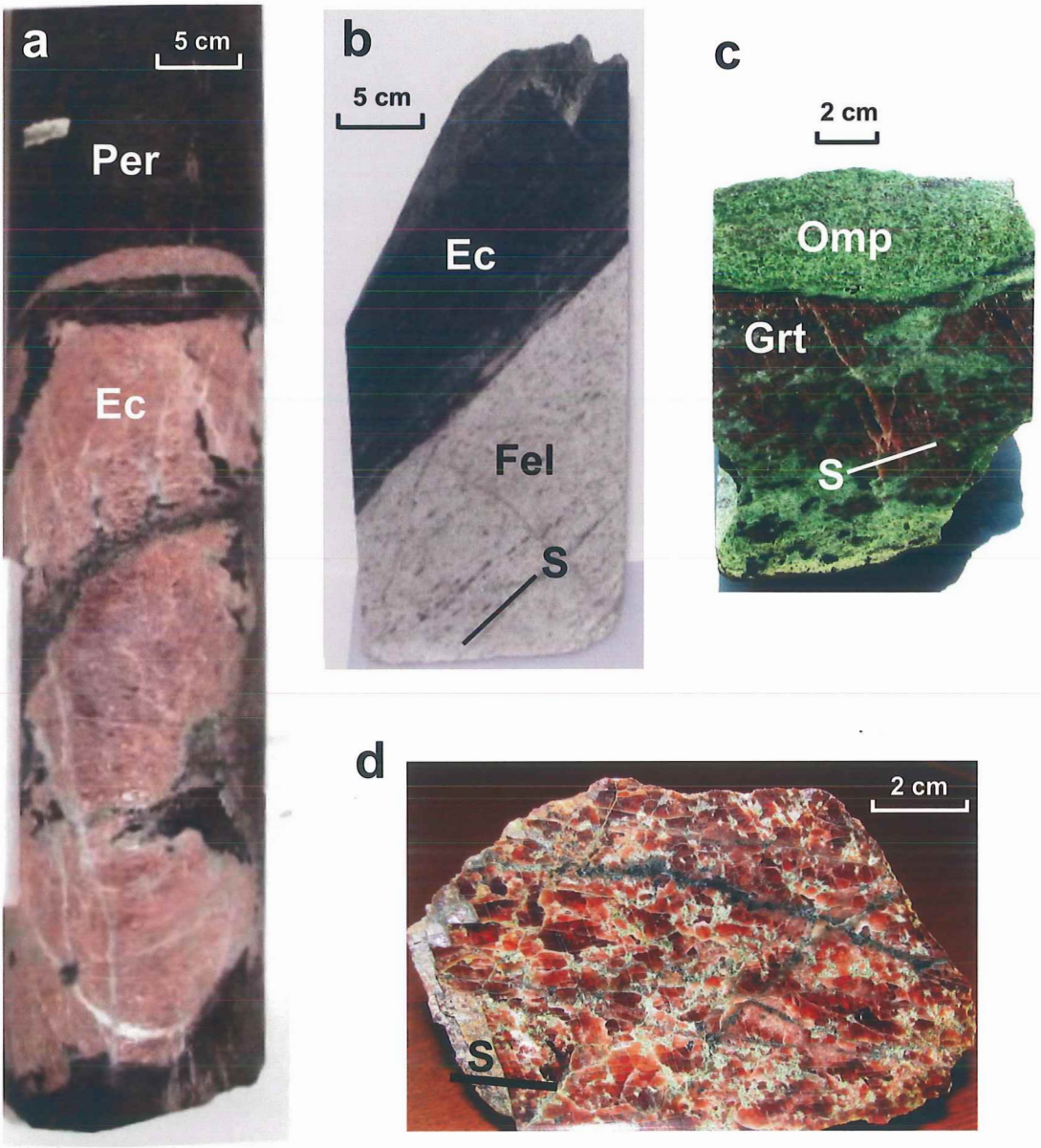


Figure 4.3 (a) Eclogite blocks in serpentinized garnet peridotite, (b) Contact between foliated, fine-grained eclogite and felsic gneiss, (c) Interlayered garnetite and omphacitite, and (d) coarse-grained eclogite. (a-b) from CCSD cores and (c-d) from surface outcrops. Foliation indicated by S. Abbreviations: Ec = eclogite, Per = peridotite, Fel = felsic gneiss, Grt = garnetite, and Omp = omphacite.

Ten of the 19 eclogites studied were collected from fresh surface outcrops in quarries at the drill site of the Chinese Continental Scientific Drilling Program (CCSD) in Maobei, Donghai County, Jiangsu Province. This drill site is located in the southern part of the Sulu UHP zone, about 30 km east of the Tan-Lu fault zone and approximately 70 km west of the Yellow sea (Figure 4.1). The CCSD drilling started in July 2001, has reached a depth of 4400 m, and is planned to reach a depth of 5000 m in the spring of 2005, penetrating through all of the high velocity layers and seismic reflectors observed within the uppermost crust on CCSD refraction and reflection surveys (Yang et al., 1999; Yang, 2002).

Two dark eclogite samples were collected from the Bixiling complex, the largest coesite-bearing mafic-ultramafic boudin (~1.5 km^2) in the Dabie Mountains (Zhang et al., 1995a). Imbedded in biotite gneisses, this boudin experienced peak UHP metamorphism at 210-220 Ma, and syn-collisional quick initial cooling (40 °C/Ma) and uplift (~10 mm/year) (Chavagnac and Jahn, 1996), which is different from the exhumation rate of the Sulu terrane (~5 mm/year) (Liu et al., 2003).

4.4 Samples and experimental technique

Table 4.1 gives the locality, lithology and modal composition of each sample studied. Three types of eclogites are distinguished according to their grain size and degree of retrograde metamorphism. Type-1 eclogites are coarse-grained eclogites with a remarkable red and green appearance due to the presence of abundant garnet and omphacite. This type of eclogite, found mainly in Maobei, Donghai County, typically displays a strong compositional banding of alternating garnet- and omphacite-rich layers (Figure 4.3c). The garnets range from 0.15 to 1.4 mm with an average grain size of 0.52 mm, while the omphacites (0.32-3.0 mm) have an average grain size of 0.93 mm (Ji et al., 2003). The typical modal composition is ~50% garnet and ~50% omphacite, with minor amounts of rutile (~1-2%), plus coesite relicts and quartz pseudomorphs after coesite

(~0.5%). The samples from garnet-rich layers, containing 80-90 vol.% garnet, are referred to as garnetites (Figure 4.3d). Type-1 eclogites were equilibrated and deformed at a peak pressure exceeding 3.2 GPa (Figure 4.4) and escaped from the later retrograde metamorphism (Ji et al., 2003).

Microcracks were characterized by optical microscopy and scanning electron microscopy (SEM) in order to assess the deformation history of the samples and the influence of cracks on the low-pressure velocity derivatives. Three types of microcracks are distinguished in Type-1 eclogites: (1) Grain boundary cracks which have a preferred orientation parallel to the foliation (Figure 4.5a). (2) Transgranular cracks that are mutually parallel within a variance of ±20°, and preferentially aligned at high angles to the foliation and lineation (Figure 4.5a). No cracks are found to offset grain boundaries, indicating that they are extensional model I fractures (Ji et al., 1997b). (3) Intragranular, radial extensional fractures around inclusions of coesite relicts and their quartz pseudomorphs in garnet and omphacite (Figure 4. 5b).

The Type-2 eclogites consist of relatively fine-grained garnet and omphacite (Figures 4.5c-d) and occur in the NE-trending, SE-dipping UHP ductile shear zones that were active during exhumation of the UHP metamorphic rocks. This type of eclogite is derived from Type-1 materials that were reworked by recrystallization-accommodated dislocation creep during the early stage of exhumation (Ji et al., 2003, Figure 4.4). Coesite relicts are only rarely observed in either garnet or omphacite from Type-2 eclogites, and quartz occurs as elongate polycrystalline aggregates along garnet/garnet, garnet/omphacite or omphacite/omphacite grain boundaries. The foliation is defined mainly by compositional layering and the lineation is defined by relict, elongate porphyroclasts of garnet and omphacite. Type-2 eclogites are characterized mainly by grain boundary cracks, some of which contain symplectites (<5%) consisting of very fine-grained amphibole, plagioclase, epidote and biotite. These crack-filling symplectites might form under the amphibolite facies conditions.

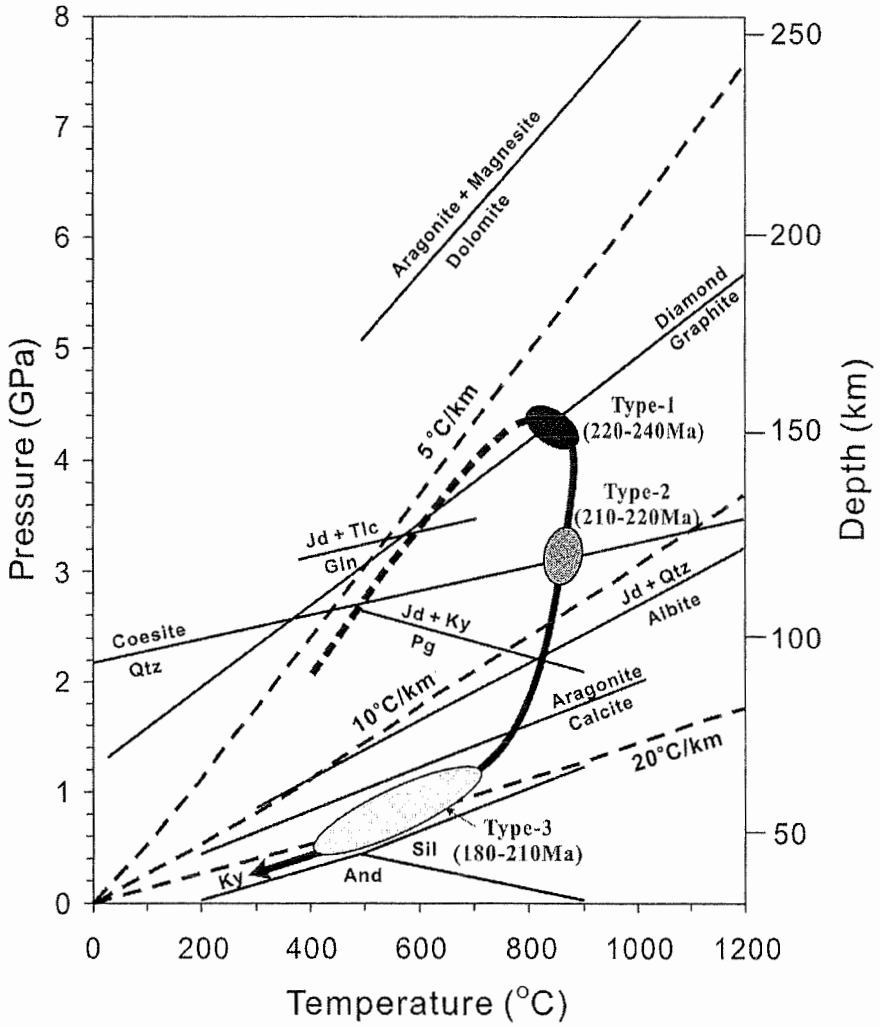


Figure 4.4 P-T-t paths of three types of Dabie-Sulu eclogites. Type-1 eclogites deformed under peak metamorphic conditions, Type-2 eclogites resulted from reworking of Type-1 eclogites along shear zones during an early stage of exhumation, and Type-3 eclogites were overprinted by extensive amphibolite facies metamorphism in the crust. Geotherms of 5°/km, 10°/km and 20°/km are indicated. Stabilities of aragonite + magnesite (Sato and Katsura, 2001), diamond (Bundy, 1980), coesite (Hemingway et al., 1998), glaucophane (Holland, 1988), jadeite + quartz (Holland, 1980), Al_2SiO_5 (Bohlen et al., 1991), paragonite (Holland, 1979), aragonite (Johannes and Puhan, 1971) are shown. The depth-pressure relation is based on an average density of 2.7 g/cm^3 for the 35-km-deep crust, and 3.3 g/cm^3 for the upper mantle. Mineral symbols: And = andalusite, Gln = glaucophane, Jd = jadeite, Ky = kyanite, Pg = paragonite, Qtz = quartz, Sil = sillimanite, Tlc = talc.

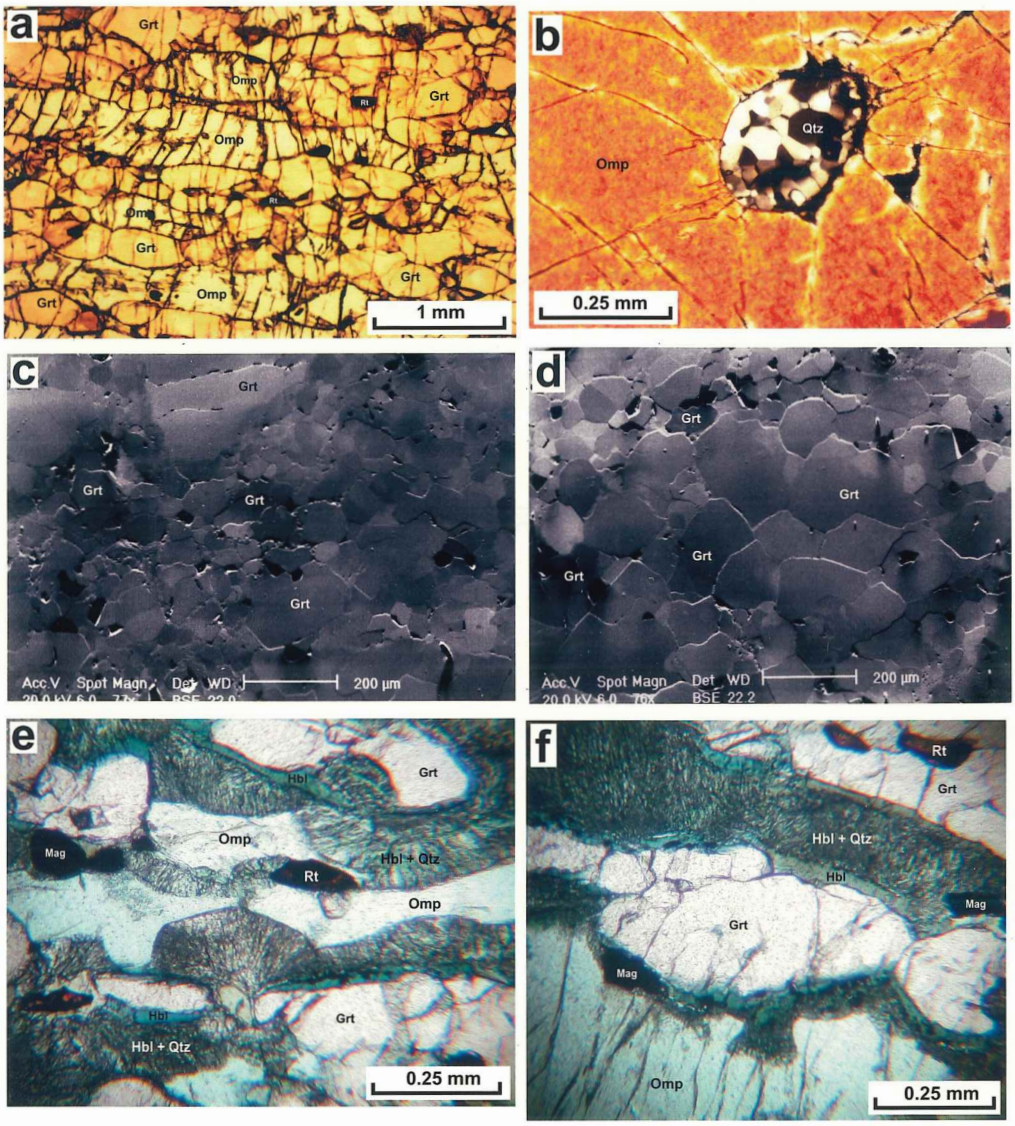


Figure 4.5 Typical microstructures of eclogites from the Sulu terrane, China. (a) Type-1 eclogite with flattened and stretched garnet and omphacite grains. (b) Radiating cracks surrounding polycrystalline quartz aggregate after a coesite inclusion in omphacite from Type-1 eclogite. (c-d) Type-2 eclogites with fine-grained recrystallized garnet and omphacite neoblasts. (e-f) Type-3 retrograded eclogites with fibrous symplectites of fine-grained hornblende, quartz and magnetite along grain boundary cracks. Mineral symbols: Grt = garnet, Hbl = hornblende, Mag = magnetite, Omp = omphacite, Qtz = quartz, Rt = rutile.

The Type-3 eclogites were overprinted by significant amphibolite facies metamorphism during a late stage of exhumation within the crust (Figure 4.4). These eclogites are composed of garnet and omphacite that have been extensively replaced by symplectitic assemblages of amphibole, quartz and plagioclase, with variable amount of phengite, kyanite, rutile and epidote (Figures 4.5e-f). Fine-grained quartz and amphibole are important phases in these strongly retrograde rocks. Quartz-filled tensional veins occur occasionally in Type-3 eclogites (e.g., sample JC1). The stretching lineation, which formed during the amphibolite facies overprint, is defined by elongate amphibole, epidote, phengite and relict garnet and omphacite. Both transgranular and grain boundary cracks occur in Type-3 eclogites (Figures 4.5e-f).

Table 4.2 lists the results of chemical analyses and the calculated mean atomic weight ($\overline{m}$) for each sample. Except for granitic gneisses (TF1, TF2 and TF3) and dolomitic marbles (YM1 and YM2), the SiO_2 content of the rocks falls in the composition range for mafic-ultramafic rocks. The values of $\overline{m}$ for the Sulu eclogites range from 21.48 to 21.93, with an average of 21.64. Type-1 eclogites have significantly higher contents of Al_2O_3 and MgO, but lower contents of SiO_2 and Na_2O than Type-2 and Type-3 eclogites (Figure 4.6). Interestingly, the Al_2O_3 or MgO content decreases almost linearly with increasing content of SiO_2 or Na_2O. This implies that the relatively mobile components were added to the reworked eclogites by ascending fluids during the early stage of exhumation along shear zones (Ji et al., 2003). In contrast, the dark eclogites from Bixiling (samples 98401 and 98501) show high $\overline{m}$ values (~22.28) and a distinct chemical composition with low SiO_2, high $FeO+Fe_2O_3$ and high TiO_2, suggesting a cumulate origin. However, the chemical compositions of three Bixiling eclogites measured by Kern et al. (1999) fall in the range of the Sulu Type-2 eclogites, probably because they were derived from similar protoliths.

Table 4.2 Chemical composition (wt.%) and mean atomic weight of samples

Sample	SiO_2	TiO_2	Al_2O_3	Fe_2O_3	FeO	MnO	MgO	CaO	Na_2O	K_2O	P_2O_5	Cr_2O_3	LOI	CO_2	Total	$\overline{m}$
Coarse-grained eclogite																
86351	45.19	0.40	20.00	4.47	4.63	0.15	10.88	10.21	1.76	0.13	0.53	0.039	0.15	1.40	99.94	21.49
MB22*	41.84	0.06	22.28	11.77		0.18	14.58	9.45	0.57	0.02	0.03	0.015	0.10		100.89	21.68
MB23*	44.75	0.23	21.92	9.69		0.15	9.39	11.82	1.95	0.12	0.02	0.031	0.34		100.41	21.67
MB25*	44.86	0.42	20.33	9.82		0.14	10.87	12.14	2.01	0.07	0.02	0.022	0.12		100.83	21.71
MB26*	42.91	0.37	22.11	11.29		0.17	11.02	11.56	1.13	0.10	0.03	0.016	0.11		100.81	21.80
MB27*	46.65	0.49	18.53	8.19		0.11	10.73	12.60	2.66	0.16	0.02	0.039	0.20		100.39	21.61
MB30*	42.70	0.09	21.95	9.56		0.14	13.16	11.92	0.87	0.02	0.03	0.007	0.32		100.77	21.64
Coarse-grained garnetite																
MB2B	44.34	0.17	21.13	4.54	3.71	0.13	12.14	11.35	1.20	0.01	0.10	0.001	0.29	0.70	99.81	21.51
MB34*	42.94	0.27	21.08	10.42		0.17	13.61	10.71	0.96	0.02	0.02	0.060	0.18		100.44	21.66
MB62*	43.51	0.06	22.01	9.02		0.13	12.86	11.57	1.21	0.05	0.03	0.005	0.21		100.66	21.58
Fine-grained eclogite																
DG1	50.52	0.67	16.08	9.20	4.07	0.24	4.43	9.07	4.32	0.03	0.73	0.001	0.15	0.45	99.96	21.86
JC2	54.54	0.93	16.03	8.04	2.96	0.27	3.74	7.08	4.22	0.01	1.33	0.011	0.45	0.20	99.81	21.54
JZ1	51.58	0.17	15.83	6.82	4.70	0.15	6.74	9.35	3.06	0.23	0.08	0.042	0.25	0.75	99.75	21.68
SB1	48.99	0.43	18.22	8.63	1.60	0.18	4.99	9.83	3.27	0.02	0.47	0.046	2.16	0.75	99.59	21.48
Retrograde eclogite																
98401	44.59	1.53	16.94	10.07	5.62	0.22	4.73	11.19	3.13	0.21	0.70	0.003	0.10	0.90	99.93	22.28
98501	44.40	1.57	17.10	10.01	5.72	0.22	4.62	11.16	3.18	0.17	0.70	0.003	0.11	0.85	99.81	22.29
JC1	50.20	0.73	16.07	11.04	2.85	0.28	3.88	9.60	2.84	0.01	1.50	0.001	0.20	0.50	99.70	21.93
QL2	49.64	0.43	17.97	6.65	3.55	0.11	5.44	9.37	3.78	0.63	0.43	0.007	0.80	0.85	99.66	21.57
QL3	49.41	0.37	17.61	6.99	3.80	0.13	5.49	9.41	3.71	0.65	0.47	0.007	0.70	0.90	99.65	21.63
Amphibolite																
QL4	48.61	0.40	19.77	5.93	3.43	0.14	5.75	9.90	3.02	0.27	0.50	0.007	1.30	0.70	99.73	21.50
QL5	51.73	1.97	17.07	9.05	1.90	0.24	3.47	6.04	4.17	1.25	0.73	0.006	2.10	0.20	99.93	21.54
YM4	48.70	1.20	17.20	3.33	4.86	0.14	7.45	11.43	2.31	0.29	0.34	0.047	1.05	1.44	99.79	21.51
Granitic gneiss																
TF-1*	77.49	0.14	10.61	2.83		0.10	0.20	0.26	4.94	2.89	0.01	0.004	0.36		99.83	20.55
TF-2*	75.58	0.15	11.78	2.78		0.08	0.18	0.17	4.91	3.97	0.02	0.002	0.36		99.98	20.63
TF-3*	76.38	0.15	11.34	2.45		0.05	0.14	0.10	4.34	4.50	0.02	0.003	0.34		99.81	20.63
Serpentinite																
XG1	37.58	0.13	2.08	4.48	1.43	0.08	37.12	0.37	0.15	0.10	0.03	0.056	15.90		99.51	20.02
XG3	37.33	0.30	1.80	4.57	1.70	0.08	37.97	0.47	0.09	0.04	0.08	0.054	15.22		99.70	20.09
Marble																
YM1	4.94	0.30	0.25	0.27	0.05	0.01	18.74	29.55	0.14	0.01	0.08	0.001	2.77	42.30	99.41	18.68
YM2	7.33	0.03	0.23	0.33	0.07	0.05	19.62	31.08	0.11	0.01	0.03	0.001	1.00	40.05	99.94	18.96

Abbreviations: $\overline{m}$, mean atomic weight; LOI, loss on ignition.

*Total iron, presented as Fe_2O_3, was measured in Geochemical Laboratories, Earth and Planetary Sciences, McGill University.

Others were analyzed at the Guangzhou Institute of Geochemistry, Chinese Academy of Sciences.

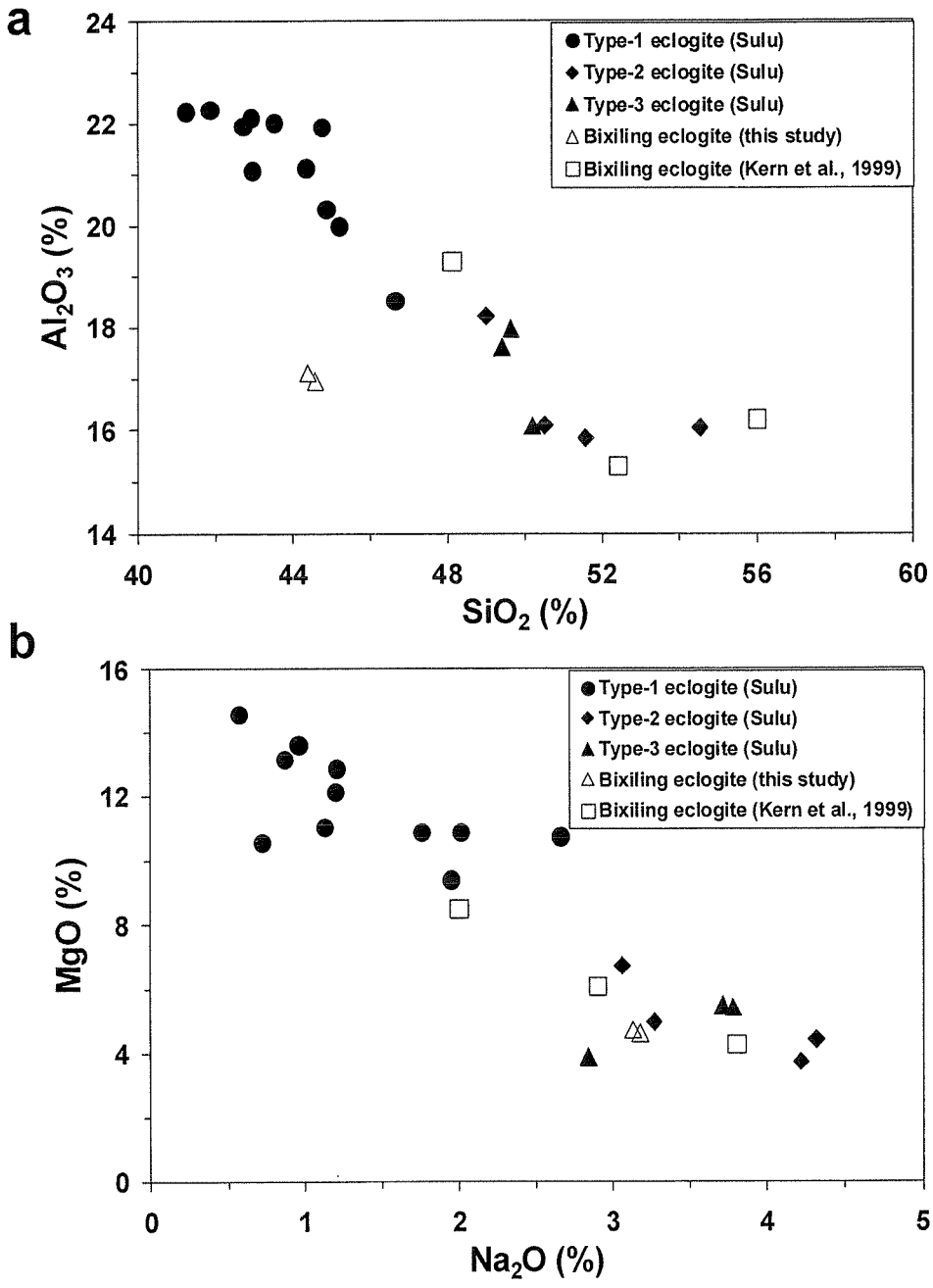


Figure 4.6 Relationships between major oxides (weight percent) of the Dabie-Sulu eclogites. (a) Al_2O_3 versus SiO_2 and (b) MgO versus Na_2O.

Measurements of *Vp* were performed at confining pressure ranging from 10 to 800 MPa for the UHP eclogites and 10 to 600 MPa for their host rocks using the pulse transmission technique (Birch, 1960; Christensen, 1974). In many instances, the velocities could be extrapolated to higher pressure since $\Delta Vp/\Delta P$ became constant at high pressure. For most of the samples, three cylindrical mini-cores, 2.54 cm in diameter and 3-5 cm in length, were cut in orthogonal directions to study anisotropy, with the X direction parallel to the stretching lineation, the Y direction perpendicular to lineation and parallel to foliation, and the Z direction normal to foliation. For small samples, only one or two directions were taken.

The *Vp* measurements were made on jacketed samples under hydrostatic conditions at the GSC/Dalhousie High Pressure Laboratory in Halifax, Nova Scotia (Ji et al., 1993; Salisbury and Fountain, 1994; Ji et al., 1997a). The principle vessel is a seven-ton, double-walled steel vessel with a 40 cm long × 10 cm diameter working chamber, which can operate to a pressure of 1.4 GPa. The pressure medium consists of light hydraulic oil pumped into the working chamber by means of a two-stage intensifier. 1 MHz lead zirconate transducers mounted on backup electrodes were used to send and receive acoustic waves through the samples. To prevent the pressure medium from invading the sample during the pressure run, the mini cores were sheathed in thin copper foil and the entire sample/transducer/electrode assembly was enclosed in neoprene tubing. Once the sample assembly was sealed in the pressure vessel and the pressure was raised, a high voltage spike from a pulse generator excited the sending transducer and the time of flight to the receiving transducer was measured using a digital oscilloscope. The accuracy is estimated to be 0.5% for *Vp*. The densities of the samples (Table 4.3) were determined using the immersion method with an accuracy of ±0.005 g/cm^3 at room conditions.

Table 4.3 *Vp* (km/s), anisotropy (%) and densities at various confining pressures of UHP rocks from the Dabie-Sulu belt

Lithology / Sample	λ	ρ (g/cm³)	Pressure (MPa)											
			20	50	80	100	150	200	250	300	400	500	600	800
Coarse-grained eclogite														
86351	X	3.51		8.19	8.37	8.45	8.56	8.62	8.66	8.69	8.72	8.74	8.76	8.79
	Z	3.50		7.69	7.91	8.01	8.12	8.16	8.19	8.22	8.24	8.26	8.28	8.30
	M	3.49		8.02	8.21	8.30	8.41	8.46	8.50	8.53	8.56	8.58	8.60	8.62
	A			6.18	5.60	5.35	5.27	5.47	5.54	5.52	5.50	5.59	5.55	5.65
MB22	X	3.55	7.36	7.63	7.81	7.89	7.99	8.06	8.11	8.15	8.20	8.24	8.27	8.30
MB23	X	3.55		7.98	8.23	8.34	8.46	8.51	8.55	8.59	8.62	8.64	8.65	8.67
	Y	3.49		7.50	7.83	7.95	8.08	8.18	8.27	8.33	8.40	8.45	8.47	8.49
	Z	3.49	7.56	7.92	8.07	8.12	8.20	8.28	8.33	8.37	8.41	8.44	8.46	8.49
	M	3.51		7.80	8.04	8.14	8.25	8.32	8.38	8.43	8.48	8.51	8.53	8.55
	A			6.23	5.05	4.84	4.56	3.92	3.41	3.06	2.55	2.41	2.28	2.18
MB25	X	3.56	7.00	7.50	7.80	7.89	7.99	8.04	8.09	8.12	8.18	8.22	8.25	8.28
	Y	3.59	6.88	7.43	7.80	7.95	8.10	8.19	8.27	8.33	8.39	8.43	8.47	8.50
	Z	3.62	7.51	8.03	8.26	8.32	8.41	8.46	8.52	8.56	8.60	8.62	8.64	8.68
	M	3.59	7.13	7.65	7.95	8.05	8.17	8.23	8.29	8.33	8.39	8.42	8.45	8.49
	A		8.77	7.84	5.85	5.32	5.09	5.13	5.17	5.22	4.97	4.76	4.58	4.64
MB26	X	3.59	7.77	7.98	8.12	8.19	8.28	8.35	8.40	8.44	8.50	8.55	8.56	8.59
	Y	3.52	7.58	7.84	8.03	8.12	8.27	8.36	8.42	8.47	8.51	8.53	8.55	8.58
	Z	3.58	7.92	8.10	8.25	8.32	8.44	8.50	8.54	8.56	8.60	8.62	8.64	8.67
	M	3.56	7.76	7.98	8.14	8.21	8.33	8.40	8.45	8.49	8.54	8.57	8.58	8.61
	A		4.31	3.26	2.65	2.44	2.03	1.82	1.64	1.47	1.18	1.04	1.05	1.02
MB27	X	3.56	7.68	8.00	8.19	8.25	8.32	8.35	8.39	8.42	8.46	8.49	8.51	8.54
	Y	3.61	7.37	7.96	8.18	8.22	8.32	8.38	8.44	8.48	8.52	8.55	8.56	8.58
	Z	3.58	7.51	7.93	8.13	8.19	8.25	8.29	8.33	8.36	8.42	8.45	8.47	8.50
	M	3.58	7.52	7.96	8.17	8.22	8.30	8.34	8.38	8.42	8.47	8.50	8.51	8.54
	A		4.14	0.97	0.75	0.75	0.81	1.05	1.29	1.41	1.26	1.11	0.98	0.96
MB30	X	3.57	7.78	7.99	8.09	8.14	8.24	8.31	8.35	8.39	8.44	8.47	8.48	8.50
	Z	3.63	7.27	7.72	7.84	7.89	7.97	8.05	8.10	8.15	8.19	8.22	8.23	8.27
	M	3.59	7.61	7.90	8.01	8.06	8.15	8.22	8.27	8.31	8.36	8.39	8.40	8.42
	A		6.70	3.42	3.21	3.13	3.26	3.10	2.96	2.87	2.99	2.97	2.91	2.77
Coarse-grained garnetite														
MB2B	X	3.61	7.77	8.01	8.19	8.28	8.39	8.45	8.51	8.55	8.59	8.61	8.63	8.64
MB34	X	3.63	7.94	8.25	8.32	8.36	8.43	8.47	8.49	8.51	8.55	8.58	8.60	8.62
	Z	3.65	7.57	7.80	8.02	8.09	8.23	8.34	8.41	8.47	8.53	8.55	8.57	8.60
	M	3.64	7.82	8.10	8.22	8.27	8.36	8.42	8.47	8.50	8.54	8.57	8.59	8.61
	A		4.74	5.55	3.75	3.22	2.30	1.51	0.94	0.48	0.21	0.30	0.28	0.24
MB62	X	3.56	7.20	7.69	7.97	8.06	8.16	8.24	8.31	8.38	8.46	8.50	8.52	8.54

Table 4.3 (continued)

Lithology / Sample	λ	ρ (g/cm³)	Pressure (MPa)											
			20	50	80	100	150	200	250	300	400	500	600	800
Fine-grained eclogite														
DG1	X	3.48	7.47	7.65	7.79	7.85	7.91	7.94	7.98	8.00	8.04	8.05	8.07	8.09
	Y	3.45	7.10	7.33	7.51	7.60	7.71	7.77	7.82	7.86	7.93	7.98	8.00	8.04
	Z	3.46	7.03	7.31	7.43	7.48	7.55	7.61	7.65	7.70	7.73	7.75	7.76	7.79
	M	3.46	7.20	7.43	7.57	7.64	7.73	7.78	7.82	7.85	7.90	7.93	7.94	7.97
	A		6.05	4.55	4.77	4.75	4.65	4.30	4.13	3.90	3.86	3.82	3.83	3.80
JC2	X	3.40	6.77	6.98	7.15	7.24	7.40	7.51	7.60	7.65	7.69	7.72	7.74	7.76
	Y	3.38	6.87	7.17	7.34	7.41	7.50	7.56	7.61	7.65	7.68	7.71	7.72	7.74
	Z	3.41	7.04	7.24	7.39	7.45	7.54	7.59	7.62	7.64	7.65	7.67	7.68	7.70
	M	3.40	6.89	7.13	7.29	7.37	7.48	7.55	7.61	7.64	7.67	7.70	7.71	7.73
	A		3.84	3.70	3.24	2.82	1.89	0.98	0.26	0.17	0.53	0.66	0.70	0.72
JZ1	Z	3.53		7.05	7.13	7.18	7.30	7.41	7.51	7.59	7.72	7.79	7.83	7.87
SB1	X	3.36	7.24	7.48	7.61	7.67	7.78	7.86	7.94	8.00	8.07	8.11	8.14	8.18
	Y	3.34	7.32	7.52	7.63	7.68	7.78	7.84	7.90	7.94	8.00	8.02	8.05	8.07
	Z	3.40	7.30	7.57	7.70	7.76	7.85	7.88	7.91	7.95	8.01	8.06	8.08	8.11
	M	3.37	7.29	7.53	7.65	7.70	7.80	7.86	7.91	7.96	8.02	8.07	8.09	8.12
	A		1.13	1.17	1.06	1.12	0.88	0.57	0.51	0.74	0.91	1.10	1.15	1.37
Retrograde eclogite														
98401	X	3.47	6.91	7.19	7.40	7.48	7.57	7.61	7.64	7.66	7.68	7.71	7.72	7.73
	Y	3.49	7.01	7.23	7.39	7.46	7.54	7.59	7.62	7.64	7.67	7.69	7.71	7.74
	M	3.48	6.96	7.21	7.39	7.47	7.56	7.60	7.63	7.65	7.68	7.70	7.71	7.73
	A		1.32	0.60	0.07	0.21	0.36	0.38	0.22	0.22	0.14	0.17	0.05	0.06
98501	X	3.49	7.25	7.50	7.58	7.61	7.67	7.72	7.76	7.79	7.83	7.86	7.87	7.90
	Y	3.46	6.99	7.14	7.24	7.28	7.36	7.44	7.48	7.52	7.56	7.57	7.59	7.61
	Z	3.47	6.18	6.36	6.49	6.54	6.60	6.62	6.65	6.66	6.69	6.71	6.72	6.74
	M	3.47	6.81	7.00	7.10	7.15	7.21	7.26	7.29	7.32	7.36	7.38	7.40	7.42
	A		15.66	16.28	15.37	15.02	14.91	15.10	15.24	15.42	15.51	15.56	15.55	15.57
JC1	X	3.49	6.09	6.30	6.44	6.50	6.57	6.61	6.63	6.65	6.68	6.70	6.71	6.74
	Y	3.41	6.39	6.62	6.76	6.82	6.91	6.98	7.04	7.07	7.10	7.12	7.13	7.15
	Z	3.36	6.74	7.00	7.15	7.20	7.25	7.29	7.32	7.35	7.39	7.42	7.44	7.47
	M	3.42	6.41	6.64	6.78	6.84	6.91	6.96	6.99	7.02	7.05	7.08	7.09	7.12
	A		10.16	10.49	10.47	10.29	9.87	9.79	9.88	9.99	10.05	10.14	10.31	10.26
QL2	X	3.41	6.18	6.71	7.03	7.17	7.38	7.49	7.58	7.66	7.80	7.89	7.95	8.01
	Y	3.42	5.83	6.12	6.39	6.54	6.81	6.97	7.08	7.17	7.34	7.45	7.50	7.54
	Z	3.43	5.47	5.75	5.94	6.03	6.18	6.29	6.37	6.42	6.53	6.59	6.65	6.71
	M	3.42	5.83	6.19	6.45	6.58	6.79	6.91	7.01	7.08	7.22	7.31	7.36	7.42
	A		12.22	15.53	16.80	17.38	17.63	17.30	17.30	17.46	17.61	17.78	17.65	17.61
QL3	X	3.43	6.39	6.79	7.02	7.14	7.29	7.42	7.52	7.59	7.71	7.76	7.82	7.88
	Z	3.43	5.74	6.16	6.46	6.60	6.87	7.02	7.12	7.23	7.37	7.46	7.52	7.59
	M	3.43	6.17	6.58	6.84	6.96	7.15	7.28	7.38	7.47	7.60	7.66	7.72	7.79
	A		10.53	9.48	8.22	7.87	5.85	5.52	5.43	4.86	4.42	3.97	3.90	3.80

Table 4.3 (continued)

Lithology / Sample	λ	ρ (g/cm³)	Pressure (MPa) 20	50	80	100	150	200	250	300	400	500	600	800
Amphibolite														
QL4	X	2.96	5.37	5.71	5.90	5.99	6.18	6.27	6.35	6.42	6.52	6.59	6.64	*6.72*
	Y	2.97	4.91	5.39	5.69	5.81	6.01	6.14	6.24	6.32	6.45	6.54	6.59	*6.64*
	Z	2.97	4.92	5.35	5.58	5.66	5.87	6.01	6.08	6.16	6.30	6.36	6.43	*6.53*
	M	2.96	5.07	5.48	5.72	5.82	6.02	6.14	6.23	6.30	6.42	6.50	6.55	*6.63*
	A		9.06	6.55	5.68	5.79	5.20	4.37	4.37	4.06	3.46	3.46	3.19	*2.88*
QL5	X	2.98	6.04	6.28	6.40	6.43	6.48	6.52	6.56	6.58	6.62	6.65	6.67	*6.72*
	Y	2.95	5.69	5.94	6.09	6.14	6.21	6.27	6.31	6.34	6.38	6.41	6.43	*6.49*
	Z	2.94	4.55	4.89	5.11	5.20	5.34	5.41	5.46	5.51	5.55	5.59	5.61	*5.68*
	M	2.96	5.43	5.70	5.87	5.92	6.01	6.06	6.11	6.14	6.18	6.21	6.24	*6.30*
	A		27.43	24.40	22.04	20.76	18.97	18.40	17.97	17.56	17.24	17.04	16.90	*16.52*
YM4	X	3.09	6.99	7.05	7.11	7.15	7.21	7.25	7.27	7.28	7.30	7.32	7.33	*7.35*
	Y	3.04	6.55	6.67	6.77	6.82	6.91	6.97	7.01	7.04	7.08	7.10	7.12	*7.17*
	Z	3.09	6.55	6.66	6.74	6.79	6.86	6.90	6.93	6.96	7.01	7.04	7.06	*7.11*
	M	3.07	6.70	6.79	6.88	6.92	6.99	7.04	7.07	7.09	7.13	7.15	7.17	*7.19*
	A		6.59	5.84	5.38	5.22	5.05	4.95	4.75	4.52	4.19	3.98	3.78	*3.56*
Granitic gneiss														
TF1	X	2.66	5.51	5.69	5.81	5.87	5.96	6.02	6.07	6.10	6.14	6.16	6.17	*6.21*
	Y	2.68	5.36	5.60	5.75	5.80	5.89	5.96	6.01	6.06	6.12	6.17	6.19	*6.25*
	Z	2.66	5.46	5.73	5.91	5.98	6.05	6.09	6.12	6.15	6.20	6.23	6.25	*6.31*
	M	2.66	5.44	5.67	5.82	5.88	5.97	6.02	6.07	6.10	6.15	6.19	6.21	*6.25*
	A		2.81	2.20	2.88	3.04	2.61	2.18	1.81	1.52	1.32	1.13	1.27	*1.52*
TF2	X	2.65	5.01	5.29	5.50	5.59	5.71	5.81	5.87	5.92	5.99	6.04	6.07	*6.14*
	Y	2.65	5.18	5.41	5.56	5.63	5.74	5.81	5.86	5.90	5.97	6.01	6.03	*6.07*
	Z	2.65	4.98	5.27	5.42	5.50	5.62	5.72	5.78	5.82	5.89	5.93	5.96	*6.03*
	M	2.65	5.05	5.32	5.49	5.57	5.69	5.78	5.84	5.88	5.95	5.99	6.02	*6.08*
	A		4.00	2.63	2.55	2.40	2.11	1.64	1.59	1.67	1.77	1.85	1.86	*1.86*
TF3	X	2.66	5.50	5.87	6.02	6.07	6.15	6.20	6.24	6.27	6.31	6.35	6.37	*6.42*
	Y	2.66	5.33	5.63	5.80	5.85	5.93	5.98	6.02	6.04	6.08	6.11	6.14	*6.18*
	Z	2.66	5.31	5.61	5.79	5.85	5.95	6.02	6.08	6.12	6.18	6.21	6.22	*6.25*
	M	2.66	5.38	5.70	5.87	5.92	6.01	6.07	6.11	6.15	6.19	6.22	6.24	6.28
	A		3.47	4.58	3.83	3.65	3.71	3.62	3.62	3.68	3.77	3.74	3.75	*3.84*
Serpentinite														
XG1	X	2.54	5.03	5.24	5.33	5.37	5.45	5.51	5.56	5.60	5.65	5.69	5.72	*5.78*
	Y	2.56	4.49	4.69	4.80	4.85	4.93	4.98	5.02	5.05	5.09	5.12	5.14	*5.20*
	Z	2.55	4.20	4.43	4.58	4.64	4.71	4.77	4.81	4.85	4.92	4.96	4.99	*5.06*
	M	2.55	4.58	4.79	4.90	4.95	5.03	5.08	5.13	5.17	5.22	5.26	5.28	*5.35*
	A		18.14	16.87	15.25	14.64	14.66	14.65	14.54	14.40	14.16	14.02	13.76	*13.30*
XG3	X	2.66	5.27	5.36	5.43	5.47	5.54	5.59	5.62	5.64	5.68	5.71	5.72	*5.77*

Table 4.3 (continued)

Lithology / Sample	λ	ρ (g/cm³)	Pressure (MPa)											
			20	50	80	100	150	200	250	300	400	500	600	800
Marble														
YM1	X	2.86	6.42	6.70	6.87	6.94	7.02	7.05	7.08	7.11	7.17	7.20	7.23	*7.28*
	Y	2.87	6.09	6.35	6.53	6.58	6.64	6.67	6.69	6.70	6.74	6.76	6.78	*6.84*
	Z	2.86	6.02	6.30	6.51	6.56	6.61	6.64	6.66	6.68	6.70	6.73	6.75	*6.79*
	M	2.86	6.18	6.45	6.63	6.69	6.76	6.79	6.81	6.83	6.87	6.90	6.92	*6.97*
	A		6.43	6.09	5.43	5.62	6.01	6.00	6.11	6.37	6.73	6.83	6.94	*7.06*
YM2	X	2.87	6.32	6.51	6.73	6.86	7.05	7.14	7.21	7.27	7.32	7.36	7.38	*7.43*
	Y	2.87		5.80	6.04	6.17	6.33	6.42	6.51	6.59	6.68	6.72	6.76	*6.83*
	Z	2.87		6.05	6.21	6.30	6.44	6.52	6.58	6.63	6.68	6.71	6.74	*6.80*
	M	2.87		6.12	6.33	6.44	6.61	6.70	6.77	6.83	6.89	6.93	6.96	*7.02*
	A			11.68	10.81	10.73	10.96	10.77	10.40	9.96	9.30	9.28	9.19	*9.09*

Abbreviations: λ, direction of wave propagation; ρ, density; M, mean; A, anisotropy. Values in italics are extrapolated.

4.5 Experimental results

4.5.1 Vp data

The P-wave velocities, anisotropy and densities of the samples are given at various confining pressures and room temperature in Table 4.3. All reported data were measured during decompression. No correction for the change of length of the specimens under pressure was applied to the *Vp* values because the greatest correction would be only about 1% at 1000 MPa (Birch, 1960). Figure 4.7 illustrates typical *Vp* versus pressure curves for the three types of eclogites from the Sulu UHP belt, with sample MB27 representing the Type-1, DG1 representing Type-2 and QL2 representing Type-3 eclogites. The curves display a rapid nonlinear increase in *Vp* at low pressures, followed by a gradual linear increase at high pressures.

As shown in Figure 4.8, the Type-1 eclogites have the highest *Vp* and density while the Type-2 and Type-3 eclogites have successively lower velocities and densities, indicating that retrograde metamorphism can significantly decrease both *Vp* and density

in eclogites. The differences among the three types of eclogites are even more pronounced at high pressures where the effect of microcracks is eliminated. For instance, at 600 MPa, the average *Vp* decreases from 8.51 km/s for Type-1 eclogites, to 7.89 km/s for Type-2 eclogites and then to 7.46 km/s for Type-3 eclogites (Figure 4.8b). For eclogites from the Dabie-Sulu belt, the relationship between *Vp* and density is best fit by $Vp = -4.754 + 3.502\rho$ at 50 MPa (Figure 4.8a) and $Vp = -2.747 + 3.095\rho$ at 600 MPa (Figure 4.8b), respectively. The decrease in *Vp* from Type-1 to Type-3 eclogites is mainly due to a decrease in garnet content (Table 4.1, Figure 4.9a) and to an increase in the volume fractions of retrograde materials such as amphibole, mica, zoisite and quartz (Figure 4.9b). *Vp* also tends to decrease with increasing SiO_2 content for both UHP (Type-1 and Type-2) and retrograde eclogites (Figure 4.10).

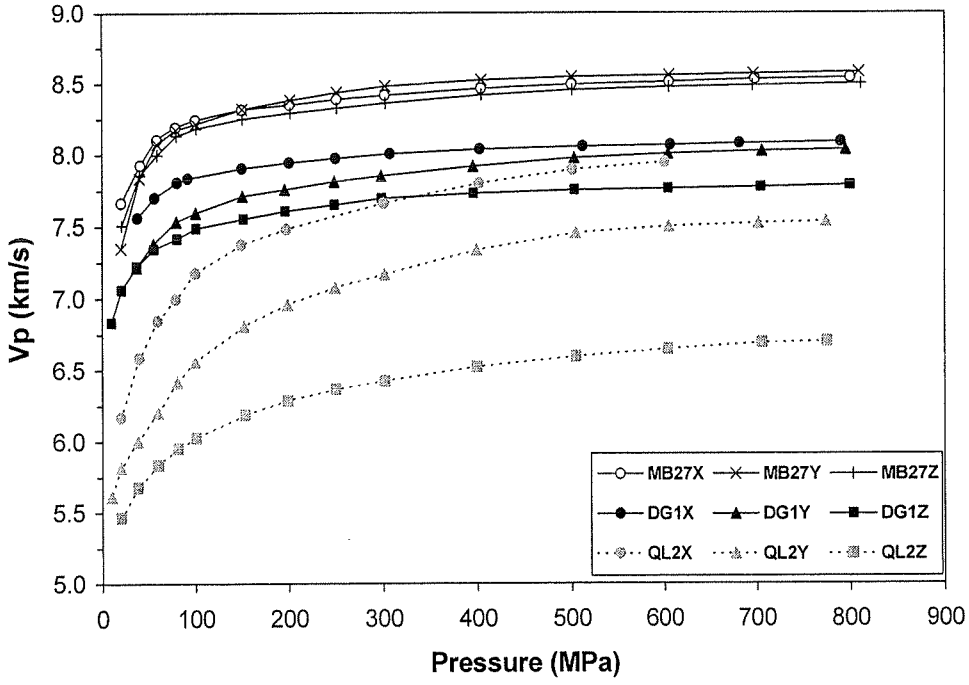


Figure 4.7 P-wave velocities versus pressure in the X, Y and Z directions for three typical eclogite samples (MB27: Type-1 eclogite; DG1: Type-2 eclogite; QL2: Type-3 eclogite) from the Sulu UHP zone.

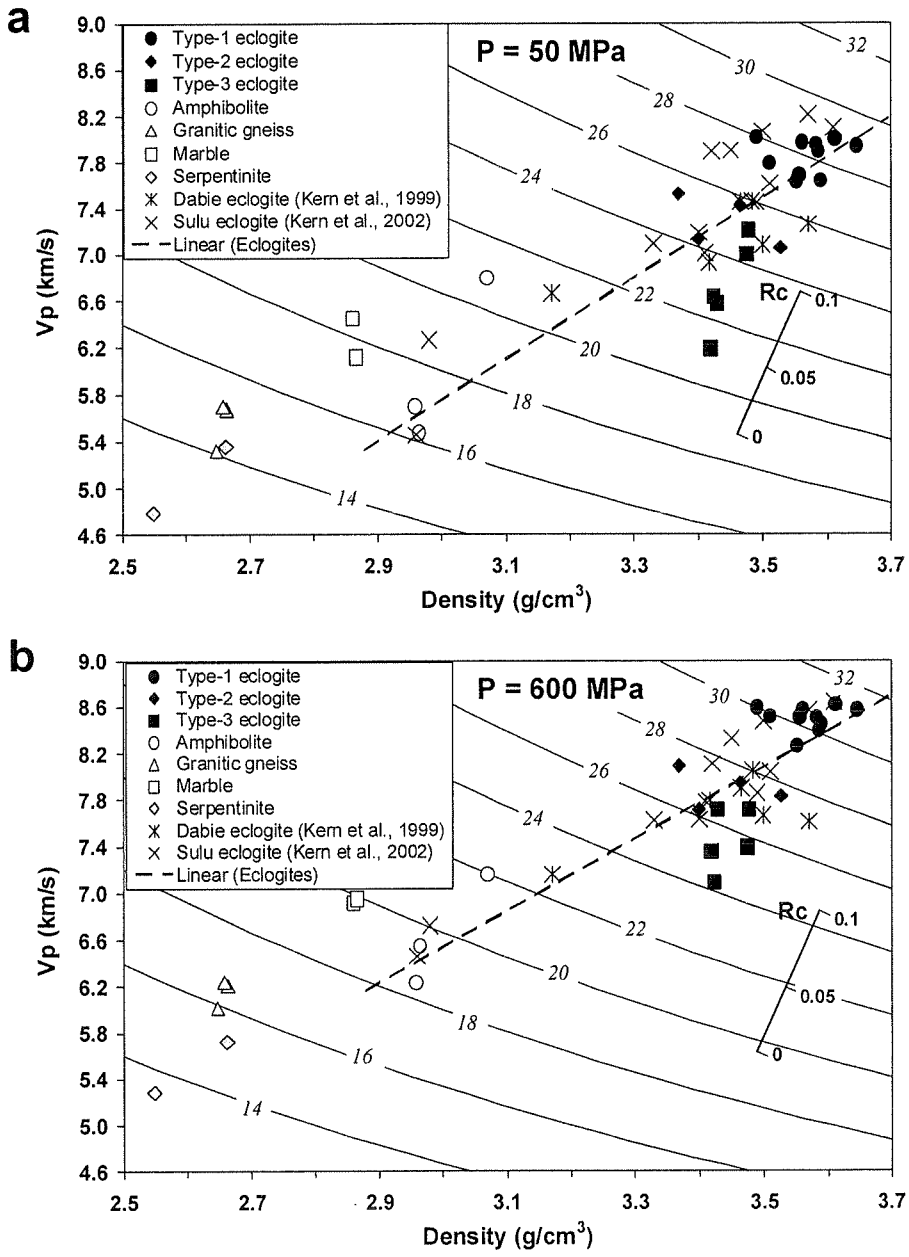


Figure 4.8 Mean P-wave velocities versus densities at 50 MPa (a) and 600 MPa (b) for Dabie-Sulu samples. The dashed line is the best-fit solution for *Vp*-density relationship of eclogites from this study and Kern et al. (1999, 2002). Also shown are lines of constant acoustic impedance and a floating reflection coefficient (Rc) scale; a coefficient of 0.06 will give a strong reflection in the crust but higher values are required in the upper mantle.

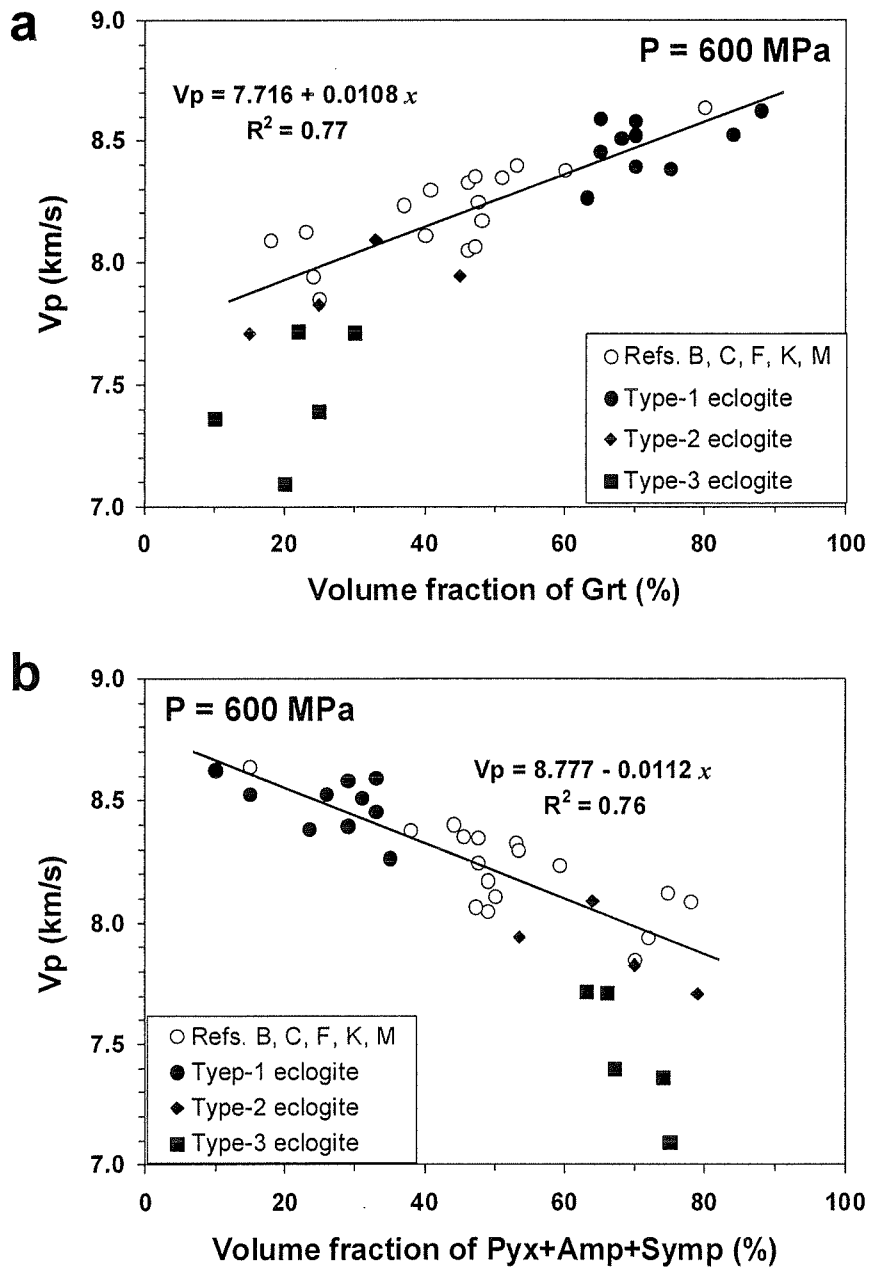


Figure 4.9 Variations of eclogite P-wave velocity at 600 MPa as a function of (a) garnet (Grt) content and (b) the volume fraction of pyroxene (Pyx), amphibole (Amp) and symplectite (Symp). Unaltered eclogites from references are also plotted. Abbreviations for references: B – Birch (1960), C – Christensen (1974), F – Fountain et al. (1994), K – Kern et al. (1999, 2002), M – Manghnani et al. (1974). Solid line is the least squares fit to data, excluding Type-3 eclogites.

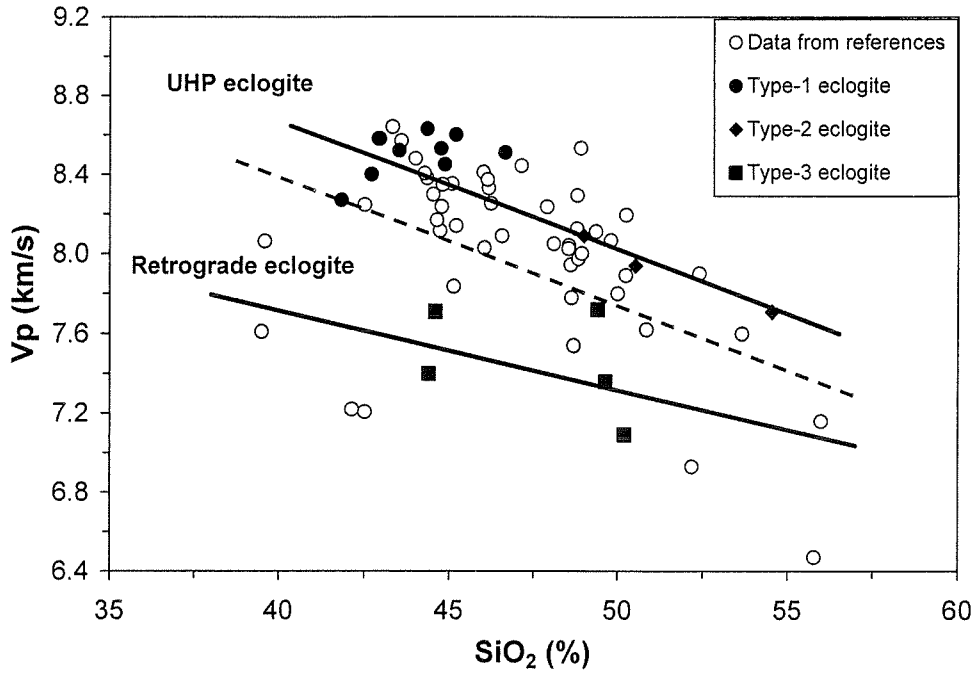


Figure 4.10 Mean P-wave velocities of eclogites at 600 MPa versus silica content. Data from this study and references: Birch (1960), Manghnani et al. (1974), Kern and Richter (1981), Kern and Tubia (1993), Fountain et al. (1994), Kern et al. (1999, 2002), Gao et al. (2001). The dashed line separates data of UHP eclogites (Type-1 and Type-2) and those of retrograde eclogites (Type-3), while solid lines represent the least squares fit to data of the two groups, respectively.

4.5.2 Vp anisotropy

Birch (1960) defined the P-wave anisotropy (A) as

$$A = (V_{\max} - V_{\min})/V_m \times 100\% \qquad (4.1)$$

where V_m is the arithmetic mean of the velocities measured from the three mutually perpendicular X, Y and Z directions. The P-wave anisotropy generally decreases with increasing pressure in the nonlinear regime and approaches a constant value in the linear

regime (Figure 4.11). Type-1 and Type-2 eclogites mostly have an anisotropy ≤5% at 600 MPa (samples MB23, MB26, MB27, MB30, MB34, DG1, JC2, SB1) which is mainly attributed to the CPO of omphacite (Fountain et al., 1994; Bascou et al., 2001; Ji et al., 2003). However, Type-1 eclogite samples 86351 and MB25 with well developed thin-layers of alternating garnet and omphacite display a significant anisotropy, reflecting the contribution of thin layering to the seismic anisotropy (Ji et al., 1997a; Mauler et al., 2000). A considerably higher anisotropy occurs in Type-3 eclogites (e.g., samples QL2, 98501 and JC1) due to the presence of anisotropic minerals such as hornblende ($A \approx$ 23.8%), phengite ($A \approx$ 44.2%) and epidote ($A \approx$ 19.9%) that formed during the amphibolite facies retrograde metamorphism.

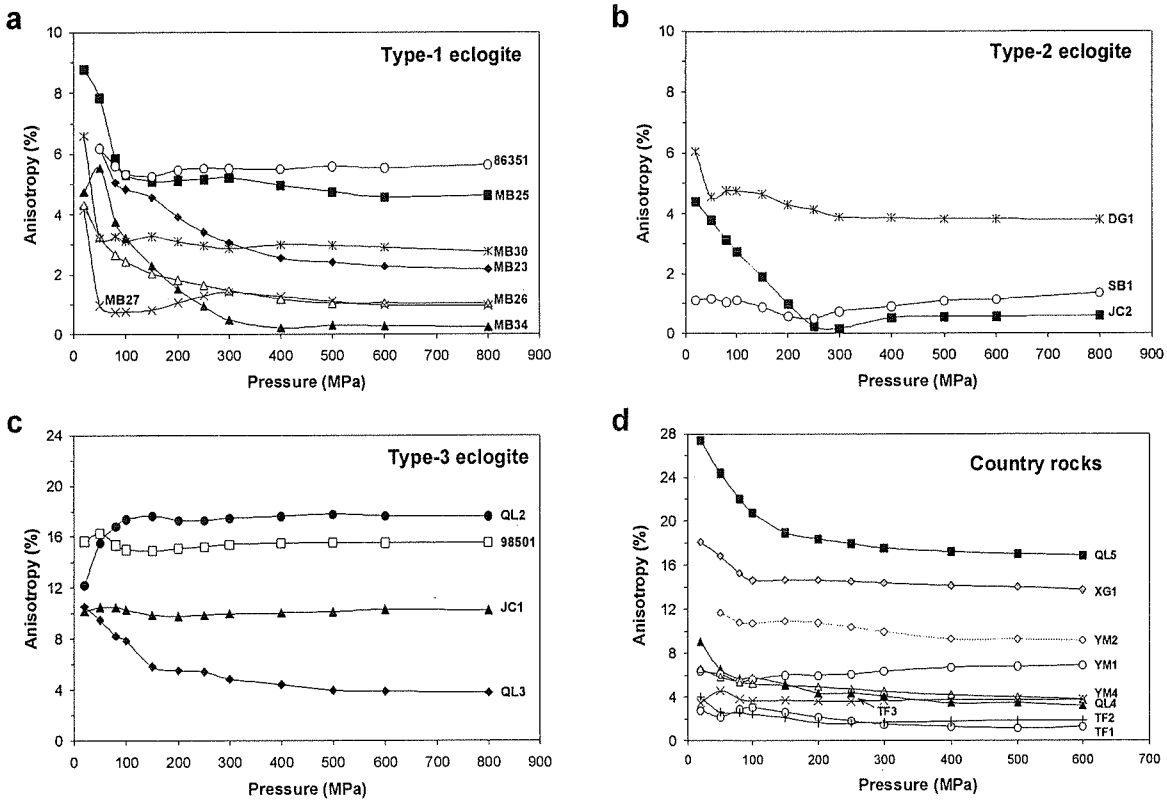


Figure 4.11 Vp anisotropy as a function of pressure for Dabie-Sulu UHP rocks. (a) Type-1 eclogites, (b) Type-2 eclogites, (c) Type-3 eclogites, and (d) Country rocks.

Among the country rocks (Figure 4.11d), the granitic gneisses (samples TF1, TF2 and TF3) display low anisotropy at high pressures (A = 1-4%) while the serpentinite and amphibolite are highly anisotropic (14% and 17% at 600 MPa, respectively, for samples XG1 and QL5). The dolomitic marbles from Yanmachang exhibit Vp anisotropy of 7-9% with transverse isotropic symmetry (Table 4.3) due to the CPO pattern of dolomite.

Three anisotropy-pressure patterns are observed (Figure 4.11): Pattern 1 is characterized by a decrease in anisotropy with increasing pressure, and occurs in most of the samples studied (e.g., MB23, MB26, QL3, QL4, QL5 and XG1). Pattern 2 displays an initial, rapid increase in anisotropy at low pressure, and then a slow decrease at higher pressures (sample QL2). Pattern 3 shows a decrease in anisotropy at low pressures (<100-150 MPa), followed by a slight increase at moderate pressures (100-300 MPa) and then a gradual decrease before a constant value is reached at high pressure (samples MB27 and DG1). Similar relationships between anisotropy and pressure have been observed in metagraywackes (Fountain et al., 1990) and granulite-facies mylonites (Ji et al., 1993).

4.6 Discussion

4.6.1 Pressure dependence of P-wave velocities

As noted above, the velocity-pressure curves obtained from laboratory experiments can be schematically represented in Figure 4.2. Several empirical equations have been proposed to describe the rapid increase at low pressures and a following asymptotic behaviour toward linear trends. Eberhart-Phillips et al. (1989), Freund (1992) and Shapiro (2003) suggested

$$V(P) = A + KP - Be^{-bP} \qquad (4.2)$$

where P is the effective pressure defined as the confining pressure minus the pore pressure; A, K, B, and b are fitting parameters for a given set of measurements. Wepfer and Christensen (1991) fit laboratory data using an empirical equation:

$$V(P) = A(P/100MPa)^a + B(1-e^{-bP}) \qquad (4.3)$$

where P is the confining pressure and a, b, A and B are adjustable parameters. Although both Equations (4.2) and (4.3) provide quite good approximation to observed velocity variations with pressure, their physical implications remain unclear. Furthermore, the pressure derivative calculated from either Equation (4.2) or Equation (4.3) is always pressure-dependent. This is not only inconsistent with experimental observations, but also makes it difficult to extrapolate the laboratory data to great depths.

It is well known that above a critical confining pressure (P_c), the rock sample can be regarded as a compacted aggregate and the linear increase in velocity with pressure indicates an elastic volume deformation. The velocity can be described by

$$V(P) = V_0 + DP \qquad (P \geq P_c) \qquad (4.4)$$

where P is the confining pressure, D is the intrinsic pressure derivative of velocity, V_0 is the projected velocity at room pressure (0.1 MPa), obtained from extrapolation of the linear velocity-pressure relationship. As shown in Figure 4.2, P_0 is the pressure at which $V = V_0$ on the observed velocity-pressure curve. V_B and V_c are, respectively, the velocities measured at room pressure and at the critical pressure P_c. Below P_c, the velocity increase from V_B to V_c in the nonlinear regime is actually attributed to two effects: V_0-V_B reflects the closing of microcracks and pore spaces (Birch, 1960; Christensen, 1974), and V_c-V_0 corresponds to lattice compression as the pressure rises from 0.1 MPa to P_c.

Using a least squares regression method, we found an alternative expression that can provide the best fit for the data in the nonlinear regime (Figure 4.12):

$$V(P) = a(\ln P)^2 + b\ln P + c \qquad (P \le P_c) \qquad (4.5)$$

where a and b are constants; c is the velocity when P is equal to unity (one MPa). At P_c, we have

$$V_0 + DP_c = a(\ln P_c)^2 + b\ln P_c + c \qquad (4.6)$$

The pressure derivative (V') of the velocity is then given by:

$$V' = (2a\ln P + b)/P \qquad (P \le P_c) \qquad (4.7)$$

for the nonlinear regime, and

$$V' = D \qquad (P \ge P_c) \qquad (4.8)$$

for the linear regime. At P_c, V' is continuous. Equations (4.7)-(4.8) provide a quantitative description of the rapid increase in velocity at low pressures, the more gradual increase at moderate pressures, and finally the constant rise at high pressures (Figure 4.13).

In order to assure that both P_0 and P_c have real solutions in Equations (4.5)-(4.6), it is necessary that $a < 0$ and $b \ge \sqrt{-4a(V_0 - c)}$. Clearly, V_0-c is an important parameter in determining the definition domains of a and b. This parameter corresponds to the velocity increase due to the closure of pores and microcracks from 1 MPa to P_0 (Figure 4.2). Parameters a and b describe the pressure sensitivity of velocity in the nonlinear regime and depend on the distribution and aspect ratios of pores and cracks.

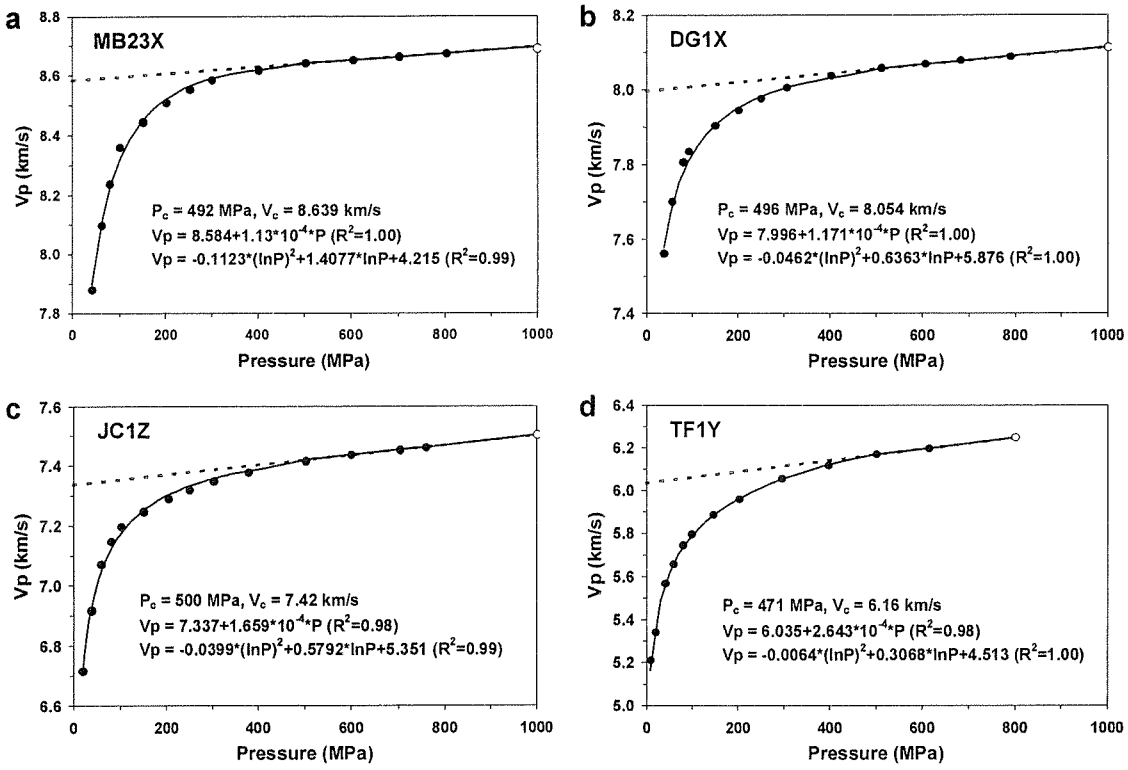


Figure 4.12 Experimental data points are best fit by the expressions $V = a(\ln P)^2 + b\ln P + c$ and $V = DP + V_0$ at pressures below and above P_c, respectively. (a) Core X from MB23 (Type-1 eclogite), (b) Core X from DG1 (Type-2 eclogite), (c) Core Z from JC1 (Type-3 eclogite), and (d) Core Y from TF1 (granitic gneiss).

Equations (4.4)-(4.5) provide simple and straightforward expressions for the poroelastic and elastic regimes, respectively. These equations can easily be used in the interpolation and extrapolation of velocities. Although five parameters are needed in curve-fitting the velocity curve in the full range of pressure, the physical meaning of each parameter is relatively clear. Based on Equations (4.4)-(4.5), a MATLAB program VPPLOT (Appendix 3) was constructed for critical point searching, velocity-pressure curve fitting and error analysis. The program is available upon request to the first author. Application of this program to *Vp* data for a Czechoslovakian eclogite to pressures of 3000 MPa (Christensen, 1974) yields a linear function $Vp = 8.336 + 1.174\times10^{-4}P$ above

739 MPa. This equation predicts a Vp value of 8.688 km/s at 3000 MPa, which is in good agreement with the experimental result of 8.690 km/s. Table 4.4 gives the least-square solutions of parameters P_c, V_c, P_0, V_0, a, b, c and D for the mean velocity of each sample. The fit to the experimental data of the Dabie-Sulu samples is excellent with most values of $R^2 \geq 0.97$ above P_c, and all $R^2 \geq 0.98$ below P_c.

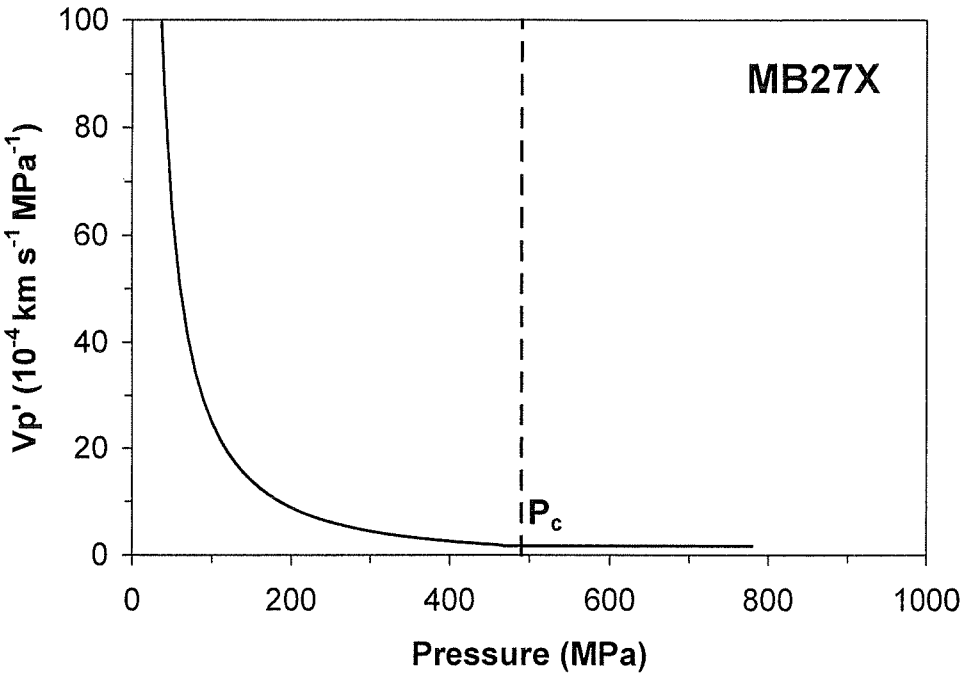


Figure 4.13 Pressure derivative (Vp') as a function of pressure for Sulu eclogite MB27X. P_c is the critical pressure above which microcracks and pores are closed and the sample behaves as a compacte aggregate.

The average values of these parameters and the pressure derivatives at various confining pressures for major rock types in the Dabie-Sulu orogenic belt are given in Table 4.5. These data display several important features. First, eclogites have higher values of P_c, V_c, P_0 and V_0 than their country rocks. Second, amphibolites have similar P_c and P_0 values but faster V_c and V_0 values than granitic gneisses. Moreover, while V_0 decreases, the average derivative D increases from 1.41×10^{-4} through 1.58×10^{-4} to

2.04×10^{-4} $kms^{-1}MPa^{-1}$, respectively, for Type-1, 2 and 3 eclogites in response to decreasing garnet and increasing retrograde mineral contents (Table 4.5 and Figure 4.9). It is probable that the values of V_0 and D are related to the modal composition while P_c and P_0 are mainly related to the crack density, aspect ratio of cracks and elasticity of rocks.

The pressure derivatives (D) are very important for interpreting seismic velocities in the lower crust and upper mantle. The measured derivatives of eclogites are compared with those reported in the literature (Figure 4.14). The compilation consists of 38 measurements at low pressures (300-600 MPa: Fountain et al., 1994; Kern and Richter, 1981; Kern and Tubia, 1993; Kern et al., 1999, 2002; Gao et al., 2001) and 59 measurements at high pressures (600-1000 MPa: this study; Birch, 1960; Kanamori and Mizutani, 1965; Kumazawa et al., 1971; Christensen, 1974; Manghnani et al., 1974; see Ji et al., 2002 for a comprehensive summary). The measured D values (1.41×10^{-4} kms^{-1} MPa^{-1} and 1.58×10^{-4} $kms^{-1}MPa^{-1}$ for Type-1 and Type-2 eclogites, respectively), which are slightly higher than those of garnet polycrystalline aggregates measured at pressures up to 3.0 GPa (Wang and Ji, 2001), are significantly lower than the low-pressure data (4.00×10^{-4} $kms^{-1}MPa^{-1}$, Figure 4.14a), but compatible with the high-pressure data (1.80×10^{-4} $kms^{-1}MPa^{-1}$, Figure 4.14b). Moreover, the average V_0 value (7.99 km/s, Figure 4.14d) extrapolated from the high-pressure data is higher than that from the low-pressure data (7.73 km/s, Figure 4.14c). Since cracks in eclogites are not fully closed until $P \geq 500$ MPa (Table 4.5), any extrapolations to higher pressures based on velocities measured below 500 MPa will be too high and cannot be used to estimate the composition of the lower crust and upper mantle from comparisons with refraction velocities. Thus, it is more appropriate to use high-pressure data to reconstruct lithologic models of subducted slabs from observed seismic data.

Table 4.4 Least square solutions of *Vp*-pressure relationships for UHP rocks from the Dabie-Sulu belt

Lithology/ Sample	P_c (MPa)	V_c (km s^{-1})	P_0 (MPa)	a (km $s^{-1}MPa^{-2}$)	b (km $s^{-1}MPa^{-1}$)	c (km s^{-1})	R^2	V_0 (km s^{-1})	D (10^{-4}km $s^{-1}MPa^{-1}$)	R^2
Coarse-grained eclogite										
86351	457	8.576	263.3	-0.0817	1.0642	5.120	1.00	8.513	1.390	0.99
MB23	613	8.527	336.4	-0.0824	1.1369	4.623	1.00	8.448	1.285	1.00
MB25	520	8.437	298.2	-0.0966	1.3021	4.059	1.00	8.343	1.815	0.98
MB26	414	8.549	297.3	-0.0245	0.4989	6.433	0.99	8.479	1.690	0.99
MB27	530	8.502	306.3	-0.0668	0.9086	5.421	0.99	8.432	1.320	1.00
MB30	449	8.377	331.6	-0.0221	0.4482	6.463	1.00	8.321	1.245	0.99
MB34	506	8.573	320.4	-0.0308	0.5185	6.539	1.00	8.505	1.342	0.99
Coarse-grained garnetite										
MB2B	468	8.613	374.7	-0.0310	0.5560	6.367	0.99	8.573	0.856	0.95
MB22	504	8.247	314.7	-0.0254	0.5063	6.080	0.99	8.152	1.883	0.98
MB62	561	8.512	385.0	-0.0713	1.0663	4.618	1.00	8.440	1.281	1.00
Fine-grained eclogite										
DG1	492	7.927	312.6	-0.0306	0.5184	5.889	1.00	7.858	1.413	1.00
JC2	441	7.689	318.8	-0.0437	0.6795	5.170	0.99	7.637	1.188	0.98
SB1	526	8.076	362.4	-0.0118	0.3544	6.318	1.00	7.997	1.494	0.98
JZ1	516	7.805	386.9	-0.0016	0.4182	5.254	1.00	7.690	2.225	0.97
Retrograde eclogite										
98501	478	7.379	304.0	-0.0180	0.3449	5.936	1.00	7.319	1.240	0.99
JC1	499	7.080	297.3	-0.0363	0.5510	5.058	1.00	7.018	1.229	1.00
QL2	536	7.341	369.4	-0.0185	0.6574	3.942	1.00	7.181	2.996	0.98
98401	536	7.707	300.6	-0.0577	0.7786	5.088	0.99	7.653	1.002	0.99
QL3	511	7.680	319.7	-0.0277	0.7426	4.127	1.00	7.488	3.754	0.99
Amphibolite										
QL4	530	6.520	301.8	-0.0270	0.7094	3.134	1.00	6.303	4.095	1.00
QL5	376	6.178	206.9	-0.0382	0.6039	3.941	1.00	6.074	2.752	1.00
YM4	374	7.124	217.8	-0.0145	0.3113	5.787	1.00	7.044	2.133	0.99
Granitic gneiss										
TF1	441	6.171	249.3	-0.0247	0.4671	4.243	1.00	6.068	2.330	1.00
TF2	416	5.960	250.2	-0.0219	0.5087	3.690	1.00	5.830	3.115	1.00
TF3	489	6.218	238.6	-0.0489	0.7167	3.650	1.00	6.107	2.269	1.00
Serpentinite										
XG1	419	5.230	214.8	-0.0085	0.2916	3.780	1.00	5.100	3.097	0.99
XG3	395	5.681	223.4	-0.0026	0.1775	4.713	1.00	5.597	2.130	0.98
Marble										
YM1	312	6.884	164.1	-0.0625	0.7979	4.318	0.99	6.763	2.592	1.00
YM2	403	6.895	246.3	-0.0765	1.1425	2.793	1.00	6.766	3.210	1.00

$Vp = a(lnP)^2 + blnP + c$ ($P \leq P_c$) and $Vp = V_0 + DP$ ($P \geq P_c$). See the text for definitions of P_c, V_c, P_0, V_0, a, b, c and D.

Table 4.5 Average values of parameters for *Vp*-pressure relationship and pressure derivatives at various confining pressure

Lithology	P_c	V_c	P_0	V_0-c	$Vp = V_0 + DP$		$Vp = a(lnP)^2 + blnP + c$			$Vp' = [(2alnP+b)/P] \times 10^4$ (10^{-4}kms^{-1}MPa^{-1})					dVp/dT
					V_0	D	a	b	c	Pressure (MPa)					
	(MPa)	(km/s)	(MPa)	(km/s)	(km/s)	(10^{-4}kms^{-1}MPa^{-1})	(kms^{-1}MPa^{-2})	(kms^{-1}MPa^{-1})	(km/s)	*50*	*100*	*200*	*400*	P_c	(-10^{-4}km s^{-1} °C^{-1})
Type-1 eclogite	502	8.491	323	2.848	8.421	1.411	-0.0533	0.8006	5.572	76.8	31.0	11.8	4.1	2.8	1.348
Type-2 eclogite	494	7.874	345	2.138	7.796	1.580	-0.0219	0.4926	5.658	64.2	29.1	13.0	5.7	4.5	2.553
Type-3 eclogite	512	7.437	318	2.502	7.332	2.044	-0.0316	0.6149	4.830	73.5	32.3	14.0	5.9	4.3	2.127
Peridotite*	505	8.131	227	2.467	7.987	2.856	-0.0442	0.6945	5.520	69.7	28.7	11.3	4.1	2.9	3.793
Srp peridotite*	484	7.185	230	2.521	7.060	2.590	-0.0488	0.7289	4.539	69.4	27.9	10.6	3.6	2.6	7.329
Mafic granulite*	436	7.062	198	1.664	6.915	3.389	-0.0211	0.4261	5.251	52.2	23.2	10.1	4.3	3.9	3.446
Amphibolite	427	6.607	242	2.186	6.474	2.993	-0.0266	0.5415	4.287	66.7	29.7	13.0	5.6	5.2	2.011
Intermediate gneiss*	397	6.471	176	1.768	6.353	2.967	-0.0329	0.5122	4.585	51.0	20.9	8.2	—	3.0	3.160
Granitic gneiss	449	6.116	246	2.141	6.002	2.571	-0.0318	0.5642	3.861	63.0	27.1	11.3	4.6	3.9	2.986
Metapelite*	314	6.642	160	1.453	6.518	3.950	-0.0176	0.3757	5.065	47.6	21.4	9.5	4.1	5.5	4.501
Paragneiss*	360	6.280	158	1.587	6.157	3.418	-0.0284	0.4572	4.570	47.0	19.6	7.8	—	3.4	4.501
Granite*	299	6.181	150	2.218	6.095	2.873	-0.0588	0.7222	3.877	52.4	18.1	5.0	—	1.7	2.964
Marble	358	6.890	205	3.209	6.765	2.901	-0.0695	0.9702	3.556	85.3	33.0	11.7	—	4.3	6.471
Serpentinite	407	5.456	219	1.102	5.349	2.614	-0.0056	0.2346	4.247	38.2	18.3	8.8	4.2	4.1	3.135

* Data from *Handbook of Seismic Properties of Minerals, Rocks and Ores* (Ji et al., 2002).

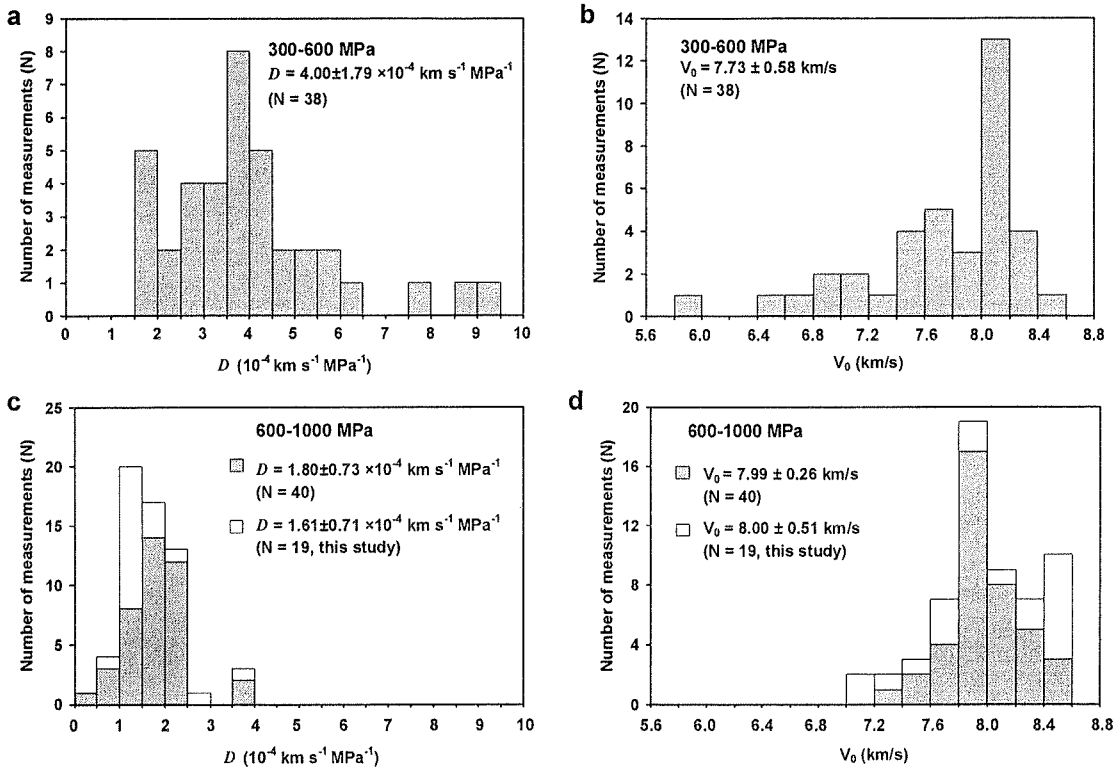


Figure 4.14 Intrinsic pressure derivatives (D) and reference velocities (V_0) of eclogites from (a-b) low-pressure (300-600 MPa) and (c-d) high-pressure (600-1000 MPa) measurements.

The pressure derivatives (Vp') in the nonlinear regime reflect the closure of microcracks in rocks at low pressure. The Vp' values are much higher at $P \leq 100$ MPa than $P > 200$ MPa (Figure 4.13 and Table 4.5), because larger grain boundary cracks and transgranular cracks and pores are more easily closed at lower pressures (e.g., Siegesmund et al., 1991). Interestingly, the three types of eclogites have similar Vp' values in the nonlinear regime but different D values in the linear regime. While the difference in D values reflects principally their differences in modal composition, the similarity in Vp' may imply that these eclogites have a similar deformation response to increasing pressure.

$V_0 - c$ reflects the crack-induced velocity variation. As shown in Table 4.5, $V_0 - c$ is equal to 2.85 km/s for Type-1, 2.14 km/s for Type-2 and 2.50 km/s for Type-3 eclogites. This seems to indicate that there are more open cracks in coarse-grained (Type-1) than in fine-grained (Type-2) and retrograde (Type-3) eclogites. This conclusion is consistent with microstructural observations (Figure 4.5) that omphacite and particularly garnet display pervasive, closely spaced, tensile, transgranular cracks in Type-1 eclogites, whereas garnet/garnet grain boundaries in Type-2 eclogites are generally narrow and most of the cracks in Type-3 eclogites have been filled by the retrograde minerals. Marbles show a quite high $V_0 - c$ value (Table 4.5) due to the pervasive presence of microcracks along $\{10\bar{1}1\}$ cleavages in dolomite and calcite.

4.6.2 Seismic anisotropy

Generally, both *Vp* and *Vp'* are direction-dependent and P_c may also vary from one direction to another in a rock sample. Assuming that P_{min} and P_{max} are, respectively, the minimum and maximum critical pressures (P_c) among the three orthogonal directions measured, Equation (4.1) can be expressed as:

$$A = \frac{a_1(\ln P)^2 + b_1 \ln P + c_1 - a_2(\ln P)^2 - b_2 \ln P - c_2}{a_m(\ln P)^2 + b_m \ln P + c_m} \times 100\% \qquad (P \le P_{\min}) \qquad (4.9)$$

$$A = \frac{D_1 P + V_{0_1} - D_2 P - V_{0_2}}{D_m P + V_{0m}} \times 100\% \qquad (P \ge P_{\max}) \qquad (4.10)$$

where the subscripts 1, 2 and *m* refer to the directions along which *Vp* has the maximum and minimum values, and the mean value of the bulk sample, respectively. Between $P_{\min}$ and $P_{\max}$, the anisotropy should be calculated from Equations (4.1), (4.4) and (4.5). Below P_{min}, the anisotropy is controlled by a series of factors such as porosity, geometry (size and shape), density and orientation of microcracks, compositional layering and the

CPO of the constituent minerals. The effects of these factors result in complex variations of anisotropy with pressure (Figure 4.11). Above P_{max}, however, the effects of pores and microcracks are entirely eliminated, the anisotropy is only fabric-related (e.g., Ji et al., 1993; Popp and Kern, 1994; Kern et al., 1999) and it approaches a constant for each sample. Because D_1, D_2 and D_m are usually very small (on the order of 10^{-4} $kms^{-1}MPa^{-1}$) for most rocks, Equation (4.10) can be approximated by

$$A \approx \frac{V_{0_1} - V_{0_2}}{V_{0_m}} \times 100\% \qquad (4.11)$$

The anisotropy calculated from Equation (4.11), which is referred to as the "intrinsic anisotropy" because it is pressure-independent, mainly depends on the CPO of minerals and compositional layering. However, if there is a substantial discrepancy in the pressure derivatives between different propagation directions over a wide range of pressure, a crossover of Vp versus P curves will occur and the intrinsic anisotropy will vary with pressure.

The anisotropy-pressure relationship, which depends on the competition between the increase in the mean velocity (V_m) and the velocity difference along the fastest and slowest directions ($V_{\max} - V_{\min}$), appears to be rather complex in the nonlinear regime. To calibrate this relationship, we define a normalized pressure derivative (δ_λ) as the ratio of Vp' along a given propagation direction λ to the average derivative V_m' of the bulk sample:

$$\delta_\lambda = \frac{Vp'_\lambda}{Vp'_m} = \frac{2a_\lambda \ln P + b_\lambda}{2a_m \ln P + b_m} \qquad (4.12)$$

Thus, δ_λ measures the relative velocity increase with pressure in a given direction with respect to that in the bulk sample, and its value is related to the direction-dependent

closure of cracks and to the distribution and geometry of the cracks. In the case of the anisotropy-pressure relationship of Pattern 1, the anisotropy decreases with increasing pressure due to a consistent increase in V_m coupled with a continuous decrease in the pressure derivative, both caused by the progressive closure of cracks. As an example, sample MB26 has a higher *Vp* value along the Z direction than along the X direction in the nonlinear regime (Table 4.3) due to the predominance of transgranular fractures over grain boundary cracks. The transgranular fractures and the grain boundary cracks are preferentially aligned normal to the lineation and parallel to the foliation, respectively (Figure 4.5a). As shown in Figure 4.15a, δ_X and δ_Z respectively increase and decrease with increasing pressure in the nonlinear regime. Consequently, the value of *Vp*(Z)-*Vp*(X) and the bulk anisotropy decrease with increasing pressure (Figure 4.11a). However, for sample QL2 (Figure 4.15b), whose anisotropy belongs to Pattern 2 (Figure 4.11c), the fastest and slowest velocities occur in the X- and Z-directions, respectively. For P < 150 MPa, δ_X is so high compared to δ_Z that the value of $V_{\max} - V_{\min}$ increases more rapidly than V_m with increasing pressure. At higher pressures, the value of δ_X - δ_Z is insufficient to let the value of $V_{\max} - V_{\min}$ overtake the increase in V_m (Figure 4.15b) and consequently, the anisotropy begins to decrease. Samples MB27 and DG1 show the anisotropy-pressure relationship of Pattern 3: the anisotropy decreases with increasing pressure at low pressures (<100-150 MPa), then increases slightly at moderate pressures (100-300 MPa), and then finally declines to a constant value (Figures 4.11a-b). This pattern is attributed to complex variations in the velocities or pressure derivatives with pressure among the different propagation directions (Figure 4.15c). Pattern 3 often occurs in quasi-isotropic rocks (Table 4.3). Moreover, δ_X or δ_Y is generally found to be larger than δ_Z, suggesting that the effects of transgranular and intragranular fractures predominate over those of grain boundary cracks in these samples.

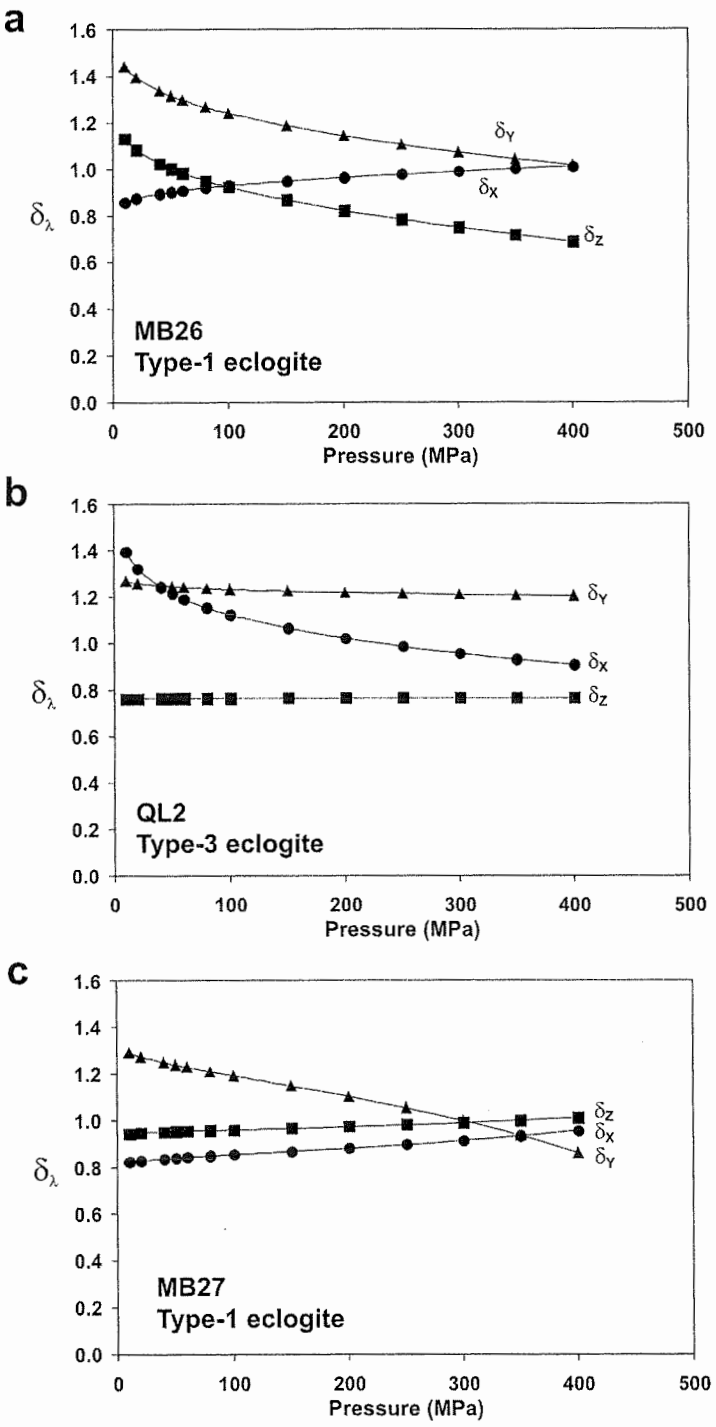


Figure 4.15 Normalized pressure derivative (δ_λ) as a function of pressure in the nonlinear regime for (a) Pattern 1, (b) Pattern 2, and (c) Pattern 3 anisotropy (see text).

4.6.3 Implications for the upper mantle structure beneath the orogenic belt

Tomographic imaging (Xu et al., 2001) indicates that a slab-like belt with a maximum 9% higher *Vp* than the mantle reference model IASPEI91 of Kennett and Engdahl (1991) dips to the NW beneath the Dabie-Sulu orogenic belt. This high *Vp* anomaly (*Vp* = 8.72 km/s at a depth of 71 km) extends from the Moho discontinuity to a depth of about 110 km. Using the pressure and temperature derivatives listed in Table 4.5, we computed velocity-depth profiles for major rock types from the Dabie-Sulu UHP belt. The results (Figure 4.16) suggest that Type-1 eclogites should be the dominant constituent of the dipping slab beneath the Dabie-Sulu belt because the P-wave velocity is too high to be explained in terms of ordinary peridotite, or Type-2 or Type-3 eclogites. Thus, the high *Vp* anomaly indicates the presence of a remnant subducted slab that has been frozen in the upper mantle since about 200-220 Ma.

Recently, Musacchio et al. (2004) documented a striking high *Vp* layer H (up to ~8.8 km/s) with significant *Vp* anisotropy (>6%) dipping northward at 50-75 km depth beneath the western Superior Province (Canada) and interpreted it as a harzburgitic layer. The authors exclude eclogites as a possible component for the layer because of the high anisotropy observed. Although omphacite-induced anisotropy is generally less than 3% for both P- and S-wave velocities (Bascou et al., 2000; Ji et al., 2003), the present study demonstrates that compositional layering (Figure 4.3c) can make an important contribution to anisotropy in eclogites and cause them to acquire the observed anisotropy of layer H. Furthermore, the observed maximum *Vp* in the northward dipping layer H lies in the E-W direction, which can be easily interpreted in terms of the preferred orientation of omphacite c-axes parallel to the EW-aligned regional stretching lineation and the compositional layering parallel to the EW-oriented tectonic foliation. Since the temperature at 50-75 km depths beneath the western Superior Province is low (~500-600 °C, Musacchio et al., 2004), Type-1 eclogites, if present, are more likely to have the *Vp* values as high as 8.8 km/s than harzburgite. Hence we believe that the upper mantle structure beneath the western Superior Province can also be explained by the presence of

UHP eclogites. The eclogites may constitute a remnant subducted oceanic or continental slab that has been frozen in the upper mantle since the Archean cratonization.

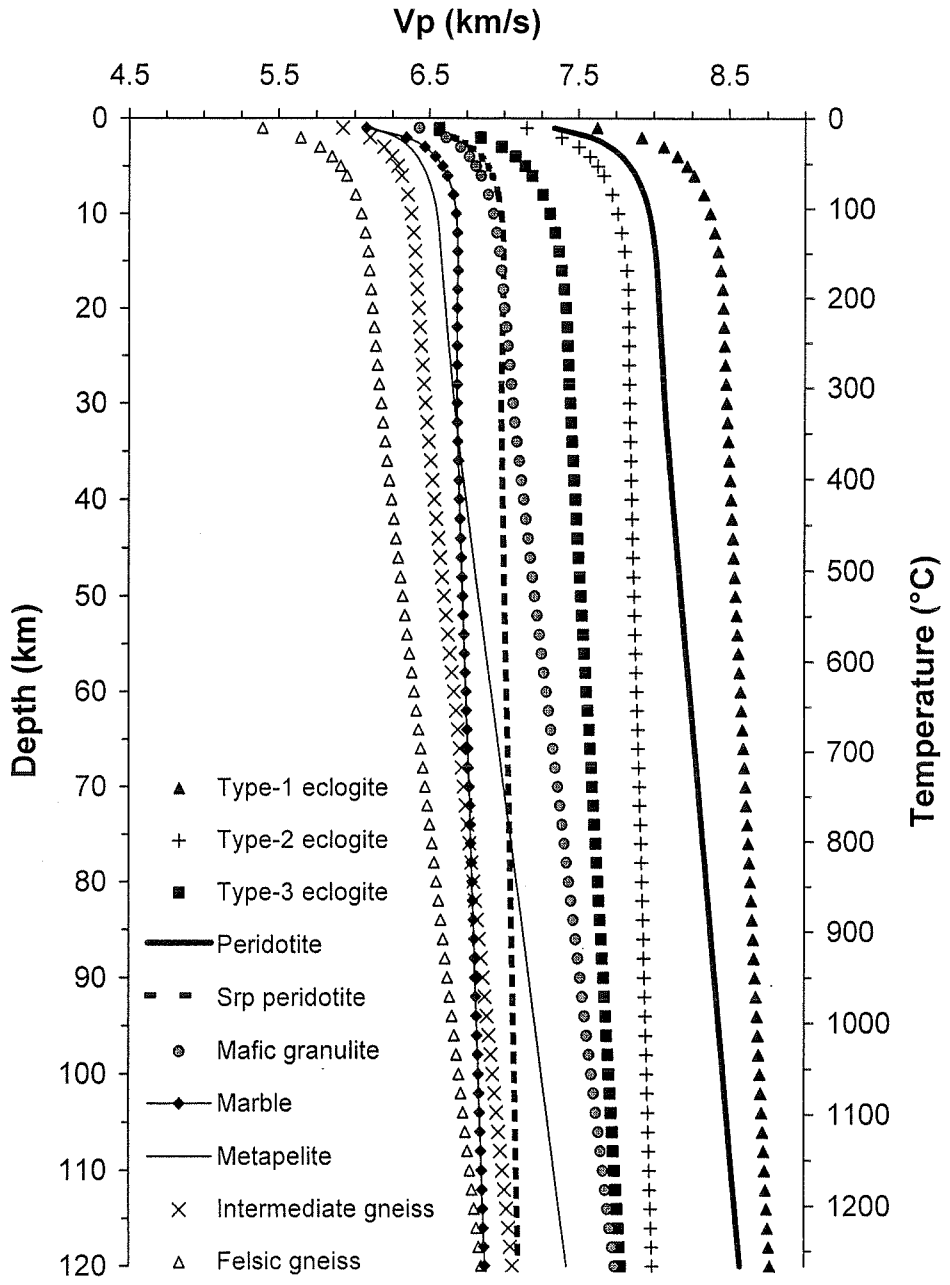


Figure 4.16 Calculated velocity-depth profiles for major lithologies from the Dabie Mountains.

4.6.4 Origin of seismic reflections in the upper mantle

Several seismic reflectors have been recognized in the uppermost part of the mantle beneath the Sulu UHP metamorphic belt (Yang, 2002, 2003). Unlike continental extensional zones beneath which the upper mantle is often seismically transparent, continent-continent collision belts usually have a reflective upper mantle, as observed for example, under the Abitibi-Opatica belt of the Canadian Superior Province (Calvert et al., 1995) and the Northwest Territories of Canada (Cook et al., 1999). These mantle reflectors are generally gently dipping and extend from the Moho to at least 100 km depth. To be detected in the mantle below 40-km-thick crust, such reflectors must represent sharp boundaries (Morgan et al., 1994; Bostock, 1997) with reflection coefficients (Rc) higher than around 0.1 (Warner and McGeary, 1987). Since seismic reflection methods have a vertical and horizontal resolution of about 75 and 3000 m, respectively, at depths of 40 km (assuming an average crustal velocity of 6 km/s and a dominant frequency of 20 Hz), mantle reflectors are thought to be caused by thick, regionally extensive layers with sharp, well defined, continuous upper surfaces and a large impedance contrast with the surrounding mantle.

Field surveys in the Dabie-Sulu area indicate that eclogites are layers or tectonically elongated boudins in country rocks composed of garnet-harzburgite, metapelite (garnet-quartz-jadeite gneisses), granitic gneiss, coesite-bearing quartzite and marble. The eclogite boudins (at Maobei and Qinlongshan, for example) have a length of 3-4 km, a width of 0.8-1.0 km and a thickness of 0.3-0.4 km. All of the UHP blocks have well-developed foliation, stretching lineation and compositional layering, which are generally parallel to each other (Figures 4.3a-c). This implies, surprisingly, that the contact relations between these UHP rocks were not severely disturbed during tectonic emplacement and that they remained structurally coherent during subduction and exhumation (e.g., Ji et al., 2003; Rolfo et al., 2004).

Figure 4.17 shows the lithologic column of drill hole ZK703, drilled at Maobei in Donghai county by geological team No. 6 from Jiangsu Province (also see Zhang et al., 2000). This 558-m-deep hole penetrated into alternating layers of Type-1 to Type-3 eclogites, felsic gneiss, amphibolite, quartzite, phengite-quartz schist, and serpentinized garnet-harzburgite. In the first 2000 m of the main hole of the CCSD project, the cumulative thickness of the various eclogites was about 1000 m, while the total thickness of mantle peridotite was only about 100 m (Figure 4.18a). This indicates that the eclogites do not always occur as small lenses or blocks as commonly observed in outcrops. The eclogites can form thick, continuous, moderately dipping layers in amphibolite-facies felsic gneisses (Figure 4.3b). The contacts between the various rock types are sharp and tectonically undisturbed.

Table 4.6 gives normal-incidence reflection coefficients (Rc) at possible lithological interfaces in the Dabie-Sulu belt, calculated using the average densities and P-wave velocities at 50 MPa and 600 MPa, respectively. The similarity between the values of Rc at 50 MPa (upper matrix) and 600 MPa (lower matrix) demonstrates that the effect of pressure on Rc values is neglectable. The boundaries between Type-1 eclogites (high *Vp* and density) and almost all other lithologies such as mafic granulite, amphibolite, felsic gneiss, paragneiss, marble, quartzite and serpentinized peridotite can have large Rc values (>0.1) and thus strong seismic reflections. Interfaces between retrograde eclogites and their intact protoliths (Type-1 eclogites) can also be seismically reflective.

We modeled the *Vp*-depth profile for the upper 2000 m of the CCSD main hole (Figure 4.18b) using Equation (4.5) to describe the velocity-pressure functions in the nonlinear regime. The calculated normal-incidence reflection coefficients (Figure 4.18c) explain quite well the seismic reflection profile (Figure 4.18d). The strong seismic reflections consistently occur at the gently dipping contacts between eclogites and their country rocks such as paragneiss and felsic gneiss. In addition, moderate reflections (G

and H in Figure 4.18c) appear at shear zones that are characterized by fine-layered paragneiss clusters within felsic gneiss (Ji et al., 1997a).

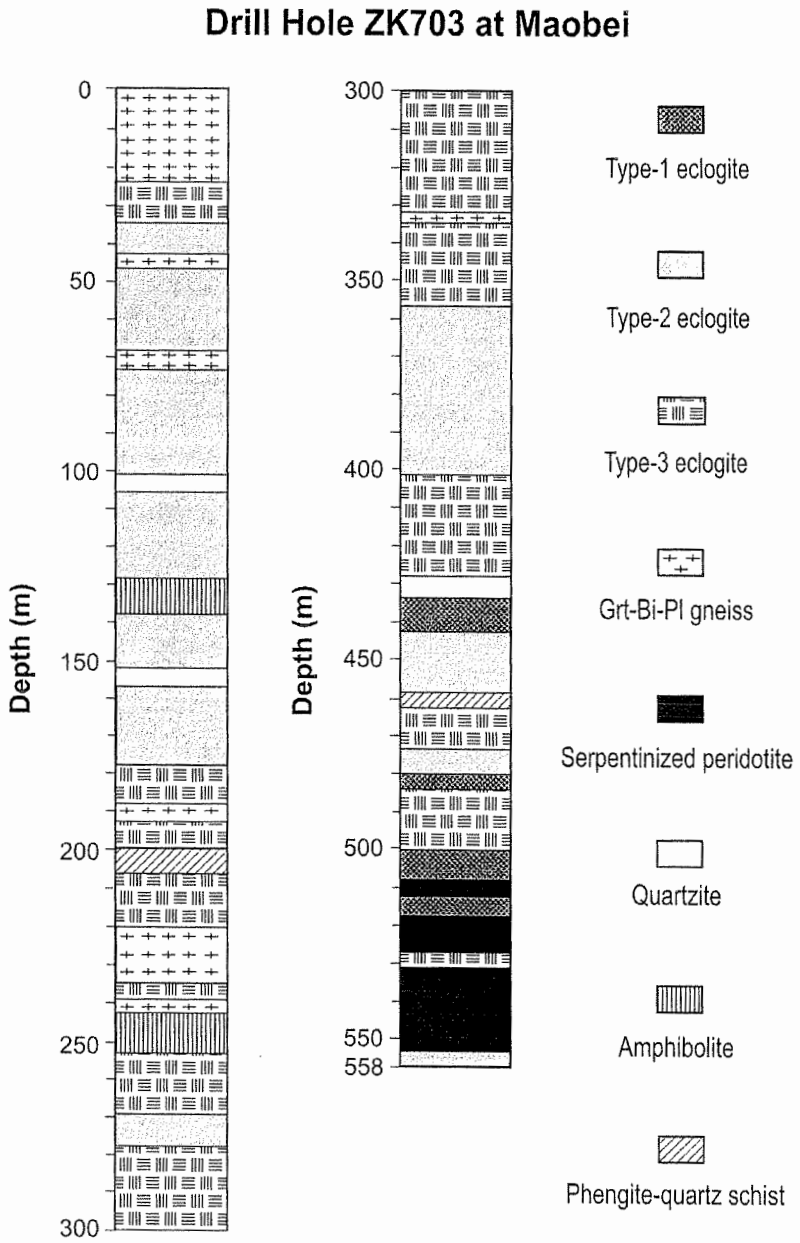


Figure 4.17 Lithologic column of drill hole ZK703 at Maobei (34°25′N, 118°40′E), Donghai County, China. Modified from Zhang et al. (2000).

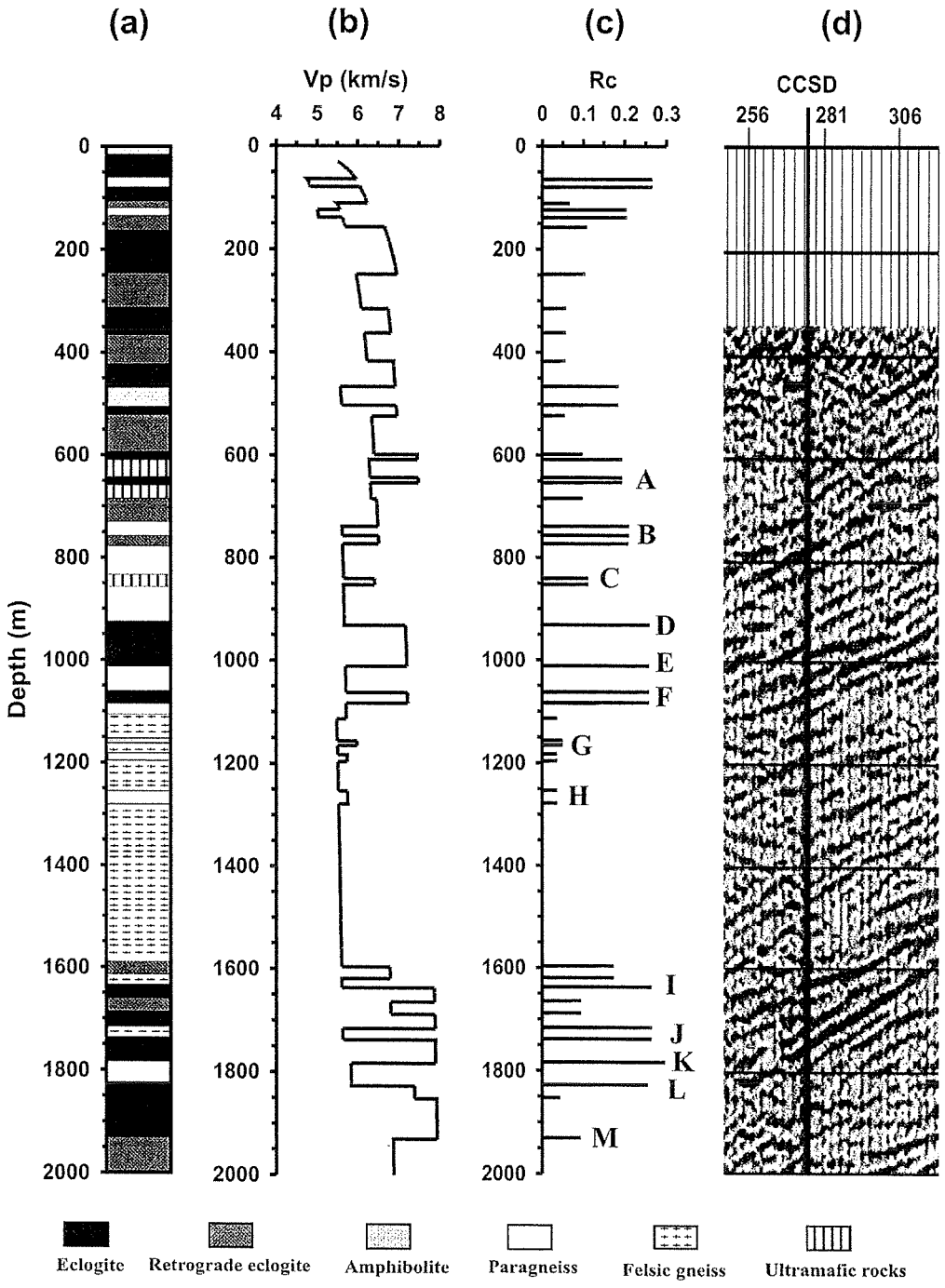


Figure 4.18 (a) A simplified lithological profile of 0-2000 m in the CCSD main hole (simplified from Xu, 2004), (b) calculated velocity-depth profile, (c) inferred P-wave reflection coefficients (Rc), and (d) reflection profile of the study area (after Zhao et al., 2004).

Table 4.6 Reflection coefficients (Rc) at possible lithological interfaces in the Dabie-Sulu UHP belt at 50 MPa and 600 MPa

Lithology	ρ	Vp (km/s)		Type-1	Peridotite	Type-2	Type-3	Srp	Mafic	Amphibolite	Marble	Paragneiss	Quartzite	Felsic	Serpentinite
	(g/cm^3)	50 MPa	600 MPa	eclogite		eclogite	eclogite	peridotite	granulite					gneiss	
Type-1 eclogite	3.57	7.87	8.51		0.06	0.06	**0.10**	**0.13**	**0.17**	**0.22**	**0.22**	**0.24**	**0.29**	**0.31**	**0.36**
Peridotite*	3.31	7.55	8.24	-0.05		0.00	0.04	0.07	**0.19**	**0.16**	**0.17**	**0.19**	**0.23**	**0.26**	**0.31**
Type-2 eclogite	3.44	7.28	7.89	-0.06	0.00		0.04	0.07	**0.19**	**0.16**	**0.17**	**0.19**	**0.23**	**0.26**	**0.31**
Type-3 eclogite	3.44	6.72	7.46	-0.08	-0.03	-0.03		0.03	**0.10**	**0.13**	**0.13**	**0.15**	**0.20**	**0.22**	**0.27**
Srp peridotite*	3.18	6.82	7.32	**-0.13**	-0.08	-0.08	-0.05		0.04	0.09	**0.10**	**0.12**	**0.17**	**0.19**	**0.24**
Mafic granulite*	3.15	6.65	6.98	**-0.16**	**-0.11**	**-0.10**	-0.08	-0.03		0.08	0.08	**0.10**	**0.15**	**0.17**	**0.23**
Amphibolite	3.00	5.99	6.65	**-0.21**	**-0.16**	**-0.15**	**-0.13**	-0.08	-0.09		0.00	0.03	0.07	**0.10**	**0.15**
Marble	2.86	6.24	6.87	**-0.21**	**-0.16**	**-0.16**	**-0.13**	-0.08	**-0.11**	-0.01		0.02	0.07	0.09	**0.15**
Paragneiss*	2.85	5.99	6.51	**-0.24**	**-0.19**	**-0.19**	**-0.16**	**-0.11**	**-0.16**	-0.04	-0.03		0.05	0.07	**0.13**
Quartzite*	2.65	5.86	6.24	**-0.29**	**-0.24**	**-0.24**	**-0.22**	**-0.17**	**-0.25**	-0.09	-0.09	-0.06		0.03	0.08
Felsic gneiss	2.66	5.56	6.16	**-0.30**	**-0.25**	**-0.25**	**-0.22**	**-0.17**	**-0.26**	**-0.10**	-0.09	-0.06	-0.01		0.06
Serpentinite	2.61	5.08	5.50	**-0.36**	**-0.31**	**-0.31**	**-0.28**	**-0.24**	**-0.35**	**-0.16**	**-0.16**	**-0.13**	-0.07	-0.07	

Rc derived from average densities at ambient conditions and velocities measured at 50 MPa (the upper matrix) and 600 MPa (the lower matrix), respectively. The bold numbers refer to possible lithologic interfaces that may generate strong seismic reflections.

* Data from *Handbook of Seismic Properties of Minerals, Rocks and Ores* (Ji et al., 2002).

As shown in Figure 4.2, phengitic mica (Massonne and Schreyer, 1989), zoisite and epidote (Cheng and Greenwood, 1989), talc (Liou et al., 1998), glaucophane (Holland, 1988), serpentinite (Ulmer and Trommsdorff, 1995) and magnesite and dolomite (Sato and Katsura, 2001) remain stable under UHP eclogite facies conditions. Under HP eclogite facies conditions, quartz and K-feldspars are stable while calcite is transformed to aragonite. When a package of such cold, interlayered crustal materials is rapidly subducted in the upper mantle, a large reflection coefficient (>0.10) should occur at interfaces between UHP eclogite or garnet peridotite and their wall rocks (i.e. quartzite, dolomitic or aragonitic marble, pelitic and felsic gneisses, serpentinized peridotite).

More problematic is whether or not these large coefficients can persist through prograde metamorphism for long period of time until the slab is completely resorbed in the mantle. The extremely low geothermal gradient ($\leq$ 5-10 °C/km) recorded in the Dabie-Sulu UHP metamorphic rocks suggests that the continental crust of the Yangtze craton was subducted so rapidly to great depths that it was still several hundreds of degrees cooler than the surrounding mantle during peak UHP metamorphism (Liou et al., 1998; 2000). Furthermore, the subduction of old, cold, dry continental crust can only provide very limited volatiles and fluids at great depths, which have mostly been stored in the HP and UHP hydrous minerals (Liou et al., 1998), preventing large-scale partial melting within the subducted crustal package. The lack of fluid flow and coeval partial melting might encourage the preservation of layered structures and metastable phase assemblages during prograde metamorphism.

Subduction zones caused by the rapid subduction of low-density crustal materials into the upper mantle are generally short-lived (Liou et al., 2000a), as suggested by oxygen isotope evidence (Zheng et al., 1998; Rumble and Yui, 1998). Garnet harzburgites associated with the UHP rocks, on the other hand, were derived from the mantle wedge that overrode the subducted slab. Over time, the interaction of subducted ancient crust with the upper mantle peridotites could cause partial melting of such metasomatized

mantle and produce the basic magma for mafic-ultramafic intrusions (Jahn et al., 1999) and possible heat sources for the massive Cretaceous granitic intrusions observed in the region (Faure et al., 2003b). Fortunately, these post-collisional tectonic events may not strongly affect the former cold, strong crustal relics in the upper mantle. As shown by seismic tomography images beneath the Dabie-Sulu orogenic belt, the remnant of the subducted Yangtze block extends from the Moho discontinuity to a depth of about 110 km, then disappear between 110-150 km, indicating that the detached slab sank into the mantle (Xu et al., 2001). Therefore, the regionally extensive mantle reflectors observed beneath both the Dabie-Sulu belt (Yang, 2002, 2003) and other orogenic belts (the Abitibi-Opatica belt of the Canadian Superior Province, Calvert et al., 1995; the Northwest Territories of Canada, Cook et al., 1999; the western Superior Province of Canada, Musacchio et al., 2004) may indicate the preservation of rapidly subducted, residual crustal materials in the lithospheric upper mantle. These results provide a new, alternative interpretation for the origin of mantle reflections because, as Ji et al. (2003) recently argued, neither ductile shear zones, metasomatic zones, nor lithological interfaces in the peridotitic upper mantle can be successful candidates.

4.7 Conclusions

We have measured P-wave velocities of eclogites and their country rocks from the Dabie-Sulu UHP metamorphic terrane (China), at ambient temperature and hydrostatic confining pressures up to 800 MPa. The velocity-pressure curves display a rapid, nonlinear rise in velocity at low pressures, followed by a slow linear increase at high pressures. The critical pressure (P_c) for the transition from the nonlinear (poroelastic) to linear (elastic) regime is significantly higher for eclogites than for country rocks such as felsic gneiss and amphibolite formed under lower P-T conditions. The velocities in the nonlinear and linear regimes can be respectively described by the expressions $V = a(\ln P)^2 + b\ln P + c$ and $V = V_0 + DP$, where a and b are two constants describing the pressure sensitivity of velocity below P_c, attributed to a combination of the gradual

closure of cracks and pore spaces and lattice compression within the sample, c is the velocity when P is set equal to unity (1 MPa); V_0 is the extrapolated velocity of the crack-free sample at room pressure, and D is the intrinsic pressure derivative. The pressure derivative (V') is pressure-dependent and equal to $(2a\ln P+b)/P$ below P_c, and pressure-independent and equal to D above P_c. Together with previous high-pressure data, the average values of a, b, c, V_0 and D as well as P_c for each lithology may provide important information for the interpretation of seismic data from both ancient and modern subducted slabs.

Three types of eclogites characterize the Sulu UHP zone: Type-1 eclogites, which are coarse-grained and display almost no retrograde metamorphism, were deformed by recovery-accommodated dislocation creep at peak metamorphic conditions in the diamond stability field. Type-2 eclogites are fine-grained eclogites composed of Type-1 materials that were reworked during recrystallization-accommodated dislocation creep in the early stage of exhumation near the quartz/coesite boundary. Type-3 eclogites are overprinted by significant amphibolite facies metamorphism during late stage of exhumation in the crust. The eclogites display a progressive increase in SiO_2 and Na_2O, and decrease in Al_2O_3 and MgO from Type-1, to Type-2 and Type-3 eclogites.

The P-wave velocities of measured eclogites decrease from an average of $Vp = 8.42+1.41\times10^{-4}P$ for Type-1, $Vp = 7.80+1.58\times10^{-4}P$ for Type-2, to $Vp = 7.33+2.04\times10^{-4}P$ for Type-3, where Vp is in km/s and P in MPa, reflecting a decreasing volume content of garnet and an increasing content of retrograde minerals such as amphibole, quartz, plagioclase and mica. The intrinsic pressure derivatives (D) are significantly lower than previous low-pressure (300-600 MPa) regression results, but compatible with high-pressure (600-1000 MPa) data reported in the literature. The D values determined at low pressures are unstable due to insufficient closure of microcracks; only the high-pressure data can be used in interpreting the seismic velocities of subducted slabs at mantle depths in terms of lithology and chemical composition. Anisotropy is generally low (<4%) for

Type-1 and Type-2 eclogites because volumetrically important garnet is elastically quasi-isotropic. However, compositional layering can give rise to anisotropy in eclogites and high anisotropy (>10%) is observed in Type-3 eclogites due to the presence of strongly anisotropic retrograde minerals.

Tomographic imaging (Xu et al., 2001) reveals a NE-SW trending and NW-dipping, slab-like high *Vp* anomaly (8.72 km/s at a depth of 71 km), which extends from the Moho to a depth of at least 110 km beneath the Dabie-Sulu region. We interpret this high *Vp* anomaly as the remnant of a subducted slab, largely composed of Type-1 and possibly Type-2 eclogites, which has been frozen in the upper mantle since about 200-220 Ma. We also propose that relic crustal materials, subducted and preserved as eclogite layers intercalated with felsic gneiss, garnet-jadeite quartzite and marble, are responsible for the regionally observed seismic reflectors in the upper mantle (Yang, 2002, 2003).

Chapter 5

Shear wave properties and Poisson's ratios of ultrahigh-pressure metamorphic rocks from the Dabie-Sulu orogenic belt, China: implications for crustal composition

Qin Wang[a], Shaocheng Ji[a,c], Matthew H. Salisbury[b], Bin Xia[c], Mingbao Pan[a,d], Zhiqin Xu[e]

[a]*Département des Génies Civil, Géologique et des Mines, École Polytechnique de Montréal, Montréal, Québec, Canada H3C 3A7*

[b]*Geological Survey of Canada-Atlantic, Bedford Institute of Oceanography, P.O Box 1006, Dartmouth, Nova Scotia, Canada B2Y 4A2*

[c]*Laboratory of Marginal Sea Geology, Guangzhou Institute of Geochemistry, Chinese Academy of Sciences, Guangzhou 510640, China*

[d] *Geological Survey of Jiangsu Province, Nanjing 210018, China*

[e]*Chinese Continental Scientific Drilling, Institute of Geology, Chinese Academy of Geological Sciences, Beijing 100037, China*

Acknowledgements

We thank NSERC, LITHOPROBE and the Chinese Academy of Sciences (KZCXZ-SW-117) for research grants. We are grateful to R. Iuliucci for his technical assistance in the laboratory, J. Martignole. W.C. Yang and S.W. Liu for helpful discussion and to S.T. Xu for providing the Bixiling eclogite samples. This is LITHOPROBE contribution No. xxxx.

This paper was submitted to Journal of Geophysical Research in September 2004.

5.1 Abstract

Shear wave velocities (*Vs*), anisotropy and shear wave splitting have been measured at pressures up to 600-800 MPa for ultrahigh-pressure (UHP) metamorphic rocks from the Dabie-Sulu orogenic belt, China, with a focus on three types of eclogites. Type-1 eclogites are coarse-grained, unaltered samples showing high densities (3.57±0.05 g/cm^3) and high *Vs* values (4.85±0.06 km/s at 600 MPa); Type-2 eclogites are fine-grained, slightly retrograde, sheared Type-1 materials with moderate densities (3.44±0.07 g/cm^3) and intermediate *Vs* values (4.53±0.04 km/s at 600 MPa); Type-3 eclogites are overprinted by amphibolite-facies metamorphism and display relatively low densities (3.44±0.03 g/cm^3) and low *Vs* values (4.30±0.08 km/s at 600 MPa). The compositional layering and retrograde metamorphism can result in significant anisotropy and shear wave splitting in eclogites, suggesting a plausible contribution to seismic anisotropy in the lower crust, upper mantle and particularly in subducted slabs. Integrating our P- and S-wave velocity results with reliable data from previous studies, we determined new estimates of the pressure and temperature derivatives of *Vp* and *Vs*, as well as Poisson's ratios for common rock types in the UHP metamorphic belt. We also used the geometric mean as a mixture rule to invert the lithological and chemical compositions of the layered crust from seismic refraction velocities. The inferred crustal composition suggests that the eclogite-bearing UHP rocks are tectonic slices of crust that have been thrust along a series of shear zones during the continental collision between the North China and Yangtze cratons over a normal UHP-free middle-lower crust with an overall intermediate composition.

Keywords: Shear wave velocity; Shear wave splitting; Poisson's ratio; Ultrahigh-pressure metamorphic rocks; Eclogite; Dabie-Sulu orogenic belt

5.2 Introduction

Beneath modern and ancient convergent orogenic belts, high velocity layers and seismic reflectors in the lower crust and uppermost mantle are often inferred to be eclogites. Examples have been found in the western Pacific (Widiyantoro et al., 1999), the Dabie-Sulu orogenic belt (Xu et al., 2001), Canada's Superior Province (Calvert et al., 1995; Bostock, 1997) and the Northwest Territories (Cook et al., 1999). Fresh eclogites, which are composed predominantly of omphacitic pyroxene and Ca-Fe-Mg-rich garnet, generally display high seismic velocities and weak anisotropy (Ji et al., 2002 for summary). However, complex eclogitization of basaltic or gabbroic rocks and particularly their retrograde metamorphism to granulite and/or amphibolite facies rocks may produce profound petrologic changes, and in turn affect their seismic velocities and reflectivity (Hacker et al., 2003). To better interpret the seismic data, it is necessary to calibrate the effects of retrograde metamorphism on the seismic velocities and anisotropy of eclogites. Furthermore, the P-wave velocity (*Vp*) and anisotropy of eclogites have been the subject of extensive experimental studies during the past 4 decades due to their importance to the interpretation of seismic data from the lower crust, upper mantle and subduction zones (e.g., Birch, 1960; Kanamori and Mizutani, 1965; Christensen, 1974; Manghnani et al., 1974; Rao et al., 1974; Kern and Richter, 1981; Fountain et al., 1994; Kern et al., 1999, 2002; Mauler et al., 2000; Wang et al., in press). Nevertheless, the experimental data on the S-wave velocity (*Vs*) and shear wave splitting of eclogites and particularly diamond/coesite-bearing ultrahigh-pressure (UHP) eclogites are still very limited (e.g., Manghnani et al., 1974; Kern et al., 1999, 2002) even though their compressional and shear wave velocities and hence Poisson's ratios are critical to interpret correctly the seismic data of lithospheric plates and subduction zones in term of petrology and tectonic processes.

The Qinling-Dabie-Sulu orogenic belt in eastern central China (Figure 5.1) is the largest of the very few UHP metamorphic belts recognized on Earth. The occurrence of

coesite and occasionally micro-diamonds in eclogite and their country rocks such as garnet peridotite, granitic gneiss, paragneiss and marble indicates that these crustal materials, initially from the continental margin of the Yangtze craton, have been subducted to more than 100 km and then rapidly emplaced by buoyancy-driven exhumation to crustal depths (e.g., Zhang et al., 1994; Liou et al., 1998; Hacker et al., 2000; Faure et al., 2003a-b). In the first 2000-meters of core from the main hole of the Chinese Continental Scientific Drilling (CCSD) project at Maobei Village, Donghai County, Jiangsu Province (Figure 1), the cumulative thickness of eclogites exceeds 1000 m (Xu, 2004; Zhang et al., 2004). Although eclogites are volumetrically important in outcrops and drill holes, how much eclogites remain in today's Dabie-Sulu deep crust? What is the tectonic implication if an UHP-free middle-lower crust occurs beneath the UHP metamorphic unit? To answer these questions, measurements of the seismic properties of eclogites and their country rocks and a comparison of the laboratory results with field seismic refraction data at in situ conditions are required.

In this paper, we first report our results on *Vs*, anisotropy (*As*), and shear wave splitting (ΔVs) of UHP rocks from the Dabie-Sulu orogenic belt under hydrostatic pressures up to 600-800 MPa, with a focus on eclogites. These results, together with our data on P-wave velocities for the same set of samples (Wang et al., in press) and reliable data of previous workers, allow us to determine new estimates of pressure and temperature derivatives of *Vp* and *Vs*, and Poisson's ratios (σ) for common rock types in the UHP metamorphic belt. Finally, we use the geometric mean as a mixture rule to invert the lithological and in turn chemical compositions of the layered crust from the integrated information on *Vp*, *Vs* and σ as well as direct examination of deeply exhumed rocks. The inferred crustal composition suggests that the eclogite-bearing UHP rocks are tectonic slices that have been thrust along a series of shear zones during the continental collision between the North China and Yangtze cratons over a normal, UHP-free middle-lower crust with an overall intermediate composition.

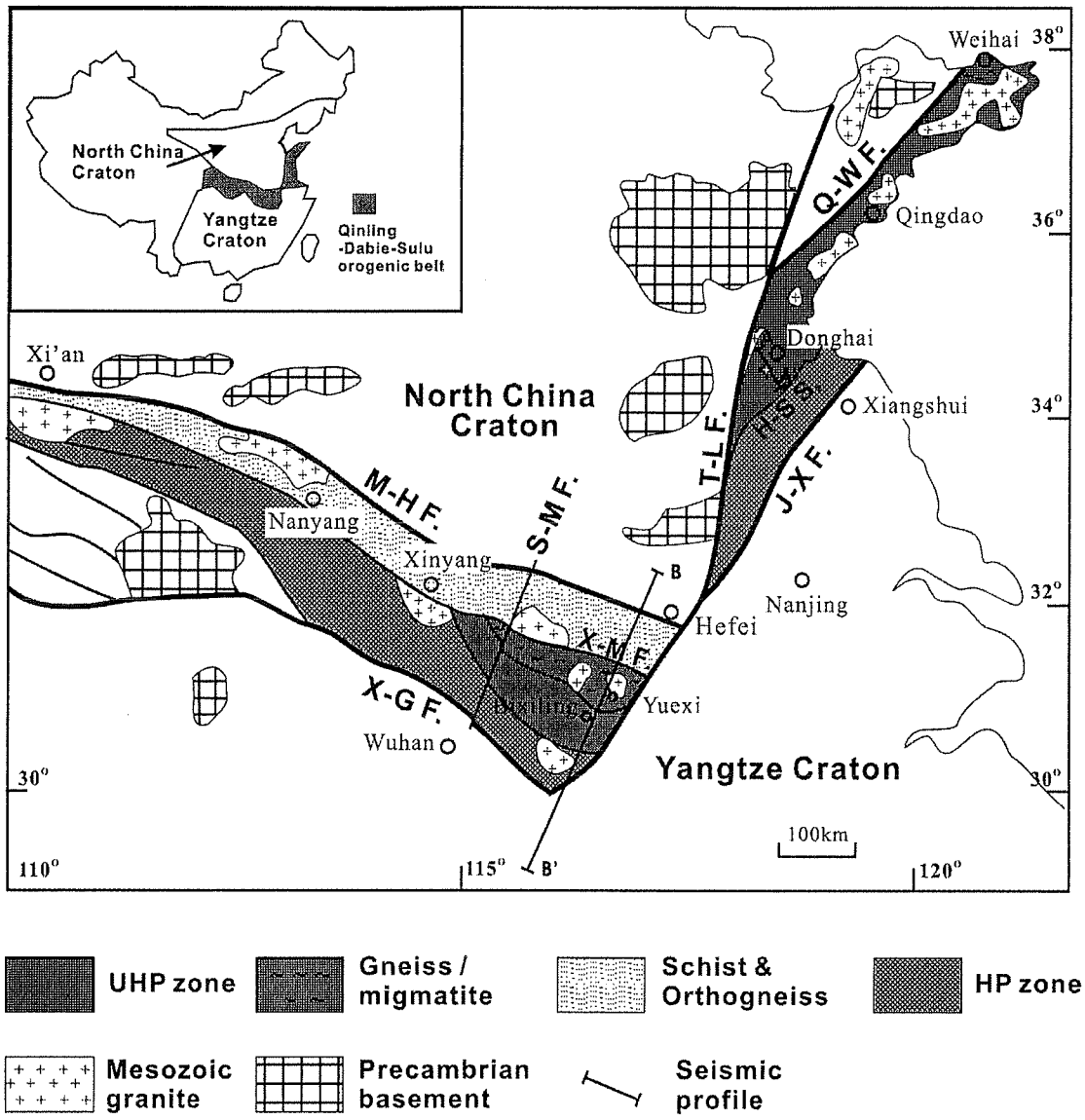


Figure 5.1 Simplified geological map of the Dabie-Sulu UHP metamorphic belt, eastern-central China. Star shows location of drill site (Maobei, Donghai County, Jiangsu Province) of the Chinese Continental Scientific Drilling (CCSD) program. AA′ and BB′ indicate seismic refraction profiles in the Dabie and Sulu areas, respectively. Bold lines denote faults or shear zones: Qingdao-Wulian fault (Q-W F.), Haizhou-Siyang shear zone (H-S S.), Jiashan-Xiangshui fault (J-X F.), Tan-Lu fault (T-L F.), Maoji-Hefei fault (M-H F.), Xiaotian-Mozitan fault (X-M F.), Xiangfan-Guangji fault (X-G F.), Shangcheng-Macheng fault (S-M F.).

5.3 Geological setting

The Qinling-Dabie-Sulu orogenic belt was formed by the collision of the North China and Yangtze cratons during the Triassic and the subsequent subduction of the Yangtze craton beneath the North China craton until the Jurassic (e.g., Liou et al., 2000b; Hacker et al., 2000; Faure et al., 2003a). The peak metamorphism conditions in the Dabie-Sulu area are estimated to have been T ≈ 600-900 °C and P > 2.6 GPa between 220-240 Ma (e.g., Li et al., 1999; Liu et al., 2004), forming diamond- and coesite-bearing UHP metamorphic rocks such as eclogite, garnet peridotite, pelitic and granitic gneisses and marble (e.g., Xu et al., 1992; Zhang et al., 1994; Liou et al., 1998). Two stages of exhumation, an earlier rapid exhumation from mantle depths to mid-crustal levels and a later slow uplift to the Earth's surface, have been revealed for the UHP rocks (e.g., Hacker et al., 1995; Liu et al., 2004).

Bounded by the Tan-Lu fault in the east and the Shangcheng-Macheng fault in the west, the region of Dabie Mountains can be divided into four EW-oriented units: the northern micaschist-orthogneiss domain, the central migmatitic dome, the southern UHP zone and the high-pressure (HP) zone (Figure 5.1). The recent discovery of eclogite xenoliths in the Cretaceous granodiorite from the central Dabie migmatitic dome indicates that UHP rocks could extend further north and underlie the greenschist to amphibolite facies metamorphic rocks of the northern Dabie domain (Faure et al., 2003b). The syn-convergence early exhumation of UHP rocks during 210-220 Ma might have triggered the migmatization and doming in the central Dabie domain. During 180-210 Ma, a regional top-to-NW thrusting under amphibolite facies conditions occurred in the Dabie Mountains (e.g., Hacker et al., 2000; Faure et al., 2003b) and the Sulu terrane (e.g., Wallis et al., 1999; Liou et al., 2000b; Faure et al., 2003a), developing a SE-SSE dipping foliation and SE-plunging stretching lineation in the south and a NW-NWW dipping foliation and NW-plunging stretching lineation in the north. Finally, the Cretaceous extension event in East China reactivated some old faults and formed

sedimentary basins, and the Yanshannian granitic to granodioritic plutons intruded in the region.

The Sulu terrane is the east segment of the Qinling-Dabie-Sulu orogenic belt, displaced about 530 km northward by the sinistral Tan-Lu fault during the Cretaceous to Cenozoic. Bounded by the Qingdao-Wulian fault in the north and the Jiashan-Xiangshui fault in the south, the Sulu terrane can be further divided into the UHP zone and the HP zone by the Haizhou-Siyang shear zone (Figure 5.1). Eclogite occurs as boudins, lenses, pods and layers ranging from tens of centimetres to hundreds of meters in size within granitic gneiss, paragneiss, marble and ultramafic rocks. A granulite facies overprint on coesite-bearing eclogites has been observed in the Taohang (Yao et al., 2000) and Weihai areas (Banno et al., 2000) in the northern part of the UHP zone. The granulite facies metamorphism might be produced by fluid infiltration during the early exhumation prior to the regional amphibolite facies retrograde metamorphism. However, evidence for granulite facies retrograde metamorphism has not been documented in the southern part of the Sulu UHP terrane.

5.4 Samples and experimental technique

We collected 17 eclogite samples and 6 country rocks including granitic gneiss, amphibolite, serpentinite and marble from the Sulu UHP zone, and two retrograde eclogites from the Bixiling complex of the Dabie Mountains (Figure 5.1). The Bixiling complex, surrounded by biotite gneisses, contains talc in eclogites, and Ti-clinohumite and magnesite in ultramafic rocks. The peak metamorphism occurred at 610-700 °C and P>2.7 GPa (Zhang et al., 1995). The complex is characterized by extremely high rates of initial cooling (40 °C/Ma) and uplift (~10 mm/year) at 210-220 Ma, followed by a slow uplift of 3 mm/year from the middle crust to the surface (Chavagnac and Jahn, 1996). Twelve eclogite samples were collected from the CCSD site and surrounding Sulu terrane. The peak metamorphism for the Sulu terrane occurred at 750-900 °C and P>2.8

GPa (Zhang et al., 1994; Ji et al., 2003). The Maobei eclogites experienced slow cooling and uplift rates of ~5 mm/year (Liu et al., 2004) between 210-230 Ma. An exhumation rate of ~1 mm/year (Jahn et al., 1996) has been reported for the eclogites from Weihai, located at the northeastern end of the Sulu UHP unit. It is likely that the Sulu and Dabie terranes have a different exhumation history.

Detailed descriptions of rock samples, their chemical composition and modal composition were reported in a separate paper on P-wave velocities (Wang et al., in press). Three types of eclogites were classified: Type-1 are coarse-grained eclogites formed in the diamond stability field, with a typical mineral assemblage Grt + Omp + Rt ± Coe/Qtz ± Phn (mineral abbreviations after Kretz, 1983), representing eclogites under the peak metamorphism conditions. Type-2 eclogites are fine-grained eclogites that experienced recrystallization-accommodated dislocation creep at quartz/coesite boundary conditions; these are Type-1 eclogites that were reworked during the early stage of exhumation. Type-3 eclogites are rocks that experienced retrograde metamorphism under amphibolite facies conditions during late exhumation within the crust. They are characterized by retrograde assemblages of amphibole, quartz, plagioclase and epidote. Type-1 eclogites are richer in Al_2O_3 and MgO but poorer in SiO_2 and Na_2O than Type-2 and Type-3 eclogites (Wang et al., in press), which is consistent with the abundance of garnet in the Type-1 eclogites.

The S-wave velocity (*Vs*) measurements were carried out at various hydrostatic pressures and room temperature on dry samples using the pulse transmission technique (Birch, 1960; Christensen, 1985). Except for samples MB27, MB30 and MB2B that were measured at confining pressures up to 800 MPa, all samples were measured up to 600 MPa. For most samples, three cylindrical cores (2.54 cm in diameter and 3-5 cm in length) were cut in orthogonal directions, with the X direction parallel to the stretching lineation, the Y direction perpendicular to lineation and parallel to foliation, and the Z direction normal to foliation. For small samples, only one or two cores were taken. The

ends of the jacketed cores were covered with copper foil and then capped with 1 MHz lead zirconate titanate shear wave transducers and copper electrodes. The method gives *Vs* accuracies within 1% (Christensen, 1985; Ji and Salisbury, 1993). In order to examine shear wave splitting, six measurements, designed XY, XZ, YX, YZ, ZX, ZY, were undertaken for each sample. The first letter refers to the propagation direction and the second to the polarization direction. The *Vs* measurements were performed at the GSC/Dalhousie High Pressure Laboratory in Halifax, Nova Scotia.

5.5 Experimental results

5.5.1 Shear wave velocities

Table 5.1 lists shear wave velocities and anisotropy of 25 UHP rocks at various confining pressures and room temperature. All reported data were measured during decompression. No correction is done for length change since the effect on velocities at 1000 MPa is less than 1% for low porosity samples (Birch, 1960). Figure 5.2 illustrates shear wave velocities for three typical eclogite samples: MB27, SB1 and 98501 representing Type-1, Type-2 and Type-3 eclogites, respectively. The velocity rises rapidly at low pressures (<300 MPa) and then increases slowly above 300-400 MPa, which is attributed to the closure of microcracks and pore spaces with increasing pressures (e.g., Christensen, 1966). The mean shear wave velocity is defined by

$$\overline{Vs} = (Vs_{XY} + Vs_{XZ} + Vs_{YX} + Vs_{YZ} + Vs_{ZX} + Vs_{ZY})/6 \qquad (5.1)$$

The different $\overline{Vs}$ values for samples MB27, SB1 and 98501 reflect differences in modal composition and microstructure (Figure 5.2d).

Table 5.1 S-wave velocities (km/s) and anisotropy (%) at various confining pressures for UHP rocks from the Dabie-Sulu belt

Sample		ρ	Pressure (MPa)											
		(g/cm³)	20	50	80	100	150	200	250	300	400	500	600	800
Coarse-grained eclogite														
86351	XY		4.23	4.46	4.58	4.64	4.69	4.71	4.74	4.76	4.80	4.83	4.85	*4.89*
	XZ		4.29	4.47	4.62	4.69	4.77	4.78	4.79	4.80	4.81	4.82	4.83	*4.85*
	Mx	3.510	4.26	4.47	4.60	4.66	4.73	4.75	4.76	4.78	4.81	4.82	4.84	*4.87*
	Ax		1.38	0.11	0.80	1.20	1.56	1.43	1.13	0.77	0.17	0.17	0.35	*0.86*
	YX		4.34	4.48	4.56	4.59	4.62	4.64	4.66	4.68	4.71	4.73	4.75	*4.81*
	YZ		4.04	4.38	4.51	4.55	4.61	4.66	4.70	4.71	4.74	4.76	4.78	*4.82*
	My	3.459	4.19	4.43	4.53	4.57	4.62	4.65	4.68	4.69	4.72	4.75	4.77	*4.82*
	Ay		7.18	2.28	1.24	0.83	0.15	0.54	0.81	0.75	0.64	0.53	0.52	*0.27*
	ZX		4.30	4.44	4.54	4.57	4.60	4.61	4.63	4.64	4.66	4.68	4.69	*4.74*
	ZY		4.25	4.43	4.49	4.51	4.56	4.58	4.60	4.61	4.63	4.65	4.67	*4.71*
	Mz	3.500	4.27	4.44	4.51	4.54	4.58	4.60	4.61	4.63	4.64	4.66	4.68	*4.72*
	Az		1.24	0.09	0.97	1.41	1.00	0.67	0.59	0.61	0.75	0.62	0.62	*0.64*
	M	3.490	4.24	4.44	4.55	4.59	4.64	4.67	4.68	4.70	4.72	4.74	4.76	*4.80*
	A		7.10	2.27	2.84	3.98	4.50	4.24	4.08	3.98	3.87	3.73	3.78	*3.91*
MB22	XY		4.39	4.53	4.60	4.63	4.67	4.71	4.73	4.75	4.77	4.79	4.80	*4.83*
	XZ		4.12	4.31	4.47	4.54	4.66	4.71	4.73	4.74	4.76	4.78	4.79	*4.82*
	Mx	3.551	4.25	4.42	4.53	4.59	4.66	4.71	4.73	4.74	4.77	4.78	4.79	*4.82*
	Ax		6.33	4.82	3.07	1.96	0.28	0.04	0.02	0.11	0.23	0.23	0.25	*0.15*
MB23	XY		4.50	4.64	4.72	4.75	4.78	4.79	4.81	4.83	4.86	4.88	4.89	*4.91*
	XZ		4.55	4.59	4.63	4.65	4.69	4.71	4.73	4.74	4.75	4.76	4.77	*4.80*
	Mx	3.548	4.53	4.61	4.67	4.70	4.73	4.75	4.77	4.78	4.81	4.82	4.83	*4.85*
	Ax		1.10	0.91	1.90	2.06	1.82	1.73	1.80	1.92	2.16	2.30	2.32	*2.31*
	YX		4.45	4.58	4.66	4.68	4.72	4.74	4.76	4.78	4.80	4.81	4.82	*4.83*
	YZ		4.24	4.36	4.44	4.47	4.51	4.54	4.55	4.56	4.58	4.60	4.62	*4.66*
	My	3.489	4.35	4.47	4.55	4.58	4.62	4.64	4.66	4.67	4.69	4.71	4.72	*4.75*
	Ay		4.74	5.06	4.79	4.59	4.42	4.48	4.60	4.63	4.65	4.38	4.18	*3.54*
	ZX		4.14	4.27	4.37	4.41	4.47	4.51	4.54	4.56	4.60	4.63	4.65	*4.68*
	ZY		4.32	4.46	4.56	4.60	4.66	4.70	4.72	4.72	4.74	4.76	4.77	*4.79*
	Mz	3.490	4.23	4.37	4.46	4.51	4.57	4.60	4.63	4.64	4.67	4.69	4.71	*4.74*
	Az		4.25	4.28	4.35	4.33	4.16	4.09	3.87	3.53	2.93	2.60	2.38	*2.39*
	M	3.509	4.37	4.48	4.56	4.59	4.64	4.66	4.68	4.70	4.72	4.74	4.75	*4.78*
	A		9.32	8.10	7.76	7.38	6.55	6.15	5.91	5.73	5.84	5.72	5.60	*5.11*
MB25	XY		3.98	4.28	4.40	4.46	4.52	4.54	4.56	4.58	4.61	4.63	4.65	*4.70*
	XZ		4.35	4.51	4.58	4.61	4.65	4.68	4.70	4.71	4.73	4.75	4.76	*4.79*
	Mx	3.561	4.16	4.39	4.49	4.53	4.59	4.61	4.63	4.64	4.67	4.69	4.70	*4.75*
	Ax		9.03	5.21	3.96	3.22	2.88	2.93	2.89	2.71	2.55	2.41	2.23	*1.85*
	YX		4.43	4.62	4.72	4.76	4.82	4.85	4.88	4.90	4.92	4.93	4.94	*4.95*
	YZ		4.44	4.57	4.67	4.70	4.74	4.75	4.77	4.79	4.82	4.84	4.86	*4.91*
	My	3.586	4.43	4.60	4.69	4.73	4.78	4.80	4.83	4.84	4.87	4.88	4.90	*4.93*
	Ay		0.20	0.94	1.21	1.23	1.68	2.08	2.24	2.29	2.03	1.72	1.55	*0.99*

Table 5.1 (continued)

Sample		ρ	Pressure (MPa)											
		(g/cm³)	20	50	80	100	150	200	250	300	400	500	600	800
MB25	ZX		4.57	4.68	4.75	4.78	4.82	4.84	4.86	4.88	4.90	4.91	4.92	*4.96*
	ZY		4.50	4.60	4.68	4.72	4.78	4.82	4.84	4.86	4.89	4.90	4.92	*4.95*
	Mz	3.621	4.54	4.64	4.72	4.75	4.80	4.83	4.85	4.87	4.89	4.91	4.92	*4.95*
	Az		1.70	1.70	1.46	1.22	0.73	0.58	0.52	0.41	0.22	0.22	0.14	*0.12*
	M	3.589	4.38	4.54	4.64	4.67	4.72	4.75	4.77	4.78	4.81	4.83	4.84	*4.88*
	A		13.66	8.87	7.53	6.87	6.31	6.53	6.69	6.67	6.43	6.09	5.85	*5.17*
MB26	XY		4.48	4.60	4.68	4.71	4.74	4.76	4.78	4.79	4.82	4.84	4.85	*4.89*
	XZ		4.36	4.53	4.63	4.67	4.73	4.76	4.78	4.79	4.82	4.84	4.85	*4.88*
	Mx	3.585	4.42	4.56	4.66	4.69	4.73	4.76	4.78	4.79	4.82	4.84	4.85	*4.89*
	Ax		2.72	1.58	0.99	0.81	0.38	0.06	0.02	0.00	0.06	0.00	0.02	*0.12*
	YX		4.47	4.56	4.63	4.67	4.73	4.75	4.77	4.79	4.81	4.83	4.84	*4.87*
	YZ		4.52	4.61	4.68	4.71	4.74	4.76	4.77	4.79	4.81	4.82	4.84	*4.86*
	My	3.523	4.49	4.58	4.65	4.69	4.73	4.76	4.77	4.79	4.81	4.83	4.84	*4.87*
	Ay		1.11	1.18	1.03	0.85	0.38	0.17	0.00	0.13	0.06	0.12	0.08	*0.16*
	ZX		4.50	4.62	4.70	4.74	4.79	4.82	4.84	4.85	4.87	4.88	4.89	*4.92*
	ZY		4.49	4.61	4.70	4.73	4.78	4.80	4.81	4.82	4.84	4.85	4.86	*4.88*
	Mz	3.575	4.50	4.61	4.70	4.74	4.79	4.81	4.82	4.83	4.85	4.87	4.87	*4.90*
	Az		0.36	0.17	0.11	0.17	0.33	0.44	0.50	0.50	0.52	0.62	0.64	*0.82*
	M	3.561	4.47	4.59	4.67	4.71	4.75	4.78	4.79	4.80	4.83	4.84	4.85	*4.88*
	A		3.56	1.96	1.58	1.62	1.45	1.42	1.31	1.27	1.18	1.16	1.11	*1.11*
MB27	XY		4.48	4.62	4.70	4.73	4.78	4.80	4.82	4.84	4.87	4.89	4.91	4.93
	XZ		4.45	4.61	4.71	4.75	4.79	4.81	4.82	4.83	4.86	4.87	4.88	4.89
	Mx	3.559	4.46	4.61	4.70	4.74	4.78	4.80	4.82	4.84	4.86	4.88	4.89	4.91
	Ax		0.65	0.24	0.28	0.30	0.15	0.12	0.04	0.14	0.21	0.39	0.61	0.84
	YX		4.56	4.64	4.71	4.75	4.80	4.82	4.84	4.85	4.87	4.88	4.90	4.92
	YZ		4.63	4.68	4.73	4.75	4.79	4.81	4.82	4.84	4.86	4.88	4.88	4.90
	My	3.609	4.59	4.66	4.72	4.75	4.79	4.82	4.83	4.84	4.87	4.88	4.89	4.91
	Ay		1.52	0.84	0.32	0.06	0.23	0.29	0.31	0.33	0.18	0.18	0.22	0.37
	ZX		4.48	4.60	4.68	4.72	4.77	4.78	4.80	4.81	4.82	4.83	4.84	4.86
	ZY		4.53	4.66	4.72	4.75	4.77	4.80	4.82	4.83	4.85	4.87	4.87	4.89
	Mz	3.578	4.50	4.63	4.70	4.73	4.77	4.79	4.81	4.82	4.84	4.85	4.86	4.87
	Az		1.18	1.34	0.83	0.46	0.13	0.25	0.44	0.52	0.68	0.70	0.64	0.55
	M	3.582	4.52	4.63	4.71	4.74	4.78	4.80	4.82	4.83	4.85	4.87	4.88	4.90
	A		4.03	1.88	0.91	0.57	0.63	0.81	0.91	0.95	1.07	1.21	1.35	1.45
MB30	XY		4.45	4.51	4.57	4.60	4.65	4.69	4.71	4.74	4.78	4.80	4.81	*4.83*
	XZ		4.31	4.46	4.56	4.60	4.65	4.68	4.69	4.71	4.73	4.75	4.76	*4.80*
	Mx	3.566	4.38	4.49	4.56	4.60	4.65	4.68	4.70	4.72	4.75	4.77	4.79	*4.82*
	Ax		3.08	1.20	0.15	0.11	0.00	0.26	0.45	0.64	0.95	1.11	1.00	*0.62*
	ZX		4.31	4.46	4.56	4.60	4.65	4.68	4.69	4.71	4.73	4.75	4.76	4.80
	ZY		4.55	4.66	4.73	4.76	4.79	4.81	4.82	4.83	4.85	4.86	4.87	4.89
	Mz	3.625	4.43	4.56	4.64	4.68	4.72	4.74	4.76	4.77	4.79	4.80	4.81	4.85
	Az		5.22	4.37	3.62	3.27	2.97	2.83	2.69	2.56	2.40	2.23	2.14	1.86
	M	3.586	4.41	4.52	4.60	4.64	4.69	4.71	4.73	4.75	4.77	4.79	4.80	4.83
	A		5.24	4.40	3.65	3.41	2.99	2.84	2.71	2.57	2.41	2.23	2.15	1.86

Table 5.1 (continued)

Sample		ρ	Pressure (MPa)											
		(g/cm³)	20	50	80	100	150	200	250	300	400	500	600	800
MB2A	XY		4.66	4.76	4.83	4.85	4.89	4.91	4.93	4.93	4.95	4.96	4.97	*4.99*
	XZ		4.48	4.63	4.71	4.73	4.75	4.76	4.77	4.78	4.80	4.81	4.82	*4.85*
	Mx	3.636	4.57	4.70	4.77	4.79	4.82	4.84	4.85	4.86	4.88	4.89	4.90	*4.92*
	Ax		3.85	2.81	2.50	2.55	2.92	3.06	3.11	3.11	2.97	2.99	3.02	*2.86*
Coarse-grained granetite														
MB2B	XY		4.63	4.73	4.80	4.82	4.86	4.88	4.90	4.92	4.94	4.95	4.96	4.97
	XZ		4.63	4.75	4.80	4.82	4.86	4.89	4.92	4.93	4.94	4.96	4.96	4.97
	Mx	3.612	4.63	4.74	4.80	4.82	4.86	4.89	4.91	4.92	4.94	4.95	4.96	4.97
	Ax		0.11	0.34	0.00	0.15	0.10	0.33	0.35	0.26	0.12	0.10	0.12	0.12
MB34	XY		4.67	4.77	4.83	4.86	4.88	4.90	4.91	4.92	4.94	4.95	4.96	*4.99*
	XZ		4.54	4.63	4.70	4.74	4.78	4.81	4.82	4.83	4.85	4.86	4.87	*4.90*
	Mx	3.628	4.61	4.70	4.77	4.80	4.83	4.85	4.86	4.88	4.89	4.90	4.92	*4.94*
	Ax		2.91	2.85	2.68	2.54	2.09	1.83	1.83	1.93	1.88	1.90	1.81	*1.76*
MB36	XY		4.38	4.50	4.60	4.65	4.73	4.78	4.81	4.84	4.88	4.90	4.91	*4.93*
	XZ		4.33	4.42	4.50	4.55	4.63	4.67	4.69	4.70	4.73	4.75	4.77	*4.81*
	Mx	3.677	4.35	4.46	4.55	4.60	4.68	4.72	4.75	4.77	4.80	4.83	4.84	*4.87*
	Ax		1.10	1.70	2.11	2.20	2.24	2.39	2.57	2.77	3.02	2.94	2.83	*2.50*
MB62	XY		4.44	4.56	4.65	4.69	4.76	4.79	4.81	4.83	4.86	4.88	4.89	*4.92*
	XZ		4.55	4.68	4.75	4.77	4.80	4.82	4.83	4.84	4.86	4.87	4.88	*4.91*
	Mx	3.556	4.50	4.62	4.70	4.73	4.78	4.80	4.82	4.84	4.86	4.88	4.89	*4.92*
	Ax		2.60	2.60	2.04	1.65	0.92	0.60	0.39	0.23	0.08	0.16	0.25	*0.20*
Fine-grained eclogite														
DG1	XY		4.20	4.27	4.33	4.35	4.40	4.42	4.45	4.47	4.51	4.53	4.55	*4.59*
	XZ		3.86	4.08	4.15	4.20	4.28	4.34	4.38	4.41	4.45	4.48	4.50	*4.57*
	Mx	3.477	4.03	4.17	4.24	4.27	4.34	4.38	4.41	4.44	4.48	4.50	4.53	*4.58*
	Ax		8.29	4.60	4.13	3.70	2.58	1.85	1.52	1.44	1.43	1.22	1.04	*0.46*
	YX		4.19	4.28	4.34	4.36	4.39	4.41	4.43	4.45	4.48	4.50	4.51	*4.54*
	YZ		4.15	4.22	4.29	4.32	4.39	4.43	4.45	4.47	4.50	4.52	4.53	*4.57*
	My	3.453	4.17	4.25	4.31	4.34	4.39	4.42	4.44	4.46	4.49	4.51	4.52	*4.55*
	Ay		0.89	1.39	1.21	0.85	0.00	0.43	0.50	0.40	0.25	0.33	0.35	*0.59*
	ZX		4.10	4.25	4.35	4.39	4.42	4.43	4.45	4.46	4.49	4.51	4.53	*4.58*
	ZY		4.05	4.19	4.28	4.31	4.35	4.37	4.39	4.41	4.44	4.46	4.49	*4.54*
	Mz	3.463	4.07	4.22	4.32	4.35	4.38	4.40	4.42	4.44	4.46	4.49	4.51	*4.56*
	Az		1.35	1.37	1.71	1.86	1.64	1.34	1.24	1.26	1.10	1.00	0.93	*0.77*
	M	3.464	4.09	4.21	4.29	4.32	4.37	4.40	4.43	4.45	4.48	4.50	4.52	*4.56*
	A		8.17	4.84	4.71	4.54	3.11	2.04	1.60	1.44	1.61	1.53	1.39	*1.01*
JC2	XY		4.23	4.38	4.49	4.53	4.57	4.59	4.61	4.62	4.63	4.64	4.65	*4.68*
	XZ		4.31	4.41	4.48	4.51	4.53	4.54	4.54	4.55	4.56	4.57	4.58	*4.61*
	Mx	3.403	4.27	4.40	4.49	4.52	4.55	4.56	4.58	4.58	4.60	4.61	4.62	*4.64*
	Ax		1.83	0.68	0.20	0.46	0.88	1.29	1.46	1.46	1.46	1.54	1.54	*1.59*
	YX		4.36	4.42	4.46	4.49	4.52	4.54	4.55	4.56	4.57	4.59	4.60	*4.62*
	YZ		4.09	4.32	4.41	4.44	4.47	4.49	4.51	4.51	4.54	4.55	4.56	*4.60*
	My	3.383	4.22	4.37	4.44	4.46	4.49	4.51	4.53	4.54	4.55	4.57	4.58	*4.61*
	Ay		6.44	2.22	1.24	1.10	1.14	1.02	0.97	0.99	0.86	0.72	0.72	*0.43*

Table 5.1 (continued)

Sample		ρ	Pressure (MPa)											
		(g/cm³)	20	50	80	100	150	200	250	300	400	500	600	800
JC2	ZX		4.02	4.17	4.28	4.33	4.40	4.42	4.44	4.45	4.47	4.49	4.50	*4.54*
	ZY		4.37	4.42	4.46	4.48	4.52	4.54	4.55	4.56	4.58	4.60	4.61	*4.65*
	Mz	3.413	4.20	4.29	4.37	4.41	4.46	4.48	4.49	4.50	4.52	4.54	4.56	4.60
	Az		8.27	5.80	4.07	3.38	2.74	2.61	2.54	2.40	2.43	2.44	2.39	2.41
	M	3.400	4.23	4.35	4.43	4.46	4.50	4.52	4.53	4.54	4.56	4.57	4.58	4.62
	A		8.20	5.74	4.76	4.44	3.87	3.85	3.84	3.70	3.55	3.41	3.32	3.03
JZ1	ZX		3.91	4.21	4.32	4.37	4.44	4.46	4.47	4.49	4.50	4.52	4.53	*4.57*
	ZY		4.13	4.24	4.31	4.34	4.37	4.39	4.40	4.41	4.42	4.43	4.45	*4.47*
	Mz	3.527	4.02	4.22	4.31	4.35	4.40	4.42	4.44	4.45	4.46	4.48	4.49	*4.52*
	Az		5.67	0.80	0.19	0.83	1.57	1.65	1.71	1.78	1.84	1.97	1.89	*2.08*
SB1	XY		4.29	4.39	4.46	4.49	4.52	4.53	4.54	4.55	4.56	4.57	4.58	*4.60*
	XZ		4.10	4.23	4.28	4.30	4.35	4.39	4.41	4.42	4.45	4.47	4.49	*4.53*
	Mx	3.358	4.20	4.31	4.37	4.39	4.44	4.46	4.47	4.48	4.50	4.52	4.54	*4.57*
	Ax		4.34	3.67	4.15	4.21	3.72	3.23	2.95	2.83	2.46	2.21	2.01	*1.58*
	YX		4.49	4.52	4.55	4.56	4.58	4.60	4.60	4.61	4.62	4.63	4.64	*4.66*
	YZ		4.26	4.34	4.39	4.41	4.43	4.44	4.45	4.46	4.48	4.50	4.52	*4.56*
	My	3.344	4.38	4.43	4.47	4.49	4.51	4.52	4.53	4.54	4.55	4.57	4.58	*4.61*
	Ay		5.12	4.13	3.56	3.39	3.35	3.39	3.27	3.22	3.03	2.76	2.58	*2.11*
	ZX		4.15	4.26	4.31	4.33	4.36	4.39	4.41	4.43	4.46	4.48	4.49	*4.53*
	ZY		4.26	4.32	4.38	4.40	4.43	4.44	4.46	4.47	4.50	4.52	4.54	*4.58*
	Mz	3.403	4.20	4.29	4.34	4.36	4.39	4.41	4.43	4.45	4.48	4.50	4.51	*4.55*
	Az		2.40	1.61	1.61	1.60	1.46	1.20	1.01	0.94	0.85	0.87	0.97	*1.23*
	M	3.368	4.26	4.34	4.39	4.41	4.45	4.46	4.48	4.49	4.51	4.53	4.54	*4.58*
	A		8.99	6.75	6.17	5.87	5.17	4.70	4.36	4.21	3.79	3.51	3.19	*2.84*
Retrograde eclogite														
98401	XY		3.97	4.15	4.22	4.25	4.28	4.30	4.32	4.33	4.35	4.37	4.39	*4.42*
	XZ		3.74	3.90	4.00	4.03	4.07	4.09	4.11	4.13	4.16	4.19	4.20	*4.26*
	Mx	3.465	3.85	4.03	4.11	4.14	4.17	4.19	4.21	4.23	4.26	4.28	4.30	*4.34*
	Ax		5.79	6.13	5.48	5.17	4.99	5.15	5.06	4.80	4.37	4.21	4.24	*3.82*
	YX		4.15	4.31	4.40	4.43	4.46	4.49	4.50	4.52	4.55	4.57	4.59	*4.64*
	YZ		4.02	4.13	4.21	4.25	4.30	4.31	4.32	4.33	4.35	4.36	4.37	*4.41*
	My	3.489	4.08	4.22	4.30	4.34	4.38	4.40	4.41	4.42	4.45	4.47	4.48	*4.53*
	Ay		3.11	4.48	4.23	3.99	3.70	4.05	4.24	4.32	4.48	4.66	4.82	*5.10*
	M	3.477	3.97	4.12	4.21	4.24	4.27	4.30	4.31	4.33	4.35	4.37	4.39	*4.43*
	A		10.13	9.97	9.46	9.29	9.12	9.29	9.23	9.02	8.78	8.76	8.77	*8.66*
98501	XY		4.29	4.35	4.39	4.41	4.45	4.46	4.47	4.48	4.49	4.51	4.52	*4.55*
	XZ		4.19	4.25	4.29	4.30	4.33	4.34	4.36	4.37	4.38	4.40	4.41	*4.44*
	Mx	3.491	4.24	4.30	4.34	4.36	4.39	4.40	4.41	4.42	4.44	4.45	4.46	*4.49*
	Ax		2.43	2.33	2.42	2.50	2.74	2.73	2.56	2.51	2.46	2.40	2.42	*2.38*
	YX		4.05	4.22	4.29	4.32	4.36	4.38	4.39	4.40	4.41	4.42	4.43	*4.46*
	YZ		3.89	4.17	4.25	4.28	4.31	4.33	4.35	4.37	4.40	4.43	4.45	*4.51*
	My	3.463	3.97	4.19	4.27	4.30	4.33	4.36	4.37	4.38	4.41	4.42	4.44	*4.48*
	Ay		3.93	1.41	0.91	1.09	1.15	0.96	0.82	0.62	0.23	0.07	0.36	*1.07*
	ZX		3.47	3.59	3.67	3.70	3.73	3.74	3.75	3.75	3.77	3.78	3.79	*3.81*

Table 5.1 (continued)

Sample		ρ	Pressure (MPa)											
		(g/cm³)	20	50	80	100	150	200	250	300	400	500	600	800
98501	ZY		3.61	3.64	3.67	3.68	3.70	3.72	3.72	3.73	3.75	3.76	3.77	*3.80*
	Mz	3.470	3.54	3.62	3.67	3.69	3.71	3.73	3.73	3.74	3.76	3.77	3.78	*3.81*
	Az		4.01	1.55	0.03	0.43	0.57	0.54	0.62	0.56	0.53	0.40	0.40	*0.21*
	M	3.475	3.92	4.03	4.09	4.12	4.14	4.16	4.17	4.18	4.20	4.21	4.23	*4.26*
	A		20.92	18.79	17.67	17.74	17.90	17.88	17.86	17.81	17.74	17.65	17.63	*17.47*
QL2	XY		3.62	4.01	4.24	4.31	4.39	4.43	4.46	4.49	4.53	4.57	4.60	*4.69*
	XZ		3.67	3.98	4.11	4.16	4.28	4.35	4.39	4.43	4.49	4.52	4.54	*4.59*
	Mx	3.413	3.65	3.99	4.17	4.23	4.34	4.39	4.42	4.46	4.51	4.55	4.57	*4.64*
	Ax		1.40	0.68	3.09	3.43	2.35	1.78	1.49	1.30	0.95	1.23	1.40	*2.11*
	YX		3.91	4.08	4.17	4.20	4.25	4.29	4.33	4.35	4.38	4.40	4.41	*4.43*
	YZ		3.88	4.00	4.08	4.12	4.18	4.21	4.24	4.26	4.30	4.33	4.35	*4.38*
	My	3.415	3.89	4.04	4.13	4.16	4.22	4.25	4.28	4.31	4.34	4.36	4.38	*4.41*
	Ay		0.85	2.08	2.01	1.85	1.73	1.90	2.03	2.07	1.91	1.58	1.39	*1.07*
	ZX		3.89	4.05	4.09	4.11	4.15	4.17	4.18	4.18	4.21	4.22	4.23	*4.25*
	ZY		3.56	3.73	3.86	3.92	3.98	4.01	4.03	4.05	4.08	4.11	4.13	*4.20*
	Mz	3.430	3.73	3.89	3.98	4.02	4.06	4.09	4.10	4.12	4.14	4.17	4.18	*4.23*
	Az		8.72	8.02	5.66	4.68	4.13	3.94	3.63	3.33	2.97	2.50	2.20	*1.30*
	M	3.419	3.76	3.97	4.09	4.14	4.20	4.24	4.27	4.29	4.33	4.36	4.38	*4.42*
	A		*9.27*	*8.71*	*9.09*	*9.26*	*9.66*	*9.88*	*10.05*	*10.27*	*10.41*	*10.53*	*10.72*	*11.06*
Amphibolite														
QL4	XY		2.95	3.14	3.28	3.34	3.42	3.46	3.49	3.53	3.58	3.60	3.62	*3.66*
	XZ		2.94	3.17	3.28	3.33	3.43	3.48	3.52	3.56	3.61	3.65	3.68	*3.73*
	Mx	2.955	2.94	3.15	3.28	3.34	3.42	3.47	3.51	3.54	3.59	3.62	3.65	*3.69*
	Ax		0.37	0.79	0.09	0.30	0.32	0.75	0.91	0.93	0.92	1.52	1.59	*1.90*
	YX		2.79	3.12	3.33	3.41	3.52	3.56	3.58	3.60	3.61	3.64	3.66	*3.70*
	YZ		2.90	3.11	3.25	3.30	3.41	3.48	3.52	3.55	3.60	3.63	3.64	*3.69*
	My	2.971	2.85	3.11	3.29	3.36	3.46	3.52	3.55	3.57	3.60	3.63	3.65	*3.69*
	Ay		3.79	0.13	2.37	3.22	3.06	2.44	1.72	1.34	0.53	0.33	0.41	*0.51*
	ZX		2.88	3.15	3.28	3.35	3.44	3.48	3.51	3.54	3.59	3.62	3.65	*3.71*
	ZY		2.86	3.07	3.20	3.26	3.36	3.42	3.47	3.50	3.54	3.56	3.58	*3.64*
	Mz	2.966	2.87	3.11	3.24	3.31	3.40	3.45	3.49	3.52	3.57	3.59	3.62	*3.67*
	Az		0.73	2.44	2.66	2.84	2.47	1.65	1.17	1.08	1.46	1.64	1.91	*2.12*
	M	2.964	2.89	3.13	3.27	3.33	3.43	3.48	3.52	3.55	3.59	3.62	3.64	*3.69*
	A		5.40	3.01	4.01	4.59	4.58	4.08	3.16	2.59	2.06	2.41	2.50	*2.50*
YM4	XY		3.96	4.02	4.06	4.08	4.10	4.11	4.12	4.13	4.14	4.16	4.16	*4.19*
	XZ		3.80	3.88	3.95	3.98	4.03	4.05	4.06	4.06	4.08	4.09	4.10	*4.12*
	Mx	3.086	3.88	3.95	4.00	4.03	4.07	4.08	4.09	4.10	4.11	4.12	4.13	*4.16*
	Ax		4.18	3.39	2.67	2.28	1.72	1.59	1.59	1.59	1.53	1.55	1.55	*1.61*
	YX		3.88	3.95	3.98	3.99	4.01	4.03	4.04	4.05	4.06	4.07	4.07	*4.09*
	YZ		3.65	3.73	3.79	3.82	3.84	3.85	3.86	3.88	3.90	3.91	3.93	*3.97*
	My	3.035	3.76	3.84	3.89	3.90	3.93	3.94	3.95	3.96	3.98	3.99	4.00	*4.03*
	Ay		6.11	5.62	4.84	4.46	4.28	4.39	4.40	4.32	4.07	3.89	3.60	*3.00*
	ZX		3.84	3.92	3.97	3.99	4.01	4.03	4.04	4.05	4.06	4.07	4.08	*4.11*
	ZY		3.61	3.68	3.73	3.76	3.81	3.83	3.85	3.86	3.88	3.90	3.91	*3.95*

Table 5.1 (continued)

Sample		ρ	Pressure (MPa)											
		(g/cm³)	20	50	80	100	150	200	250	300	400	500	600	800
YM4	Mz	3.089	3.73	3.80	3.85	3.87	3.91	3.93	3.94	3.95	3.97	3.99	4.00	*4.03*
	Az		6.09	6.40	6.18	5.89	5.24	4.94	4.82	4.83	4.69	4.47	4.30	*3.77*
	M	3.070	3.79	3.86	3.91	3.94	3.97	3.98	3.99	4.00	4.02	4.03	4.04	*4.07*
	A		9.10	8.75	8.33	8.03	7.33	6.96	6.86	6.85	6.59	6.42	6.21	*5.80*
Granitic gneiss														
TF1	XY		3.54	3.64	3.71	3.74	3.79	3.81	3.82	3.83	3.84	3.85	3.86	*3.88*
	XZ		3.55	3.62	3.67	3.70	3.74	3.76	3.77	3.78	3.79	3.80	3.81	*3.83*
	Mx	2.655	3.54	3.63	3.69	3.72	3.76	3.79	3.80	3.80	3.82	3.83	3.84	*3.86*
	Ax		0.17	0.61	1.00	1.16	1.28	1.16	1.16	1.24	1.31	1.31	1.30	*1.24*
	YX		3.23	3.45	3.55	3.60	3.68	3.72	3.74	3.75	3.78	3.81	3.82	*3.84*
	YZ		3.55	3.70	3.74	3.75	3.77	3.79	3.80	3.80	3.81	3.82	3.83	*3.85*
	My	2.679	3.39	3.57	3.64	3.68	3.72	3.75	3.77	3.78	3.80	3.81	3.82	*3.84*
	Ay		9.41	7.00	4.99	4.24	2.60	2.02	1.67	1.30	0.79	0.45	0.31	*0.31*
	ZX		3.86	3.94	3.99	4.00	4.02	4.02	4.03	4.04	4.05	4.06	4.06	*4.08*
	ZY		3.84	3.91	3.97	3.99	4.02	4.03	4.03	4.03	4.05	4.06	4.06	*4.08*
	Mz	2.657	3.85	3.93	3.98	4.00	4.02	4.02	4.03	4.04	4.05	4.06	4.06	*4.08*
	Az		0.39	0.79	0.60	0.35	0.02	0.05	0.00	0.05	0.00	0.00	0.02	*0.05*
	M	2.664	3.59	3.71	3.77	3.80	3.84	3.85	3.86	3.87	3.89	3.90	3.91	*3.93*
	A		17.45	13.43	11.59	10.72	8.89	8.02	7.53	7.31	6.79	6.49	6.43	*6.37*
TF3	XY		3.33	3.48	3.56	3.59	3.63	3.65	3.67	3.68	3.70	3.71	3.72	*3.74*
	XZ		3.32	3.44	3.51	3.55	3.60	3.63	3.65	3.66	3.68	3.69	3.70	*3.72*
	Mx	2.659	3.33	3.46	3.54	3.57	3.62	3.64	3.66	3.67	3.69	3.70	3.71	*3.73*
	Ax		0.30	1.21	1.39	1.20	0.77	0.58	0.55	0.60	0.54	0.59	0.54	*0.54*
	YX		3.34	3.49	3.54	3.55	3.57	3.59	3.60	3.61	3.63	3.64	3.65	*3.68*
	YZ		3.24	3.41	3.48	3.51	3.55	3.57	3.58	3.60	3.62	3.65	3.66	*3.72*
	My	2.655	3.29	3.45	3.51	3.53	3.56	3.58	3.59	3.60	3.62	3.64	3.66	*3.70*
	Ay		3.22	2.29	1.71	1.10	0.59	0.50	0.47	0.39	0.11	0.22	0.38	*0.97*
	ZX		3.11	3.29	3.40	3.44	3.47	3.50	3.52	3.53	3.56	3.57	3.58	*3.62*
	ZY		3.25	3.38	3.45	3.48	3.51	3.53	3.55	3.56	3.58	3.60	3.61	*3.63*
	Mz	2.660	3.18	3.33	3.43	3.46	3.49	3.51	3.53	3.55	3.57	3.58	3.59	*3.62*
	Az		4.28	2.58	1.43	1.13	1.00	0.88	0.85	0.85	0.78	0.64	0.67	*0.39*
	M	2.658	3.27	3.41	3.49	3.52	3.56	3.58	3.59	3.61	3.63	3.64	3.65	*3.68*
	A		7.01	5.80	4.58	4.35	4.39	4.36	4.31	4.27	3.89	3.76	3.67	*3.37*
Serpentinite														
XG3	XY		2.84	2.86	2.87	2.87	2.88	2.89	2.89	2.90	2.91	2.91	2.92	*2.93*
	XZ		2.83	2.84	2.85	2.86	2.87	2.88	2.88	2.88	2.89	2.89	2.90	*2.90*
	Mx	2.662	2.84	2.85	2.86	2.87	2.88	2.88	2.89	2.89	2.90	2.90	2.91	*2.92*
	Ax		0.49	0.49	0.45	0.45	0.42	0.45	0.45	0.48	0.66	0.72	0.76	*0.99*
Marble														
YM1	XY		3.66	3.80	3.85	3.87	3.90	3.92	3.93	3.94	3.96	3.97	3.98	*4.02*
	XZ		3.71	3.80	3.86	3.88	3.92	3.94	3.95	3.96	3.97	3.98	3.99	*4.01*
	Mx	2.862	3.68	3.80	3.86	3.88	3.91	3.93	3.94	3.95	3.96	3.98	3.98	*4.01*
	Ax		1.55	0.16	0.23	0.34	0.46	0.48	0.53	0.53	0.33	0.13	0.10	*0.25*
	YX		3.63	3.71	3.78	3.81	3.85	3.87	3.88	3.89	3.90	3.92	3.93	*3.95*

Table 5.1 (continued)

Sample		ρ	Pressure (MPa)											
		(g/cm³)	20	50	80	100	150	200	250	300	400	500	600	800
YM1	YZ		3.56	3.63	3.69	3.72	3.76	3.78	3.79	3.80	3.82	3.83	3.85	*3.88*
	My	2.867	3.59	3.67	3.74	3.76	3.81	3.82	3.83	3.84	3.86	3.88	3.89	*3.92*
	Ay		2.00	2.10	2.20	2.23	2.23	2.22	2.27	2.19	2.20	2.14	2.06	*1.86*
	ZX		3.74	3.90	3.97	4.00	4.01	4.02	4.03	4.03	4.04	4.05	4.06	*4.08*
	ZY		3.63	3.76	3.82	3.84	3.87	3.89	3.91	3.92	3.94	3.96	3.98	*4.03*
	Mz	2.855	3.68	3.83	3.90	3.92	3.94	3.96	3.97	3.98	3.99	4.01	4.02	*4.05*
	Az		2.85	3.63	3.87	3.90	3.65	3.26	2.92	2.69	2.41	2.10	1.82	*1.21*
	M	2.861	3.65	3.77	3.83	3.85	3.88	3.90	3.91	3.92	3.94	3.95	3.96	*3.99*
	A		4.84	6.93	7.29	7.09	6.41	6.10	5.98	5.79	5.64	5.41	5.30	*4.88*

Abbreviations: ρ, density; M, mean; A, anisotropy; the subscript of X, Y or Z refers to the propagation direction; XY, XZ, YX, YZ, ZX and ZY, the first letter signifies the propagation direction and the second indicates the polarization direction. Values in italics are extrapolated.

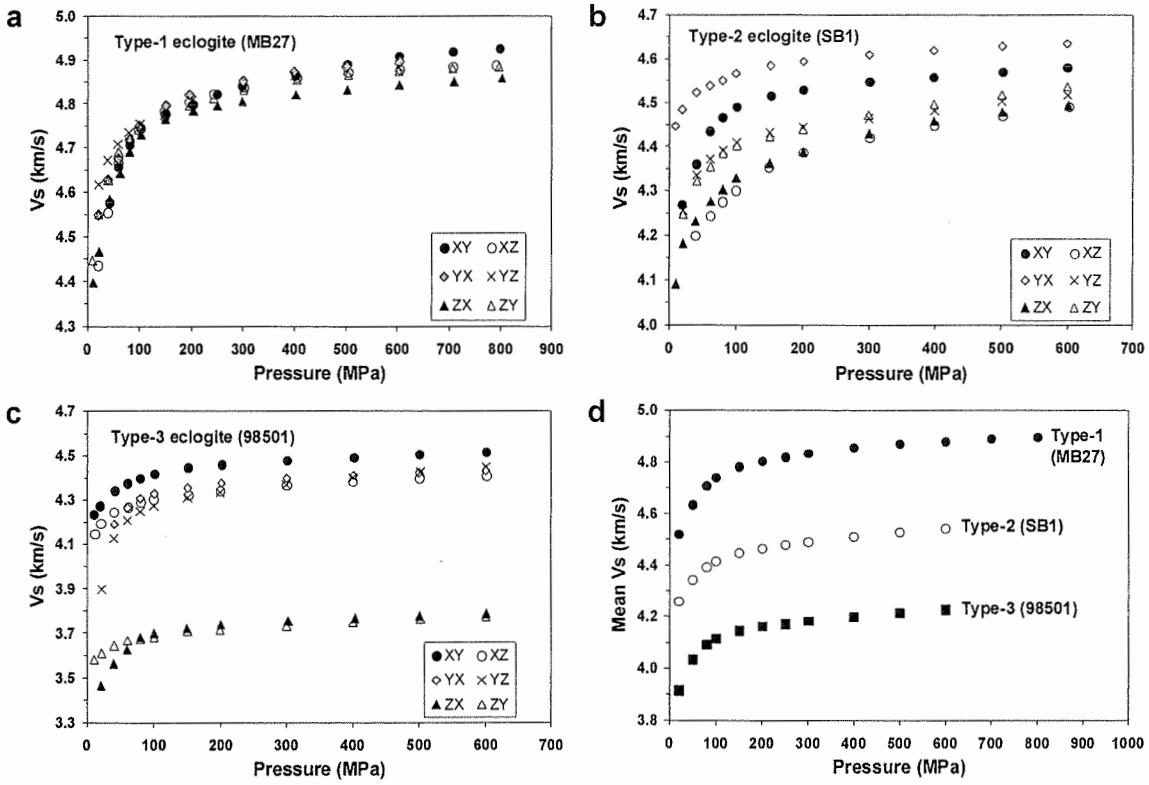


Figure 5.2 Plot of shear wave velocity (*Vs*) versus confining pressure for three typical types of eclogites: (a) Type-1 eclogite MB27, (b) Type-2 eclogite SB1, (c) Type-3 eclogite 98501, and (d) mean shear wave velocities of these three samples.

As shown in Figure 5.3, $\overline{Vs}$ at 50 MPa and 600 MPa increases almost linearly with density at room temperature. The correlation between $\overline{Vs}$ and density is particularly obvious at 600 MPa because the effect of microcracks is eliminated. The best-fit linear $\overline{Vs}$-density equations for 55 eclogites from this study and the literature (Simmons 1964; Manghnani et al., 1974; Kern and Tubia, 1993; Kern et al., 1999, 2002) are $\overline{Vs} = -1.775 + 1.76\rho$ at 50 MPa and $\overline{Vs} = -1.319 + 1.702\rho$ at 600 MPa, respectively, where ρ is the density in g/cm^3. Type-1 eclogites have higher velocities and densities than Type-2 and Type-3 eclogites. At 600 MPa, the average shear wave velocities of eclogites decrease from 4.85 km/s for Type-1, to 4.53 km/s for Type-2 and to 4.30 km/s for Type-3, corresponding to a decrease in garnet content (Figure 5.4a) and an increase in retrograde minerals such as amphibole, mica, zoisite, quartz and chlorite (Figure 5.4b). The retrograde metamorphism can significantly decrease the shear wave velocities of eclogites.

It is interesting to note that $\overline{Vs}$ at 600 MPa for Type-1 and Type-2 eclogites from the Sulu terrane decreases with increasing SiO_2 and Na_2O contents (Figures 5.5a-5b). A similar trend has been observed for P-wave velocities (Wang et al., in press). The increase in SiO_2 and Na_2O contents from Type-1 to Type-2 eclogites implies that relatively mobile elements such as SiO_2 and Na_2O were added to the UHP eclogites in the early exhumation stage. Dilation induced by rapid uplift of the eclogites may facilitate chemical exchange between eclogites, host sialic rocks and fluids. After integrating our *Vs* data and with data from the literature (Manghnani et al., 1974; Kern and Tubia, 1993; Kern et al., 1999, 2002; Gao et al., 2001), it is evident that the above velocity-chemistry trend is complicated by retrograde metamorphism and alteration.

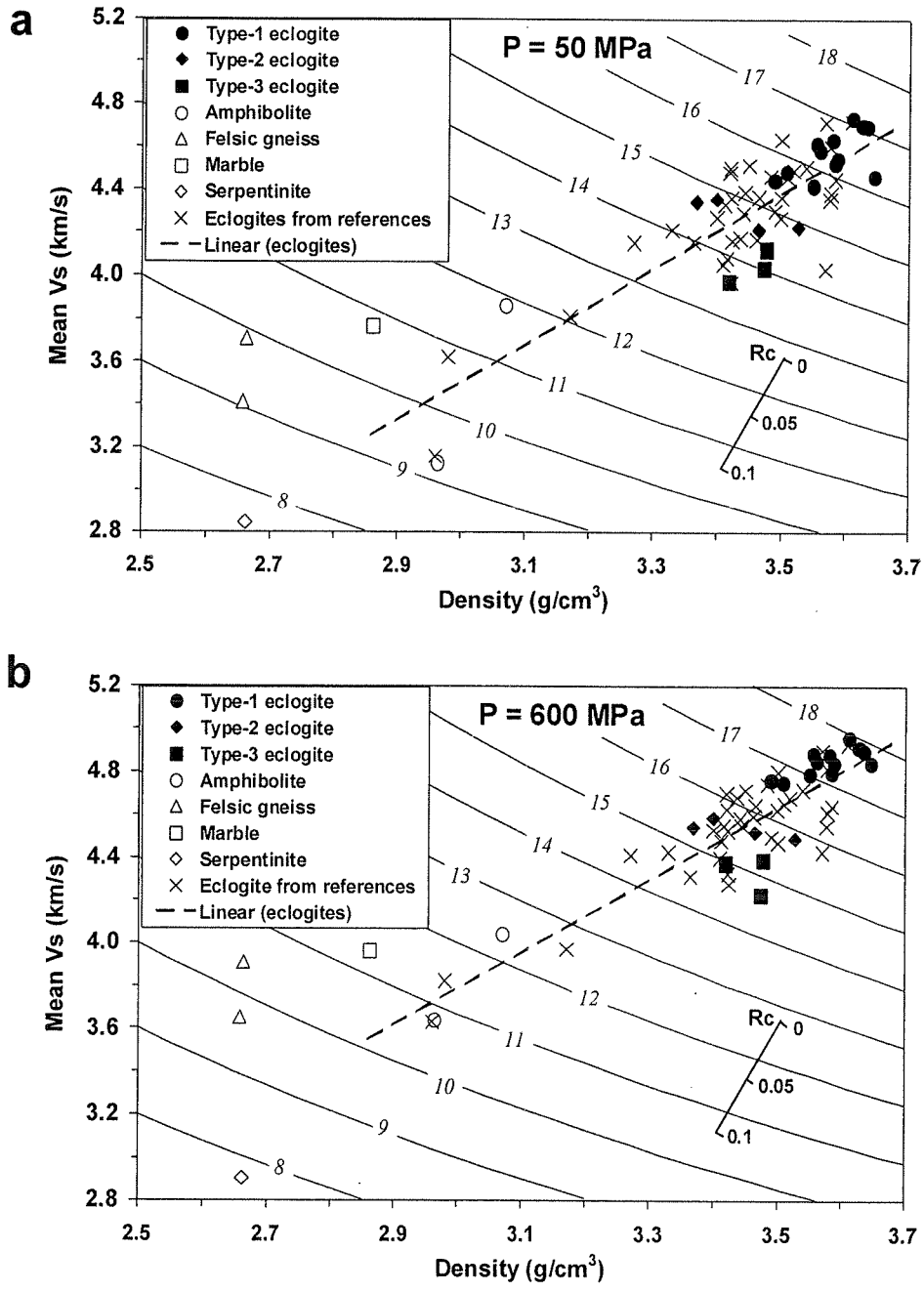


Figure 5.3 Mean shear wave velocities ($\overline{Vs}$) versus densities at (a) 50 MPa and (b) 600 MPa of Dabie-Sulu UHP rocks. The dashed line is the best-fit solution for $\overline{Vs}$ versus density for eclogites from this study and references. Also shown are lines of constant acoustic impedance and a floating reflection coefficient (*Rc*) scale.

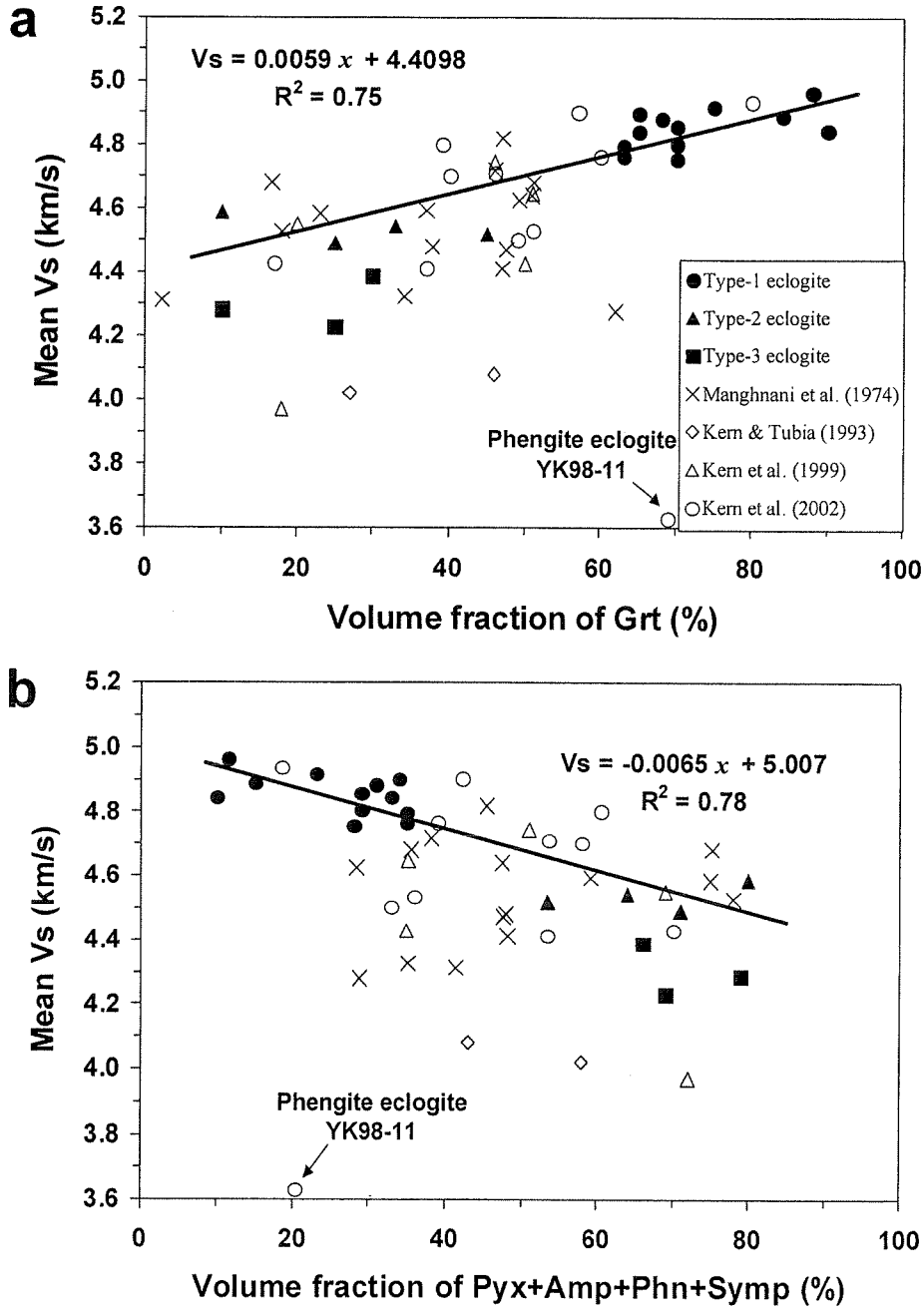


Figure 5.4 Mean shear wave velocities (*Vs*) of eclogites at 600 MPa versus volume fraction of (a) garnet (Grt) and (b) pyroxene (Pyx), amphibole (Amp), phengite (Phn) and symplectite (Symp). Solid line is the least squares fit to the data for Type-1 and Type-2 eclogites from the Sulu UHP metamorphic belt.

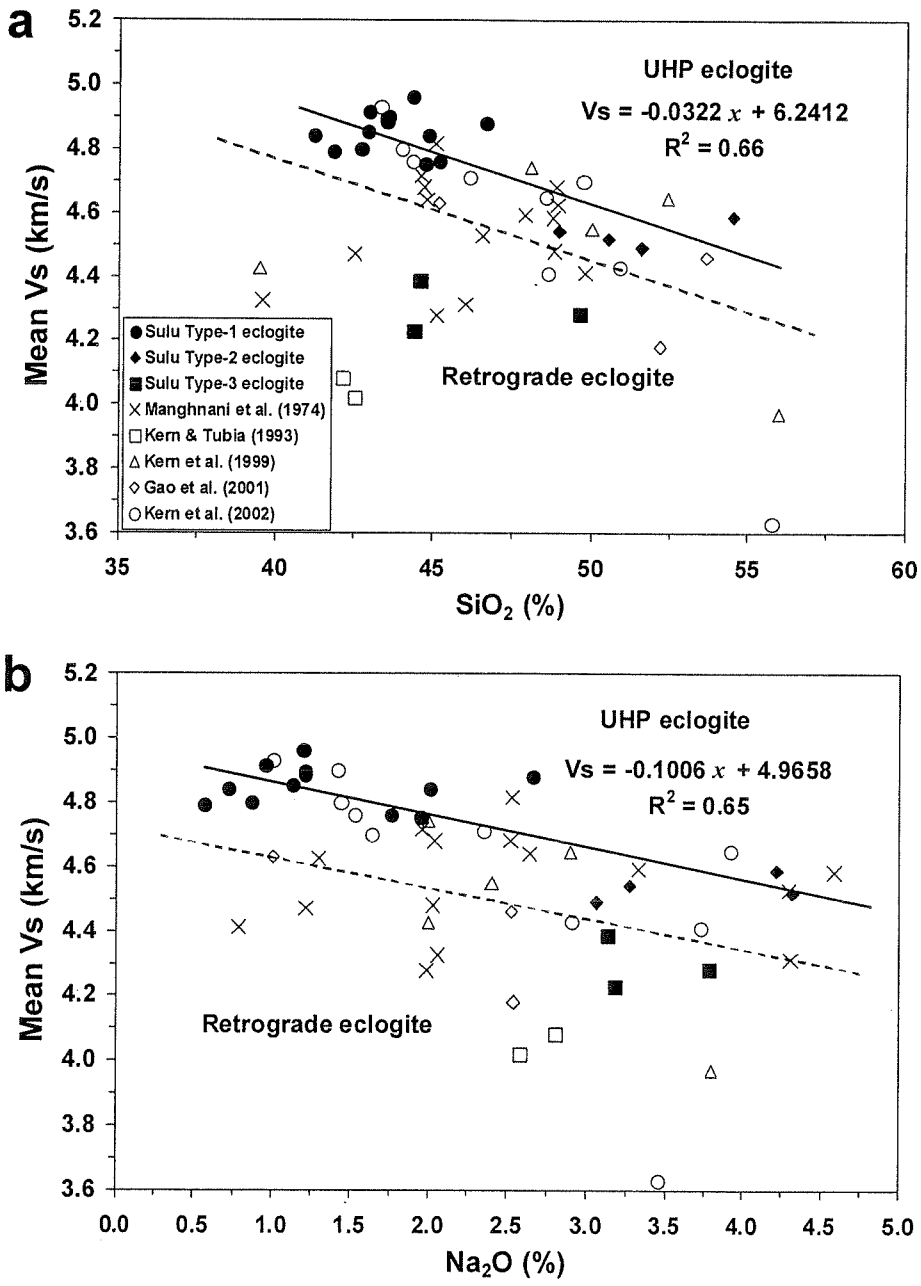


Figure 5.5 Chemical dependence of shear wave velocities at 600 MPa of eclogites: (a) $\overline{Vs}$ -SiO_2 content, (b) $\overline{Vs}$ -Na_2O content. The dashed line separates UHP eclogites and retrograde eclogites, while the solid line represents the least squares fit to the data for Type-1 and Type-2 eclogites from Sulu.

5.5.2 Shear wave anisotropy

Shear wave anisotropy of a bulk sample is defined as:

$$As = 100\% \times (Vs_{max} - Vs_{min}) / \overline{Vs} \qquad (5.2)$$

The value of As is sensitive to a variety of factors such as pressure, modal composition, compositional layering, shape and lattice preferred orientation (LPO) of minerals, and alignment of cracks and pores (e.g., Ji and Salisbury, 1993; Kern et al., 2002). At low pressures the competition of oriented microcracks and LPO of minerals can produce complex As versus pressure patterns, but As tends to approach a constant value at pressures >400 MPa, where most cracks and pores are closed and the LPO of minerals becomes dominant. The variation of As at low pressures can be classified into three patterns (Figure 5.6): Pattern 1, which is the most common (e.g., samples JC2, MB23, TF1 and SB1), is characterized by a rapid decrease in anisotropy with increasing pressure due to a strong increase in $\overline{Vs}$ with the progressive closure of microcracks. Pattern 2 is caused by the closure of oriented microcracks that oppose the fabric-related anisotropy. In sample YM1, for example, As rises at low pressues as an increase in the difference between Vs_{max} and Vs_{min} overwhelms the increase in $\overline{Vs}$, but then declines slowly with increasing pressure when the effect of cracks becomes smaller. Pattern 3, which is a mode combining Pattern 1 and Pattern 2, displays a decrease in anisotropy at low pressures (<100 MPa), followed by a slight increase at higher pressures (100-300 MPa) (e.g., sample 86351). This pattern often occurs in quasi-isotropic rocks.

High overall shear wave anisotropy at low pressures is dominated by oriented microcracks and pores. At high pressure, most Type-1 and Type-2 eclogites are weakly anisotropic with As < 3% (Table 1), which can be attributed to the LPO of omphacite since garnet is quasi-isotropic (e.g., Bascou et al., 2001; Ji et al., 2003). Relatively high As at 600 MPa is observed in Type-1 eclogite samples MB25 (As = 5.85%) and MB23

(*As* = 5.59%), suggesting a significant contribution of compositional layering. For Type-3 eclogites, the presence of strongly anisotropic retrograde minerals such as amphibole, plagioclase and mica gives rise to high *As* values. For example, in sample 98501 containing 37 vol.% amphibole, *As* reaches 17.6% at 600 MPa.

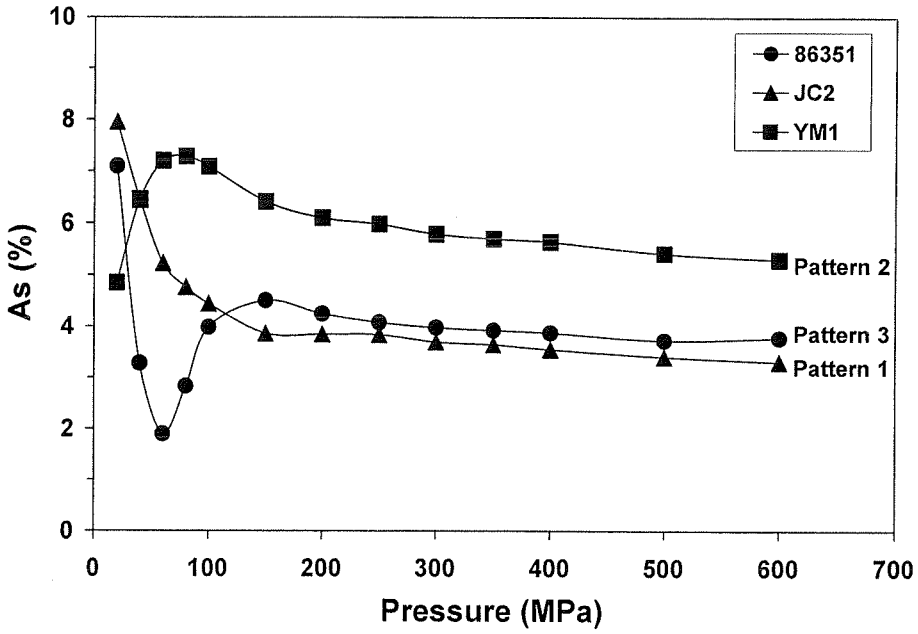


Figure 5.6 Pressure dependence of shear wave anisotropy (*As*). Three distinct patterns are represented by samples 86351, JC2 and YM1.

5.5.3 Shear wave splitting

For a given propagation direction λ (i.e., X, Y or Z), shear wave splitting $(\Delta Vs)_\lambda$ is defined as $(\Delta Vs)x = Vs_{XY} - Vs_{XZ}$, $(\Delta Vs)y = Vs_{YX} - Vs_{YZ}$ and $(\Delta Vs)z = Vs_{ZX} - Vs_{ZY}$, respectively. The anisotropy in a given propagation direction λ is calculated by

$$A_\lambda = \frac{|(\Delta Vs)_\lambda|}{Vs_\lambda} \qquad (5.3)$$

where Vs_λ is the average shear wave velocity propagating along λ. Both $(\Delta Vs)_\lambda$ and A_λ are direction- and pressure-dependent. Similar to shear wave anisotropy for a bulk sample (As), A_λ varies in a complex manner at low pressures and gradually reaches a constant with increasing pressure. Figure 5.7 presents the pressure dependence of $(\Delta Vs)_\lambda$, A_λ and As for three typical eclogite samples MB27, SB1 and 98501. Because the minerals are preferentially aligned parallel to foliation, the polarization direction of the fast shear wave generally lies in the foliation plane for propagation parallel to foliation [i.e., $(\Delta Vs)x > 0$ and $(\Delta Vs)y > 0$], or lies parallel to lineation for propagation perpendicular to foliation [i.e., $(\Delta Vs)z > 0$]. This is usually observed in metamorphic rocks (e.g., Christensen, 1966; Kern and Wenk, 1990; Ji and Salisbury, 1993) and layered sedimentary rocks (e.g., Johnston and Christensen, 1992). However, some exceptions with negative values of shear wave splitting are also observed and are thought to be due to sample heterogeneity (Figure 5.7c) or the combined effect of different sets of microcracks (Figure 5.7e). It is interesting to note that the bulk anisotropy (As) does not show any correlation with directional splitting ($|(\Delta Vs)_\lambda|$). For example, samples SB1 (Figure 5.7d) and 98501 (Figure 5.7f) display As values of 3.2% and 17.7%, respectively, at 600 MPa although there is little difference in A_λ between these two samples.

To study the effects of microcracks and LPO of minerals on shear wave splitting in UHP rocks, we compared Vs values propagating along X-, Y- and Z-directions at 50 MPa and 600 MPa, respectively (Figure 5.8). A diagonal is drawn to indicate zero shear wave splitting. At low pressures, the predominance of transgranular fractures over grain boundary cracks (Ji et al., 1997) may result in negative shear wave splitting in which $Vs_{XY}<Vs_{XZ}$, $Vs_{YX}<Vs_{YZ}$, $Vs_{ZX}<Vs_{ZY}$ (e.g., Type-1 eclogites in Figure 5.8c). At high pressures, however, samples generally display positive shear wave splitting with $Vs_{XY} \geq Vs_{XZ}$ and $Vs_{YX} \geq Vs_{YZ}$ (Figures 5.8d-e). For propagation perpendicular to foliation at 600 MPa (Figure 5.8f), the splitting is very small and the fast polarization direction does not show a clear correlation with the lineation in most of the UHP eclogites. Relatively high shear wave splitting has been observed in some eclogites with well-developed

compositional layering. For example, sample MB2A, a Type-1 eclogite, has $(\Delta Vs)x$ = 0.15 km/s at 600 MPa, and sample 98401 (Type-3) has $(\Delta Vs)y$ = 0.22 km/s. Such magnitudes are comparable to the splitting observed in the peridotitic upper mantle and attributed to moderate olivine LPO (Ji et al., 1994; Ben Ismaïl and Mainprice, 1998). Thus, laminated eclogites, if volumetrically important, may contribute to the formation of shear wave splitting in the upper mantle and particularly in subducted slabs (Bostock, 1997).

5.6 Discussion

5.6.1 Pressure dependence of shear wave velocity

As discussed earlier and shown in Figure 5.2, rock samples display an initial rapid, nonlinear increase in velocity at low pressures, and then a slow, linear increase at high pressures. The nonlinear rise is mainly attributed to the closure of microcracks and pores, while the linear rise reflects elastic deformation above a critical pressure (P_c) where all cracks and pores are closed and the rock is regarded as a compact aggregate (e.g., Birch, 1960; Christensen, 1966). We applied a MATLAB program "VPPLOT" (Appendix 3) to determine P_c and characterize the velocity-pressure curve. The Vs-pressure curve is described by

$$Vs = \begin{cases} a(\ln P)^2 + b\ln P + c & (P \le P_c) \\ V_0 + DP & (P \ge P_c) \end{cases} \qquad (5.4)$$

for the nonlinear and linear regimes, respectively, where P is the confining pressure; P_c is the critical pressure separating the poroelastic regime from the elastic regime; a and b are parameters describing the closure of microcracks below P_c and are controlled by the density and distribution of microcracks; c is the velocity when P is equal to unity (i.e., one MPa); V_0 is the projected velocity of a crack-free sample at room pressure, and D is

the intrinsic pressure derivative of velocity above P_c. Equation (5.4) can be easily applied to the interpolation and extrapolation of the laboratory-derived seismic velocities.

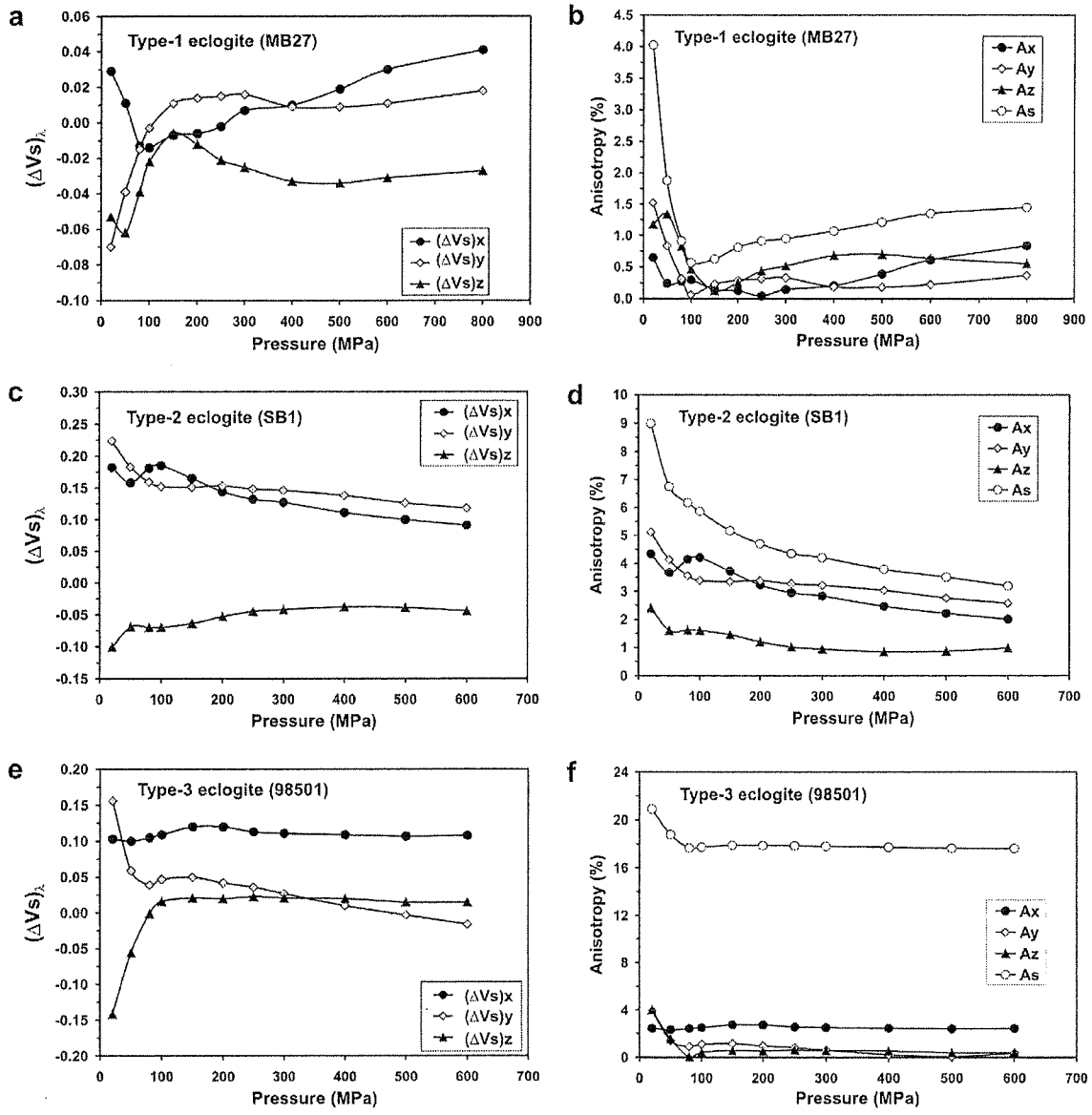


Figure 5.7 Pressure dependence of shear wave splitting (ΔVs), splitting-produced anisotropy (A_λ) along a given propagation direction λ (X, Y or Z) and bulk anisotropy (As) for (a-b) Type-1 eclogite MB27, (c-d) Type-2 eclogite SB1 and (e-f) Type-3 eclogite 98501, respectively.

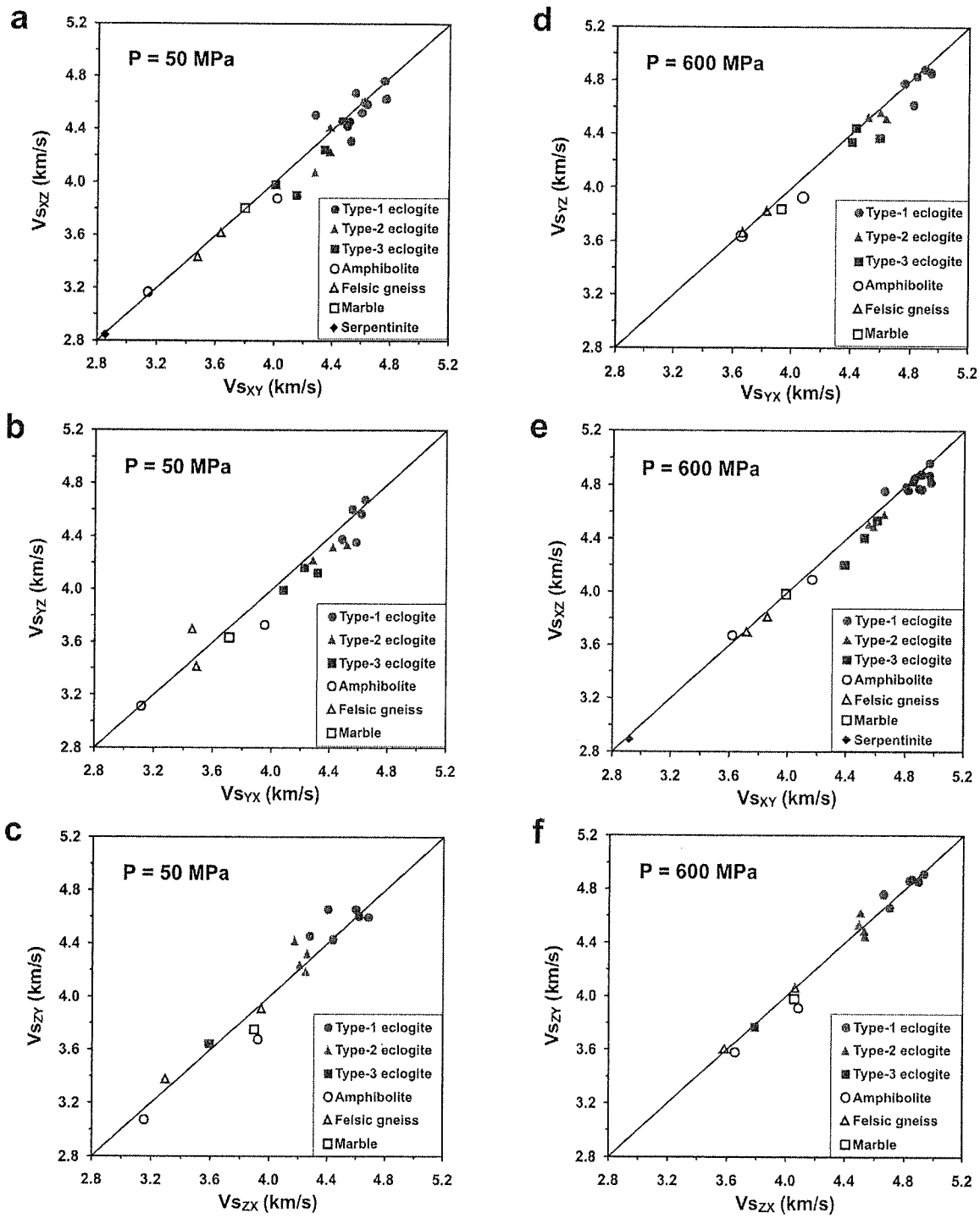


Figure 5.8 Split shear wave velocities along X-, Y- and Z-directions at (a-c) 50 MPa and (d-f) 600 MPa. The diagonal represents zero shear wave splitting.

The pressure derivative (Vs') of shear wave velocity is then expressed as

$$Vs' = \begin{cases} (2a\ln P + b)/P & (P \le P_c) \\ D & (P \ge P_c) \end{cases} \qquad (5.5)$$

Figure 5.9a illustrates the regression results of Vs_{ZX} for sample MB26, with goodness-of-fit $R^2 > 0.99$. In Figure 9b, Vs_{ZX}' for sample MB26 decreases quickly below 100 MPa, reflecting a rapid closure of microcracks at low pressures. Above 200 MPa, Vs_{ZX}' gradually decreases until it reaches a constant, the intrinsic pressure derivative D, at $P \geq P_c$. Although Equation (5.5) is a continuous function, a slight jump in Vs' occasionally arises at P_c when calculating derivatives from least-squares regressions of small data sets.

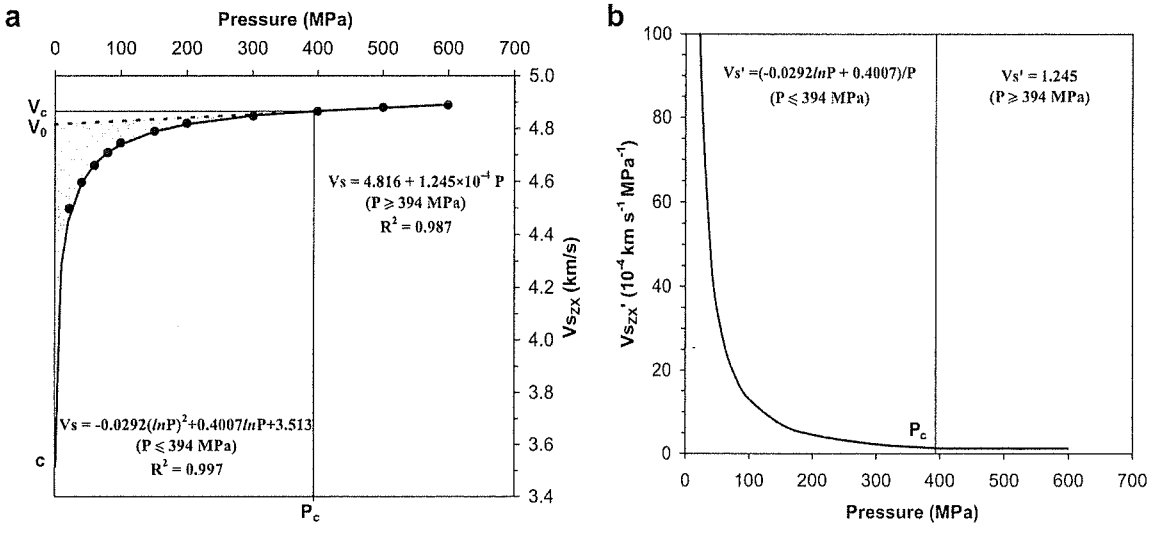


Figure 5.9 (a) Laboratory Vs_{ZX} data and regression results for Type-1 eclogite MB26 and (b) its pressure derivative (Vs_{ZX}'). See text for the explanation of c, V_0, V_c and P_c.

Regression results for the mean velocities of 25 samples consistently show values of $R^2 > 0.98$ (Table 5.2). The D values range from 0.49 to 3.91×10^{-4} $kms^{-1}MPa^{-1}$ for eclogites. The lowest D value occurs in coarse-grained garnetite MB2B, while the highest

occurs in phengite eclogite QL2. The average *Vs* values in the linear regime are: $4.762+1.464\times10^{-4}P$, $4.435+1.671\times10^{-4}P$ and $4.212+2.025\times10^{-4}P$ for Type-1, Type-2 and Type-3 eclogites, respectively, where P is in MPa and *Vs* is in km/s. The decrease in V_0 and increase in D from Type-1 to Type-3 eclogites correlate with a decrease in garnet and an increase in retrograde minerals (Figure 5.4). For the country rocks, the D values vary between 0.51-2.44 $\times10^{-4}$ $kms^{-1}MPa^{-1}$ with the lowest and highest values in serpentinite XG3 and amphibolite QL4, respectively.

Figure 5.10 summarizes V_0 and D for eclogites from this study and the literature (Simmons, 1964; Manghnani et al., 1974; Kern and Tobia, 1993; Kern et al., 1999; 2002; Gao et al., 2001). The UHP eclogites have similar D values but higher V_0 values than retrograde samples, because V_0, the reference velocity of a crack-free sample at room conditions, is mainly controlled by the modal composition. For all eclogite samples, the average D is 1.417±0.66 $\times10^{-4}$ $kms^{-1}MPa^{-1}$ and V_0 is 4.475±0.288 km/s. Deviations of V_0 and D from the mean values principally reflect the types and abdundance of retrograde minerals in the samples.

5.6.2 Velocity-depth behavior of Dabie-Sulu lithologies

In order to compare experimental velocities with seismic refraction survey results, we corrected the laboratory data for in situ *P-T* conditions of the crust and upper mantle beneath the Dabie-Sulu region. The seismic velocities were computed according to:

$$V(z)=\begin{cases} a(\ln P)^2+b\ln P+c+(dV/dT)T & (P\le P_c) \\ V_0+DP+(dV/dT)T & (P\ge P_c) \end{cases} \qquad (5.6)$$

where z is the depth, dV/dT is the temperature derivative of velocity and P is the lithostatic pressure, equal to ρgz. The average densities of the rocks were assumed to be

Table 5.2 Mean *Vs*-pressure relationships for samples from the Dabie-Sulu UHP belt

Lithology / Sample	P_c	V_c	$V = a(\ln P)^2 + b\ln P + c$ $(P<Pc)$			R^2	$V = V_n + DP$ $(P>Pc)$		R^2
			a	b	c		V_0	D	
	(MPa)	(km s^{-1})	(km $s^{-1}MPa^{-2}$)	(km $s^{-1}MPa^{-1}$)	(km s^{-1})		(km s^{-1})	(10^{-4} km $s^{-1}MPa^{-1}$)	
Coarse-grained eclogite									
86351	319	4.707	-0.0390	0.5127	3.046	0.994	4.644	1.979	0.994
MB22	316	4.753	-0.0337	0.4970	3.009	0.992	4.705	1.505	0.982
MB23	377	4.720	-0.0162	0.2730	3.671	0.996	4.663	1.514	0.990
MB25	383	4.806	-0.0309	0.4310	3.334	0.998	4.743	1.643	0.994
MB26	380	4.826	-0.0211	0.3200	3.668	0.994	4.774	1.370	0.987
MB27	390	4.854	-0.0193	0.2944	3.785	0.995	4.804	1.283	0.994
MB30	383	4.768	-0.0178	0.2915	3.664	0.995	4.709	1.551	0.991
MB2A	327	4.867	-0.0269	0.3486	3.747	0.994	4.829	1.144	0.986
MB2B	329	4.931	-0.0101	0.2019	4.100	0.998	4.891	1.195	0.990
MB34	290	4.876	-0.0154	0.2423	3.998	0.991	4.838	1.316	0.991
MB36	379	4.802	-0.0059	0.2142	3.739	0.987	4.737	1.712	0.977
MB62	423	4.865	-0.0198	0.3098	3.716	0.996	4.807	1.361	0.979
Fine-grained eclogite									
DG1	476	4.494	-0.0123	0.2470	3.439	0.999	4.399	1.992	0.996
JC2	260	4.538	-0.0273	0.3658	3.348	0.993	4.499	1.501	0.994
JZ1	284	4.445	-0.0483	0.5875	2.667	0.998	4.403	1.472	0.995
SB1	286	4.490	-0.0074	0.1556	3.848	0.995	4.440	1.717	0.995
Retrograde eclogite									
98401	284	4.324	-0.0315	0.4162	2.980	0.995	4.265	2.109	0.992
98501	287	4.182	-0.0238	0.3128	3.174	0.996	4.138	1.501	0.997
QL2	405	4.334	-0.0318	0.4818	2.582	0.996	4.234	2.465	0.990
Amphibolite									
QL4	414	3.594	-0.0396	0.6090	1.364	0.998	3.493	2.437	0.993
YM4	272	4.001	-0.0082	0.1566	3.381	0.991	3.963	1.366	0.991
Granitic gneiss									
TF1	380	3.886	-0.0243	0.3258	2.809	0.995	3.850	0.962	0.984
TF3	349	3.619	-0.0286	0.3834	2.352	0.997	3.570	1.390	0.991
Serpentinite									
XG3	326	2.892	0.0060	-0.0372	2.908	0.979	2.876	0.509	0.991
Marble									
YM1	242	3.915	-0.0210	0.2908	2.951	0.995	3.881	1.391	0.995

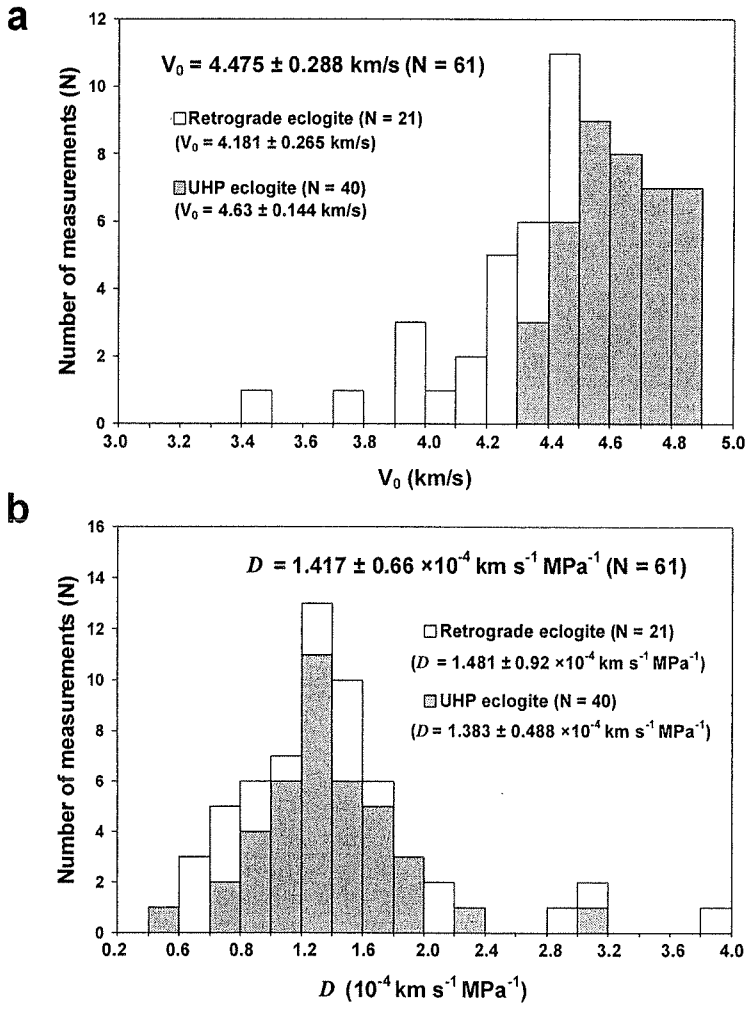


Figure 5.10 Histograms of (a) reference shear wave velocities (V_0) and (b) intrinsic pressure derivatives (D) of eclogites from this study and the literature.

2.85 g/cm^3 and 3.3 g/cm^3 for the crust and upper mantle, respectively. The temperature-depth profile was estimated from heat flow data and the thermal conductivities of rocks, assuming a stable conductive thermal regime.

Wang et al. (2001) obtained heat flow values of 76-80 mW/m^2 in the Sulu UHP zone, which is higher than the average value of the adjacent North Jiangsu basin (68 mW/m^2, Wang et al., 1995) and western Shangdong region (50 mW/m^2, Ma et al., 1991), as well as that for continental China as a whole (61±15.5 mW/m^2, Hu et al., 2001). In contrast,

the Dabie Mountains have an average heat flow of only about 52 mW/m^2 (Wang and Huang, 1990; Hu et al., 2001). Figure 5.11a illustrates layered crustal models inferred from seismic refraction and reflection data for the Sulu terrane, Dabie Mountains, North Jiangsu basin, Lower Yangtze region, western Shangdong block, North China craton and Yangtze craton. Figure 5.11b shows calculated geothermal profiles for the same regions. The Dabie Mountains and the Sulu terrane have different crustal and geothermal structures although they belong to the same collision belt, implying that they have experienced different post-collisional evolution. Compared with the Sulu terrane, the Dabie Mountains have a colder, thicker crust and thermal lithosphere. In addition, the North China craton (Figure 5.1) has a regional heat flow of 56 mW/m^2 and an average lithospheric thickness of 100 km. The average heat flow of the Yangtze craton is ~53 mW/m^2, with higher values east of the Tan-Lu fault (the Lower Yangtze region, ~60 mW/m^2; Wang et al., 1995) and lower values west of the fault (Middle and Upper Yangtze regions, ~ 50 mW/m^2; Wang and Huang, 1990; Hu et al., 2001). Thus, the surface heat flow and lithospheric thickness in different areas of eastern-central China strongly depend on the extent of tectonic reactivation which occurred during the Mesozoic and Cenozoic.

Table 5.3 lists various parameters including the P- and S-wave pressure and temperature derivatives of 13 major rock types, used in the modeling of velocity-depth profiles. These parameters were derived by averaging all of the reliable experimental data measured on dry samples at confining pressures $\geq$600 MPa (this study; Ji et al., 2002). Xenoliths are not included in the dataset because their experimentally determined velocities are generally lower than theoretical values due to the presence of interstitial glass and incomplete crack closure (e.g., Gao et al., 2000). Following Rudnick and Fountain (1995), we divided metamorphosed pelitic rocks into two subgroups: amphibolite facies biotite-rich paragneiss and granulite facies garnet-rich metapelite. Generally, the metapelites have higher densities, higher velocities and less SiO_2 than the paragneisses (Table 5.3). The temperature derivatives listed in Table 5.3 are from H.

Kern's laboratory (See Ji et al., 2002 for a summary). Paragneiss, for which temperature derivative has not been determined experimentally, is assumed to have the same value as metapelite. *Vp* and *Vs* at 600 MPa and room temperature are also given for each lithology in order to compare with previous compilations (Christensen and Mooney, 1995; Rudnick and Fountain, 1995; Christensen, 1996).

Table 5.3 Average parameters describing variations of P- and S-wave velocities with pressure and temperature

Lithology	ρ	SiO_2	*V* (600 MPa, 25 °C)	P_c	$V = a(lnP)^2 + blnP + c$ ($P \leq Pc$)			$V = V_0 + DP$ ($P \geq Pc$)		dV/dT
					a	*b*	*c*	V_0	*D*	
	(g/cm^3)	(%)	($km\,s^{-1}$)	(MPa)	($km\,s^{-1}MPa^{-2}$)	($km\,s^{-1}MPa^{-1}$)	($km\,s^{-1}$)	($km\,s^{-1}$)	($10^{-4}km\,s^{-1}MPa^{-1}$)	($-10^{-4}km\,s^{-1}\,°C^{-1}$)
P-wave velocity										
Type-1 eclogite	3.55	44.0	8.51	521	-0.0586	0.8588	5.417	8.422	1.389	1.348
Type-2 eclogite	3.47	48.5	7.91	516	-0.0392	0.6323	5.484	7.836	1.285	2.553
Type-3 eclogite	3.35	47.3	7.49	564	-0.0443	0.7326	4.619	7.381	1.803	2.127
Peridotite	3.30	41.2	8.16	505	-0.0442	0.6945	5.520	7.987	2.856	3.793
Srp peridotite	3.10	41.3	7.22	484	-0.0488	0.7289	4.539	7.060	2.590	7.329
Mafic granulite	3.15	48.2	7.12	436	-0.0211	0.4261	5.251	6.915	3.389	3.446
Amphibolite	3.01	49.8	6.91	447	-0.0563	0.8290	3.889	6.716	3.177	2.011
Intermediate gneiss	2.84	62.8	6.53	397	-0.0329	0.5122	4.585	6.353	2.967	3.160
Granitic gneiss	2.69	73.0	6.22	393	-0.0442	0.6979	3.563	6.026	3.223	2.986
Paragneiss	2.78	65.0	6.36	360	-0.0284	0.4572	4.570	6.157	3.418	4.501
Metapelite	2.95	54.0	6.76	314	-0.0176	0.3757	5.065	6.518	3.950	4.501
Marble	2.85	5.1	6.88	423	-0.0608	0.8455	3.947	6.730	2.588	6.471
Granite	2.67	72.7	6.27	299	-0.0558	0.7222	3.877	6.095	2.873	2.964
S-wave velocity										
Type-1 eclogite	3.55	44.0	4.84	469	-0.0232	0.3494	3.553	4.762	1.362	0.813
Type-2 eclogite	3.47	48.5	4.55	347	-0.0102	0.1975	3.699	4.444	1.768	1.523
Type-3 eclogite	3.35	47.3	4.24	469	-0.0230	0.3473	2.962	4.169	1.261	1.420
Peridotite	3.30	41.2	4.57	578	-0.0294	0.4301	3.015	4.509	0.978	2.456
Srp peridotite	3.10	41.3	3.77	498	-0.0177	0.2668	2.787	3.715	0.932	2.991
Mafic granulite	3.15	48.2	3.92	373	-0.0019	0.1060	3.332	3.846	1.290	2.128
Amphibolite	3.01	49.8	3.89	402	-0.0193	0.3067	2.718	3.810	1.320	2.014
Intermediate gneiss	2.84	62.8	3.72	328	-0.0117	0.2005	2.923	3.652	1.163	1.323
Granitic gneiss	2.69	73.0	3.66	377	-0.0356	0.4921	1.966	3.593	1.065	0.802
Paragneiss	2.78	65.0	3.74	377	-0.0143	0.2358	2.816	3.663	1.276	2.235
Metapelite	2.95	54.0	3.82	317	-0.0058	0.1476	3.123	3.733	1.489	2.235
Marble	2.85	5.1	3.73	405	-0.0251	0.3326	2.640	3.702	0.764	4.350
Granite	2.67	72.7	3.69	278	-0.0213	0.2903	2.698	3.631	1.018	1.423

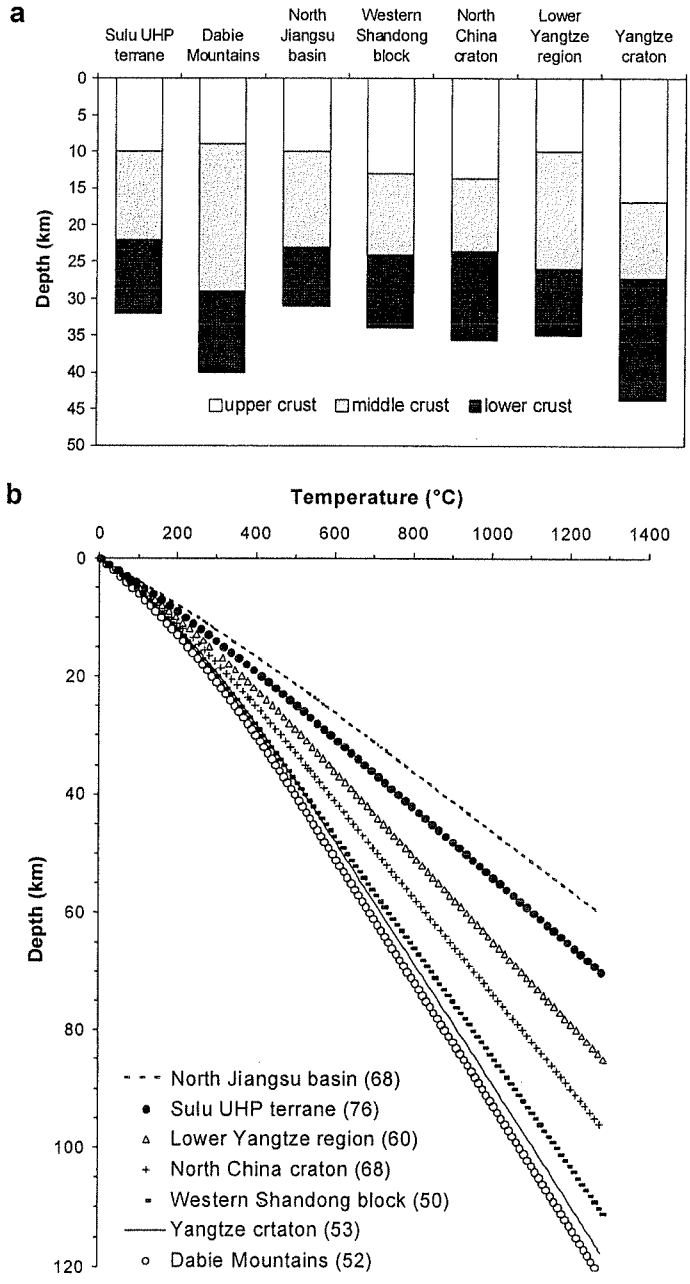


Figure 5.11 (a) Three-layered crustal models of the Sulu UHP terrane (Yang et al., 2004), the Dabie Mountains and the Lower Yangtze region (Wang et al., 2000), North Jiangsu basin and Western Shandong block (Ma et al., 1991), Yangtze craton and North China craton (Gao et al., 1998). (b) Calculated geotherms for the tectonic regions shown in (a). Numbers in parenthesis indicate the surface heat flow data, Q_0.

Figure 5.12 illustrates calculated P- and S-wave velocities with depth for major rock types from the Sulu terrane. In the upper crust (<10 km), the rapid increase of velocity with depth reflects the closure of microcracks with increasing pressure while the effects of temperature are minor. Below 15-20 km, the contribution of pressure to seismic velocities is partially offset by the increase of temperature. Although most lithologies display progressively increasing velocities with depth, serpentinized peridotite and marble exhibit velocity reversals due to their large temperature derivatives. If the standard deviations of the average velocities (Table 5.5) are taken into account, it will be difficult to distinguish felsic gneiss, intermediate gneiss, paragneiss and metapelites on the basis of their P- or S-wave velocities.

The shear wave reflection coefficients of possible lithologic contacts in the Dabie-Sulu UHP belt were calculated for 50 MPa and 600 MPa, assuming normal incidence reflection. As shown in Table 5.4, the approximate symmetry of the upper matrix (Rc at 50 MPa) and the lower matrix (Rc at 600 MPa) indicates that the effect of pressure on Rc is negligible although elevated pressures can significantly increase velocities. Either eclogite or peridotite can produce fairly large Rc values (>0.1) when in contact with other lithologies (e.g., felsic gneiss, quartzite, marble and amphibolite). The similarity of the acoustic impedances of fresh peridotites and the three types of eclogites would make them indistinguishable in seismic reflections. However, the serpentinization of peridotites will increase the reflectivity of their contacts with eclogites. The interfaces between serpentinite and all other lithologies will also have large reflection coefficients, but it is still uncertain whether any of the coefficients listed in Table 5.4 are sufficient to cause shear wave reflections since their paucity even in shear wave surveys.

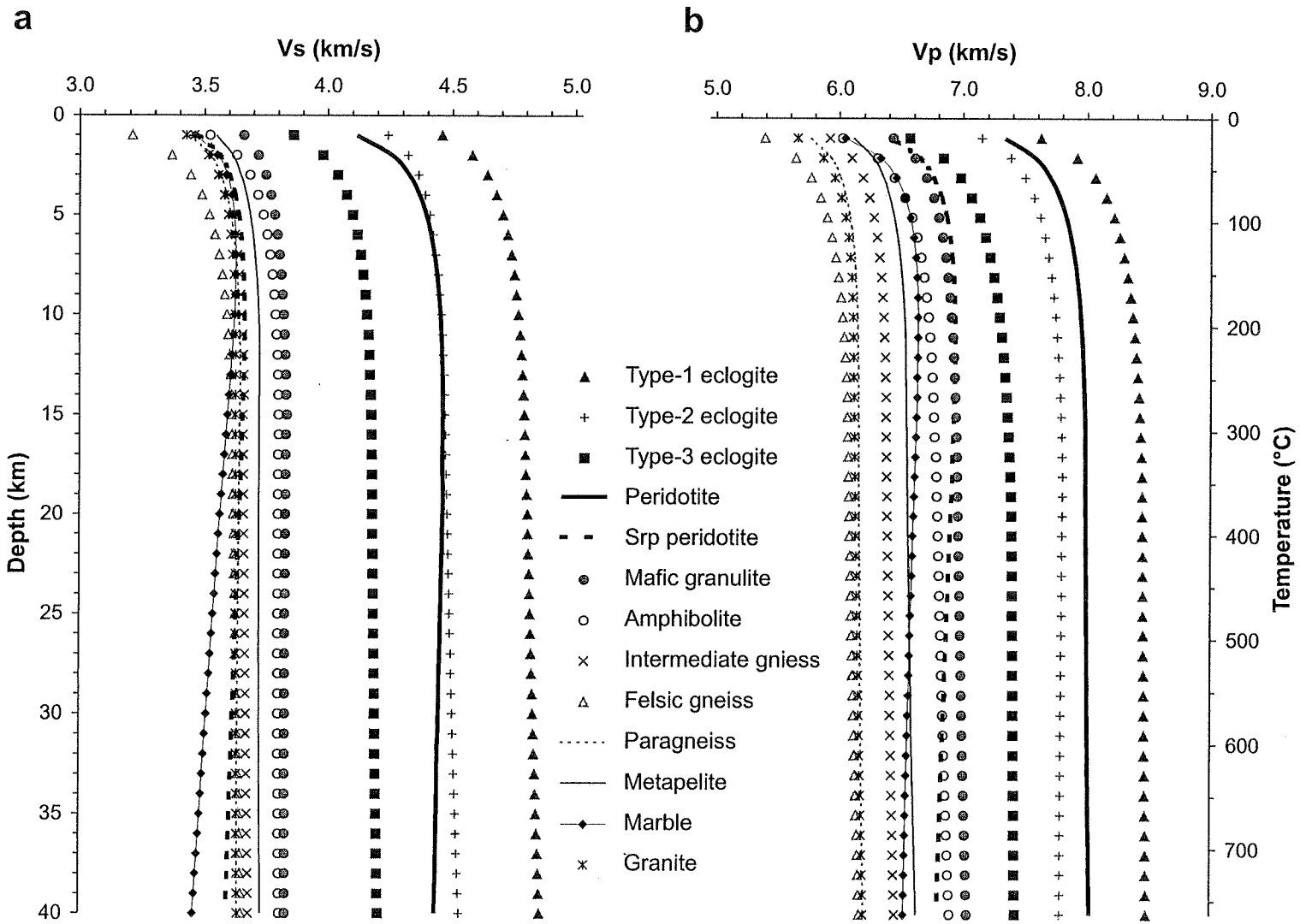


Figure 5.12 Calculated in situ (a) S-wave velocities and (b) P-wave velocities with depth for the Sulu crust.

Table 5.4 Shear wave reflection coefficients (Rc) at possible lithological interfaces in the Dabie-Sulu UHP belt at 50 MPa and 600 MPa

Lithology	ρ (g/cm^3)	Type-1 eclogite	Type-2 eclogite	Peridotite	Type-3 eclogite	Mafic granulite	Srp peridotite	Amphibolite	Marble	Metapelite	Intermediate gneiss	Paragneiss	Quartzite	Felsic gneiss	Serpentinite
Type-1 eclogite	3.55		0.04	0.07	0.09	0.16	0.18	0.21	0.20	0.21	0.24	0.25	0.25	0.26	0.37
Type-2 eclogite	3.47	-0.04		0.03	0.05	0.11	0.14	0.17	0.16	0.17	0.20	0.21	0.21	0.22	0.33
Peridotite*	3.30	-0.06	-0.02		0.02	0.09	0.11	0.14	0.13	0.14	0.17	0.18	0.18	0.19	0.31
Type-3 eclogite	3.35	-0.09	-0.04	-0.03		0.06	0.09	0.12	0.11	0.12	0.15	0.16	0.16	0.17	0.29
Mafic granulite*	3.15	-0.17	-0.12	-0.11	-0.08		0.03	0.06	0.05	0.05	0.08	0.10	0.09	0.11	0.23
Srp peridotite*	3.10	-0.18	-0.14	-0.12	-0.09	-0.01		0.03	0.02	0.03	0.06	0.07	0.07	0.08	0.20
Amphibolite	3.01	-0.20	-0.15	-0.13	-0.11	-0.03	-0.01		-0.01	0.00	0.03	0.04	0.04	0.05	0.17
Marble	2.85	-0.21	-0.16	-0.15	-0.12	-0.04	-0.03	-0.01		0.00	0.04	0.05	0.05	0.06	0.18
Metapelite*	2.95	-0.21	-0.16	-0.15	-0.12	-0.04	-0.03	-0.01	0.00		0.03	0.05	0.04	0.05	0.18
Intermediate gneiss*	2.84	-0.24	-0.20	-0.18	-0.15	-0.08	-0.06	-0.05	-0.03	-0.03		0.01	0.01	0.02	0.15
Paragneiss*	2.78	-0.24	-0.20	-0.18	-0.16	-0.08	-0.06	-0.05	-0.04	-0.04	0.00		0.00	0.01	0.13
Quartzite*	2.65	-0.24	-0.20	-0.18	-0.16	-0.08	-0.07	-0.05	-0.04	-0.04	0.00	0.00		0.01	0.14
Felsic gneiss	2.69	-0.26	-0.22	-0.20	-0.17	-0.09	-0.08	-0.07	-0.05	-0.05	-0.02	-0.02	-0.01		0.13
Serpentinite	2.61	-0.39	-0.35	-0.33	-0.31	-0.24	-0.22	-0.21	-0.20	-0.20	-0.16	-0.16	-0.16	-0.14	

Rc derived from average densities at ambient conditions and velocities measured at 50 MPa (the upper matrix) and 600 MPa (the lower matrix), respectively.

* Data from *Handbook of Seismic Properties of Minerals, Rocks and Ores* (Ji et al., 2002).

5.6.3 Poisson's ratio

Poisson's ratio (σ) has been determined for each sample from the ratio of the average *Vp* to *Vs*. According to Christensen and Ramananantoandro (1971), the simple average of velocities measured in three mutually perpendicular directions can give a value very close to the true value even in highly anisotropic rocks. Figure 5.13 summarizes the available P- and S- wave velocity data for eclogites at 600 MPa and room temperature, their *Vp/Vs* ratios, Poisson's ratios, densities and silica contents (17 samples from this study; 15 samples from Manghnani et al., 1974; 2 from Kern and Richter, 1981; 2 from Kern and Tobia, 1993; 5 from Kern et al., 1999; 3 from Gao et al., 2001; 13 from Kern et al., 2002). From Type-1, Type-2, to Type-3 eclogites, the average *Vp* decreases from 8.48 km/s, to 8.03 km/s and 7.54 km/s (Figure 5.13a) and the average *Vs* drops from 4.82 km/s, to 4.61 km/s and 4.27 km/s (Figure 5.13b), respectively. The average *Vp/Vs* and Poisson's ratios (Figures 5.13c-5.13d), however, do not change much among these three types of eclogites. The average density of all eclogites is 3.45±0.13 g/cm^3 with 3.56 g/cm^3, 3.46 g/cm^3 and 3.35 g/cm^3 for Type-1, Type-2 and Type-3 eclogites, respectively (Figure 5.13e). The average seismic properties of all eclogites at 600 MPa are: *Vp* = 7.991±0.489 km/s, *Vs* = 4.552±0.279 km/s, *Vp/Vs* = 1.756±0.044 and σ = 0.259±0.018. The results are slightly different from the previous compilations of Rudnick and Fountain (1995) (*Vp* = 8.127±0.205 km/s, *Vs* = 4.583±0.151 km/s and σ = 0.266±0.018) and Christensen (1996) (*Vp* = 8.127±0.156 km/s, *Vs* = 4.553±0.143 km/s, σ = 0.271±0.016).

The Poisson's ratios of garnet and omphacite are 0.265-0.275 (Wang and Ji, 2001) and 0.248 (Bhagat et al., 1992), respectively. This explains why the fresh Type-1 eclogites have an average σ value of 0.26, given that these rocks contain approximately equal volume fractions of garnet and omphacite. However, retrograde eclogites (Type-3) display a large variation in σ (0.214-0.298) with lower values in quartz-bearing eclogites and higher values in amphibole-, phyllosilicate- and/or plagioclase-bearing eclogites. It is not surprising that the presence of quartz, which has an extremely low Poisson's ratio (σ = 0.08), will markedly decrease the bulk Poisson's ratio of eclogites. In contrast, the

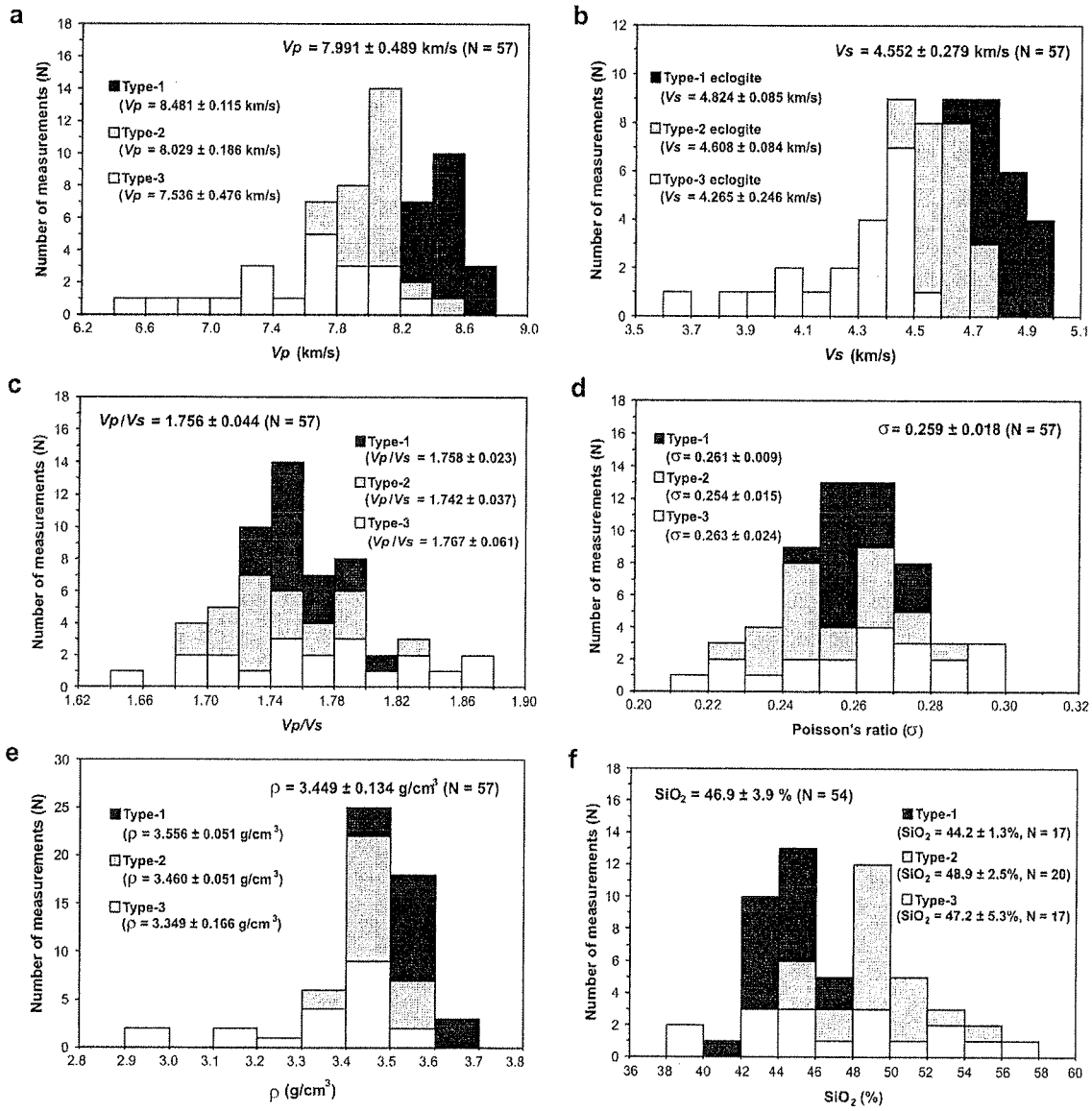


Figure 5.13 Histograms of petrophysical properties of eclogites: (a) P-wave velocity (*Vp*), (b) S-wave velocity (*Vs*), (c) *Vp*/*Vs* ratio, (d) Poisson's ratio, (e) density and (f) SiO_2 content. *Vp*, *Vs*, *Vp*/*Vs* ratio and Poisson's ratio are given at 600 MPa and room temperature. N: number of measurements.

addition of hornblende (σ = 0.287), plagioclase ($\sigma \approx 0.29$) and phyllosilicates such as phlogopite (σ = 0.300) or biotite (σ = 0.288) will yield an increase in the Poisson's ratio. During exhumation, fluid infiltration formed hydrated minerals such as hornblende and

phyllosilicates that in turn increased the Poisson's ratio of eclogites. On the other hand, SiO_2, which is a mobile component, precipitated from the fluid and decreased the Poisson's ratio. As a result, the retrograde eclogites have almost the same average value of Poisson's ratio (0.263) as Type-1 eclogites (0.261) although individual values may vary from sample to sample due to different contents of retrograde minerals.

Table 5.5 presents a new compilation of seismic velocities and Poisson's ratios at confining pressures of 200, 400 and 600 MPa for 22 common lithologies. Eclogites, with high P- and S-wave velocities and moderate Poisson's ratios (0.26), can be easily distinguished from crustal rocks such as granite, felsic gneiss, paragneiss/schist and diorite that all have much low velocities and Poisson's ratios of 0.24-0.25, and from amphibolite, gabbro-diabase and mafic granulite that have lower velocities and higher Poisson's ratios. Peridotites display similar seismic velocities to eclogites, especially with Type-2 eclogites (Figure 5.12). However, different temperature derivatives (Table 5.3) will generate Poisson's ratios of 0.28-0.29 for peridotites and 0.24-0.25 for UHP eclogites at mantle depths, suggesting a way to distinguish them using integrated P- and S-wave velocity data. Moreover, the serpentinization of peridotites markedly decreases their velocities and increases the Poisson's ratios. When eclogites occur along with serpentinized peridotites in a subducting slab (e.g., Schwartz et al., 2001), the difference in their Poisson's ratios will make them easily distinguishable.

5.6.4 Implications for crustal composition and exhumation of UHP rocks

Unlike the upper oceanic mantle, which is dominated by peridotite, the continental crust is much more varied, both laterally and vertically, in terms of its lithological and chemical compositions. In addition, metamorphic reactions and interactions with fluids or melts can markedly modify the petrophysical properties of rocks. Estimates of the composition of the deep crust from measured in situ P- or S-wave velocities are often limited by non-uniqueness. The latter can be partially alleviated by the integration of *Vp*,

Table 5.5 Average densities, *Vp*, *Vs* and Poisson's ratios of 22 common rock types at confining pressures of 200, 400 and 600 MPa

Rock type	N	ρ	200 MPa			400 MPa			600 MPa		
		(g/cm^3)	Vp (km/s)	Vs (km/s)	σ	Vp (km/s)	Vs (km/s)	σ	Vp (km/s)	Vs (km/s)	σ
Quartzite	7	2.647	5.951±0.079	3.991±0.076	0.091±0.019	6.028±0.065	4.032±0.062	0.095±0.025	6.055±0.078	4.016±0.039	0.104±0.032
Sandstone	9	2.521	5.097±0.409	3.243±0.257	0.153±0.059	5.690±0.418	3.540±0.296	0.176±0.068	5.968±0.347	3.586±0.308	0.182±0.068
Metasandstone	11	2.763	6.143±0.375	3.675±0.206	0.221±0.024	6.228±0.334	3.711±0.183	0.223±0.024	6.291±0.321	3.735±0.177	0.226±0.024
Granite-granodiorite	37	2.706	6.222±0.226	3.629±0.156	0.239±0.036	6.290±0.213	3.656±0.160	0.242±0.037	6.344±0.208	3.675±0.159	0.244±0.036
Siltstone	7	2.663	5.520±0.248	3.227±0.139	0.237±0.040	5.680±0.214	3.300±0.137	0.242±0.037	5.840±0.182	3.372±0.138	0.247±0.035
Felsic gneiss/granulite	66	2.743	6.187±0.360	3.598±0.180	0.243±0.025	6.281±0.332	3.637±0.170	0.246±0.023	6.353±0.315	3.665±0.166	0.249±0.022
Paragneiss/schist	32	2.751	6.127±0.338	3.541±0.206	0.247±0.037	6.259±0.307	3.602±0.186	0.250±0.036	6.332±0.300	3.632±0.182	0.252±0.035
Andesite-diorite-syenite	27	2.822	6.430±0.271	3.700±0.152	0.251±0.020	6.503±0.272	3.726±0.146	0.254±0.020	6.549±0.273	3.742±0.145	0.256±0.021
Intermediate gneiss/granulite	44	2.842	6.383±0.316	3.647±0.163	0.255±0.031	6.474±0.296	3.685±0.150	0.258±0.029	6.539±0.289	3.709±0.150	0.260±0.028
Eclogite	53	3.452	7.828±0.504	4.474±0.287	0.256±0.021	7.956±0.492	4.531±0.284	0.259±0.019	8.016±0.484	4.561±0.284	0.260±0.018
Amphibolite	42	3.012	6.656±0.329	3.802±0.194	0.257±0.019	6.798±0.328	3.863±0.194	0.261±0.018	6.873±0.330	3.893±0.197	0.263±0.017
Peridotite	16	3.296	8.068±0.298	4.584±0.190	0.261±0.018	8.164±0.251	4.632±0.156	0.262±0.017	8.217±0.245	4.657±0.148	0.263±0.016
Basalt	21	2.885	6.390±0.447	3.611±0.296	0.264±0.025	6.457±0.422	3.646±0.286	0.265±0.024	6.506±0.430	3.667±0.292	0.266±0.023
Metapelite	43	2.919	6.580±0.458	3.692±0.248	0.268±0.029	6.671±0.440	3.738±0.240	0.269±0.027	6.746±0.431	3.744±0.233	0.270±0.026
Gabbro-diabase	66	2.982	6.782±0.315	3.797±0.189	0.271±0.021	6.847±0.335	3.824±0.196	0.272±0.020	6.896±0.342	3.845±0.196	0.273±0.021
Pyroxenite	17	3.265	7.654±0.376	4.295±0.125	0.268±0.024	7.731±0.360	4.324±0.124	0.271±0.023	7.795±0.338	4.345±0.120	0.273±0.022
Mafic granulite	47	3.064	6.936±0.28	3.86±0.155	0.275±0.016	7.041±0.287	3.901±0.159	0.278±0.016	7.102±0.291	3.922±0.163	0.280±0.015
Gabbro-diabase (wet)	146	2.915	6.770±0.498	3.736±0.290	0.280±0.020	6.842±0.475	3.772±0.280	0.281±0.019	6.885±0.464	3.791±0.274	0.282±0.019
Dolomite	6	2.821	6.902±0.130	3.785±0.059	0.285±0.005	6.976±0.132	3.808±0.058	0.288±0.006	7.051±0.136	3.832±0.058	0.290±0.006
Basalt (wet)	186	2.860	6.112±0.439	3.303±0.273	0.293±0.017	6.197±0.430	3.352±0.268	0.293±0.016	6.263±0.423	3.384±0.270	0.294±0.017
Srp peridotite	22	3.087	7.009±0.504	3.726±0.326	0.302±0.027	7.129±0.502	3.775±0.348	0.304±0.027	7.208±0.501	3.802±0.359	0.306±0.026
Anorthosite	8	2.771	6.884±0.141	3.642±0.063	0.305±0.016	6.954±0.129	3.676±0.061	0.305±0.015	6.997±0.122	3.694±0.059	0.306±0.015
Limestone	28	2.716	6.355±0.202	3.331±0.162	0.309±0.027	6.426±0.184	3.354±0.0160	0.311±0.026	6.494±0.175	3.375±0.163	0.313±0.025
Serpentinite	10	2.594	5.550±0.863	2.769±0.544	0.336±0.020	5.694±0.821	2.805±0.528	0.341±0.021	5.798±0.794	2.830±0.52	0.345±0.022

N is the number of measured samples. Data from this study and *Handbook of Seismic Properties of Minerals, Rocks and Ores* (Ji et al., 2002)

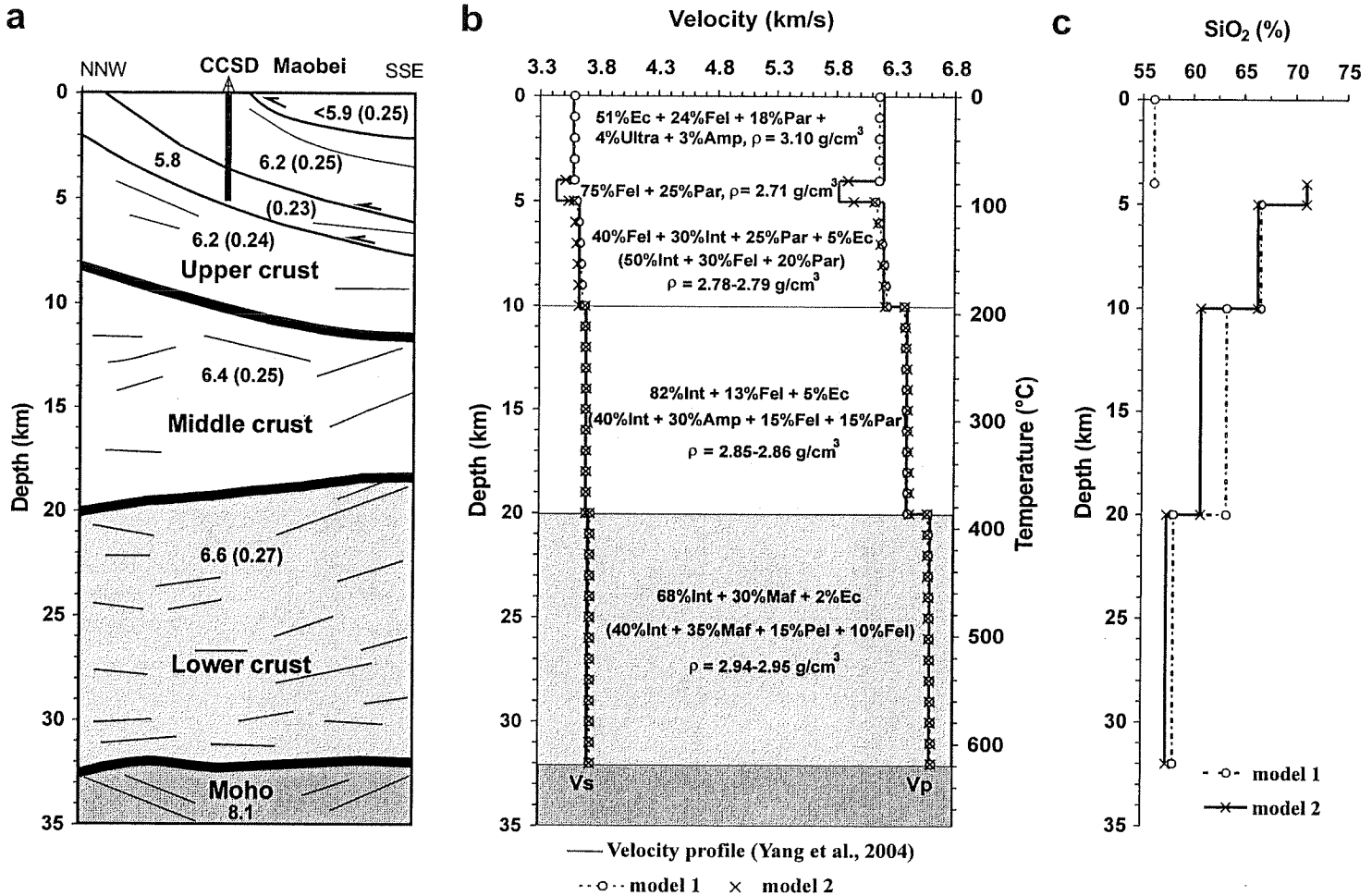


Figure 5.14 (a) Seismic profile AA′ in the Sulu terrane (see Figure 5.1) with *Vp* and Poisson's ratios in parentheses (after Yang et al., 2004). (B) Inferred crustal composition beneath the CCSD main hole assuming an eclogite-bearing model (Model 1) and an eclogite-free model (Model 2). Lithology symbols are: Amp: amphibolite; Ec: a mixture of 30% Type-1, 30% Type-2 and 40% Type-3 eclogites; Fel: felsic gneiss; Par: paragneiss; Int:intermediate gneiss; Pel: metapelite; Mar: marble; Maf: mafic granulite; Ultra: ultramafic rocks. (c) SiO_2 content with depth, calculated using Model 1and Model 2.

Vs and Poisson's ratio data as well as by direct examination of deeply exhumed continental rocks. On the basis of exposed geology and deep drilling data, we interpret the upper crust of the Dabie-Sulu UHP metamorphic belt to contain eclogites. In the first 2000 m of the main hole of the CCSD project, for example, the cumulative thickness of various eclogites was about 1000 m (Xu, 2004). Nevertheless it is uncertain whether the middle and lower crust beneath the tectonically exhumed UHP rocks contain eclogites. Thus two models, one eclogite-bearing and one eclogite-free, were used to estimate the lithological composition of the crust beneath the UHP rocks. In the modeling, we have inverted the integrated field-measured P- and S-wave velocities, and hence Poisson's ratios for the volume fractions of the major lithologies (i.e., felsic gneiss/granulite, paragneiss, intermediate gneiss/granulite, amphibolite, metapelite, mafic granulite and eclogite) in the crust beneath the Sulu and Dabie UHP units. The discrepancy in computed results is <5% between the Voigt (lower bound) and the Reuss (upper bound) averages. The geometric mean (Ji et al., 2003), which lie between the upper and lower bounds, was chosen for our modeling because the method yields an accuracy that is better than 3% in volume fraction estimation and better than 1% in estimating the velocity for each lithological assemblage.

5.6.4.1 Composition of the Sulu crust

Recent seismic reflection and refraction data from the CCSD drilling site (Yang et al., 2004) reveals a three-layered crust with an average *Vp* of 6.2 km/s, 6.4 km/s and 6.6 km/s for the upper, middle and lower crust, respectively (Figure 5.14a). Poisson's ratio increases from 0.24-0.25 in the upper and middle crust to 0.27 in the lower crust. Compared with the average global continental crust (~ 41-km-thickness, *Vp* >6.9 km/s in the lower crust; Christensen and Mooney, 1995; Rudnick and Fountain, 1995), the Sulu region has an extended crust with 32-km-thickness and *Vp* of 6.8 km/s in the lower crust, when corrected to 600 MPa and room temperature. Based on the calculated velocities of major rock types (Figure 5.12), we established eclogite-bearing (Model 1) and eclogite-free (Model 2) models for the composition of the Sulu crust (Figure 5.14b). The

computed variations of density and silica content with depth are also shown in Figure 5.14b and Figure 5.14c, respectively.

The upper crust of the Sulu UHP zone is tectonically sandwiched by ductile shear zones. Below the sedimentary cover (Vp < 5.9 km/s), a high velocity layer (Vp > 6.05 km/s) at shallow depths has been determined by the CCSD experiments to be a mixture of UHP eclogite, retrograde eclogite, paragneiss, granitic gneiss, serpentinized peridotite and amphibolite (Xu, 2004; Zhang et al., 2004). The average density of the UHP complex is estimated to be 3.10 g/cm^3, consistent with the high gravity anomaly beneath the CCSD site (Yang, 2002). In the footwall of the UHP metamorphic rocks, a thin layer displays relatively low velocity (Vp = 5.80-5.85 km/s) and moderately dipping reflections, which can be modeled by 75% felsic gneiss and 25% paragneiss. At 5-10 km depth, model 1 requires about 5% eclogite within 40% felsic gneiss, 30% intermediate gneiss and 25% paragneiss; and model 2 works equally well with 50% intermediate gneiss, 30% felsic gneiss and 20% paragneiss. Both models yield a density of 2.78-2.79 g/cm^3 and SiO_2 content of 66-67%. The calculations suggest that the Sulu UHP terrane has a bulk upper crust consisting of approximately 35% felsic gneiss, 22% eclogite, 20% paragneiss, 15-25% intermediate gneiss and minor amphibolite and ultramafic rocks, with a bulk composition of ~63% SiO_2.

In the middle crust, the Sulu terrane could be composed of 82% intermediate gneiss, 13% felsic gneiss and 5% eclogite (Model 1). A mixture of 35-40% intermediate gneiss, 25-35% amphibolite, and ~30% felsic gneiss or paragneiss (Model 2) can also satisfy the in situ refraction data. Since all of these lithologies are possible constituents for the middle crust, we prefer a combination of 40% intermediate gneiss, 30% amphibolite, 15% felsic gneiss and 15% paragneiss. With similar densities (2.85-2.86 g/cm^3), the eclogite-bearing model 1 is a little bit more silicic (SiO_2 = 63%) than eclogite-free model 2 (SiO_2 = 61%). With increasing metamorphic grade, a mixture of 68% intermediate gneiss/granulite, 30% mafic granulite and 2% eclogite (Model 1), or 40% intermediate

gneiss/granulite, 35% mafic granulite, 15% metapelite and 10% felsic gneiss (Model 2) would give a lower crust with an average density of 2.94-2.95 g/cm^3 and a silica content of 57-58%.

There are two volcanic cones (Pingmingshan and Anfengshan) of late Miocene-Pliocene age near the CCSD site in Donghai County. The basanitic lava flows contain abundant lower crustal and upper mantle xenoliths. Mantle rocks include spinel peridotite and pyroxenite while crustal rocks include mafic granulite, amphibolite, and intermediate and felsic gneisses (Yang et al., 2004). The xenoliths lack any eclogite. Therefore, the evidence from both seismic and xenolith studies indicates that eclogite, despite its common exposure at the surface, does not appear to be volumetrically important in the middle or lower crust beneath the Sulu region.

There are two end-member scenarios to explain the scarcity of eclogites in the deep crust. First, the Sulu UHP metamorphic terrane is composed of several tectonic slices of the exhumed, formerly deep-subducted continental Yangtze slab. During the exhumation driven by either forced return flow in a narrowing subduction channel (Figure 5.15a) or buoyancy of continental compositions (Figure 5.15b), these slices were rapidly thrust over a normal, UHP-free, middle-lower crust along a series of shear zones. Second, the exhumed UHP eclogites were distributed homogeneously throughout the crust of the central orogenic belt. In the case of the Dabie-Sulu belt, the slab was abandoned and exhumed when a newly created subduction zone appeared further south. The new subduction triggered the exhmation of overriding subducted continental crust, which could be a former microcontinent or island arc belonging to the Yangtze craton (Figure 5.15c). On the other hand, the continental collision will stimulate eclogitization of the lower crust beneath the thickened orogenic belt. When the lithosphere was subsequently subjected to significant extension and thinning during the Cenozoic, most of the eclogites were delaminated from the rheologically weak middle-lower crust and sank into the upper mantle, resulting in an intermediate lower crust beneath the Sulu terrane (Figure

5.15d). We prefer the first scenario because it is more consistent with exhumation models (Faure et al., 2003a; Xu et al., 2004) based on the known regional structural geology, petrology and geochronology

5.6.4.2. Composition of the Dabie crust

Wang et al. (2000) proposed a three-layer crustal model for the Dabie Mountains based on a newly acquired refraction profile (Figure 5.16a). A 6.5-km-thick crustal root is observed beneath the northern margin of the Dabie Mountains, where the maximum crustal thickness reaches 41.5 km. Unlike the Sulu terrane (Figure 5.14a), the Dabie Mountains are characterized by a moderate crustal root, a thick middle crust and a fast lower crust.

Our modeling results for the crustal column beneath the Dabie UHP unit are illustrated in Figures 5.16b-5.16c. The uppermost part of the crust can be represented by 60% felsic gneiss, 23% paragneiss and 5% eclogite with minor marble, amphibolite and ultramafic rocks. Two high velocity layers occur at 3-5 km (Vp = 6.2-6.3 km/s) and at 8-9 km (Vp = 6.4 km/s), which could be interpreted as a mixture of 20% eclogite, 30-40% felsic gneiss and 40-50% paragneiss. The calculated density of these high velocity layers is 2.88 g/cm^3, consistent with a gravity anomaly over the UHP unit (Yang, 2003). Inversion suggests that the medium between these two high velocity layers consisting of 48% felsic gneiss, 40% paragneiss and 12% eclogite. Apparently, the velocity variations with depth in the upper crust beneath the Dabie UHP unit can be attributed to varying propotions of eclogite in different layers. The layers are most likely tectonic slices of UHP rocks juxtaposed by a series of thrust zones that were active during exhumation. The upper crust as a whole is estimated to contain 48% felsic gneiss, 35% paragneiss, 11% eclogite and minor marble, amphibolite and ultramafic rocks, and to have a bulk SiO_2 content of 65%.

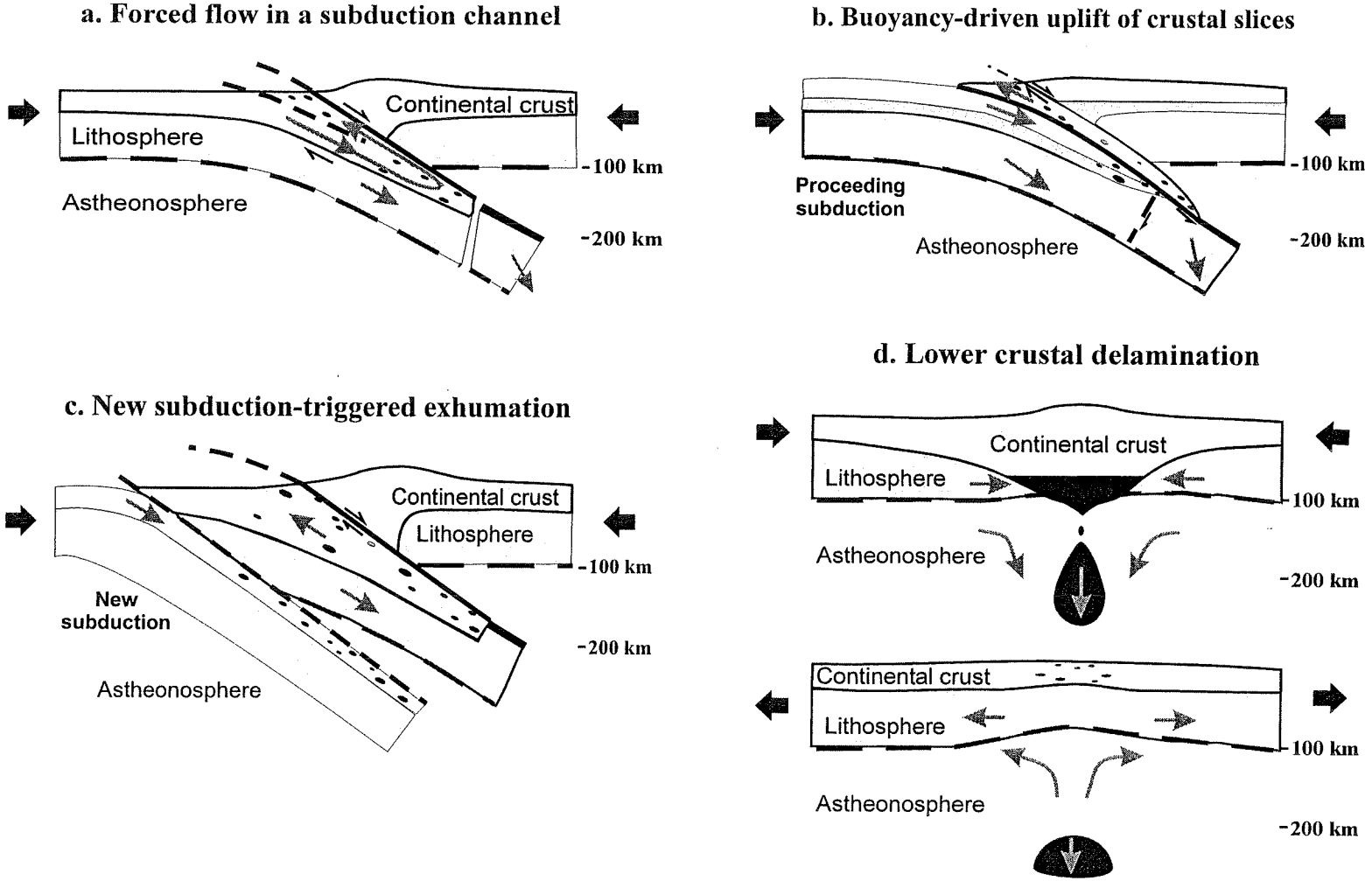


Figure 5.15 Schematic representation of different exhumation models. (a) Subduction flow and return flow in a narrowing channel (e.g., Cloos, 1982; Gerya and Stöckhert, 2002); (b) Buoyancy-driven exhumation of upper crustal slices (e.g., Chemenda et al., 1995; Ernst and Peacock, 1996); (c) New subduction-triggered exhumation; (d) Lower crustal delamination (Kay and Kay, 1991).

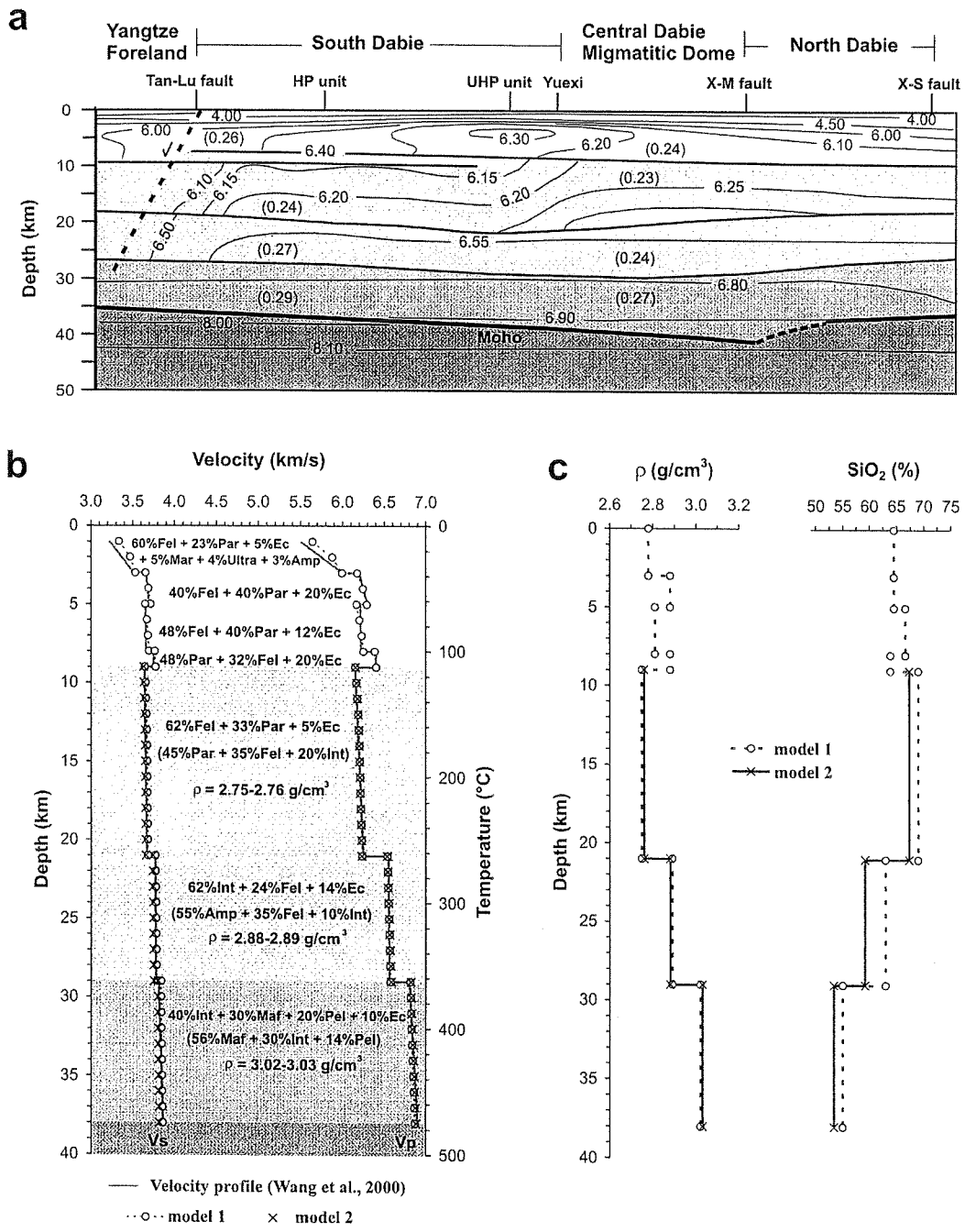


Figure 5.16 (a) Seismic refraction profile BB′ across the Dabie Mountains (see Figure 5.1) with *Vp* and Poisson's ratios in parentheses (after Wang et al., 2000), X-M fault: Xiaotian-Mozitan fault; X-S fault, Xinyang-Shucheng fault. (b) Inferred crustal composition beneath the Dabie UHP unit. Lithology symbols are defined in Figure 14b. (c) Density and SiO_2 content with depth, calculated using Model 1 and Model 2.

Below 9 km, the middle crust of the Dabie Mountains is characterized by a low velocity (6.1-6.25 km/s) upper layer between 9-21 km and a fast velocity (~6.55 km/s) lower layer between 21-29 km, both with a Poisson's ratio of 0.23-0.24. The upper middle crust is estimated to consist of 62% felsic gneiss, 33% paragneiss and 5% eclogite (Model 1), or 45% paragneiss, 35% felsic gneiss and 20% intermediate gneiss (Model 2). These models yield an average density of 2.75-2.76 g/cm^3 and a bulk composition of 67-69% SiO_2. At a depth of 21 km, *Vp* increases abruptly from 6.25 to 6.55 km/s. For the layer between 21-29 km, Model 1 predicts a mixture of 62% intermediate gneiss, 24% felsic gneiss and 14% eclogite, with an average density of 2.89 g/cm^3 and a composition of 63% SiO_2. For the same layer, Model 2 yields a mixture of 55% amphibolite, 35% felsic gneiss and 9% intermediate gneiss, with a density of 2.88 g/cm^3 and a composition of 59% SiO_2.

The lower crust (from 29 km to 38-41 km) beneath the Dabie UHP unit has a *Vp* of 6.8-6.9 km/s and a Poisson's ratio of 0.27. Model 1 suggests that the layer consists of 40% intermediate granulite, 30% mafic granulite, 20% metapelite and 10% eclogite, with an average density of 3.02 g/cm^3 and a composition of 55-56% SiO_2. If felsic granulites are included, then an assemblage of 61% mafic granulite, 31% felsic granulite and 8% eclogite is alos consistent with the refraction velocities. Model 2 with 56% mafic granulite, 30% intermediate granulite and 14% metapelites is also a good approximation to match the observed *Vp*, *Vs* and Poisson's ratio values from the lower crust. Such a lower crust has a density of 3.03 g/cm^3 and 53% SiO_2.

According to the exhumation models proposed by Hacker et al. (2000), Liou et al. (2000) and Faure et al. (2003b), the Dabie UHP unit was emplaced over the UHP-free middle-lower crust by a top-to-the-south thrusting between 210-220 Ma. If this exhumation model is correct, our eclogite-free model should offer a better description for the middle and lower crust of the Dabie Mountains than the eclogite-bearing model. Thus, the eclogite-bearing UHP terrane in today's upper crust reprensents a tectonic slice

juxtaposed upon a normal middle-lower crust along a major shear zone at a depth of 8-9 km in the Dabie Mountains.

5.7 Conclusions

We measured the shear wave velocities, shear wave splitting and anisotropy of eclogites and country rocks from the Dabie-Sulu UHP metamorphic belt, China, at room temperature and hydrostatic confining pressures up to 600-800 MPa. Three types of eclogites have been distinguished according to their grain size, degree of retrograde metamorphism and petrophysical properties (Table 5.6). Although eclogites generally have high densities, high velocities and weak anisotropy, the differences in seismic properties among the three types of eclogites are remarkable. Due to compositional layering and retrograde metamorphism, eclogites can display significant anisotropy and shear wave splitting, implying their possible contribution to seismic anisotropy in the lower crust, upper mantle and particularly in subducted slabs.

Combined with previous published data, average petrophysical and chemical properties of eclogites at 600 MPa and room temperature are summarized as: Vp = 7.991±0.489 km/s, Vs = 4.552±0.279 km/s, Vp/Vs = 1.756±0.044, σ = 0.259±0.018, ρ = 3.449±0.134 g/cm^3 and SiO_2 = 46.9±3.9%. From Type-1 to Type-2 and to Type-3 eclogites, Vp, Vs and density decrease gradually while Vp/Vs ratios and Poisson's ratios display similar mean values but wider ranges. At depth of upper mantle, Poisson's ratios equal 0.24-0.25 for Type-1 and Type-2 eclogites, which can be distinguished from fresh peridotite (σ = 0.28-0.29) and serpentinized peridotite (σ = 0.30-0.31) by means of seismic refraction experiments.

The laboratory-measured Vs-pressure curves can be described by the relations, $Vs = a(\ln P)^2 + b\ln P + c$ ($P \leq P_c$) in the nonlinear regime and $Vs = V_0 + DP$ ($P \geq P_c$) in linear regime, where P_c is the critical pressure separating the nonlinear and linear

regimes; a and b are parameters characterizing the closure of microcracks below P_c; c is the velocity when P is equal to unity (1 MPa); V_0 is the projected velocity of a crack-free sample at room pressure, and D is the intrinsic pressure derivative of velocity above P_c. The pressure derivative Vs' equals $(2a\ln P + b)/P$ below P_c and is a constant D above P_c. Regression results for a, b, c, V_0, D and P_c for the average S-wave velocity of each rock sample consistently display values of $R^2 > 0.98$.

Table 5.6 Characteristics of three types of eclogites from the Dabie-Sulu UHP belt, China

		Type-1 eclogite	Type-2 eclogite	Type-3 eclogite
Grain size		Coarse	Fine	Fine
Metamorphism		Graphite / diamond, Unaltered	Quartz / coesite, Sheared	Amphibolite facies, Retrograde
Mineralogy		Grt + Omp ± Rt ± Coe/Qtz	Grt + Omp + Qtz + Rt ± Phn ± Amp	Grt (<30%) + Omp + Amp ± Phn ± Qtz ± Ep ± Pl ± Opq ± Rt
Major oxides (wt. %)	SiO_2	43.87 ± 1.41	49.84 ± 2.46	49.62 ± 5.68
	Al_2O_3	21.44 ± 1.13	15.72 ± 2.63	15.66 ± 2.02
	MgO	11.32 ± 1.73	7.16 ± 3.32	4.97 ± 0.40
	Na_2O	1.41 ± 0.57	2.95 ± 1.09	3.04 ± 0.61
Density (g/cm^3)		3.57 ± 0.05	3.44 ± 0.07	3.44 ± 0.03
Vp (km/s)	50 MPa	7.86 ± 0.15	7.28 ± 0.23	6.73 ± 0.40
	600 MPa	8.51 ± 0.11	7.89 ± 0.16	7.46 ± 0.26
Linear *Vp-P* equation		$Vp=8.421+1.411\times10^{-4}P$	$Vp=7.796+1.58\times10^{-4}P$	$Vp=7.332+2.044\times10^{-4}P$
Vs (km/s)	50 MPa	4.57 ± 0.11	4.28 ± 0.07	4.04 ± 0.08
	600 MPa	4.85 ± 0.06	4.53 ± 0.04	4.33 ± 0.09
Linear *Vs-P* equation		$Vs=4.762+1.464\times10^{-4}P$	$Vs=4.435+1.671\times10^{-4}P$	$Vs=4.212+2.025\times10^{-4}P$
Anisotropy		Low (<5% at 600 MPa)	Low (<5% at 600 MPa)	High
σ at 600 MPa		0.260 ± 0.010	0.243 ± 0.028	0.251 ± 0.021

Inverting field-measured P-wave velocities and Poisson's ratios for the volume fractions of major lithologies yields some valuable constraints on the composition of the crust beneath the Sulu and Dabie UHP terranes although uncertainties are inherent in this approach. The high velocity layers in the uppermost crust of the Dabie-Sulu UHP belt can be attributed to the presence of eclogite and ultramafic rocks, which are interlayered with felsic gneiss, paragneiss, amphibolite and marble. Beneath the Dabie or Sulu UHP unit, the middle and lower crust has an intermediate bulk composition, and is almost free of eclogites. Thus our primary conclusion is that the eclogite-bearing UHP rocks were thrust as tectonic slices over a normal, UHP-free middle-lower crust by the syn-collisional exhumation.

Chapter 6
General discussion and conclusions

The past 4 decades have been a virtual explosion in the amount of data available on the seismic velocities and anisotropy of rocks from around the world. There was neither single book nor Internet database for information on seismic properties of hundreds different types of rocks from continents and oceans. Therefore we established an Internet Database of Rock Seismic Properties (DRSP) and published *Handbook of Seismic Properties of Minerals, Rocks and Ores* (Ji et al., 2002; 630 pp). They comprise almost all data available in the literature published in English and French during last 4 decades and are more complete than any previous compilations. Obviously, such a database and a handbook can serve as a convenient, compact, and comprehensive source of basic information for physical properties of rocks and minerals, and permit enormous volumes of data to be studied in a far more efficient fashion than has hitherto been attempted.

The first part of our handbook addresses single crystal elasticity and seismic properties of 53 common rock-forming minerals, and the overall elastic moduli of their polycrystalline aggregates. The second part deals with P- and S-wave velocities and anisotropy of various rocks as functions of pressure, temperature, and propagation and vibration directions. Also given are: geographic location, tectonic setting, lithology, original sample number, density, porosity, humidity (dry or wet), and source literature for each sample. Two tables are also used to summarize chemical and mineral modal compositions of the samples whose seismic velocities and anisotropy have been measured. Finally, it presents the relationship between seismic velocities (*Vp* and *Vs*) and density, seismic anisotropy and the mean Poisson's ratio of each main lithologic category, and the effects of phase transformation on seismic properties.

Both the handbook and the Internet database are an educational resource to both the undergraduate and graduate levels. With the help of the handbook or the database,

students can better understand the P-and S-wave velocities and their anisotropy for rocks that constitutes the crust and upper mantle at different depths. Such knowledge is needed in order to interpret the seismic data from refraction and reflection experiments. As a bridge between petrophysics and engineering, and between geology and geophysics, the handbook and the database provides infrastructure to the increasingly interdisciplinary nature of modern research, and keeps the world earth science and geotechnical communities informed about the growing body of rock physical property data.

To examine different elastic mixture rules used in calculation seismic properties of polyphase rocks, we compared experimentally derived P-wave velocities of 696 dry samples with values calculated from the volume fraction and room pressure elastic constants of each constituent minerals. The calculated P-wave velocities agree well with laboratory values measured at about 300 MPa, even though elastic constants of only 22 common minerals were taken into account in the computation. The mean *Vp* of polymineralic rocks is exclusively controlled by the volume fractions of its constituent minerals while grain shape and crystallographic preferred orientations, anisotropy and other perturbations have minimum effects. As long as an appropriate averaging scheme is selected and the volume fraction is correctly determined for each mineral, average seismic velocities of most crustal and upper mantle rocks can be estimated with good quality. Therefore judicial selection of relevant mixture rule is critical to interpret the crustal and upper mantle seismic data in terms of mineralogical compositions and structures.

Knowledge of the seismic properties of ultrahigh-pressure (UHP) metamorphic rocks is the basis for interpretation of seismic data from modern and ancient subduction zones and for understanding the evolution of subducted slabs. As the most important part of this thesis, P- and S-wave velocities, pressure derivatives, anisotropy and shear wave splitting of eclogites and country rocks from the Dabie-Sulu UHP metamorphic belt, China, have been measured under confining pressures up to 800 MPa. Three types of eclogites in the Dabie-Sulu UHP terrane are distinguished according to their grain size, degree of

retrograde metamorphism and petrophysical properties. Type-1 eclogites are coarse-grained and almost unaffected by retrograde metamorphism, experienced recovery-accommodated dislocation creep at peak metamorphic conditions (in the diamond stability field). Type-2 eclogites are fine-grained reworked Type-1 materials that experienced recrystallization-accommodated dislocation creep under quartz/coesite boundary conditions during the early stage of exhumation. Type-3 eclogites are overprinted by significant amphibolite facies metamorphism during a late stage of exhumation within the crust. Type-1 eclogites are richer in Al_2O_3 and MgO but poorer in SiO_2 and Na_2O than Type-2 and Type-3 eclogites. From Type-1 to Type-2 and to Type-3 eclogites, seismic velocities and density (ρ) successively decrease. Seismic anisotropy of Type-1 and Type-2 eclogites is generally low (<5%) because volumetrically important garnet is elastically quasi-isotropic. The compositional layering and retrograde metamorphism can result in significant anisotropy and shear wave splitting in eclogites, suggesting a plausible contribution of eclogites to seismic anisotropy of the upper mantle.

The transition of the pressure dependence of velocity from the poroelastic to elastic regimes occurs at a critical pressure (P_c), which depends mainly on the density and distribution of microcracks and in turn on the exhumation history of rocks. We proposed an empirical equation to describe the nonlinear increase of velocity at low pressures: $V = a(\ln P)^2 + b\ln P + c$ ($P \leq P_c$), where P is the confining pressure; a and b are constants describing the closure of microcracks below P_c; c is the velocity when P is equal to unity (i.e., 1 MPa). This equation provides more simple and straightforward expression for prediction seismic velocities at shallow depth. Above P_c, the velocity-pressure linear relationship is $V = V_0 + DP$, where V_0 is the projected velocity of a crack-free sample at room pressure, and D is the intrinsic pressure derivative. When data are curve-fit, pressure derivatives and anisotropy as functions of pressure can be determined. The average velocity of Dabie-Sulu eclogites in the linear regime is $Vp = 8.42 + 1.41\times10^{-4}P$ and $Vs = 4.76+1.46\times10^{-4}P$ for Type-1, $Vp = 7.80 + 1.58\times10^{-4}P$ and

$Vs = 4.44 + 1.67 \times 10^{-4} P$ for Type-2, and $Vp = 7.33 + 2.04 \times 10^{-4} P$ and $Vs = 4.21 + 2.02 \times 10^{-4} P$ for Type-3, where Vp and Vs are in km/s and P in MPa. The decrease in V_0 and increase in D from Type-1 to Type-3 eclogites are attributed to a decrease in garnet content and an increase in retrograde minerals.

Integrating our results of Vp and Vs with reliable data from previous studies, we performed new estimates of pressure and temperature derivatives of Vp and Vs and Poisson's ratios for common rock types in the UHP metamorphic belt. Average petrophysical properties of eclogites at 600 MPa and room temperature are summarized as: Vp = 7.991±0.489 km/s, Vs = 4.552±0.279 km/s, Vp/Vs = 1.756±0.044, σ = 0.259±0.018, ρ = 3.449±0.134 g/cm^3 and SiO_2 = 46.9±3.9%. From Type-1 to Type-2 to Type-3 eclogites, Vp, Vs and density decrease gradually while Vp/Vs ratios and Poisson's ratios display similar mean values but wider deviation. A new compilation for Poisson's ratio of 22 major lithologies provides more constraints on relating velocity with lithology. Poisson's ratios will reach 0.24-0.25 for Type-1 and Type-2 eclogites, 0.28-0.29 for peridotite and 0.30-0.31 for serpentinized peridotite in the upper mantle, suggesting a way to distinguish them in seismic refraction surveys.

Due to high density and high velocity of eclogites, contacts of eclogites with granitic gneiss, paragneiss, marble, amphibolite, granulite and serpentinized peridotite can produce strong seismic reflections. The NE-SW trending, NW-dipping, slab-like high Vp anomaly (8.72 km/s at a depth of 71 km) which extends from the Moho to at least 110 km beneath the Dabie-Sulu region, can be interpreted as the remnant of a subducted slab which is dominated by Type-1 eclogites and has been arrested in the upper mantle since about 200-220 Ma. Such relic crustal materials, subducted and preserved as eclogite layers intercalated with felsic gneisses, garnet-jadeite quartzite, marble and serpentinized peridotite, could be responsible for observed mantle reflections beneath other orogenic belts (e.g., the Abitibi-Opatica belt of the Canadian Superior Province, the Northwest Territories of Canada, the western Superior Province).

Based on experimentally derived seismic velocities of UHP rocks, seismic refraction velocities, geological observations and direct examination of deeply exhumed rocks, we used the geometric mean as a mixture rule to invert the lithological and chemical compositions of the layered crust beneath the Dabie-Sulu UHP belt and to decipher the exhumation of UHP rocks. Most eclogites are concentrated in the uppermost crust and result in high velocity layers and strong reflections in the upper crust. The Sulu terrane and the Dabie Mountains display a bulk intermediate lower crust, however, the Dabie Mountains may contain more mafic granulite and become denser than the Sulu terrane, suggesting different post-collisional evolution in these two segments. The scarcity of eclogites in the deep crust suggests that the eclogite-bearing UHP rocks are tectonic slices thrust, along a series of shear zones during the continental collision between the North China and Yangtze cratons, over a normal UHP-free middle-lower crust.

Our work provides a solid basis for further research. During next several years, Professor Shaocheng Ji and I will carry out an integrated study of field mapping, structural analysis, microstructure, petrophysics and rheology of UHP eclogites and garnet peridotites as well as their wall rocks from the cores of the Chinese Continental Scientific Drilling (CCSD) and key surface outcrops (particularly those of UHP shear zones) in the Sulu region. The prospected work will focus on:

(1) Key mapping and field structural analysis of both typical outcrops and CCSD drill cores will be performed to characterize 3D patterns of deformation of UHP rocks, magnitude of finite strains, relative rheological strengths of minerals, strain localization and kinematic indicators. Furthermore, most UHP metamorphic rocks in the Sulu region have not been subjected to modern structural analyses in term of composite rheology. Thus the impact of our further work will be high given current international interest in UHP tectonics.

(2) Microstructural analysis using electron backscatter diffraction (EBSD) technique will specially address the questions: (a) What is the typical LPO that develops in eclogites and peridotites undergoing UHP metamorphism and deformation and what is the deformation mechanism (dislocation creep, diffusion creep or solution-precipitation) operating under the UHP conditions? (b) What is the role of dynamic recrystallization on the dislocation creep and on the development of LPO and seismic anisotropy? (c) How does the LPO vary with magnitude of finite strain, strain history, temperature, pressure, water content (hydrolytic weakening), degree of dynamic recrystallization and tectonic kinematics? (d) Which theoretical model of LPO development best fits the fabric data for cubic garnet, orthorhombic olivine, monoclinic omphacite and tetragonal rutile? (e) Can LPOs of these minerals help determine the strain history of deformed UHP rocks and kinematics?

(3) Chemical analysis. Fluid inclusions, stable isotope, and major, minor, trace and REE analyses coupled with microstructural, geochronological and thermochronological data will be done for three types of UHP eclogites in collaborations with Prof. Bin Xia (Guangzhou Institute of Geochemistry) and Prof. Zhiqin Xu (Director of CCSD) in order to constrain effects of metamorphic reactions and fluid-rock interactions on rheology over geological time.

(4) Petrophysical study. P- and S-wave velocities, anisotropy and shear wave splitting of UHP rocks sampled from CCSD cores will be measured under hydrostatic pressures ranging from 0.1 MPa to 1000 MPa at the GSC/Dalhousie High Pressure Laboratory in Halifax in collaboration with Prof. M.H. Salisbury. Comparison of the results with previous data on surface outcrop samples will offer the unique possibility to examine the nonlinear velocity-pressure relationship of hard rocks due to microcracks. The eclogites are typical bi-mineralogical rocks with varying contents of garnet and omphacite. The measured velocities and anisotropy will be quantitatively compared with the theoretical values calculated from elastic constants, EBSD fabrics and

volume fractions of the constituents. Variations of seismic properties with garnet volume fraction will be determined to test the mixture rules. The modal compositions will benefit from the ameliorated image analysis tools (NIH Image freeware). We are also interested in the role of retrograde metamorphism on Poisson's ratio of eclogite and peridotite. Collaborated with Wencai Yang (Chief-seismologist for CCSD project), we will analyze and interpret the 3D reflection and refraction seismic data acquired from the CCSD site and vicinities. Our further petrophysical study undoubtedly stimulates progress in understanding the deep structures of this interesting region, and hopefully leads to a resolution of the question of whether the eclogites have sunk into the mantle by delamination.

(5) Geothermal modeling. New results on rheology and elasticity of eclogites and their country rocks will be helpful to model evolution of the continental collision zone and preservation of primary textures and UHP minerals in UHP terrains, which provide an ideal opportunity to test different hypotheses on subduction and exhumation of UHP rocks. After constructing a unified seismic and petrological model of the Dabie-Sulu orogenic belt, a new thermomechanical evolution model will reveal how these continental materials subducted to depths more than 100 km and exhumed rapidly, how mountain and fold-and-thrust foreland belt were built, and how the subduction and post-collisional events result in different geological and geophysical signatures along the strike of the collision zone.

References

AKAOGI, M., ITO, E., NAVROTSKY, A. 1989. "Olivine-modified spinel-spinel transitions in the system Mg_2SiO_4-Fe_2SiO_4: Calorimetric measurements, thermochemical calculation, and geophysical application". *Journal of Geophysical Research*, 94:11. 15671-15685.

ALEKSANDROV, K.S., RYZHOVA, T.V., BELIKOV, B.P. 1964. "The elastic properties of pyroxenes". *Soviet Physics – Crystallography*. 8, 589-591.

ARZI, A.A. 1978. "Critical phenomena in the rheology of partially melted rocks". *Tectonophysics*. 44:1-4. 173-184.

BABUSKA, V. 1972. "Elasticity and anisotropy of dunite and bronzitite". *Journal of Geophysical Research*. 77:35. 6955-6965.

BABUSKA, V., FIALA, J., KUMAZAWA, M., OHNO, I., SUMINO, Y. 1978. "Elastic properties of garnet solid solution series". *Physics of the Earth and Planetary Interiors*. 16:2. 157-176.

BAKER, D.W. CARTER, N.L. 1972. "Seismic velocity anisotropy calculated for ultramafic minerals and aggregates". In *Flow and Fracture of Rocks*. HEARD, H., BORG, I., CARTER, N.L., RALEIGH, B. (Eds.). Washington, D.C.: American Geophysical Union. P. 157-166.

BANNO, S., ENAMI, M., HIRAJIMA, T., ISHIWATARI, A., WANG, Q.C. 2000. "Decompression P-T path of coesite eclogite to granulite from Weihai, eastern China". *Lithos*. 52:1-4. 97-108.

BARRUOL, G. 1993. *Pétrophysique de la croûte inférieure. Rôle de l'anisotropie sismique sur la réflectivité et le déphasage des ondes S*. Ph.D Thesis. Université de Montpellier II, France. 272p.

BARRUOL, G., GRANET, M. 2002. "A Tertiary asthenospheric flow beneath the southern French Massif Central indicated by upper mantle seismic anisotropy and

related to the west Mediterranean extension". *Earth and Planetary Science Letters.* 202:1. 31-47.

BARRUOL, G., KERN, H. 1996. "Seismic anisotropy and shear-wave splitting in lower-crustal and upper-mantle rocks from the Ivrea zone – experimental and calculated data". *Physics of the Earth and Planetary Interiors.* 95:3-4. 175-194.

BARRUOL, G., MAINPRICE, D. 1993. "3-D seismic velocities calculated from lattice-preferred orientation and reflectivity of a lower crustal section: examples of the Val Sesia section (Ivrea zone, northern Italy)". *Geophysical Journal International.* 115:3. 1169-1188.

BARRUOL, G., SILVER, P.G., VAUCHEZ, A. 1997. "Seismic anisotropy in the eastern US: deep structure of a complex continental plate". *Journal of Geophysical Research.* 102:4. 8329-8348.

BARRUOL, G., SOURIAU, A., VAUCHEZ, A., DIAZ, J., GALLART, J., TUBIA, J., CUEVAS, J. 1998. "Lithospheric anisotropy beneath the Pyrenees from shear wave splitting". *Journal of Geophysical Research.* 103:12. 30039-30053.

BASCOU, J., BARRUOL, G., VAUCHEZ, A., MAINPRICE, D., EGYDIO-SILVA, M. 2001. "EBSD-measured lattice-preferred orientations and seismic properties of eclogites". *Tectonophysics.* 342:1-2. 61-80.

BEN ISMAÏL, W., MAINPRICE, D. 1998. "An olivine fabric database: an overview of upper mantle fabrics and seismic anisotropy". *Tectonophysics.* 296:1-2. 145-157.

BENZ, H.M., VIDALE, J.E. 1993. "Sharpness of upper mantle discontinuities determined from high-frequency reflections". *Nature.* 365:6442. 147-150.

BERGE, P.A., BONNER, B.P., BERRYMAN, J.G. 1995. "Ultrasonic velocity-porosity relationship for sandstone analogs made from fused glass beads". *Geophysics.* 60:1. 108-119.

BERRYMAN, J.G. 1994. "Role of porosity in estimates of composite elastic constants". *Journal of Energy Resources Technology.* 116:2. 87-96.

BERRYMAN, J.G. 1995. "Mixture theories of rock properties". In *Rock Physics and Phase Relations: A Handbook on Physical Constants.* Ahrens, T.J (Ed.). Washington, D. C.: AGU Ref. Shelf, vol. 3. P. 205-228.

BHAGAT, S., BASS, J.D., SMYTH, J. 1992. "Single-crystal elastic properties of omphacite-C2/c by Brillouin spectroscopy". *Journal of Geophysical Research.* 97:5. 6843-6848.

BINA, C.R., KUMAZAWA, M. 1993. "Thermodynamic coupling of phase and chemical boundaries". *Physics of the Earth and Planetary Interiors.* 76:3-4. 329-341.

BIRCH, F. 1960. "The velocity of compressional waves in rocks to 10 kilobar, Part 1". *Journal of Geophysical Research.* 65:4. 1083-1102.

BIRCH, F. 1961. "The velocity of compressional waves in rocks to 10 kilobar, Part 2". *Journal of Geophysical Research.* 66:7. 2199-2224.

BLACKMAN, D.K., WENK, H.R., KENDALL, J.M. 2002. "Seismic anisotropy of the upper mantle 1. Factors that affect mineral texture and effective elastic properties". *Geochemistry Geophysics Geosystems.* 3:9, 8601, doi:10.1029/2001GC00248.

BLAKSLEE, O.L., PROCTOR, D.G., SELDIN, E.J., SPENCE, G.B., WENG, T. 1970. "Elastic constants of compression-annealed pyrolytic graphite". *Journal of Applied Physics.* 41:8, 3373-3382.

BOHLEN, S.R., MONTANA, A., KERRICK, D.M. 1991. "Precise determinations of the equilibriums kyanite = sillimanite and kyanite = andalusite and a revised triple point for Al_2SiO_5 polymorphs". *American Mineralogist.* 76:3-4. 677-680.

BOKELMANN, G.H.R., HARJES, H.P. 2000. "Evidence for temporal variation of seismic velocity within the upper continental crust". *Journal of Geophysical Research.* 105:10. 23879-23894.

BOSTOCK, M.G. 1997. "Anisotropic upper-mantle stratigraphy and architecture of the Slave craton". *Nature.* 390:6658. 392-395.

BRAEM, M., VAN DOREN, V.E., LAMBRECHTS, P., VANHERLE, G. 1987. "Determination of Young's modulus of dental composites: a phenomenological model". *Journal of Materials Science.* 22:6. 2037-2042.

BUNDY, F.P. 1980. "The P, T phase and reaction diagram for elemental carbon". *Journal of Geophysical Research.* 85:12. 6930-6936.

BURLINI, L., MARQUER, D., CHALLANDES, N., MAZZOLA, S., ZANGARINI, N. 1998. "Seismic properties of highly strained marbles from the Splügenpass, central Alps". *Journal of Structural Geology.* 20:2-3. 277-292.

CALVERT, A.J., SAWYER, E.W., DAVIS, W.J., LUDDEN, J.N. 1995. "Archean subduction inferred from seismic images of a mantle suture in the Superior Province". *Nature.* 375:6533. 670-674.

CAMPBELL, A.J., HEINZ, D.L. 1992. "A high pressure test of Birch's law". *Science.* 257:5066. 66-67.

CHANG, Z.P., BARSCH, G.R. 1973. "Pressure dependence of single crystal elastic constants and anharmonic properties of spinel". *Journal of Geophysical Research.* 78:4. 2418-2433.

CHAVAGNAC, V., JAHN, B.M. 1996. "Coesite-bearing eclogites from the Bixiling Complex, Dabie Mountains, China: Sm-Nd ages, geochemical characteristics and tectonic implications". *Chemical Geology.* 133:1-4. 29-51.

CHEMENDA, A.I., MATTAUER, M., BOKUN, A.N. 1996. "Continental subduction and a mechanism for exhumation of high-pressure metamorphic rocks: new modelling and field data from Oman". *Earth and Planetary Science Letters.* 143:1-4. 173-182.

CHEMENDA, A.I., MATTAUER, M., MALAVIEILLE, J., BOKUN, A.N. 1995. "A mechanism for syn-collisional deep rock exhumation and associated normal faulting: results from physical modeling." *Earth and Planetary Science Letters.* 132: 1-4. 225-232.

CHEN, P.E., LIN, J.M. 1969. "Transverse properties of fibrous composites". *Materials Research and Standards.* 9. 29-33.

CHENG, W., GREENWOOD, H.J. 1989. "The stability of the assemblage zoisite + diopside". *The Canadian Mineralogist.* 27:4. 657-662.

CHRISTENSEN, N.I. 1965. "Compressional wave velocities in metamorphic rocks at pressures to 10 kilobars". *Journal of Geophysical Research.* 70:24. 6147-6164.

CHRISTENSEN, N.I. 1966. "Shear wave velocities in metamorphic rocks at pressures to 10 kilobars". *Journal of Geophysical Research.* 71:12. 3549-3556.

CHRISTENSEN, N.I. 1974. "Compressional wave velocities in possible mantle rocks to pressures of 30 kilobars". *Journal of Geophysical Research.* 79:2. 407-412.

CHRISTENSEN, N.I. 1978. "Ophiolites, seismic velocities, and oceanic crustal structure". *Tectonophysics.* 47:1-2. 131-157.

CHRISTENSEN, N.I. 1985. "Measurement of dynamic properties of rock at elevated temperatures and pressures". In *ASTM Special Technical Publication 869.* Pincus, H.J., Hoskins, E.R. (Eds.). Philadelphia, America: American Society of Testing and Materials. P. 93-107.

CHRISTENSEN, N.I. 1989. "Seismic velocities". In *Practical Handbook of Physical Properties of Rocks and Minerals.* Carmichael, R.S. (Ed.). Boca Raton, Florida, America: CRC Press Inc. P. 429-546.

CHRISTENSEN, N.I. 1996. "Poisson's ratio and crustal seismology". *Journal of Geophysical Research.* 101:2. 3139-3156.

CHRISTENSEN, N.I. 2002. "Continental mantle seismic anisotropy: a new look at the Twin Sisters massif". *Tectonophysics.* 355:1-4. 163-170.

CHRISTENSEN, N.I., MOONEY, W.D. 1995. "Seismic velocity structure and composition of the continental crust: a global view". *Journal of Geophysical Research.* 100:6. 9761-9788.

CHRISTENSEN, N.I., RAMANANANTOANDRO, R. 1971. "Elastic moduli and anisotropy of dunite to 10 kilobars". *Journal of Geophysical Research.* 76:17. 4003-4010.

CLOOS, M. 1982. "Flow mélange: numerical modeling and geologic constraints on their origin in the Franciscan subduction complex, California." *Geological Society of American Bulletin.* 93:4. 330-345.

CLYNE, T.W., WITHERS, P.J. 1993. *An Introduction to Metal Matrix Composites.* New York: Cambridge University Press. 509p.

COOK, F.A., VAN DER VELDEN, A.J., HALL, K.W. 1999. "Frozen subduction in Canada's Northwest Territories: Lithoprobe deep lithospheric reflection profiling of the western Canadian Shield". *Tectonics.* 18:1. 1-24.

CRAMPIN, S. 1999. "Calculable fluid-rock interactions". *Journal of the Geological Society of London.* 156. 501-514.

CROSSON, R.S., LIN, J.W. 1971. "Voigt and Reuss prediction of anisotropic elasticity of dunite". *Journal of Geophysical Research.* 76:2. 570-578.

DOI, H., FUJIWARA, Y., MIYAKE, K., OOSAWA, Y. 1970. "A systematic investigation of elastic moduli of WC-Co alloys". *Metallurgical Transactions.* 1:5. 1417-1425.

DZIEWONSKI, A.M., ANDERSON, D.L. 1981. "Preliminary reference Earth model". *Physics of the Earth and Planetary Interiors.* 25:4. 297-356.

EBERHART-PHILLIPS, D., HAN, D.H., ZOBACK, M.D. 1989. "Empirical relationships among seismic velocity, effective pressure, porosity, and clay content in sandstone". *Geophysics.* 54:1. 82-89.

EINSTEIN, A. 1906, "Eine neue Bestimmung der Molekuldimensionen". *Ann. Phys. (Leipzig).* 19. 289-306.

EINSTEIN, A. 1911. "Berichtigung zu meiner arbeit - Eine neue Bestimmung der Molekuledimensionen". *Ann. Phys. (Leipzig).* 34, 591-592.

ERNST, W.G. 2001. "Subduction, ultrahigh-pressure metamorphism, and regurgitation of buoyant crustal slices – implications for arcs and continental growth". *Physics of the Earth and Planetary Interiors.* 127:1-4. 253-275.

ERNST, W.G., PEACOCK, S.M. 1996. "A thermotectonic model for preservation of ultrahigh-pressure phases in metamorphosed continental crust". In *Subduction top to bottom.* Washington, D.C., America: Geophysical Monograph. 96. Americal Geophysical Union. P. 171-178.

FAURE, M., LIN, W. 2001. "Where is the North China-South China block boundary in eastern China?" *Geology.* 29:2. 119-122.

FAURE, M., LIN, W., MONIÉ, P., LE BRETON, N., POUSSINEAU, S., PANIS, D., DELOULE, E. 2003a. "Exhumation tectonics of the ultrahigh-pressure metamorphic rocks in the Qinling orogen in East China: New petrological-structural-radiometric insights from the Shandong Peninsula". *Tectonics.* 22:3. 1018, doi: 10.1029/ 2002TC001450.

FAURE, M., LIN, W., SCHÄRER, U., SHU, L.S., SUN, Y., ARNAUD, N. 2003b. "Continental subduction and exhumation of UHP rocks: structural and geochronological insights from the Dabieshan (East China)". *Lithos.* 70:3-4. 213-241.

FEI, Y.W., MAO, H.K., MYSEN, B.O. 1991. "Experimental determination of element partitioning and calculation of phase relations in the MgO-FeO-SiO_2 system at high pressure and high temperature". *Journal of Geophysical Research.* 96:2. 2157-2170.

FOUNTAIN, D.M., BOUNDY, T.M., AUSTRHEIM, H., REY, P. 1994. "Eclogite-facies shear zones – deep crustal reflectors?" *Tectonophysics.* 232:1-4. 411-424.

FOUNTAIN, D.M., CHRISTENSEN, N.I. 1989. "Composition of the continental crust and upper mantle: A review". *Memoir - Geological Society of America.* 172. 711-742.

FOUNTAIN, D.M., HURICH, C.A., SMITHSON, S.B. 1984. "Seismic reflectivity of mylonitic zones in the crust". *Geology.* 12:4. 195-198.

FOUNTAIN, D.M., SALISBURY, M.H., PERCIVAL, J. 1990. "Seismic structure of the continental crust based on rock velocity measurements from the Kapuskasing uplift". *Journal of Geophysical Research.* 95:2. 1167-1186.

FREUND, D. 1992. "Ultrasonic compressional and shear velocities in dry clastic rocks as a function of porosity, clay content, and confining pressure". *Geophysical Journal International.* 108:1. 125-135.

FRISILLO, A.L., BARSCH, G.R. 1972. "Measurements of single-crystal elastic constants of bronzite as a function of pressure and temperature". *Journal of Geophysical Research.* 77:32. 6360-6384.

GAO, S., KERN, H., JIN, Z.M., POPP, T., JIN, S.Y., ZHANG, H., ZHANG, B. 2001. "Poisson's ratio of eclogite: the role of retrogression". *Earth and Planetary Science Letters.* 192:4. 523-531.

GAO, S., KERN, H., LIU, Y., JIN, S.Y., POPP, T., JIN, Z.M., FENG, J., SUN, M., ZHAO, Z. 2000. "Measured and calculated seismic velocities and densities for granulites from xenolith occurrences and adjacent exposed lower crustal sections: a comparative study from the North China craton". *Journal of Geophysical Research.* 105:8. 18965-18976.

GAO, S., ZHANG, B.R., JIN, Z.M., KERN, H., LUO, T.C., ZHAO, Z.D. 1998. "How mafic is the lower continental crust?" *Earth and Planetary Science Letters.* 161:1-4. 101-117.

GERYA, T.V., STÖCKHERT, B. 2002. "Exhumation rates of high pressure metamorphic rocks in subduction channels: the effect of rheology". *Geophysical Research Letters.* 29:8. 1261, doi:10.1029/2001GL014307.

GURLAND, J. 1979. "Structural approach to the yield strength of two-phase alloys with coarse microstructures". *Materials Science and Engineering.* 40:1. 59-71.

GUSTAFSON, T.W., PANDA, P.C., SONG, G., RAJ, R. 1997. "Influence of microstructural scale on plastic flow behavior of metal matrix composites". *Acta Materialia.* 45:4. 1633-1643.

GUYER, R.A., JOHNSON, P.A. 1999. "Nonlinear mesoscopic elasticity: evidence for a new class of materials". *Physics Today.* 52:4. 30-36.

HACKER, B. R., ABERS, G. A., PEACOCK, S.M. 2003. "Subduction factory, 1. Theoretical mineralogy, densities, seismic wave speed and H_2O contents". *Journal of Geophysical Research.* 108:1. 2029, doi: 10.1029/2001JB001127.

HACKER, B. R., RATSCHBACHER, L., WEBB, L. E., DONG, S. W. 1995. "What brought them up? Exhumation of the Dabie Shan ultrahigh-pressure rocks". *Geology.* 23:8. 743-746.

HACKER, B.R., RATSCHBACHER, L., WEBB, L.E., IRELAND, T., DOUGLAS, W., DONG, S. 1998. "U/Pb zircon ages constrain the architecture of the ultrahigh-pressure Qinling-Dabie Orogen, China". *Earth and Planetary Science Letters.* 161:1-4. 215-230.

HACKER, B.R., RATSCHBACHER, L., WEBB, L.E., MCWILLIAMS, M.O., IRELAND, T., CALVERT, A., DONG, S., WENK, H., CHATEIGNER, D. 2000. "Exhumation of ultrahigh-pressure continental crust in east central China: Late Triassic-early Jurassic tectonic unroofing". *Journal of Geophysical Research.* 105:6. 13339-13364.

HASHIN, Z. 1983. "Analysis of composite Materials — A survey". *Journal of Applied Mechanics, Transactions ASME.* 50:3. 481-505.

HASHIN, Z., SHTRIKMAN S. 1963. "A variation approach to the theory of the elastic behavior of multiphase materials". *Journal of Mechanics and Physics of Solids.* 11:2. 127-140.

HASHIN, Z., SHTRIKMAN, S. 1962a. "On some variational principles in anisotropic and nonhomogeneous elasticity". *Journal of Mechanics and Physics of Solids.* 10:Oct-Dec. 335-342.

HASHIN, Z., SHTRIKMAN, S. 1962b. "A variational approach to the theory of the elastic behaviour of polycrystals". *Journal of Mechanics and Physics of Solids.* 10:Oct-Dec. 343-352.

HASSELMAN, D.P., FULRATH, R.M. 1965a. "Effect of alumina dispersion on Young's modulus of a glass". *Journal of the American Ceramic Society.* 48:4. 218-219.

HASSELMAN, D.P., FULRATH, R.M. 1965b. "Effect of spherical tungsten dispersion on Young's modulus of a glass". *Journal of the American Ceramic Society.* 48:10. 548-549.

HEARMON, R.F.S. 1979. "The elastic constants of crystals and other anisotropic materials". In *Landolt-Bornstein Tables.* HELLWEGE, K.H., HELLWEGE, A.M. (Eds.). Berlin: Springer-Verlag. III/11. P.1-244.

HEARMON, R.F.S. 1984. "The elastic constants of crystals and other anisotropic materials". In *Landolt-Bornstein Tables.* HELLWEGE, K.H., HELLWEGE, A.M. (Eds.). Berlin: Springer-Verlag. III/18. P. 1-154.

HEMINGWAY, B.S., BOHLEN, S.R., HANKINS, W.B., WESTRUM, E.F. JR., KOSCOV, O.L. 1998. "Heat capacity and thermodynamic properties for coesite and

jadeite, reexamination of the quartz-coesite equilibrium boundary". *American Mineralogist*. 83:5-6. 409-418.

HILL, R. 1952. "The elastic behavior of a crystalline aggregate". *Physical Society -- Proceedings*. 65:389A. 349-354.

HILL, R. 1963. "Elastic properties of reinforced solids: some theoretical principles". *Journal of Mechanics and Physics of Solids*. 11:5. 357-372.

HILL, R. 1965. "A self-consistent mechanics of composite materials". *Journal of Mechanics and Physics of Solids*. 13:4. 213-222.

HOLBROOK, W.S., MOONEY, W.D., CHRISTENSEN, N.I. 1992. "The seismic velocity structure of the deep continental crust". In *Continental Lower Crust*. FOUNTAIN, D.M., ARCULUS, R. KEY, R.W. (Eds.). New York: Elsevier Science Publishers. P. 1-44.

HOLLAND, T.J.B. 1979. "Experimental determination of the reaction paragonite = jadeite + kyanite + H_2O and internally consistent thermodynamic data for part of the system Na_2O-Al_2O_3 -SiO_2 -H_2O, with applications to eclogites and blueschists". *Contributions to Mineralogy and Petrology*. 68:3. 293-301.

HOLLAND, T.J.B. 1980. "The reaction albite = jadeite + quartz determined experimentally in the range 600-1200 °C". *American Mineralogist*. 65:1-2. 129-134.

HOLLAND, T.J.B. 1988. "Preliminary phase reactions involving glaucophane and applications to high pressure petrology; new heat capacity and thermodynamic data". *Contributions to Mineralogy and Petrology*. 99:1. 134-142.

HU, S.B., HE, L.J., WANG, J.Y. 2001. "Compilation of heat flow data in the China continental area (3rd edition)". *Chinese Journal of Geophysics*. 44:5. 611-626.

HURICH, C.A., DEEMER, S.J., INDARES, A., SALISBURY, M. 2001. "Compositional and metamorphic controls on velocity and reflectivity in the continental crust: An example from the Grenville Province of eastern Quebec". *Journal of Geophysical Research*. 106:1. 665-682.

ISHAI, O., COHEN, L.J. 1967. Elastic properties of filled and porous epoxy composites. *International Journal of Mechanical Sciences*. 9:8. 539-546.

JAHN, B.M., CORNICHET, J., CONG, B., YUI, T.F. 1996. "Ultrahigh-ε_{Nd} eclogites from an ultrahigh-pressure metamorphic terrane of China". *Chemical Geology*. 127:1-3. 61-79.

JAHN, B.M., WU, F., LO, C., TSIA, C. 1999. "Crust-mantle interaction induced by deep subduction of the continental crust; geochemical and Sr-Nd isotropic evidence from post-collisional mafic-ultramafic intrusions of the northern Dabie Complex, central China". *Chemical Geology*. 157:1-2. 119-146.

JEANLOZ, R., THOMPSON, A.B. 1983. "Phase transitions and mantle discontinuities". *Reviews of Geophysics and Space Physics*. 21:1. 51-74.

JI, S.C., LONG, C., MARTIGNOLE, J., SALISBURY, M. 1997a. "Seismic reflectivity of a finely layered, granulite-facies ductile shear zone in the southern Grenville Province (Quebec)". *Tectonophysics*. 279:1-4. 113-133.

JI, S.C., MAINPRICE, D. 1988. "Natural deformation fabrics of plagioclase: implications for slip systems and seismic anisotropy". *Tectonophysics*. 147:1-2. 145-163.

JI, S.C., SALISBURY, M.H. 1993. "Shear-wave velocities, anisotropy and splitting in high-grade mylonites". *Tectonophysics*. 221:3-4. 453-473.

JI, S.C., SALISBURY, M.H., HANMER, S. 1993. "Petrofabric, P-wave anisotropy and seismic reflectivity of high-grade tectonites". *Tectonophysics*. 222:2. 195-226.

JI, S.C., SARUWATARI, K., MAINPRICE, D., WIRTH, R., XU, Z.Q., XIA, B., 2003. "Microstructures, petrofabrics and seismic properties of ultrahigh-pressure eclogites from the Sulu region, China: Implications for rheology of subducted continental crust and origin of mantle reflections". *Tectonophysics*. 370:1-4, 49-76.

JI, S.C., WANG, Q., XIA, B. 2002. *Handbook of Seismic Properties of Minerals, Rocks and Ores*. Montreal: Polytechnic International Press. 630 p.

JI, S.C., WANG, Q., XIA, B. 2003. "P-wave velocities of polymineralic rocks: comparison of theory and experiment and test of elastic mixture rules". *Tectonophysics*. 366 :1-2. 165-185.

JI, S.C., WANG, Q., XIA, B., MARCOTTE, D. 2004. "Mechanical properties of multiphase materials and rocks: a phenomenological approach using generalized means." *Journal of Structural Geology*. 26:8. 1377-1390.

JI, S.C., WANG, Z.C. 1999. "Elastic properties of forsterite-enstatite composites up to 3.0 GPa". *Journal of Geodynamics*. 28:2-3. 147-174.

JI, S.C., WANG, Z.C., WIRTH, R. 2001. "Bulk flow strength of forsterite-enstatite composites as a function of forsterite content". *Tectonophysics*. 341:1-4. 69-93.

JI, S.C., WIRTH, R., RYBACKI, E., JIANG, Z. 2000. "High-temperature plastic deformation of quartz-plagioclase multilayers by layer-normal compression". *Journal of Geophysical Research*. 105:7. 16651-16664.

JI, S.C., XIA, B. 2002. *Rheology of Polyphase Earth Materials*. Montreal: Polytechnic International Press. 260 p.

JI, S.C., ZHAO, P. 1994. "Strength of two-phase rocks: a model based on fiber-loading theory". *Journal of Structural Geology*. 16:2. 253-262.

JI, S.C., ZHAO, P., SARUWATARI, K. 1997b. "Fracturing of garnet crystals in anisotropic metamorphic rocks during uplift". *Journal of Structural Geology*. 19:5. 603-620.

JI, S.C., ZHAO, X., FRANCIS, D. 1994. "Calibration of shear-wave splitting in the subcontinental upper mantle beneath active orogenic belts using ultramafic xenoliths from the Canadian Cordillera and Alaska". *Tectonophysics*. 239:1-4. 1-27.

JOHANNES, W., PUHAN, D. 1971. "The calcite-aragonite transition, reinvestigated". *Contributions to Mineralogy and Petrology*. 31:1. 28-38.

JOHNSTON, J.E., CHRISTENSEN, N.I. 1992. "Shear wave reflectivity, anisotropies, Poisson's ratios, and densities of a southern Appalachian Paleozoic sedimentary sequence". *Tectonophysics*, 210:1-2. 1-20.

JONES, T.D., NUR, A. 1984. "The nature of seismic reflections from deep crustal fault zones". *Journal of Geophysical Research*. 89:5. 3153-3171.

KANAMORI, H., MIZUTANI, H. 1965. "Ultrasonic measurements of elastic constants of rocks under high pressures". *Bulletin of the Earthquake Research Institute.* 43, 173-194.

KATSURA, T., ITO, E. 1989. "The system Mg_2SiO_4-Fe_2SiO_4 at high-pressures and temperatures: precise determination of stabilities of olivine, modified spinel, and spinel". *Journal of Geophysical Research.* 94:11. 15663-15670.

KAY, R.W., KAY, S.M. 1991. "Creation and destruction of lower continental crust". *Geologische Rundschau.* 80. 259-278.

KENNETT, B.L.N., ENGDAHL, E.R. 1991. "Travel times for global earthquake location and phase identification". *Geophysical Journal International.* 105:2. 429-465.

KENYON, A.S., DUFFEY, H.J. 1967. "Properties of a particulate-filled polymer". *Polymer Engineering and Science.* 7:3. 189-193.

KERN, H. 1979. "Effect of high-low quartz transition on compressional and shear wave velocities in rocks under high pressure". *Physics and Chemistry of Minerals.* 4:2. 161-171.

KERN, H. 1982a. "P- and S-wave velocities in crustal and mantle rocks under the simultaneous action of high confining pressure and high temperature and the effect of the rock microstructure". In: *High-Pressure Research in Geosciences.* Schreyer, W. (Ed.). Stuttgart: E. Schweizerbart'sche Verlagsbuchhandlung, pp. 15-45.

KERN, H. 1982b. "Elastic-wave velocity in crustal and mantle rocks at high pressure and temperature: the role of the high-low quartz transition and of dehydration reactions". *Physics of the Earth and Planetary Interiors.* 29:1. 12-23.

KERN, H. 1993. "P- and S-wave anisotropy and shear-wave splitting at pressure and temperature in possible mantle rocks and their relation to the rock fabric". *Physics of the Earth and Planetary Interiors.* 78:3-4. 245-256.

KERN, H., BURLINI, L., ASHCHEPKOV, I.V. 1996. "Fabric-related seismic anisotropy in upper-mantle xenoliths: evidence from measurements and calculations". *Physics of the Earth and Planetary Interiors.* 95:3-4. 195-209.

KERN, H., GAO, S., JIN, Z., POPP, T., JIN, S. 1999. "Petrophysical studies on rocks from the Dabie ultrahigh-pressure (UHP) metamorphic belt, central China: implications for the composition and delamination of the lower crust". *Tectonophysics*. 301:3-4. 191-216.

KERN, H., GAO, S., LUI, Q.S. 1996. "Seismic properties and densities of middle and lower crustal rocks exposed along the North China Geoscience Transect". *Earth and Planetary Science Letters*. 139:3-4. 439-455.

KERN, H., JIN, Z., GAO, S., POPP, T., XU, Z.Q. 2002. "Physical properties of ultrahigh-pressure metamorphic rocks from the Sulu terrain, eastern central China: implications for the seismic structure at the Donghai (CCSD) drilling site". *Tectonophysics*. 354:3-4. 315-330.

KERN, H., POPP, T., GORBATSEVICH, F., ZHARIKOV, A., LOBANOV, K.V., SMIRNOV, Y.P. 2001. "Pressure and temperature dependence of Vp and Vs in rocks from the superdeep well and from surface analogues at Kola and the nature of velocity anisotropy". *Tectonophysics*. 338:2. 113-134.

KERN, H., RICHTER, A. 1981. "Temperature derivatives of compressional and shear wave velocities in crustal and mantle rocks at 6 kbar confining pressure". *Journal of Geophysics*. 49:1. 47-56.

KERN, H., TUBIA, J.M. 1993. "Pressure and temperature dependence of P- and S-wave velocities, seismic anisotropy and density of sheared rocks from Sierra Alpujata massif (Ronda peridotites, southern Spain)". *Earth and Planetary Science Letters*. 119:1-2. 191-205.

KERN, H., WENK, H.R. 1990. "Fabric-related velocity anisotropy and shear wave splitting in rocks from the Santa Rosa mylonite zone, California". *Journal of Geophysical Research*. 95:7. 11213-11223.

KNUDSON, F.P. 1962. "Effect of porosity on Young's modulus of alumina". *Journal of the American Ceramic Society*. 45:2. 94-95.

KORVIN, G. 1982. "Axiomatic characterization of the general mixture rule". *Geoexploration*. 19:4. 267-276.

KRETZ, R. 1983. "Symbols for rock-forming minerals". *American Mineralogist.* 68:1-2. 277-279.

KRONER, E. 1958. "Berechnung der elastischen Konstanten des Vielkristalle aus dem Konstanten des Einkristalls". *Zeitschrift für Physik.* 151, 504-518.

KUMAZAWA, M., ANDERSON, O.L. 1969. "Elastic moduli, pressure derivatives, and temperature derivatives of single-crystal olivine and single-crystal forsterite". *Journal of Geophysical Research.* 74:5. 5961-5972.

KUMAZAWA, M., HELMSTAEDT, H., MASAKI, K. 1971. "Elastic properties of eclogite xenoliths from diatremes of the east Colorado plateau and their implications to the upper mantle structure". *Journal of Geophysical Research.* 76:5. 1231-1247.

LEBEDEV, S., CHEVROT, S., VAN DER HILST, R.D. 2002. "Seismic evidence for olivine phase changes at the 410- and 660-kilometer discontinuities". *Science.* 296:5571. 1300-1302.

LEES, A.C., BUKOWINSKI, M.S.T., JEANLOZ, R. 1983. "Reflection properties of phase transition and compositional change models of the 670-km discontinuity". *Journal of Geophysical Research.* 88:10. 8145-8159.

LEJEUNE, A.M., RICHET, P. 1995. "Rheology of crystal-bearing silicate melts: an experimental study at high viscosities". *Journal of Geophysical Research.* 100:3. 4215-4229.

LEVEN, J.H. 1985. "The application of synthetic seismograms to the interpretation of the upper mantle P-wave velocity structure in northern Australia". *Physics of the Earth and Planetary Interiors.* 38:1. 9-27.

LEVIEN, L., WEIDNER, D.J., PREWITT, C.T. 1979. "Elasticity of diopside". *Physics and Chemistry of Minerals.* 4:2. 105-113.

LEVIN, V., MENKE, W., PARK, J. 1999. "Shear wave splitting in the Appalachians and the Urals: A case for multilayered anisotropy". *Journal of Geophysical Research.* 104:8. 17975-17993.

LI, B., KUNG, J., LIEBERMANN, R.C. 2004. "Modern techniques in measuring elasticity of Earth materials at high pressure and high temperature using ultrasonic

interferometry in conjunction with synchrotron X-radiation in multi-anvil apparatus". *Physics of the Earth and Planetary Interiors*. 143-144. 559-574.

LI, S., JAGOUTZ, E., LO, C., CHEN, Y., LI, Q., XIAO, Y. 1999. "Sm/Nd, Rb/Sr, and $^{40}Ar/^{39}Ar$ isotopic systematics of the ultrahigh-pressure metamorphic rocks in the Dabie-Sulu Belt, central China: a retrospective view". *International Geology Review*. 41:12. 1114-1124.

LIOU, J.G., HACKER, B.R., ZHANG, R.Y. 2000a. "Into the forbidden zone". *Science*. 287:5456. 1215-1216.

LIOU, J.G., ZHANG, R.Y., ERNST, W.G., RUMBLE, D., SHIGENORI, M. 1998. "High-pressure minerals from deeply subducted metamorphic rocks". In *Ultrahigh-pressure mineralogy; physics and chemistry of the Earth's deep interior. Reviews in Mineralogy*. Hemley, R.J. (Ed.). Washington, D.C.: Mineralogical Society of America. vol. 37. P. 33-96.

LIOU, J.G., ZHANG, R.Y., JAHN, B.M. 2000b. "Petrological and geochemical characteristics of ultrahigh-pressure metamorphic rocks from the Dabie-Sulu terrane, East-Central China". *International Geology Review*. 42:4. 328-352.

LITTLE, T.A., SAVAGE, M.K., TIKOFF, B. 2002. "Relationship between crustal finite strain and seismic anisotropy in the mantle, Pacific-Australia plate boundary zone, South Island, New Zealand". *Geophysical Journal International*. 151:1. 106-116.

LIU, F. L., XU, Z. Q., LIOU, J. G., SONG, S. 2004. "SHRIMP U-Pb ages of ultrahigh-pressure and retrograde metamorphism of gneisses, south-western Sulu terrane, eastern China". *Journal of Metamorphic Geology*. 22:4. 315-326.

LIU, J., CHEN, G., GWANMESIA, G.D., LIEBERMANN, R.C. 2000. "Elastic wave velocities of pyrope-majorite garnets ($Py_{62}Mj_{38}$ and $Py_{50}Mj_{50}$) to 9 GPa". *Physics of the Earth and Planetary Interiors*. 120:1-2. 153-163.

LLOYD, D.J. 1991. "Aspects of fracture in particulate reinforced metal matrix composites". *Acta Metallurgica et Materialia*, 39:1. 59-71.

LOKMER, I., HERAK, M. 1999. "Anisotropy of P-wave velocity in the upper crust of the central External Dinarides". *Studia Geophysica et Geodetica*. 43:4. 345-356.

LONG, C., CHRISTENSEN, N.I. 2000. "Seismic anisotropy of South African upper mantle xenoliths". *Earth and Planetary Science Letters*. 179:3-4. 551-565.

MA, X.Y., LIU, C.Q., LIU, G.D. 1991. "Global Geoscience Transect 2: Xiangshui to Mandal Transect, North China". *Publication No. 188 of the International Lithosphere Program*. P. 1-42.

MACBETH, C., BOYD, M., RIZER, W., QUEEN, J. 1998. "Estimation of reservoir fracturing from marine VSP using local shear-wave conversion". *Geophysical Prospecting*. 46:1. 29-50.

MAINPRICE, D. 1990. "A Fortran program to calculate seismic anisotropy from the lattice preferred orientation of minerals". *Computers & Geosciences*. 16:3. 385-393.

MAINPRICE, D., CASEY, M. 1990. "The calculated seismic properties of quartz mylonites with typical fabrics: relationship to kinematics and temperature". *Geophysical Journal International*. 103:3. 599-608.

MAINPRICE, D., HUMBERT, M. 1994. "Methods of calculating petrophysical properties from lattice preferred orientation data". *Surveys in Geophysics*. 15:5. 575-592.

MANGHNANI, M.H., RAMANANANTOANDRO, R., CLARK, S.P. 1974. "Compressional and shear wave velocities in granulite facies rocks and eclogites to 10 kilobars". *Journal of Geophysical Research*. 79:35. 5427-5445.

MASSONNE, H.J., SCHREYER, W. 1989. "Stability field of the high-pressure assemblage talc + phengite and two new phengite barometers". *European Journal of Mineralogy*. 1:3. 391-410.

MATTHIES, S., HUMBERT, M. 1993. "The realization of the concept of a geometric mean for calculating physical constants of polycrystalline materials". *Physica Status Solidi*. B177:2. K47-50.

MAULER, A., BURLINI, L., KUNZE, K., PHILIPPOT, P., BURG, J.P. 2000. "P-wave anisotropy in eclogites and relationship to the omphacite crystallographic fabric". *Physics and Chemistry of the Earth*. A25:2. 119-126.

MCDANELS, D.L. 1985. "Analysis of stress-strain, fracture and ductility of aluminium matrix composites containing discontinuous silicon carbide reinforcement". *Metallurgical Transactions.* A16:6. 1105-1115.

MCSKIMIN, H.J. 1950. "Ultrasonic measurement technique applicable to small solid specimens". *Acoustical Society of America.* 22:4. 413-418.

MECHIE, J., SOBOLEV, S.V., RATSCHBACHER, L., BABEYKO, A.Y., BOCK, G., JONES, A.G., NELSON, K.D., SOLON, K.D., BROWN, L.D., ZHAO, W. 2004. "Precise temperature estimation in the Tibetan crust from seismic detection of the α-β quartz transition". *Geology.* 32:7. 601-604.

MEISTER, R., PESELNICK, L. 1966. "Variational method of determining effective moduli of polycrystals with tetragonal symmetry". *Journal of Applied Physics.* 37:11. 4121-4125.

MEISTER, R., ROBERTSON, E.C., WERRE, R.W., RASPET, R. 1980. "Elastic moduli of rock glasses under pressure to 8 kilobars and geophysical implications". *Journal of Geophysical Research.* 85:11. 6461-6470.

MEWIS, J., MACOSKO, C.W. 1994. "Suspension rheology". In: *Rheology: Principles, Measurements and Applications.* MACOSKO, C.W. (Ed.). New York: VCH. P. 425-474.

MIZUNO, T., YOMOGIDA, K., ITO, H., KUWAHARA, Y. 2001. "Spatial distribution of shear wave anisotropy in the crust of the southern Hyogo region by borehole observations". *Geophysical Journal International.* 147:3. 528-542.

MONTAGNER J.P., ANDERSON, D.L. 1989. "Constrained reference mantle model". *Physics of the Earth and Planetary Interiors.* 58:2-3. 205-227.

MOONEY, W.D., MEISSNER, R. 1992. "Multi-genetic origin of crustal reflectivity: a review of seismic reflection profiling of the continental lower crust and Moho". *Continental Lower Crust.* FOUNTAIN, D.M., ARCULUS, R., KEY, R.W. (Eds.). New York: Elsevier Science Publishers. P. 45-80.

MOONEY, W.D., NATLAND, J.H. 2001. "Earth crust". In *AccessScience@McGraw-Hill*. [on line]. http://www.accessscience.com, DOI 10.1036/1097-8542.208970. (Last modified: November 16, 2001).

MORGAN, J.V., HADWIN, M., WARNER, M.R., BARTON, P.J., MORGAN, R., LI, P. 1994. "The polarity of deep seismic reflection from the lithospheric mantle: evidence for a relict subduction zone". *Tectonophysics*. 232:1-4. 319-328.

MUSACCHIO, G., WHITE, D.J., ASUDEH, I., THOMSON, C.J. 2004. "Lithospheric structure and composition of the Archean western Superior Province from seismic refraction/wide-angle reflection and gravity modeling". *Journal of Geophysical Research*. 109, B03304, doi: 10.1029/2003JB002427.

MUTTER, J., LERNER-LAM, A. 2002. "Seismology". In *AccessScience@McGraw-Hill*. [on line]. http://www.accessscience.com, DOI 10.1036/1097-8542.613300. (Last modified: August 16, 2002).

NYE, J.F. 1957. *Physical Properties of Crystals: Their Representation by Tensors and Matrices*. London: Oxford University Press, Amen House. pp. 82-92.

O'NEILL, B., BASS, J.D., ROSSMAN, G.R., GEIGER, C.A., LANGER, K. 1991. "Elastic properties of pyrope". *Physics and Chemistry of Minerals*. 17:7. 617-621.

PARK, J., LEVIN, V. 2002. "Seismic anisotropy: tracing plate dynamics in the mantle". *Science*. 296:5567. 485-489.

PAUL, B. 1960. "Prediction of elastic constants of multiphase materials". *Transactions of the Metallurgical Society of AIME*. 218. 36-41.

PAULSSEN, H. 1988. "Evidence for a sharp 670-km discontinuity as inferred from P-to-S converted waves". *Journal of Geophysical Research*. 93:9. 10489-10500.

PERROTT, C.M. 1978. "On the indentation fracture of cemented carbide II – the nature of surface fracture toughness". *Wear*. 47:1. 81-91.

PESELNICK, L., MEISTER, R. 1965. "Variational method of determining effective moduli of polycrystals: (A) hexagonal symmetry, (B) trigonal symmetry". *Journal of Applied Physics*. 36:9. 2879-2884.

PESELNICK, L., NICOLAS, A., STEVENSON, P.R. 1974. "Velocity anisotropy in a mantle peridotite from the Ivrea zone: application to upper mantle anisotropy". *Journal of Geophysical Research*. 79:8. 1175-1182.

POPP, T., KERN, H. 1994. "The influence of dry and water saturated cracks on seismic velocities of crustal rocks a comparison of experimental data with theoretical model". *Surveys in Geophysics*. 15:5. 443-465.

RAO, M., RAMANA, Y.V., GOGTE, B.S. 1974. "Dependence of compressional velocity on the mineral chemistry of eclogites". *Earth and Planetary Science Letters*. 23:1. 15-20.

RAVICHANDRAN, K.S. 1994. « Elastic properties of two-phase composites". *Journal of the American Ceramic Society*. 77:5. 1178-1184.

RAYMOND, L.A. 1995. *Petrology: the Study of Igneous, Sedimentary and Metamorphic Rocks*. Dubuque, Iowa; Toronto: Wm. C. Brown Publishers. 742p.

REUSS, A. 1929. "Berechnung der Fliessgrenze von Mischkristallen (Calculation of flow limits of mixed crystals on basis of plasticity of monocrystals)". *Zeitschrift fuer Angewandte Mathematik und Mechanik*. 9:1. 49-58.

RICHARD, T.G. 1975. "The mechanical behavior of a solid microsphere filled composite". *Journal of Composite Materials*. 9:2. 108-113.

ROLFO, F., COMPAGNONI, R., WU, W.P., XU, S.T. 2004. "A coherent lithostratigraphic unit in the coesite-eclogite complex of Dabie Shan, China: geologic and petrologic evidence". *Lithos*. 73:1-2. 71-94.

ROWLEY, D.B., XUE, F., TUCKER, R.D., PENG, Z.X., BAKER, J., DAVIS, A. 1997. "Ages of ultrahigh pressure metamorphism and protolith orthogneisses from the eastern Dabie Shan; U/Pb zircon geochronology". *Earth and Planetary Science Letters*. 151:3-4. 191-203.

RUDNICK, R.L., FOUNTAIN, D.M. 1995. "Nature and composition of the continental crust: A lower crustal perspective". *Reviews of Geophysics*. 33:3. 267-309.

RUMBLE, D., WANG, Q.C., ZHANG, R.Y. 2000. "Stable isotope geochemistry of marbles from the coesite UHP terrains of Dabieshan and Sulu, China". *Lithos*. 52:1-4. 79-95.

RUMBLE, D., YUI, T.F. 1998. "The Qinglongshan oxygen and hydrogen isotope anomaly near Donghai in Jiangsu Province, China". *Geochimica et Cosmochimica Acta*. 62:19-20. 3307-3321.

RUTTER, E.H., NEUMANN, D.H.K. 1995. "Experimental deformation of partially molten Westerly granite under fluid-absent conditions, with implications for the extraction of granitic magma". *Journal of Geophysical Research*. 100:8. 15697-15715.

RYZHOVA, T.V., ALEKSANDROV, K.S., KOROBKOVA, V.M. 1966. "The elastic properties of rock-forming minerals. V. Additional data on silicates." *Physics of the Solid Earth*. 2, 63-65.

SALISBURY, M.H., FOUNTAIN, D.M. 1994. "The seismic velocity and Poisson's ratio structure of the Kapuskasing uplift from laboratory measurements". *Canadian Journal of Earth Sciences*. 31:7. 1052-1063.

SARUWATARI, K., JI, S., LONG, C., SALISBURY, M.H. 2001. "Seismic anisotropy of mantle xenoliths and constraints on upper mantle structure beneath the southern Canadian Cordillera". *Tectonophysics*. 339:3-4. 403-426.

SATO, K., KATSURA, T. 2001. "Experimental investigation on dolomite dissociation into aragonite + magnesite up to 8.5 GPa". *Earth and Planetary Science Letters*. 184:2. 529-534.

SAVAGE, M.K. 1999. "Seismic anisotropy and mantle deformation: what have we learned from shear wave splitting?" *Reviews of Geophysics*. 37:1. 65-106.

SCHÖN, J.H. 1996. *Physical Properties of Rocks: Fundamentals and Principles of Petrophysics* (*Seismic Exploration Series, vol. 18*). Tarrytown, New York: Pergamon Press. 583p.

SCHWARTZ, S., ALLEMAND, P., GUILLOT, S. 2001. "Numerical model of the effect of serpentinites on the exhumation of eclogitic rocks: insights from the Monviso ophiolitic massif (Western Alps)". *Tectonophysics*. 342:1-2. 191-206.

SERONT, B., MAINPRICE, D., CHRISTENSEN, N.I. 1993. "A determination of the three-dimensional seismic properties of anorthosite: comparison between values calculated from the petrofabric and direct laboratory measurements". *Journal of Geophysical Research*. 98:2. 2209-2221.

SHAPIRO, S.A. 2003. "Elastic piezosensitivity of porous and fractured rocks". *Geophysics*. 68:2. 482-486.

SIEGESMUND, S., KERN, H., VOLLBRECHT, A. 1991. "The effect of orientated microcracks on seismic velocities in an ultramylonite". *Tectonophysics*. 186:3-4. 241-251.

SIEGESMUND, S., TAKESHITA, T., KERN, H. 1989. "Anisotropy of Vp and Vs in an amphibolite of the deeper crust and its relationship to the mineralogical, microstructural and textural characteristics of the rock". *Tectonophysics*. 157:1-3. 25-38.

SILVER, P.G., GAO, S. S., LIU, K.H. 2001. "Mantle deformation beneath Southern Africa". *Geophysical Research Letters*. 28:13. 2493-2496.

SIMMONS, G. 1964. "Velocity of shear waves in rocks to 10 kilobars, 1". *Journal of Geophysical Research*. 69:6. 1123-1130.

SMITH, J.C. 1976. "Experimental values for the elastic constants of a particulate-filled glassy polymer". *Journal of Research of the National Bureau of Standards – A. Physics and Chemistry*. 80A, 45-49.

SOLOMATOV, V.S., STEVENSON, D.J. 1994. "Can sharp seismic discontinuities be caused by nonequilibrium phase transitions?" *Earth and Planetary Science Letters*. 125:1-4. 267-279.

SPRIGGS, R.M. 1961. "Expression for effect of porosity on elastic modulus of polycrystalline refractory materials, particularly aluminium oxide". *Journal of American Ceramic Society*. 44 :12. 628-629.

SPRIGGS, R.M., BRISSETTE, L.A., VASILOS, T. 1962. "Effect of porosity on elastic and shear moduli of polycrystalline magnesium oxide". *Journal of American Ceramic Society*. 45:8. 400.

STIXRUDE, L. 1997. "Structure and sharpness of phase transitions and mantle discontinuities". *Journal of Geophysical Research*. 102:7. 14835-14852.

SVETLOV, I.L., EPISTIAN, A.I., KRIVKO, A.I., SAMOIL, A.I., ODINTSEV, I.N., ANDREEV, A.P. 1988. "Anisotropy of Poisson's ratio of single crystals of nickel alloy". *Soviet Physics – Doklady*. 33, 771-773.

THARP, T.M. 1983. "Analogies between the high-temperature deformation of polyphase rocks and the mechanical behavior of porous powder metal". *Tectonophysics*. 96:3-4. T1-11.

TOMMASI, A., VAUCHEZ, A. 2001. "Continental rifting parallel to ancient collisional belts: an effect of the mechanical anisotropy of the lithospheric mantle". *Earth and Planetary Science letters*. 185:1-2. 199-210.

TREAGUS, S.H. 2002. "Modeling the bulk viscosity of two-phase mixtures in terms of clast shape". *Journal of Structural Geology*. 24:1. 57-76.

TULLIS, T., HOROWITZ, F.G., TULLIS, J. 1991. "Flow laws of polyphase aggregates from end-member flow". *Journal of Geophysical Research*. 96:5. 8081-8096.

ULMER, P., TROMMSDORFF, V. 1995. "Serpentine stability to mantle depths and subduction-related magmatism". *Science*. 268:5212. 859-861.

UNDERWOOD, E.E. 1970. *Quantitative Stereology*. Reading, Massachusetts: Addison-Wesley Publishing Company. 274p.

VAUGHAN, M.T., GUGGENHEIM, S. 1986. "Elasticity of muscovite and its relationship to crystal structure". *Journal of Geophysical Research*. 91:5. 4657-4664.

VAUGHAN, M.T., WEIDNER, D.J. 1978. "The relationship of elasticity and crystal structure in andalusite and sillimanite". *Physics and Chemistry of Minerals*. 3:2. 133-144.

VOIGT, W. 1928. *Lehrbuch der Kristallphysik*. Berlin-Leipzig: Teubner Verlag. 962p.

WALLIS, S., ENAMI, M., BANNO, S. 1999. "The Sulu UHP terrane: a review of the petrology and structural geology". *International Geology Review*. 41:10, 901-920.

WALSH, J.B., BRACE, W.F., ENGLAND, A.W. 1965. "Effect of porosity on compressibility of glass". *Journal of American Ceramic Society*. 48:12. 605-608.

WANG, C. 1966. "Velocity of compressional waves in limestones, marbles and a single crystal of calcite to 20 kilobars". *Journal of Geophysical Research*. 71:14. 3543-3547.

WANG, C.Y., ZENG, R.S., MOONEY, W.D., HACKER, B.R. 2000. "A crustal model of the ultrahigh-pressure Dabie Shan orogenic belt, China, derived from deep seismic refraction profiling". *Journal of Geophysical Research*. 105:5. 10857-10869.

WANG, J.Y., HU, S.B., YANG, W.C., CHEN, B., CHEN, Z., LI, T. 2001. "Geothermal measurements in the pilot-boreholes of the China Continental Scientific Drilling". *Chinese Science Bulletin*. 46:10. 847-850.

WANG, J.Y., HUANG, S.P. 1990. "Compilation of heat flow data in the China continental area (2nd edition)". *Seismology and Geology*. 12:4. 351-366.

WANG, L.S., LI, C., SHI, Y.S., WANG, Y.H. 1995. "Distribution of geotemperature and terrestrial heat flow density in the Lower Yangtze area". *Chinese Journal of Geophysics*. 38:3. 393-402.

WANG, X.M., LIOU, J.G. 1991. "Regional ultrahigh-pressure coesite-bearing eclogite terrane in central China: evidence from country rocks, gneiss, marble and metapelite". *Geology*. 19:9. 933-936.

WANG, Z.C., JI, S.C. 2001. "Elasticity of six polycrystalline silicate garnets at pressure up to 3.0 GPa". *American Mineralogist*. 86:10. 1209-1218.

WARNER, M., MCGEARY, S. 1987. "Seismic reflection coefficients from mantle fault zones". *The Geophysical Journal of the Royal Astronomical Society*. 89:1. 223-230.

WATT, J.P. 1987. "POLYXSTAL: A Fortran program to calculate average elastic properties of minerals from single-crystal elasticity data". *Computers & Geosciences*. 13:5. 441-462.

WATT, J.P. 1988. "Elastic properties of polycrystalline minerals: comparison of theory and experiments". *Physics and Chemistry of Minerals*. 15:6. 579-587.

WATT, J.P., DAVIES, G.F., O'CONNELL, R.J. 1976. "The elastic properties of composite materials". *Reviews of Geophysics and Space Physics*. 14:4. 541-563.

WATT, J.P., O'CONNELL R. J. 1980. "An experimental investigation of the Hashin-Shtrikman bounds on two-phase aggregate elastic properties". *Physics of the Earth and Planetary Interiors*. 21:4. 359-370.

WATT, J.P., PESELNICK, L. 1980. "Clarification of the Hashin-Shtrikman bounds on the effective elastic moduli of polycrystals with hexagonal, trigonal, and tetragonal symmetry". *Journal of Applied Physics*. 51:3. 1525-1531.

WEIDNER, D.J., ITO, E. 1985. "Elasticity of MgSiO3 in the ilmenite phase". *Physics of the Earth and Planetary Interiors*. 40:1. 65-70.

WEISS, T., SIEGESMUND, S., RABBEL, W., BOHLEN, T., POHL, M. 1999. "Seismic velocities and anisotropy of the lower continental crust: a review". *Pure and Applied Geophysics*. 156:1-2. 97-122.

WEPFER, W.W., CHRISTENSEN, N.I. 1991. "A seismic velocity-confining pressure relation, with applications". *International Journal of Rock Mechanics and Mining Sciences & Geomechanics Abstracts*. 28:5. 451-456.

WIDIYANTORO, S., KENNETT, B.L.N., VAN DES HILST, R.D. 1999. "Seismic tomography with P and S data reveals lateral variations in the rigidity of deep slabs". *Earth and Planetary Science Letters*. 173:1-2. 91-100.

WOLFE, C.J., SOLOMON, S.C. 1998. "Shear-wave splitting and implications for mantle flow beneath the MELT region of the East Pacific Rise". *Science*. 280:5367. 1230-1232.

WOOD, B.J. 1995. "The effect of H_2O on the 410-kilometer seismic discontinuity". *Nature*. 268:5207. 74-76.

WYLLIE, M.R.J., GREGORY, A.R., GARDNER, L.W. 1956. "Elastic wave velocities in heterogeneous and porous media". *Geophysics*. 21:1. 41-70.

XU, P. F., LIU, F.T., WANG, Q.C., CONG, B.L., CHEN, H. 2001. "Slab-like high velocity anomaly in the upper most mantle beneath the Dabie-Sulu orogen". *Geophysical Research Letters*. 28:9.1847-1850.

XU, S.T., OKAY, A.I., JI, S., SENGŐR, A.M.C., SU, W., LIU, Y., JIANG, L. 1992. "Diamond from the Dabie Shan metamorphic rocks and its implication for tectonic setting". *Science*. 256:5053. 80-82.

XU, Z.Q. 2004. "The scientific goals and investigation progresses of the Chinese Continental Drilling Project". *Acta Petrologica Sinica*. 20:1. 1-8.

XU, Z.Q., ZHANG, Z.M., LIU, F.L., YANG, J.S., TANG, Z.M., CHENG, S.Z., CAI, Y.C., LI, T.F., CHENG, F.Y. 2004. "The structure profile of 0-1200 m in the main borehole, Chinese Continental Scientific Drilling and its preliminary deformation analysis". *Acta Petrologica Sinica*. 20:1. 53-72.

YANG, J., PICKARD, S.M., CADY, C., EVANS, A.G., MEHRABIAN, R. 1991. "The stress-strain behavior of aluminum matrix composites with discontinuous reinforcements". *Acta Metallurgica et Materialia*. 39:8. 1863-1869.

YANG, J.S., WOODEN, J.L., WU, C.L., LIU, F.L., XU, Z.Q., SHI, R.D., KATAYAMA, I., LIOU, J.G., MARUYAMA, S. 2003. "SHRIMP U-Pb dating of coesite-bearing zircon from the ultrahigh-pressure metamorphic rock, Sulu terrane, east China". *Journal of Metamorphic Geology*. 21:6. 551-560.

YANG, W.C. 2002. "Geophysical profiling across the Sulu ultra-high-pressure metamorphic belt, eastern China". *Tectonophysics*. 354:3-4. 277-288.

YANG, W.C. 2003. "Flat mantle reflectors in eastern China: possible evidence of lithospheric thinning". *Tectonophisics*. 369:3-4. 219-230.

YANG, W.C., CHENG, Z., CHEN, G., HU, Z., BAI, J. 1999. "Geophysical investigations of northern Sulu HPM Belt; (I), Deep seismic reflection". *Chinese Journal of Geophysics*. 42:1. 57-69.

YANG, W.C., CHENG, Z.Y., ZHANG, C.H., 2003. "Geophysical investigation for site-selection of Chinese Continental Scientific Drilling and Dabie-Sulu lithosphere". *Acta Geoscientia Sinica*. 24:5. 391-404.

YANG, W.C., YANG, W.Y., JIN, Z.M., CHENG, Z.Y. 2004. "Lithospheric seismic fabrics of Sulu ultrahigh-pressure metamorphic belt". *Science in China*. 34D:4. 307-319.

YAO, Y.P., YE, K., LIU, J.B., CONG, B.L., WANG, Q.C. 2000. "A transitional eclogite- to high pressure granulite-facies overprint on coesite-eclogite at Taohang in the Sulu ultrahigh-pressure terrane, eastern China". *Lithos*. 52:1-4. 109-120.

ZHANG, M., EBROM, D.A., MCDONALD, J.A., TATHAM, R.H. 1996. "Comparison of experimental velocity measurements with theoretical results in a solid-solid composite materials". *Geophysics*. 61:5. 1429-1435.

ZHANG, R.Y., LIOU, J.G., CONG, B.L. 1994. "Petrogenesis of garnet-bearing ultramafic rocks and associated eclogites in the Su-Lu ultrahigh-P metamorphic terrane, eastern China". *Journal of Metamorphic Geology*. 12:2.169-186.

ZHANG, R.Y., LIOU, J.G., CONG, B.L. 1995a. "Talc-, magnesite-, and Ti-clinohumite bearing ultrahigh-pressure meta-mafic and ultramafic complex in the Dabie Mountains, China". *Journal of Petrology*. 36:4. 1011-1037.

ZHANG, R.Y., LIOU, J.G., ERNST, W.G. 1995b. "Ultrahigh-pressure metamorphism and decompression P-T paths of eclogites and country rocks from Weihai, eastern China". *Island Arc*. 4:4. 293-309.

ZHANG, Z.M., XU, Z.Q., LIU, F. L., YOU, Z. D., SHEN, K., YANG, J., S. LI, T. F., CHEN, S.Z. 2004. "Geochemistry of eclogites from the main hole (100~2050 m) of the Chinese Continental Scientific Drilling Project". *Acta Petrologica Sinica*. 20:1. 27-42.

ZHANG, Z.M., XU, Z.Q., XU, H. 2000. "Petrology of ultrahigh-pressure eclogites from the ZK703 drillhole in the Donghai, eastern China". *Lithos*. 52:1-4. 35-50.

ZHAO, P., JI, S.C. 1997. "Refinements of shear-lag model and its applications". *Tectonophysics*. 279:1-4. 37-53.

ZHAO, Y., ANDERSON, D.L. 1994. "Mineral physics constraints on the chemical composition of the Earth's lower mantle". *Physics of the Earth and Planetary Interiors*. 85:3-4. 273-292.

ZHAO, Z.X., XU, J.R., YANG, W.C., CHENG, Z.Y. 2004. "Simulations of reflection seismic profile of borehole area of Chinese Continental Scientific Drilling site". *Acta Petrologica Sinica*. 20:1. 139-148.

ZHENG, Y.F., FU, B., LI, Y.L., XIAO, Y.L., LI, S.G. 1998. "Oxygen and hydrogen isotope geochemistry of ultrahigh-pressure eclogites from the Dabie Mountains and the Sulu terrane". *Earth and Planetary Science Letters*. 155:1-2. 113-129.

ZHU, R., YANG, Z., WU, H., MA, X., HUANG, B., MENG, Z., FANG, D. 1998. "Paleomagnetic constraints on the tectonic history of the major blocks of China during the Phanerozoic". *Science in China*. 41D:Supplememt. 1-19.

ZORIN, Y.A., MORDVINOVA, V.V., TURUTANOV, E.K., BELICHENKO, B.G., ARTEMYEV, A.A., KOSAREV, G.L., GAO, S.S. 2002. Low seismic velocity layers in the Earth's crust beneath Eastern Siberia (Russia) and Central Mongolia: receiver function data and their possible geological implication. *Tectonophysics*. 359:3-4. 307-327.

Appendix 1

Mechanical properties of multiphase materials and rocks: A phenomenological approach using generalized means

Shaocheng Ji[a,b], Qin Wang[a], Bin Xia[b], Denis Marcotte[a]

[a]Département des Génies Civil, Géologique et des Mines, École Polytechnique de Montréal, Montréal, H3C 3A7, Canada

[b]Institute of Geochemistry, Chinese Academy of Sciences, Wushan, Guangzhou, P.R. China

Acknowledgments

We thank the NSERC and LITHOPROBE of Canada and Guangzhou Institute of Geochemistry (Chinese Academy of Sciences, KZCX2-SW-117) for research grants. We appreciate the constructive reviewing comments of J.G. Berryman, T.M. Tharp and C.W. Passchier. This is LITHOPROBE contribution No. 1350.

This paper was published in Journal of Structural Geology, 2004, Vol. 26, 1377-1390.

A1.1 Abstract

Difficulties associated with specifying details of microstructure and distributions of internal stress and strain within multiphase rocks prompt the development of semi-empirical models to connect the effective properties of composites to the properties of their components. We apply here generalized means to describe the elastic moduli (E, K and G) and flow strength of an isotropic multiphase composite material in terms of its component properties, volume fractions and microstructures. The microstructures are expressed by a scaling parameter J, which is mainly controlled by the shape and distribution (continuity and connectivity) of the phases. The case $J = 1$ yields the arithmetic mean or Voigt average and the case $J = -1$ yields the harmonic mean or Reuss average. The geometric mean occurs as J approaches 0. The means with $J = 0.5$ or $J = -0.5$ provides good agreement with the experimental data of Young's modulus for the two-phase composites in which inclusions are shaped like spheres isolated in a continuous host medium. For most composite materials in which the inclusions are of somewhat arbitrary geometry, the means with $J = -0.25$ and $J = 0.25$ do well at predicting the measured values of Young's modulus for those with weak-phase continuous (the volume fraction of strong phase $f_s \leq 0.5$) and strong-phase continuous ($f_s \geq 0.7$) structures, respectively. In the intermediate range ($0.5 \leq f_s \leq 0.7$), J is expected to vary progressively from -0.5 to 0.5 or from -0.25 to 0.25 due to the transition in microstructure. Thus the generalized means offer a promising, phenomenological approach for the prediction of elastic and rheological properties of multiphase materials and rocks, especially for those consisting of more than two unlike phases. As an example, the approach is applied to interpret the sharpness of the 410 km seismic discontinuity as a corollary of the transition from olivine-dominant structure to wadsleyite-dominant structure.

Keywords: Generalized means; Elastic properties; Rheology; Multiphase rocks; Composite materials; Seismic discontinuities

A1.2 Introduction

It is virtually impossible to obtain exact analytical solutions for mechanical properties (Young's modulus E, shear modulus G, bulk modulus K, and flow strength σ) of a multiphase mixture with a heterogeneous microstructure due to the fact that the local distributions of stress and strain of each constituent are influenced by the details of microstructure. Although advanced numerical techniques such as finite element modeling (e.g., Tullis, et al., 1991; Treagus, 2002) have some inherent advantages for solving the above problem, they are too tedious to employ for each new composite. The numerical modeling results generally cannot be readily used in an efficient, straightforward manner in calculating the bulk mechanical properties of multiphase materials. Therefore, it is necessary to develop semi-empirical models to connect the overall properties of composites to the properties of their components. In this paper we use the generalized means as a phenomenological approach to calculate the elastic moduli (E, K and G) and flow strength of an isotropic composite material in terms of its component properties and volume fractions.

A1.3 Mechanical properties of multiphase aggregates

The generalized (weighted) means can be expressed as:

$$M_c(J) = \left[\sum_{i=1}^{N} \left(f_i {M_i}^J \right) \right]^{1/J} \qquad \text{(A1.1)}$$

where M is a specific mechanical property (E, K, G, or σ), f is the volume fraction of component, the subscripts i and c represent, respectively, the ith phase and the composite consisting of N phases, and J is a scaling parameter.

$$\sum_{i=1}^{N} f_i = 1 \qquad \text{(A1.2)}$$

Here we propose that Equation (A1.1) is generically useful in the calculations of mechanical properties of multiphase materials. For example, the case $J = 1$ yields the arithmetic mean or Voigt average, which represents equal strain rate between phases. The case $J = -1$ yields the harmonic mean or Reuss average, which represents equal stress between phases. For statistically isotropic composites in which there is no mechanical interaction between phases (see Ji et al., 2000 for discussion), the Voigt and Reuss averages are generally regarded as the upper and lower bounds for effective properties and bracket the permissible range in which the effective properties must lie. The Voigt bound is linear with the volume fraction. The case $J = 1$ yields a formula like Wyllie's "time-average equation" (Wyllie et al., 1956) for fluid-filled sedimentary rocks:

$$\frac{1}{V_c} = \frac{\phi}{V_1} + \frac{1-\phi}{V_2} \qquad \text{(A1.3)}$$

where V is a given seismic velocity, ϕ is the porosity, the subscripts 1, 2 and c represent, respectively, the fluid-filled pores, the solid medium and the composite. The Hill or the Voigt-Reuss-Hill average is an arithmetic mean of the Voigt and Reuss bounds (Hill, 1963).

Equation (A1.1) can be written as

$$M_c^J = \sum_{i=1}^{N} (f_i M_i^J) \qquad \text{(A1.4)}$$

Taking the derivative of Equation (A1.4), and then let $J \to 0$, we have

$$\ln M_c = \sum_{i=1}^{N} f_i \ln M_i = \sum_{i=1}^{N} \ln M_i^{f_i} = \ln\left(\prod_{i=1}^{N} M_i^{f_i}\right) \qquad \text{(A1.5)}$$

Equation (A1.5) clearly shows that as J approaches 0, the limit of $M_c(J)$ is the geometric mean:

$$\lim_{J\to 0} M_c(J) = \prod_{i=1}^{N} M_i^{f_i} \qquad \text{(A1.6)}$$

The geometric mean has been found to yield a result very close to the much more complicated iterative self-consistent micromechanical models (Matthies and Humbert, 1993; Mainprice and Humbert, 1994).

In the extreme cases, $M_c(J\to -\infty)$ and $M_c(J\to +\infty)$ define the minimum and the maximum, respectively. $M_c(J)$ has the following characteristics: (a) $M_c(J)$ is a continuous, monotone increasing function for all J in the ranges $(-\infty \le J \le \infty)$. This monotonicity stands with respect to either the volume fractions or the physical properties (Korvin, 1982). (b) For $J < 1$, $J = 1$ and $J > 1$, $M_c(J)$ as a function of the individual grades of membership M_i is strongly concave, linear, and strongly convex, respectively. (c) For a simple two-phase composite system that consists of the strong phase (s) and weak phase (w), the generalized means fulfill the following obvious requirements: for $f_s = 0$ (pure weak phase aggregate), the effective properties are equivalent to the properties of the weak phase for all values of J. Similarly, for $f_s = 1$ (pure strong phase aggregate), the effective properties are equivalent to the properties of the strong phase for all values of J. In the event that $M_s = M_w$ (two phases have an equivalent property), then $M_c = M_s = M_w$ for all values of J and all values of f_s.

In Equation (A1.1), J can be viewed as a compensation coefficient whose value depends on characteristics of the composite microstructure such as the nature of

interphase boundaries, phase continuity and connectivity. If the bonding between the phases is perfect, then the J value could be mainly controlled by the phase continuity and connectivity. Composites consisting of a strong and a weak constituent can be classified into three categories according to their phase continuity and connectivity (e.g., Gurland, 1979; Ji and Xia, 2002):

(1) Composites with a strong-phase supported structure (SPSS), in which the strong phase is continuous while the weak phase is discontinuous in the direction of the applied load;

(2) Composites with a weak-phase supported structure (WPSS), in which the strong phase is discontinuous while the weak phase is continuous in the loading direction;

(3) Composites with a transitional structure (TS), in which both the strong and the weak phase are continuous or discontinuous in the loading direction.

The structures of granular materials generally depend on the volume fraction of constituent minerals. In hot-pressed forsterite-enstatite aggregates (Ji et al., 2001), for example, the SPSS, WPSS and TS occur, respectively, in composites with $f_s > 0.7$, < 0.5, and 0.5-0.7. In addition to the volume fractions, the phase continuity and connectivity are of course affected by many other structural variables such as the morphology, grain size and the orientation of the constituents, which will be considered in a future study. The phase continuity also changes with increasing progressive strain. A transition from SPSS to WPSS may result in drastic decrease in effective elastic moduli or flow strength of the composites. This critical phenomenon has been used to explain the rheology of partially melted materials (e.g., Arzi, 1978; Rutter and Neumann, 1995) and solid-state rocks (e.g., Ji and Xia, 2002).

The overall mechanical properties can thus be estimated according to Equation (A1.1) if J is known. Then the problem at hand is to determine whether the J value is approximately constant for each of the structural categories. If J is a constant for a given

type of structure, what is its value? The J value has to be determined by fitting the equation to experimental data.

A1.4 Comparison with experiments

In order to test the theoretical model, high quality experimental data are needed for a series of macroscopically homogeneous and isotropic two-phase composites containing various known volume fractions of each constituent over a range as wide as possible. The polycrystalline aggregate of each end member phase should be isotropic so that only two elastic constants are necessary to characterize the bulk properties. These two elastic constants should be obtained by simultaneous measurements on the same specimen type in order to minimize effects due to experimental techniques and specimen variation. Any chemical interaction between phases or eutectic partial melting may introduce additional phases, consequently making the system complicated. The volume fraction of each phase should be accurately determined. For example, the presence of small amounts of residual void space (on the order of 1% by volume) is sufficient to make estimates of composite elastic constants (obtained while ignoring this porosity) fall below the lower Hashin-Shtrikman (HS) bound in many cases (Berryman, 1994, 1995). Furthermore, a shape preferred orientation may cause the composite to be anisotropic, but this effect can be avoided by using spherical particles in an isotropic matrix or random orientations of the grains. In addition, the contrast in elastic moduli between the phases should be large. Previous experimental checks of mixture rules (Ji and Wang, 1999; Watt and O'Connell, 1980) probably did not meet this criterion.

Elasticity and seismic velocities have been extensively measured for natural polyphase rocks (see Ji et al., 2002 for a comprehensive summary). However, such natural rocks are not optimal for the comparison between theory and experiment in order to determine the J value as a function of microstructure (e.g., phase continuity) primarily for the reasons below: (a) Natural rocks have complex mineralogical and chemical

compositions and are rarely composed of only two minerals. (b) Natural rocks are generally anisotropic due to the presence of crystallographic preferred orientation and/or compositional layering. (c) Elasticity of each given natural composite system can hardly been determined over a full range of modal composition (Ji et al., 2003). (d) The volume fractions of constituent minerals reported for the rocks whose seismic velocities have been measured generally are not precise enough to yield an exact J value. It is thus especially important to determine the J value through carefully designed experiments using synthetic two-phase aggregates of well-controlled modal compositions and microstructures. Unfortunately, such elastic data are still very scarce for synthetic multiphase rocks. Thus the elastic properties predicted by the expressions proposed in this paper were compared with the experimentally measured values of various synthetic composites, reported in the materials science and geophysics literature, in order to constrain the J value and its variation with composition.

A1.4.1 SPSS composites

Porous materials are a special class of SPSS composites in which pores are dispersed within a continuous nonporous body. Pores act like a constituent with null elastic constants. Porous powder metals, ceramics, sedimentary rocks and cracked rocks belong to this category. Powder metals and ceramics are usually manufactured by sintering or hot pressing. Polyphase materials in which the weak phases are at least two orders of magnitude weaker than the strong phases (e.g., partially melted rocks) can also be regarded as an analogy of porous materials (Arzi, 1978; Tharp, 1983; Ji and Xia, 2002). In Equation (A1.1), setting the elastic properties of a phase equal to zero allows an estimation of the effect of porosity on elastic properties of porous materials. As shown in Figure A1.1, the relative Young's moduli calculated from Equation (A1.1) and using J = 0.25 are in good agreement with experimental data for porous Al_2O_3 (Knudson, 1962; Spriggs, 1961) and porous MgO (Spriggs et al., 1962) polycrystalline aggregates with porosities less than about 40% (i.e., $f_s > 60\%$). The relative Young's modulus is defined as $(E_c\text{-}E_w)/(E_s\text{-}E_w)$, where E_s, E_w and E_c are the Young's moduli of the strong phase, weak

phase and the composite, respectively. For porosities less than 20%, the discrepancy between the experimental and theoretical results predicted with $J = 0.25$ is no more than a few percent. In contrast, the Hill average cannot yield a good fit to the experimental data. Thus, $J = 0.25$ is apparently an appropriate assumption for the porous Al_2O_3 and MgO investigated.

Walsh et al. (1965) carried out a series of experiments on the compressibility ($1/K$) of porous glass (glass foams) over a range of porosities from 0 to 0.7. The glass has the composition (in weight) 54.4% SiO_2, 14.4% B_2O_3, 14.1% CaO, 10% Al_2O_3, 6.5% Na_2O and 0.7% K_2O, $K = 46$ GPa and $G = 30.5$ GPa. Porosity measurements were stated to be accurate ± 0.01. The experimental data are plotted in Figure A1.2 for comparison with the theoretical relation proposed in the present paper and with the Hashin-Shtrikman (HS) bounds. The upper and lower HS bounds were derived by Hashin and Shtrikman (1963) using a linear theory of elasticity with the elastic polarization tensor method. In their derivation, potential energy and complementary energy were assumed to be minimum. The experimental data of Walsh et al. (1965) essentially track the theoretical curve of $J = 0.5$ for samples of low or immediate porosity ($f_s \geq 0.5$). In these samples, the pores are nearly spherical and non-interconnecting (Walsh et al., 1965). It is clear that the geometry of pore space is another important factor other than the phase continuity to affect the J value and further elastic properties of the composite. Isolated spherical pores cause the J value to be higher than sharp-cornered holes or flat elliptical cavities. Likely, $J \approx 0.5$ for the case of identically spherical pores while $J \approx 0.25$ for that of non-spherical or non-symmetric cavities. Figure A1.2 also displays that the model with $J = 0.5$ yields a better prediction than the upper HS bound in the case of the porous glass investigated by Walsh et al. (1965).

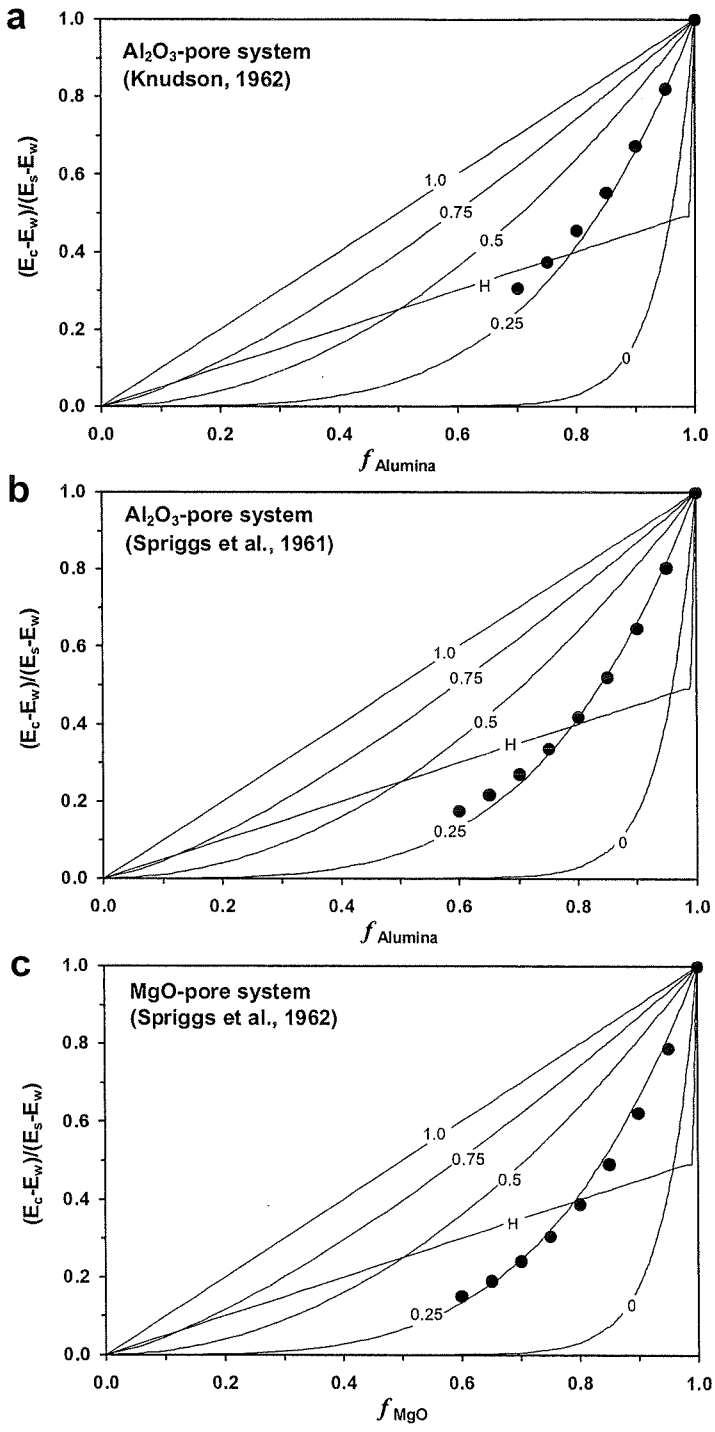


Figure A1.1 Experimental and theoretical results for relative Young's modulus of porous Al_2O_3 (a and b) and MgO (c) as a function of the volume fraction of solid component. Curves labelled according to J value. H represents the Hill average.

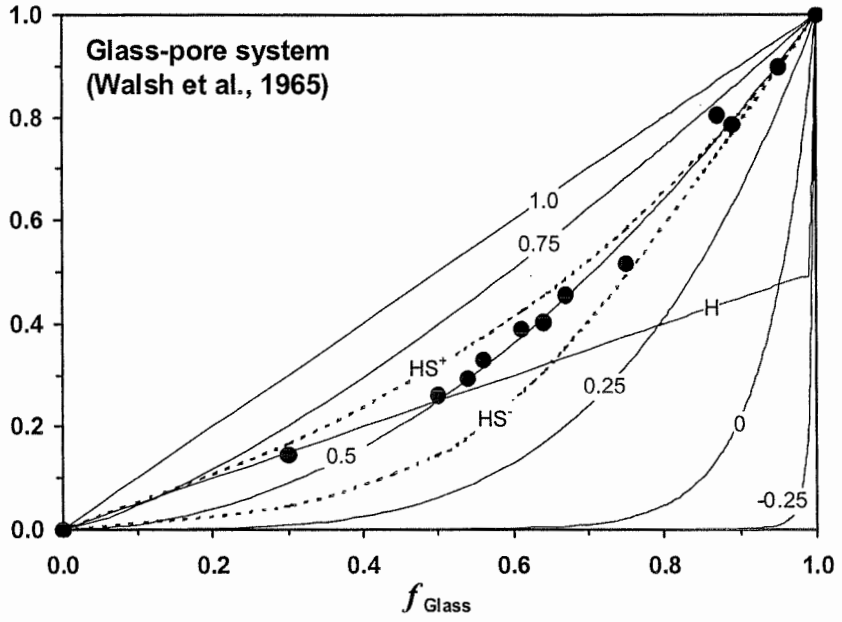


Figure A1.2 Comparison between experimental and theoretical results for relative bulk modulus (Kc-Kw)/(Ks-Kw) for glass foams. Theoretical curves labeled according to J value. H, HS+ and HS- represent the Hill average, the Hashin-Shtrikman upper and lower bounds, respectively.

Berge et al. (1995) measured P- and S-wave velocities of synthetic sandstone using sintered glass beads with porosities ranging from 1% to 43%. The glass has composition 71-74% by weight SiO_2, 12-15% NaO_2, 8-10% CaO, 1.5-3.8% MgO, 0.2-1.5% Al_2O_3, and 0-0.2% K_2O, and elastic properties K = 46.1 GPa, G = 29.8 GPa, ρ = 2.48 g/cm^3, Vp = 5.86 km/s and Vs = 3.43 km/s. The overall Young's, bulk and shear moduli of composites were computed from measured densities and acoustic velocities. Comparison between theory and experiment (Figure A1.3) shows a clear drop of the relative E, G and K towards a critical porosity of about 0.26. For porosities below about 0.26 ($f_s > 0.74$), the samples have similar microstructures with isolated spherical pores embedded in a continuous solid glass (Berge et al., 1995) and the experimental data can be well described by the generalized means with J = 0.5 or by the upper HS bound. The critical porosity presumably coincides with the minimum porosity for closely packed identical spheres.

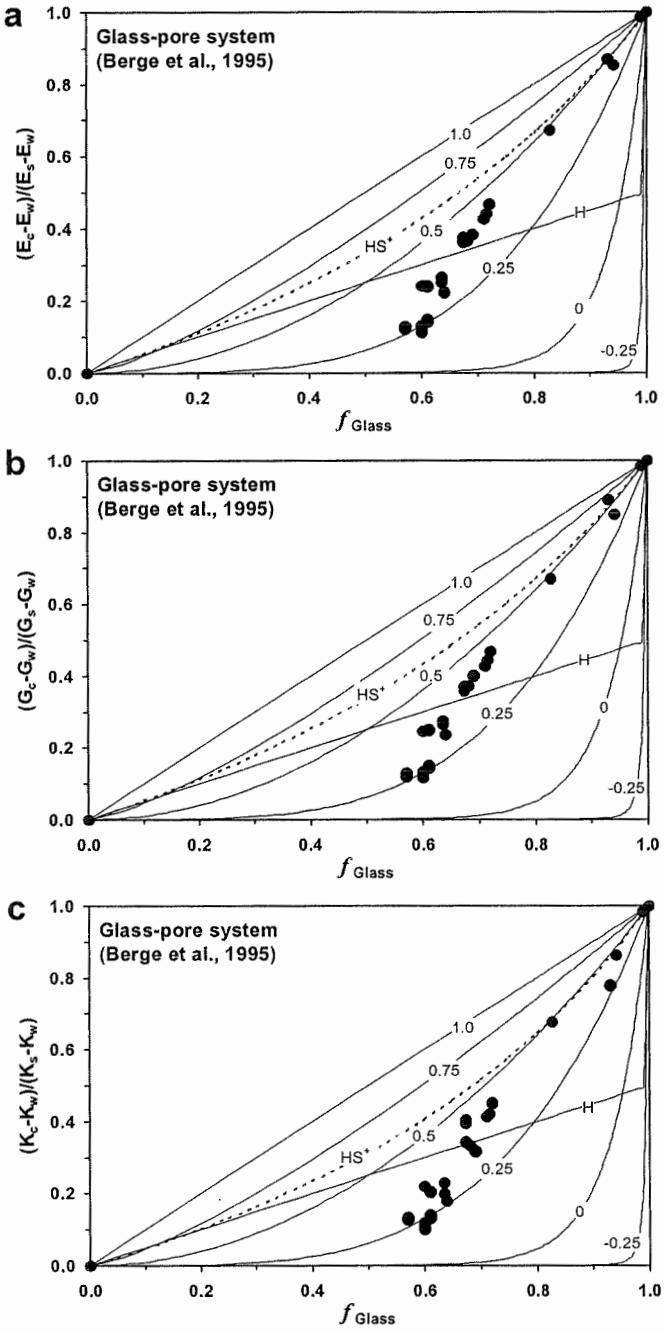


Figure A1.3 Comparison between experimental and theoretical results for relative Young's modulus (a), shear modulus (b) and bulk modulus (c) for sandstone analogs made from fused glass beads. Theoretical curves labeled according to J value. H and HS^+ represent the Hill average and the Hashin-Shtrikman upper bound, respectively.

In Figure A1.4, we plot measured P- and S-wave velocities of the sandstone analogs together with the theoretical predictions. Both P- and S-wave velocities of synthetic sandstone containing isolate pores and having porosities lower than 0.26 are in agreement with the theoretical curves for $J = 1.5$. In sandstones with higher porosities (0.26-0.43), the geometry of pores becomes complex and interaction between pores occurs. Consequently, the J value decreases progressively with increasing porosity. It is important to note that both P- and S-wave velocities of the composites with SPSS are virtually higher than the Voigt bounds ($J = 1$). Hence, a systematic investigation is urged to determine whether the above observation is a common situation for all types of materials.

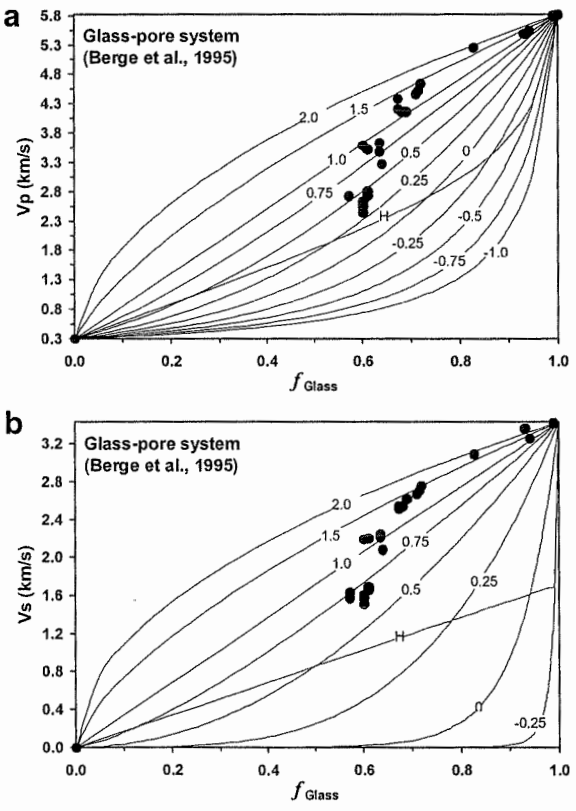


Figure A1.4 P-wave (a) and S-wave (b) velocities for sandstone analogs made from fused glass beads plotted against volume fraction of solid glass. Theoretical curves labeled according to J value. H represents the Hill average.

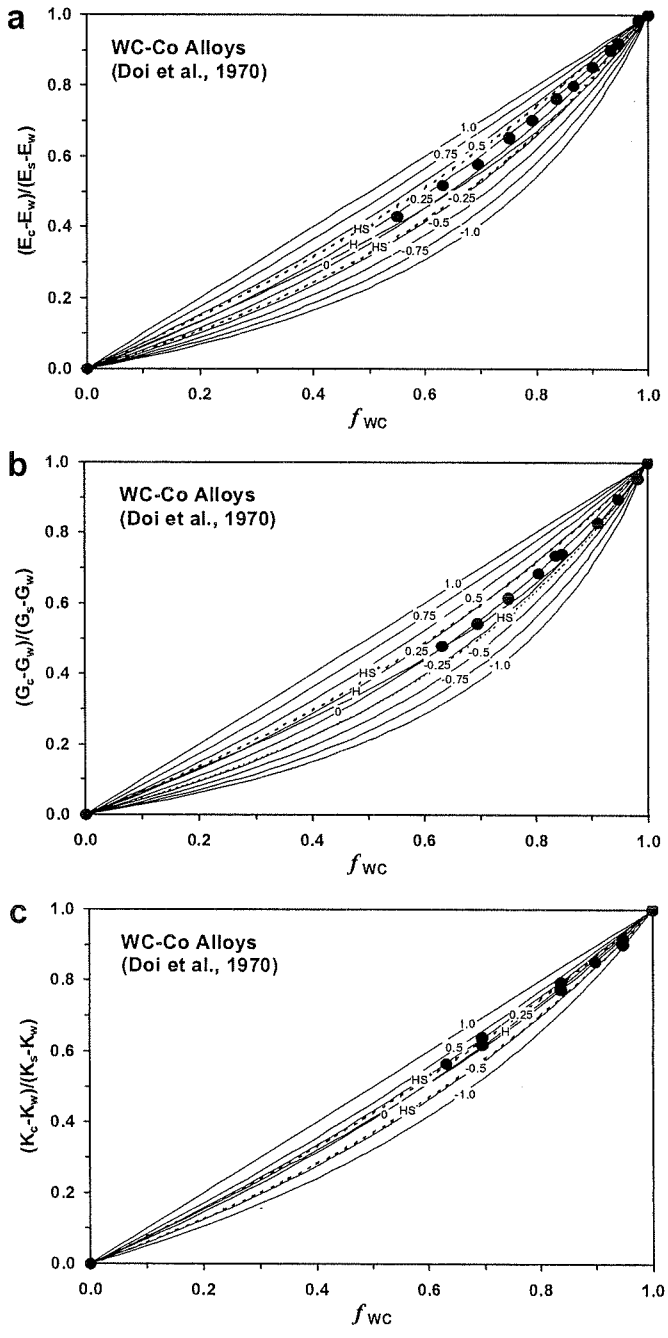


Figure A1.5 Relative Young's modulus (a), shear modulus (b) and bulk modulus (c) for WC-Co alloys plotted against volume fraction of WC. Theoretical curves labeled according to J value. H, HS^+ and HS^- represent the Hill average, the Hashin-Shtrikman upper and lower bounds, respectively.

In Figures A1.5 and A1.6, the theoretical predictions are plotted in junction with experimental data for WC-Co cermets (Doi et al., 1970; Perrott, 1978). E = 700 GPa and G = 297.9 GPa for WC, and E = 207 GPa and G = 79.4 GPa for Co. In these alloys, the volume fraction of WC (strong phase) is higher than 0.55 and Co (weak phase) shows a homogeneous dispersion in the matrix of WC. It can be clearly seen that the simple expression with J = 0.25 gives a good prediction of both the E and K variations over the composition range of $f_{WC} > 0.55$, where the strong phase forms a continuous load-carrying framework. For the shear modulus G, however, J = 0 (i.e., geometric mean) seems to give the best prediction for the experimental data. The reason for the discrepancy among the E, K and G variations with the volume fractions is unclear yet.

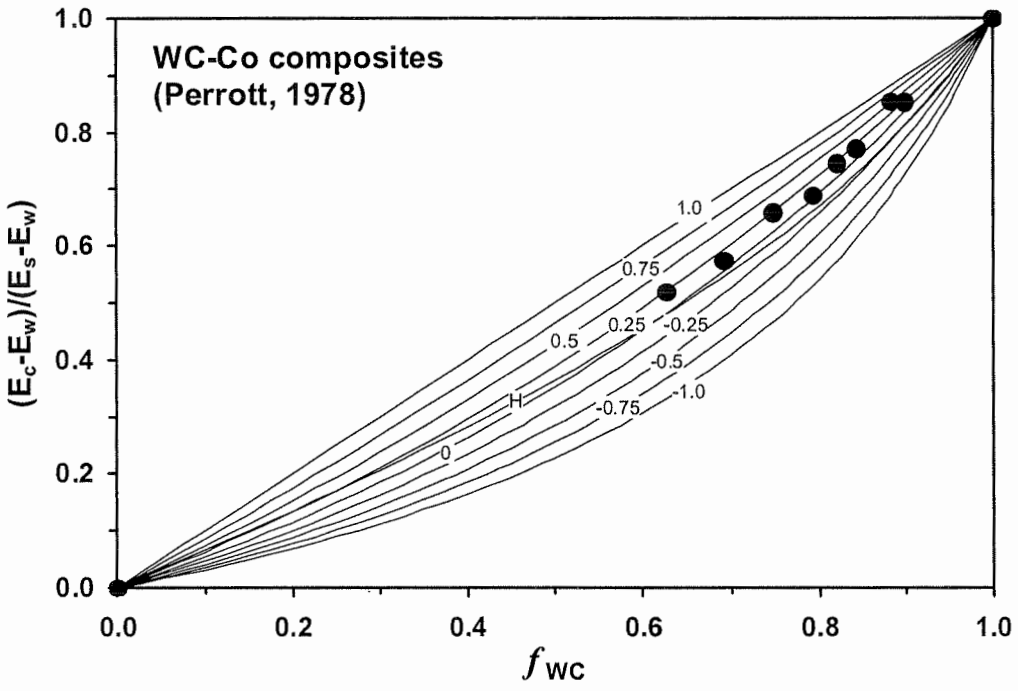


Figure A1.6 Relative Young's modulus for WC-Co alloys plotted against volume fraction of WC. Theoretical curves labelled according to J value. H represents the Hill average.

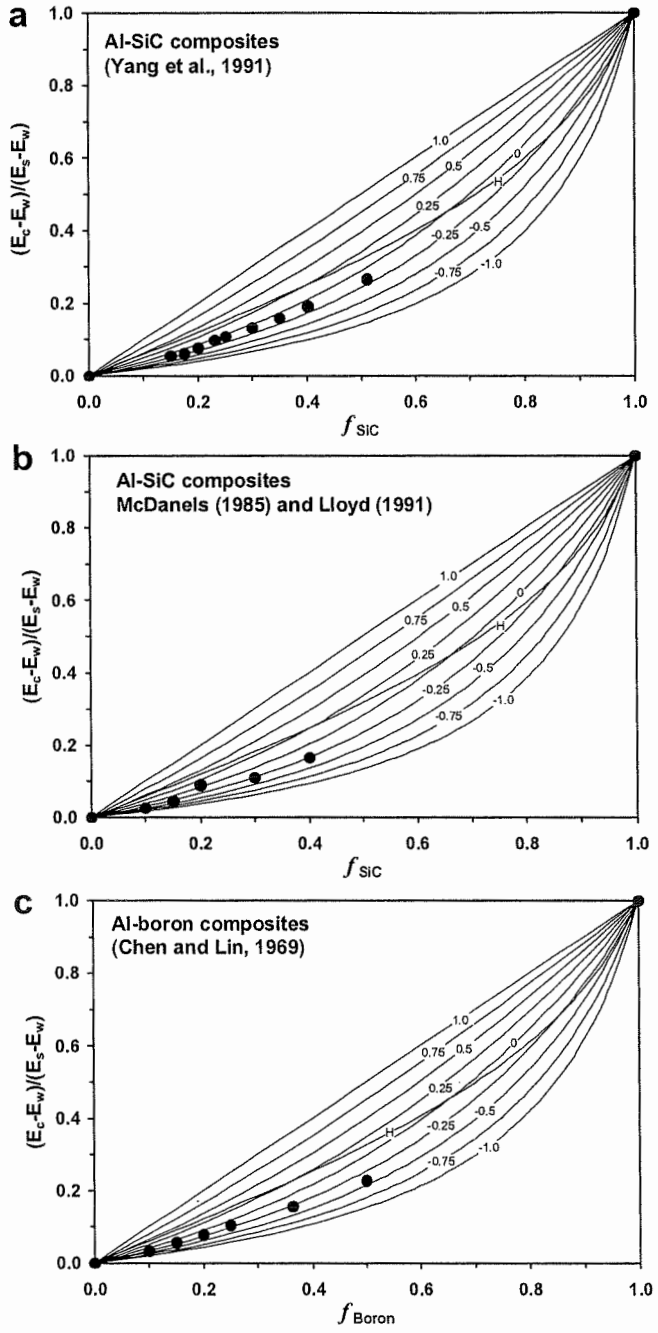


Figure A1.7 Theoretical curves on relative Young's modulus $(E_c-E_m)/(E_s-E_m)$ for aluminium-matrix composites plotted against volume fraction of reinforcement. Al-SiC composites (a and b) and Al-boron composites (c). *J* value is given in number. H represents the Hill average.

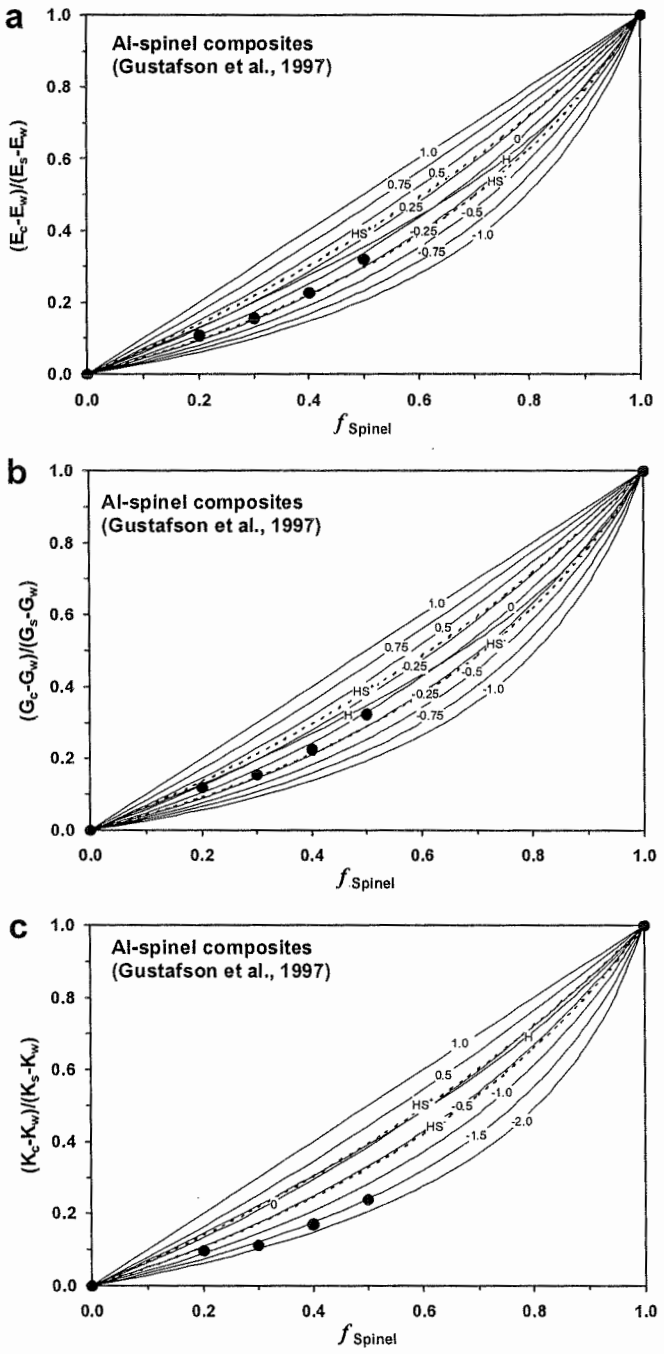


Figure A1.8 Relative Young's modulus (a), shear modulus (b) and bulk modulus (c) for Al-spinel composite plotted against volume fraction of spinel. Theoretical curves labeled according to J value. H, HS^+ and HS^- represent the Hill average, the Hashin-Shtrikman upper and lower bounds, respectively.

A1.4.2 WPSS composites

Extensive measurements of elastic properties have been carried out on WPSS composites that include Al-SiC, glass-Al_2O_3, epoxy-glass, epoxy-silica, epoxy-Al, polymer-glass, Al-spinel and Al alloy-boron mixtures. These experimental results may shed light on the understanding of the mechanical properties and rheological behaviour of natural rocks of WPSS such as quartzofeldspathic mylonites, peridotites, eclogites and partially crystallized rocks.

Utilizing the values of Young's moduli of Al (E_w=74 GPa) and SiC (E_s=450 GPa) and Equation (A1.1), we made some quantitative comparisons of the Young's moduli between theory and experiment (McDanels, 1985; Lloyd, 1991; Yang et al., 1991) for Al-SiC composites (Figure A1.7a-b). The experimental points of Young's moduli run very closely to the curves for $J = -0.25$. The composition dependence of Young's moduli of Al matrix composites with boron (Chen and Lin, 1969; Figure A1.7c) or spinel (Gustafson et al., 1997; Figure 8a) reinforcements also suggests that $J = -0.25$ gives the best prediction for the experimental results. However, the experimental points for G and K of Al-spinel composites (Figure A1.8b-c) fall closely to curves with $J = 0$ and $J = -1.5$, respectively.

Composites composed of solid glass or silica microspheres embedded in an epoxy resin or polymer matrix have been investigated by Braem (1987), Ishai and Cohen (1967), Kenyon and Duffey (1967), Richard (1975) and Smith (1976). These experimental data are plotted among the analytical predictions for different J values in Figures A1.9-4.10. In all cases, the prediction with $J = -0.25$ provides the best fit to the experimental data of Young's moduli. It is interesting to note that the calculated Young's moduli from either the upper or lower HS bound in all cases have larger deviations from experimental data than those calculated from Equation (A1.1) with $J = -0.25$. Figure 10c shows a good correlation of the experimental data of bulk modulus with the theoretical prediction with $J = -1.5$. This is similar to the case of Al-spinel composites

(Figure A1.8c). Why do the data of K fall outside the HS bounds while both E and G inside the bounds for certain types of materials such as Al-spinel (Gustatson et al., 1997) and epoxy-glass (Richard, 1975) composites? Without a detailed examination of their samples, we can only speculate that the paradox is due to the presence of small amounts of residual void space in the samples that are treated for purposes of modeling as if they have no porosity (Berryman, 1994, 1995).

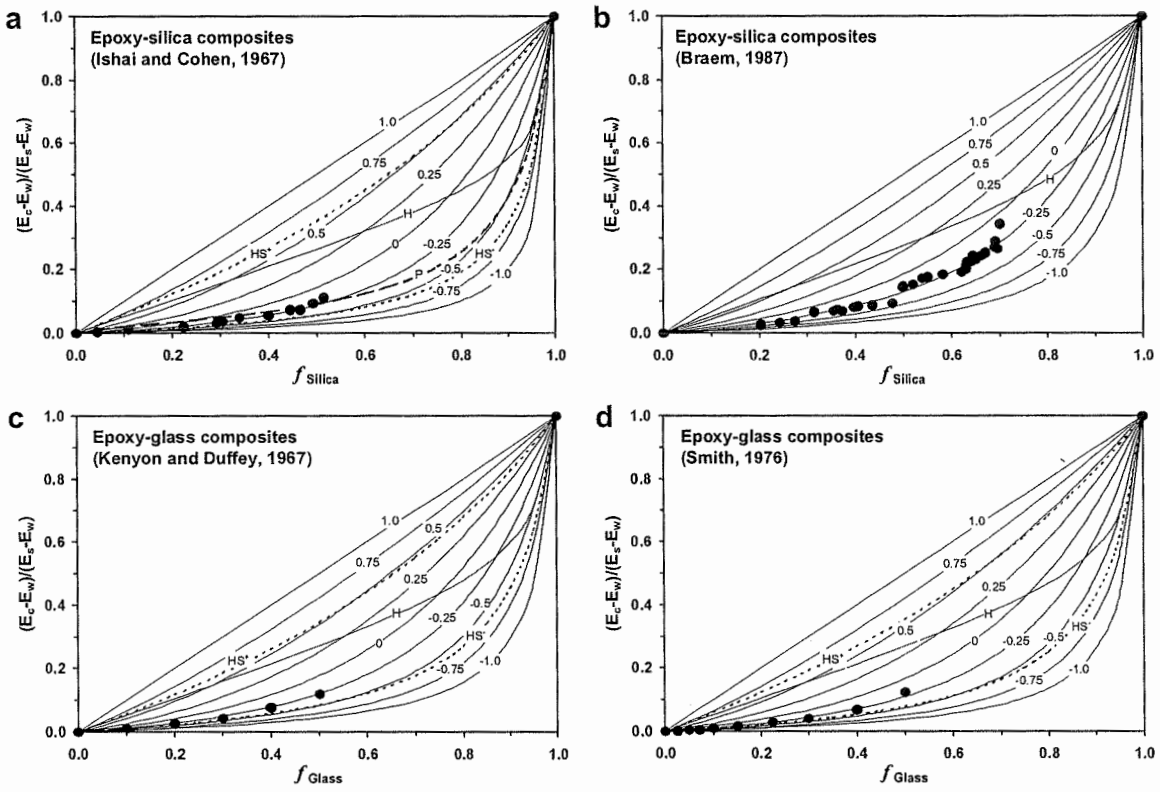


Figure A1.9 Comparison of the predictions of the present approach, the Hashin-Shtrikman upper (HS^+) and lower (HS^-) bounds, Paul's (1960) calculations (P) with experimental data on relative elastic Young's moduli of epoxy resin-based composites. Epoxy-Silica composites (a and b) and epoxy-glass composites (c-d). J value is given in number. H represents the Hill average.

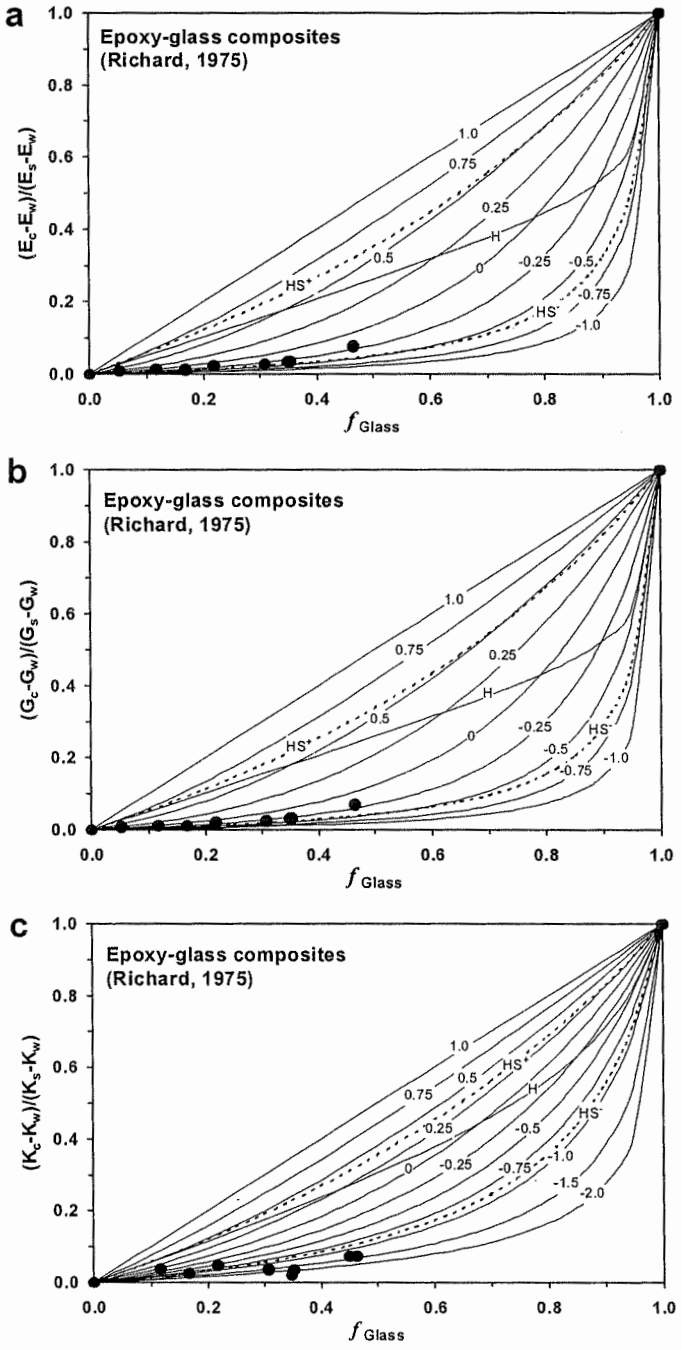


Figure A1.10 Comparison of the predictions of the present approach, the Hashin-Shtrikman upper (HS^+) and (HS^-) bounds with experimental data on relative Young's modulus (a), shear modulus (b) and bulk modulus (c) of epoxy-glass composites. *J* value is given in number. H represents the Hill average.

Zhang et al. (1996) investigated the effective elastic properties of a two-phase composite consisting of aluminum particles embedded randomly in a continuous resin matrix. Bulk and shear moduli for aluminum are 77.44 GPa and 5.31 GPa, respectively. Bulk and shear moduli for resin are 5.31 GPa and 1.82 GPa, respectively. The shapes of the Al inclusions are elongate with aspect ratios (width/length) ranging from 0.1 to 1.0, averaging about 0.25. The bulk, shear and Young's moduli of the composites, obtained from velocities of ultrasonic waves, are plotted in Figure A1.11. The observed relative Young's and shear moduli can be best fitted by the theoretical curve of $J = -0.25$ (Figure A1.11a-b). In contrast, the relative bulk modulus is best fitted by the theoretical curves of $J = -0.5$ (Figure A1.11c). In addition, measured P- and S-wave velocities of the composites (Figure A1.12) correspond to theoretical curves of $J = -2.0$ and $J = -1.0$, respectively. Hence even for the composites with the same composition and same microstructure, J values are different for different elastic moduli or mechanical properties. This aspect should receive a further detailed study.

Glass-Al_2O_3 composites investigated by Hasselman and Fulruth (1965a) are characterized by a sodium borosilicate glass (16% Na_2O, 14% B_2O_3, and 70% SiO_2) containing dispersions of alumina particles. The composite aggregates were prepared using vacuum hot-pressing technique at 725° C. The alumina particles, which are crushed sapphire, are quite jagged and nonspherical in shape and have a mean particle size of about 50 μm. The Young's moduli for the glass and the alumina are 80.5 and 411 GPa, respectively (Hasselman and Fulrath, 1965a). The Poisson's ratios the glass and the alumina are 0.194 and 0.257, respectively. As shown in Figure A1.13a, the theoretical curve with $J = -0.25$ tracks the lower HS bound at $f_s \leq 0.4$, where both predictions agree very well with the experimental results. At higher f_s, however, the generalized means give definitely better agreement with the data than the lower HS bound.

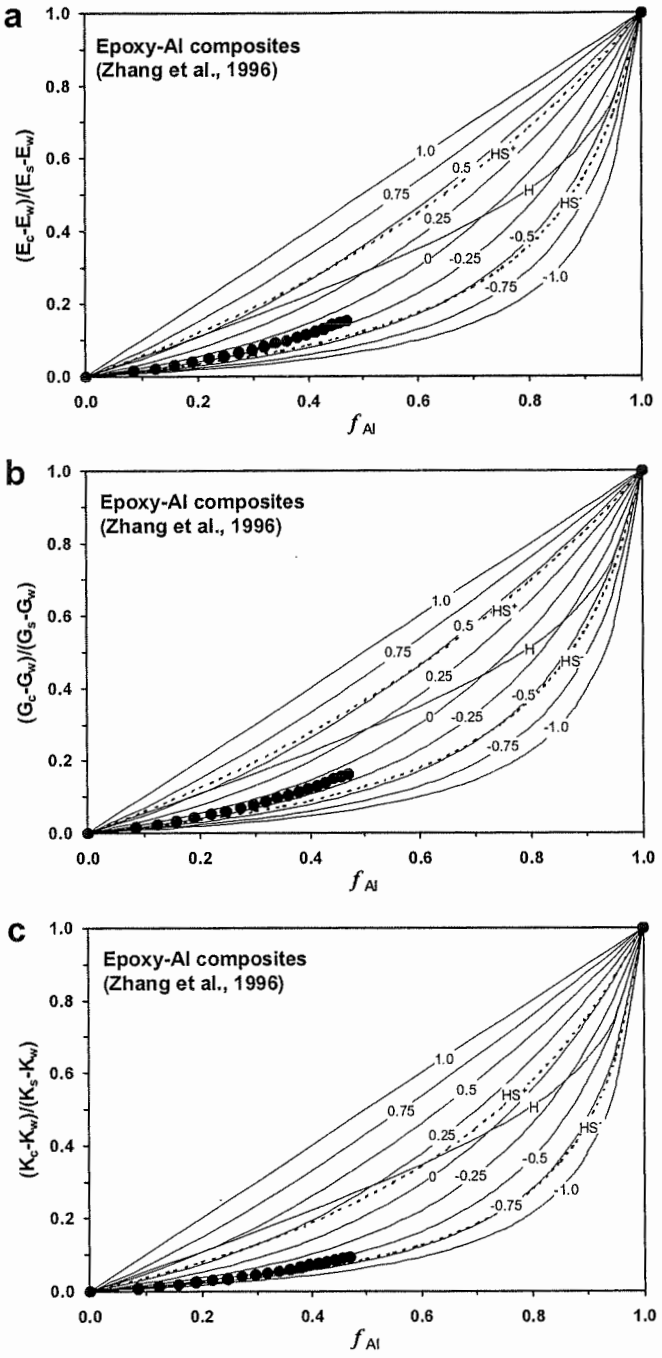


Figure A1.11 Relative Young's modulus (a), shear modulus (b) and bulk modulus (c) for epoxy-Al composite plotted against volume fraction of Al. Theoretical curves labeled according to J value. H, HS^+ and HS^- represent the Hill average, the Hashin-Shtrikman upper and lower bounds, respectively.

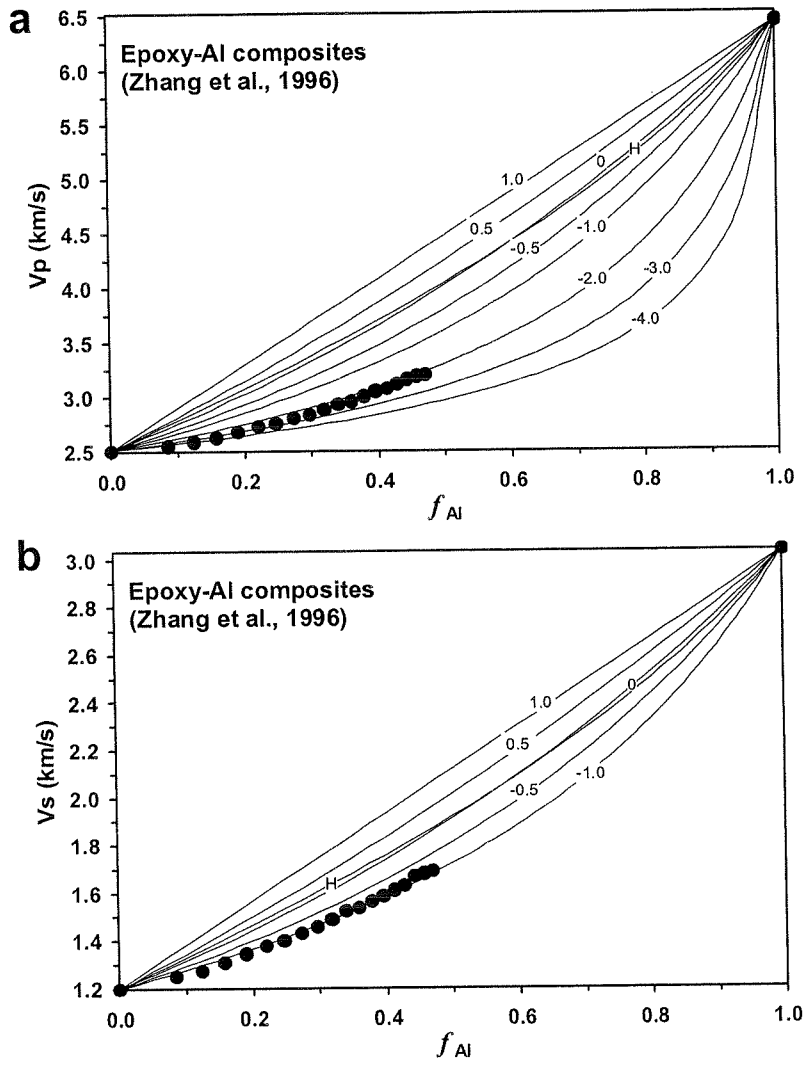


Figure A1.12 P-wave (a) and S-wave (b) velocities for epoxy-Al composites plotted against volume fraction of Al. Theoretical curves labelled according to J value. H represents the Hill average.

Hasselman and Fulrath (1965b) also measured the Young's moduli of glass-tungsten composites with $f_s \leq 0.5$. The Young's moduli and Poisson's ratios for the glass and the tungsten are 80.5 and 355 GPa, 0.197 and 0.198, respectively. There is a good consistence between their experimental results and our theoretical curve with $J = -0.25$ (Figure A1.13b). Similarly, the generalized means provide a better prediction than the

lower HS bound. Thus, a good agreement of the calculated and experimental data for a large number of two-phase composite systems evaluated above supports that $J = -0.25$ for predicting effective Young's modulus of the composites with WPSS.

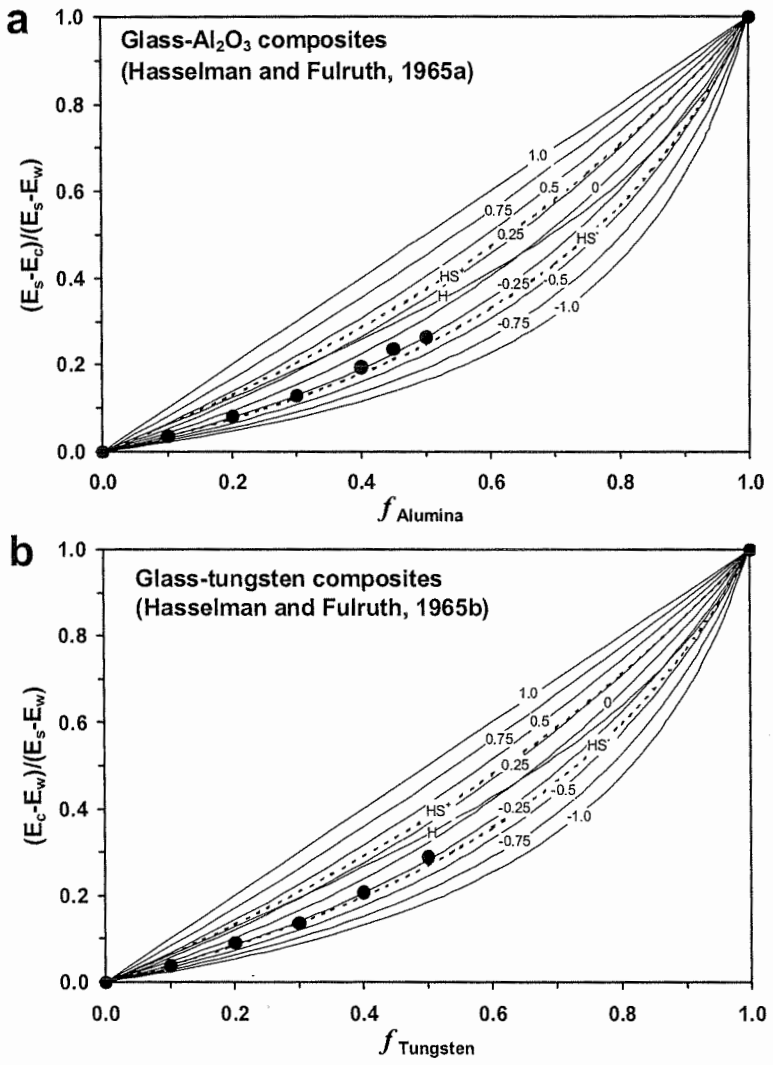


Figure A1.13 Theoretical curves on relative Young's modulus $(E_c-E_w)/(E_s-E_w)$ for glass-matrix composites plotted against volume fraction of reinforcement. Glass-Al_2O_3 composites (a) and glass-tungsten composites (b). Theoretical curves labelled according to J value. H, HS^+ and HS^- represent the Hill average, the Hashin-Shtrikman upper and lower bounds, respectively.

Einstein (1906, 1911) theoretically analyzed the rheology of a specific WPSS composite, which is a dilute suspension of identical rigid spheres in a Newtonian viscous liquid, and obtained

$$\eta_c = \eta_w(1+2.5f_s) \qquad \text{(A1.7)}$$

where η_c and η_w are the bulk viscosity of the suspension and the viscosity of the liquid, and f_s is the volume fraction of rigid spheres. In the dilute system, each single sphere is isolated in the continuous liquid matrix, and no slip occurs between the spheres and the liquid. This famous Einstein equation, which agrees with many experimental data (e.g., Mewis and Macosko, 1994), has been widely used in the rheological study of solid-liquid suspensions such as partially melted rocks (Arzi, 1978; Lejeune and Richet, 1995). As shown in Figure A1.14, the generalized means with $J=-0.5$ yield a very close approximation to the Einstein equation with a relative error less than 1% as long as the two-phase composite is a really dilute suspension (i.e., $f_s \le 0.15$). The above comparison again suggests that $J=-0.5$ for the WPSS composites with their strong phases being identically spherical.

A1.5 Application to the interpretation of 410-km seismic discontinuity

The seismic discontinuity at 410 km depth is considered to be caused by a phase transition of the main constituent of the upper mantle - olivine to wadsleyite [i.e., modified spinel or β phase of $(Mg, Fe)_2SiO_4$, Lebedev et al., 2002]. Seismological studies using high-frequency reflected and converted waves indicate that this discontinuity has a width of less than 4-6 km (Leven, 1985; Paulssen, 1988; Benz and Vidale, 1993), which is much too thin to be explained by the depth interval (~14 km corresponding to 0.5 GPa at 1600 °C, Katsura and Ito, 1989; Akaogi et al., 1989; Fei et al., 1991) over which olivine transforms fully to wadsleyite. A number of hypotheses have been proposed to

explain why the phase transition is much sharper than the prediction based on the width of the binary coexistence region. These hypotheses include:

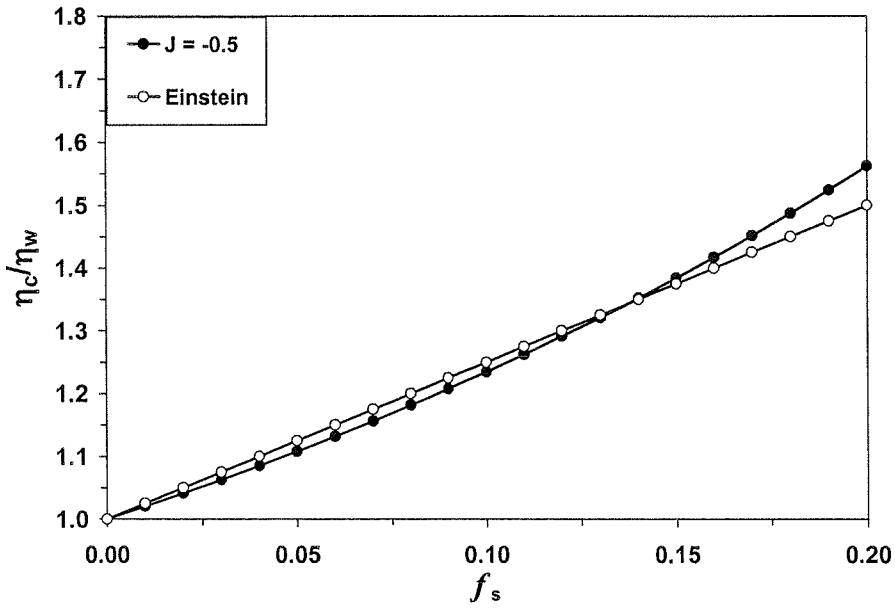


Figure A1.14 Comparison between the predictions of the present approach and the Einstein equation for the relative viscosity of a suspension as a function of identically spherical, solid inclusions.

(1) Seismic discontinuities originate from so-called univariant phase transitions that occur suddenly at a very narrow pressure interval (Jeanloz and Thompson, 1983). However, the chemical system of the upper mantle is multicomponent, and simple phase relations show that the transition from olivine to wadsleyite must occur in a divariant loop (Wood, 1995). Furthermore, for a univariant phase transition to produce the 410 km discontinuity, the Fe content of the upper mantle should be substantially different from that generally accepted on the basis of geochemical data from mantle xenoliths (Stixrude, 1997).

(2) Seismic discontinuities are caused by a change not only of phase but also of composition (Lees et al., 1983; Bina and Kumazawa, 1993) over a narrow depth

interval. As pointed out by Stixrude (1997), however, the formation of a well developed compositionally stratification in the upper mantle would require large chemical diffusivities that in turn require substantial amounts of fluids.

(3) Seismic discontinuities are caused by phase transitions that occur under non-equilibrium conditions in a dynamic system (Solomatov and Stevenson, 1994). This mechanism is most likely to occur in subducting slabs rather than in most of the mantle.

(4) The volume fraction of the high pressure phase (generally elastically stiffer) increases nonlinearly with temperature and pressure so that most of the phase transition is completed over a narrow depth interval (Stixrude, 1997).

(5) Non-transforming phases such as pyroxenes and garnet act as buffers to reduce the total width over which a transition occurs (Stixrude, 1997).

(6) The paradox is due to the difference in H_2O content between actual upper mantle and experimental samples because the pressure interval of the olivine to wadsleyite transformation increases with increasing the H_2O content (Wood, 1995).

In all the above models, the width of the phase transition is taken as controlled by the width of the coexistence region (i.e., equilibrium phase loop of Stixrude, 1997). Here we propose that the sharpness is essentially governed by a critical high pressure phase volume fraction range over which the transition is completed from weak-phase supported structure (WPSS) to strong-phase supported structure (SPSS). When olivine progressively transforms to wadsleyite with increasing depth in the transition zone, an increase in wadsleyite volume fraction is accompanied by a change in microstructure (i.e., phase continuity and connectivity). The composition dependence of the elastic moduli then cannot be expressed by an equation like Equation (A1.1) with a single J value valid over the whole range of $f_{\text{wadsleyite}}$ from zero to unity. Figure A1.15a-b illustrates the variation of P- and S-wave impedances for olivine-wadsleyite mixtures due to the WPSS to SPSS transition. For the SPSS mixtures, the impedance varies with wadsleyite volume fraction according to curve ABCD. For the WPSS mixtures, however,

the impedance varies with wadsleyite volume fraction according to curve DEFA. When the volume fraction of wadsleyite reaches a critical value, say about 40-45%, the olivine frame begins to be progressively dismembered by wadsleyite grains. After the volume fraction of wadsleyite is larger than a second critical value, say 70-75%, olivine grains are fully dispersed as residuals in a continuous matrix of wadsleyite. Therefore, there is an evolution in seismic impedance for the olivine-wadsleyite mixture from D, through E and B, finally to A (Figure A1.15) during progressive olivine to wadsleyite transformation with increasing pressure or depth.

No model is available for describing the elastic properties or flow strength of two-phase composites in the transitional regime (Ji et al., 2001). Let M_1, f_1 and M_2, f_2 be the overall elastic moduli and the strong phase volume fractions at the lower and upper boundaries of the transition range (E and B points in Figure A1.15), respectively. We assume that a mathematic expression $M_c(f_s)$ for the transitional regime should be constrained by the following conditions: (1) $M_c(f_s)$ is a continuous, monotonically increasing function in the range from f_1 to f_2. (2) $M_c = M_1$ at $f_s = f_1$ and $M_c = M_2$ at $f_s = f_2$. (3) The curve $M_c(f_s)$ is symmetrical with respect to the mid-point where $f_s = (f_1 + f_2)/2$ and $M_c = (M_1 + M_2)/2$, therefore, $M_c(f_s)$ is an odd function of f_s, and $M_c\left(f_s - \frac{f_1 + f_2}{2}\right) = -M_c\left(\frac{f_1 + f_2}{2} - f_s\right)$. (4) $M_c(f_s)$ is concave when $f_s \le (f_1 + f_2)/2$, and convex when $f_s \ge (f_1 + f_2)/2$. The simplest expression that satisfies with the above limiting conditions is the following smooth function:

$$M_c = \frac{M_1 + M_2}{2} + \delta \frac{M_2 - M_1}{2} \left(\frac{\left| f_s - \frac{f_1 + f_2}{2} \right|}{\frac{f_2 - f_1}{2}} \right)^{1/k} \qquad \text{(A1.8)}$$

where k is an odd number, $\delta = 1$ when $f_s \geq (f_1 + f_2)/2$, and $\delta = -1$ when $f_s \leq (f_1 + f_2)/2$. Although Equation (A1.8) is certainly not a unique solution to the limiting conditions, we could not find any additional constraints to warrant the use of a more complicated expression.

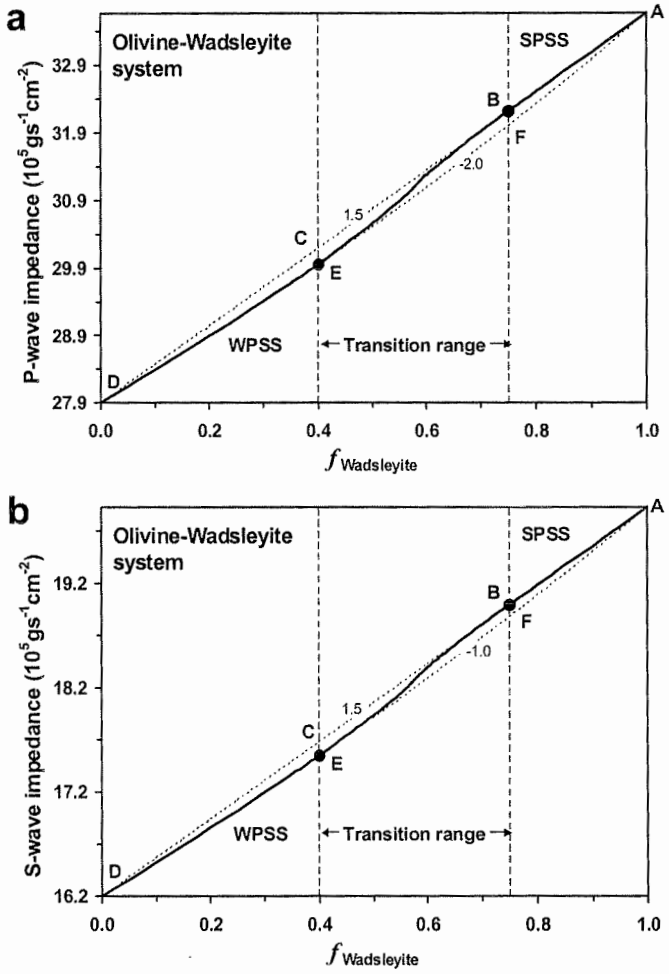


Figure A1.15 Variation of P-wave (a) and S-wave (b) impedances for olivine-wadsleyite system with its composition for three typical structure: curve ABCD, discontinuous weak phase (olivine) grains in continuous strong framework of wadsleyite; curve DEFA, discontinuous strong phase (wadsleyite) embedded in a continuous weak matrix; curve EB, calculated from Equation (A1.8) with J = 0.5 and k = 1.1, both phases are either discontinuous or continuous and there is a transition from an olivine-dominant configuration to a wadsleyite-dominant configuration with increasing the volume fraction of wadsleyite (from E to B).

The P- and S-wave impedance contrasts are about 3.6%, across the critical $f_{\text{wadsleyite}}$ range over which WPSS transforms to SPSS. This impedance contrast agrees with the value in the preliminary reference Earth model (Dziewonski and Anderson, 1981). The volume fraction range for the WPSS to SPSS transition is only one third the width of the olivine-wadsleyite coexistence region. This means that the effective width of the seismic discontinuity at 410 km mainly indicates the width of the transition from olivine-supported structure to wadsleyite-supported structure rather than that of a full experimentally determined binary phase loop. The latter is substantially larger than the actual width of the seismic discontinuity. For temperatures and pressures in a typical transition zone the effective width of the WPSS to SPSS transition lies between 4 and 6 km. This agrees with the maximum width of an equivalent linear discontinuity (4-6 km) found in reflections from the 410 km discontinuity (Leven, 1985; Benz and Vidale, 1993).

When effects of the structural transition on the effective elastic properties of multiphase mixtures are taken into account, the transition from olivine to wadsleyite is sufficient to explain the sharp seismic discontinuity at 410 km depth, and any other special processes or properties implied in models (1-6) are not required. It may be reasonable to conclude that any seismic discontinuity due to phase transformations has a width equivalent to that of the transition between WPSS and SPSS and being about one third of the width of the binary phase loop. Therefore, the sharpness of the 410 km seismic discontinuity is a corollary of the transition from olivine-dominant structure to wadsleyite-dominant structure.

A1.6 Discussion and conclusions

The elastic properties of multiphase composites can be calculated according to the simple expression proposed in this paper, which involves utilization of the generalized means. The approach is believed to be relevant if one phase is a homogeneous and

isotropic continuum (the matrix) with embedded inclusions of the other phase which is also homogeneous, isotropic and randomly distributed through the matrix. The approach postulates neither untested nor poorly constrained physical properties or processes (e.g., isostrain or isostress), nor any approximation of composite microstructure to an idealized, somehow oversimplified unit cell (e.g., Tullis et al., 1991; Treagus, 2002). The calculations require only the knowledge of the elastic modulus and the volume fraction of each individual phase and a pertinent value of the microstructural parameter J. The means with $J = 0.5$ or $J = -0.5$ provides good agreement with the experimental data of Young's modulus for the two-phase composites in which inclusions are shaped like spheres isolated in a continuous host medium (Table A1.1). For most composite materials in which the inclusions are shaped somewhat randomly, the means with $J = -0.25$ and $J = 0.25$ do well at predicting the measured values of Young's modulus for those with weak-phase continuous (the volume fraction of strong phase $f_s \leq 0.5$) and strong-phase continuous ($f_s \geq 0.7$) structures, respectively (Table A1.1). In the intermediate compositional range ($0.4 - 0.5 \leq f_s \leq 0.6 - 0.7$), J most likely varies progressively from -0.5 to 0.5 or from -0.25 to 0.25 due to the transition in microstructure. Thus we believe that the generalized means offer a great potential for providing useful predictive relationships between the composite properties and the component contents for various multiphase materials and rocks.

Table A1.1 J-value as functions of the phase shape and distribution

Shape of inclusion	|J|	Inclusion as	Microstructure	J	Exemples
Sphere	0.50	Weak phase	SPSS	0.50	Porous glass
		Strong phase	WPSS	-0.50	Dilute suspension in a Newtonian liquid
Random geometry	0.25	Weak phase	SPSS	0.25	Porous Al_2O_3, porous MgO, WC-Co
		Strong phase	WPSS	-0.25	Al-SiC, Al-boron, Al-spinel, Epoxy-silica, Epoxy-glass, Epoxy-Al, Glass-Al_2O_3, Glass-tungsten

The coefficient J in the generalized mean formula is shown to be constant for a given elastic modulus of composites of a particular microstructure, regardless of the elastic contrast between constituent phases. Thus, the J value is referred as a microstructural coefficient, which depends on the shape and distribution (continuity and connectivity) of the phases. For isotropic granular materials and rocks, the phase continuity and connectivity are a function of phase volume fractions, and therefore the J value should depend on the phase volume fractions. J value changes when a weak-phase supported structure transforms to a strong-phase support structure. Furthermore, for a multiphase material with a constant microstructure, different J values may be needed to describe different mechanical properties. Hence, a systematic study is urged to determine the J values for G, K, P- and S-wave velocities, viscosity and flow strength.

The theoretical values of Young's modulus for composites with weak phase support structure and strong phase support structure coincide nearly with the commonly used Hashin and Shtrikman's (1963) lower and upper bounds, respectively. The theoretical values calculated with $J = -0.25$ also agree well with Paul's (1960) model for arbitrary phase geometry. The calculations using the generalized means are direct without needing to know bulk or shear moduli separately. However, the calculations of Hashin and Shtrikman bounds require full information on the bulk and shear moduli of each phase of the two-phase composites. A full set of elastic data is usually lacking because only one elastic constant (i.e., Young's, shear or bulk modulus) is often measured for the components (See Berryman, 1995 for a review). In the latter cases, the Hashin and Shtrikman's upper and lower bounds cannot be calculated. Moreover, the Hashin-Shtrikman bounds generally lie too far apart to be useful for practical purposes because no effect of the composite microstructure has been taken into consideration. Nevertheless, the generalized means have the advantage that they make use of the microstructure (by choosing properly the J value) to obtain more accurate estimates than the Hashin-Shtrikman bounds. In addition, the validity of the Hashin-Shtrikman bounds actually depends on the relative magnitudes of K_s, K_w, G_s, G_w, υ_s and υ_w, where υ is

Poisson's ratio. An inversion of the upper and lower bounds often occurs at high values of K_w/K_s (>0.2) and/or at low values of υ_w/υ_s (<1.0) (Ji and Wang, 1999).

The Hill average has been widely used in the modeling of the overall elastic properties of polycrystalline aggregates (e.g., Montagner and Anderson, 1989; Zhao and Anderson, 1994; and many others). However, the present study proved that the elastic constants of the composites could not be precisely estimated using the Hill scheme for most two-phase composites investigated.

Although the comparison between theory and experiment was done for the elastic properties, the present approach can be easily extended to the prediction of other mechanical and physical properties of multiphase composites (e.g., flow strength, electrical conductivity and thermal conductivity). Furthermore, unlike many other models that apply to only two-phase composites (e.g., Ji and Zhao, 1994; Ravichandran, 1994; Zhao and Ji, 1997), the present model is also adequate for all composites consisting of more than 2 phases. We hope that the present study will encourage systematic measurements of the J value for composite materials and rocks with various microstructural characteristics.

Importantly, the generalized means proposed here are obviously advantageous to have an analytical formula rather than a computational one. This advantage is extremely useful if it is desired to invert the elastic data or seismic velocities to the volume fractions of the composite constituent phases and the microstructure. The theory presented in this paper can be used to develop some new techniques to determine how much volume fraction of diamond has formed during the phase transition from graphite in high temperature and high pressure anvils through in-situ, non-destructive acoustic measurements.

As an application, the effect of the structural transition on effective elastic properties of binary olivine-wadsleyite mixtures has been analyzed. The analysis suggests that the width of the seismic discontinuity at 410 km should be directly governed by the width of the transition from olivine-supported structure to wadsleyite-supported structure rather than that of an experimentally determined binary phase loop. The width of the discontinuity is likely reduced by a factor of 3 with respect to that of the binary coexistence region. The change in effective elastic properties due to the structural transition is effectively much sharper than the width of the binary coexistence region.

Appendix 2

Classification of rock category

Igneous Rocks		
Rock category	Lithology	Rock name
Ultramafic rocks	Peridotite	Chr dunite, Dunite, Grt harzburgite, Grt lherzolite, Grt peridotite, Harzburgite, Hortonolite dunite, Lherzolite, Peridotite, Pl dunite, Spl lherzolite, Spl-Grt lherzolite, Srp peridotite, Wehrlite
	Pyroxenite	Bronzitite, Clinopyroxenite, Grt pyroxenite, Ol pyroxenite, Ol websterite, Pl pyroxenite, Pl websterite, Pyroxenite, Srp-Ol clinopyroxenite, Websterite
	Hornblendite	Grt hornblendite, Hornblendite
	Kimberlite	Kimberlite
	Lamprophyre	Lamprophyre
Mafic rocks	Basalt	Basalt, Basalt glass, Dolerite, Lava flow, Ne basalt, Ol basalt, Pillow basalt, Pillow lava, Spilite, Tholeiitic basalt
	Anorthosite	Anorthosite, Anorthositic gabbro, Gabbroic anorthosite, Anorthositic granulite (Met)
	Gabbro-Norite-Troctolite	Fe-Ti oxide gabbro, Gabbro, Gabbronorite, Gabbropegmatite, Grt gabbro, Hbl gabbro, Hbl-Ol gabbro, Mafic cumulate, Norite Ol gabbro, Ol gabbronorite, Troctolite
	Diabase	Diabase, Mafic dyke, Prophyry
Intermediate rocks	Diorite-Tonalite-Andesite	Andesite, Andesite flow, Diorite, Gabbro-diorire, Hbl diorite, Monzodiorite, Qtz diorite, Qtz mangerite, Sanukite, Tuffaceous andesite
	Syenite-Monzonite	Albitite, Latite lava, Mangerite, Monzonite, Syenite, Trachytic lava
Felsic rocks	Granite-Granodiorite	Bt granite, Charnockite, Felsic dyke, Granite, Granite-granodiorite, Granodiorite, Granophyre, Leucocharnockite, Leucogranite, Migmatite, Ms granite, Porphyry, Qtz granodiorite, Qtz mangerite, Qtz monzodiorite, Qtz monzonite, Tonalite, Trondhjemite
	Rhyolite	Obsidian, Rhyolite
Volcaniclastic Rocks	Breccia	Andesite breccia, Basalt breccia, Lapillistone, Volcanic breccia, Volcaniclastic breccia
	Tuff	Acid tuff, Felsic lapilli tuff, Trachytic tuff, Tuff, Tuffite

Metamorphic Rocks		
Rock category	Lithology	Rock name
Ultramafic-Mafic rocks	Eclogite	Altered eclogite, Eclogite, Mafic eclogite, Mylonitic eclogite, Retrograde eclogite
	Serpentinized peridotite	Dunite, Grt lherzolite, Harzburgite, Lherzolite, Mica peridotite, Srp dunite, Srp harzburgite, Srp peridotite, Srp-Hbl peridotite
	Serpentinite	Serpentinite
	Metagabbro-Metadiabase	Altered gabbro, Altered Hbl gabbro, Grt-Hbl gabbro, Metabasite, Metadiabase, Metagabbro, Opx-Cpx-Bt metabasite
	Metabasalt	Altered basalt, Chloritized basalt, Idd basalt, Metabasalt, Metadolerite
	Amphibolite	Amphibolite, Amphibolitic gneiss, Amphibolitic mylonite, Amphibolitic ultramylonite, Cpx mylonitic amphibolite, Ep amphibolite, Grt amphibolite, Mafic gneiss, Mylonitic amphibolite, Retrograde granulite
	Mafic granulite	Gabbroic granulite, Granulite, Grt granulite, Hbl-Grt granulite, Hbl-Pyx granofels, Mafic granulite, Pyriclasite, Pyx granulite
	Mafic gneiss	Bt-Hbl gneiss, Gneiss, Greenstone, Grt-Hbl gneiss, Hbl gneiss, Hbl-Bt gneiss, Ky-Grt-Bt gneiss, Mafic gneiss, Noritic gneiss, Pl-Qtz-Hbl gneiss
	Mafic mylonite	Blastomylonite, Grt-Ep-Hbl-Ms mylonite, Grt-Hbl-Czo-Ms mylonite, Hbl-Ser-Ep-Chl, mylonite, Mafic mylonite, Mylonite, Mylonitic dunite
Intermediate rocks	Intermediate granulite	Granulite, Grt leptynite, Intermediate granulite
	Intermediate gneiss	Bt gneiss, Bt-Cpx-Pl gneiss, Bt-Pl gneiss, Cpx-Pl-Grt gneiss, Dioritic gneiss, Grt-Bt gneiss, Hbl-Pl gneiss, Intermediate gneiss, Metaandesite, Metadacite, Metadiorite, Metamonzodiorite, Monzodioritic gneiss, Opx-Pl gneiss
	Intermediate mylonite	Ep-Chl-Ms mylonite, Hbl-Ep-Ser mylonite, Ms-Bt-Ep mylonite, Qtz-Kfs mylonite

Metamorphic Rocks (continued)		
Rock category	Lithology	Rock name
Felsic rocks	Felsic granulite	Felsic granulite, Granulite, Hy-Qtz-Fsp granulite, Hy-Qtz-Pl granulite, Ms-Grt leptynite, Qtz-Kfs granulite
	Felsic gneiss	Augen gneiss, Bt gneiss, Bt tonalitic gneiss, Bt-Opx-Pl gneiss, Bt-Qtz-Fsp gneiss, Enderbitic gneiss, Felsic gneiss, Gneiss, Granitic augen gneiss, Granitic gneiss, Granitoid gneiss, Granodioritic gneiss, Grt trondhjemitic gneiss, Kfs gneiss, Metarhyolite, Orthogneiss, Qtz-Kfs gneiss, Quartzofeldspathic mylonitic gneiss, Tonalitic gneiss, Trondhjemitic gneiss
	Felsic mylonite	Diatexitic ultramylonite, Ep-Hbl-Ms mylonite, Ep-Ms mylonite, Ep-Ms ultramylonite, Granitoid mylonite, Granitoid ultramylonite, Granodioritic mylonite, Grt-Hbl-Ep-Ms mylonite, Hbl granitic mylonite, Hbl-Grt granitic mylonite, Mylonite, Qtz-Kfs mylonite, Qtz-Kfs ultramylonite, Ser ultramylonite, Tonalitic mylonite, Trondhjemitic mylonite, Ultramylonite
Metavolcanite	Metatuff	Acid tuff, Felsic lapilli tuff, Metatuff, Tuff
Metasedimentary rocks	Slate	Slate
	Marble	Cal marble, Marble
	Quartzite	Feldspathic mica quartzite, Gr quartzite, Quartzite, Quartzitic ultramylonite
	Schist	Act schist, Bt schist, Bt-Qtz schist, Cld-St micaschist, Grt schist, Ky schist, Mafic gneiss, Mica schist, Mica-Qtz schist, Ms-Chl mylonite, Phyllite, Phyllitic schist, Phyllonite, Phyllosilicate-rich mylonite, Qtz phyllite, Qtz-Mica schist, Schist, Sil schist, St-Grt micaschist, St-Grt schist
	Metasediment	Acid granulite, Bt gneiss, Cld-Bt gneiss, Felsic granulite, Gneiss, Granofels, Granulite, Grt gneiss, Grt-Bt-Pl gneiss, Grt-Crd-Sil-Bt gneiss, Grt-Sil-Bt gneiss, Hbl-Pl-Grt gneiss, Kinzigite, Mag-bearing gneiss, Metaarkose, Metagraywacke, Metapsammite, Metasandstone, Metasediment, Paragneiss, Paragranulite, Psammitic gneiss, Pyx-Pl-Grt gneiss, Qtz-Pl-Hbl gneiss, Sil-Grt gneiss, Stronalite
	Metapelite	Metapelite, Migmatitic metapelite
Cataclastic Rocks	Cataclasite	Blastocataclasite, Felsic cataclasite, Mafic cataclastic

Sedimentary Rocks		
	Rock Category	Lithology
Clastic Sediments	Sandstone	Chert, Dol sandstone, Graywacke, Sandstone
	Siltstone-Mudstone	Argillaceous siltstone, Calcareous siltstone, Siltstone
	Shale	Claystone, Mudstone, Shale, Silty shale
Carbonate	Carbonate	Argillaceous limestone, Calcarenite, Calcilutite, Calcirudite, Carbonate, Carbonate-clay rock, Limestone, Silty limestone, Tlc carbonate
	Dolostone	Dolomite, Dolostone

Mineral Aggregates		
Salts	Salts	Anhydrite, Barite, Gypsum, KCl, Magnesite, NaCl, Rhodochrosite, Siderite
Sulfides	Sulfides	Bornite, Chalcopyrite, Galena, Gersdorffite, Millerite, Niccolite, Pentlandite, Pentlandite-pyrrhotite, Py breccia, Py-Anh breccia, Pyrite, Pyrite-chalcopyrite, Pyrite-pyrrhotite-pentlandite, Pyrite-sphalerite, Pyrrhotite, Pyrrhotite-arsenite, Pyrrhotite-pentlandite, Py-silica breccia, Silicified breccia, Sphalerite Sphalerite-chalcopyrite-pyrite Sulphide
Oxides	Oxides	Chromite
Silicates	Silicates	Analcime, Idocrase, Jadeite, Monticellite, Sillimanite

Appendix 3

Regression analysis of velocity-pressure relationship

A3.1 Least-squares method

No matter how seismic velocities of rocks vary with pressure more or less linearly, the statistical tool to characterize this relationship is regression. In order to obtain regression equations for linear and nonlinear segments of the velocity-pressure curve (Figure 4.2), the key is to find the critical point (P_c, V_c). Below P_c, a quadratic natural logarithmic function is found to be able to give the best approximation of nonlinear velocity-pressure behavior because it increases fast when pressure is low while goes similar to a linear increase when pressure is large. Above P_c, a linear function is better to describe the pure elastic deformation of rocks.

For observation point i, velocity V is the regressed variable, designated V_i, and pressure P is the regressor variable, denoted P_i. The estimated velocity $\hat{V}_i$ at specified pressure P_i is

$$\hat{V}_i = a(\ln P_i)^2 + b \ln P_i + c \qquad (P_i \le P_c) \qquad \text{(A3.1)}$$

and

$$\hat{V}_i = DP_i + V \qquad (P_i \ge P_c) \qquad \text{(A3.2)}$$

for the nonlinear and linear increase of velocity, respectively. The deviation is $V_i - \hat{V}_i$ and the best model should be the function giving best adjustment in the sense of least squares of deviation:

$$SS_D = \sum_{i=1}^{n} (V_i - \hat{V}_i)^2 = \min \tag{A3.3}$$

When the sum of squared deviation (SS_D) is minimized, we can use the normal equations to define a line with the desired characteristics:

$$\begin{bmatrix} n & \sum P \\ \sum P & \sum P^2 \end{bmatrix} \bullet \begin{bmatrix} V_0 \\ D \end{bmatrix} = \begin{bmatrix} \sum V \\ \sum VP \end{bmatrix} \tag{A3.4}$$

where n is the number of observations. Below the critical pressure P_c, we can transform the regressor variable P_i to lnP_i, and expand the normal equations to get parameters a, b and c:

$$\begin{bmatrix} n & \sum \ln P_i & \sum (\ln P_i)^2 \\ \sum \ln P_i & \sum (\ln P_i)^2 & \sum (\ln P_i)^3 \\ \sum (\ln P_i)^2 & \sum (\ln P)^3 & \sum (\ln P_i)^4 \end{bmatrix} \bullet \begin{bmatrix} c \\ b \\ a \end{bmatrix} = \begin{bmatrix} \sum V_i \\ \sum V_i \ln P_i \\ \sum V_i (\ln P_i)^2 \end{bmatrix} \tag{A3.5}$$

The goodness-of-fit of the least-squares solution to the observations is defined by

$$R^2 = \frac{\sum_{i=1}^{n} (\hat{V}_i - \overline{V})^2}{\sum_{i=1}^{n} (V_i - \overline{V})^2} = 1 - \frac{SS_D}{\sum_{i=1}^{n} (V_i - \overline{V})^2} \tag{A3.6}$$

where $\overline{V}$ is the mean velocity of n measurements. If the line is a good estimator of the data, SS_D should be small and R^2 will be near unity, and the R^2 of model will be considerably larger than the critical R^2 for a positive F test

$$\frac{R^2(n-p-1)}{(1-R^2)p} \sim F_{p,n-p-1} \qquad \text{(A3.7)}$$

where the degree of freedom $p = 1$ for a linear equation and $p = 2$ for a quadric equation.

However, the significance doesn't prove that there is only one acceptable model (Davis, 1986). All statistic tests are valid only when the residuals of model are independent and normally distributed. In order to validate our regression equations, we need to judge the behavior of residuals. The relative error (R_e) between the calculated and measured velocities of each point is defined as:

$$R_e(\%) = \frac{\hat{V}_i - V_i}{V_i} \times 100\% \qquad \text{(A3.8)}$$

When there is a high correlation between R_e and the variable P, the residuals are not independent. A particular tendency in R_e suggests that a new variable or a transformation of variables is possible to improve the model. In addition, the residual larger than three times of $(SS_D/(n-p-1))^{0.5}$ should be examined with attention. Such abnormal data may be caused by random experimental error or by inappropriate model.

A3.2 MATLAB program VPPLOT

A MATLAB program VPPLOT is constructed for critical point searching, velocity-pressure curve fitting and error analysis. It can give regression results with $R^2 > 0.97$ in a sense of least squared errors. The procedure can be concluded as following three steps.

A3.2.1 Interpolate data

In order to avoid insignificant regression, we need to interpolate data with equal pressure interval before modeling. Here we take 1 MPa as pressure interval, and the minimum measured velocity multiplied by 0.5% as the error tolerance for interpolation considering the experimental accuracy (±0.5% for *Vp* and ±1% for *Vs*, Kern, 1982a; Christensen, 1989). A MATLAB function *SPAPS* returns the smoothest function that lies within the given tolerance for the given data (*x, y*). Smoothest means that the following measure of roughness is minimized:

$$F(D^m f) = \int_{x(1)}^{x(n)} (D^m f)^2 \qquad \text{(A 3.9)}$$

where D^m is derivative of a function *f(x)*. The default value for m is 2, leading to second derivative f'' and a cubic smoothing spline, the choice m=1 for the first derivative f' and a linear smoothing spline. Moreover, the distance of the function *f(x)* from the given data is measured by

$$E(f) = \sum_{j=1}^{n} w(j)(y_j - f(x_j))^2 \qquad \text{(A 3.10)}$$

The default value for the weight vector w makes *E(f)* the composite trapezoidal rule approximation to $\int_{x(1)}^{x(n)} (y - f)^2$. *E(f)* is no bigger than tolerance with the chosen weight vector w. In this step, we take m = 1 to get a linear smoothing spline interpolation to the given velocity-pressure data.

A3.2.2 Find the critical point and regression functions

A MATLAB function *POLYFIT(x,y,k)* can find the coefficients of a polynomial $f(x) = d_1 x^k + d_2 x^{k-1} + \cdots + d_k x + d_{k+1}$ of degree k that fits the data, *f(x(i)) ~= y(i),* in a least-squares sense. Beginning from the lowest pressure and assuming it as P_c, when

choose k=1, *POLYFIT* returns linear velocity-pressure regression function from P_c to the highest pressure. Whenever $R^2 < 0.97$, take the next point as critical point and continue this loop. A graphical solution is then used to find the intersection of the significant linear segment ($R^2 \geq 0.97$) with velocity-pressure spline curve *f(P)*. This intersection is the real critical point (P_c, V_c) in statistical sense, and the final linear section will be obtained by using *POLYFIT* from P_c to highest pressure. For some runs that may never become linear in the experimental pressure range, the highest experimental pressure will be regarded as P_c, and the coefficients calculated from the last efficient loop of *POLYFIT* will be taken as D and V_0 in Equation (A3.2).

Below P_c, Equation (A5.1) is used to describe the nonlinear part of velocity-pressure curve. First set $m = 2$ in *SPAPS* to make a cubic interpolation for observations, then take *ln(P)* as the independent in *POLYFIT* and $k = 2$ to return the best fitting quadratic natural logarithmic function for data from lowest pressure to P_c. The whole expressions for the velocity-pressure curve are thus obtained (Figure A3.1a).

A3.2.3 Study residuals

A graphical solution is proposed for studying residuals: plot R_e versus the variable P to see if residuals are independent of pressure (Figure A3.1b), and draw a histogram of R_e to check the distribution of residuals (Figures A3.1c-d). Although VPPLOT can give satisfying results with most $R^2 > 0.98$ and normal distribution of residuals, it is noted that below 50 MPa, the residuals become larger and sometimes R_e can reach 2-3 %. It may be due to the lift-off of the transducers from the sample at low pressures during decompressing. Moreover, the signal of "first arrival" is often not strong enough to be picked up from noisy background at low pressures, which limits the accuracy of velocity measurement. Therefore, the last 1 or 2 points are rejected in retrogression when the data obviously deviate the trend ($R_e > 5\%$). It is found that smaller experimental interval of data at low pressures will improve the quality of modeling.

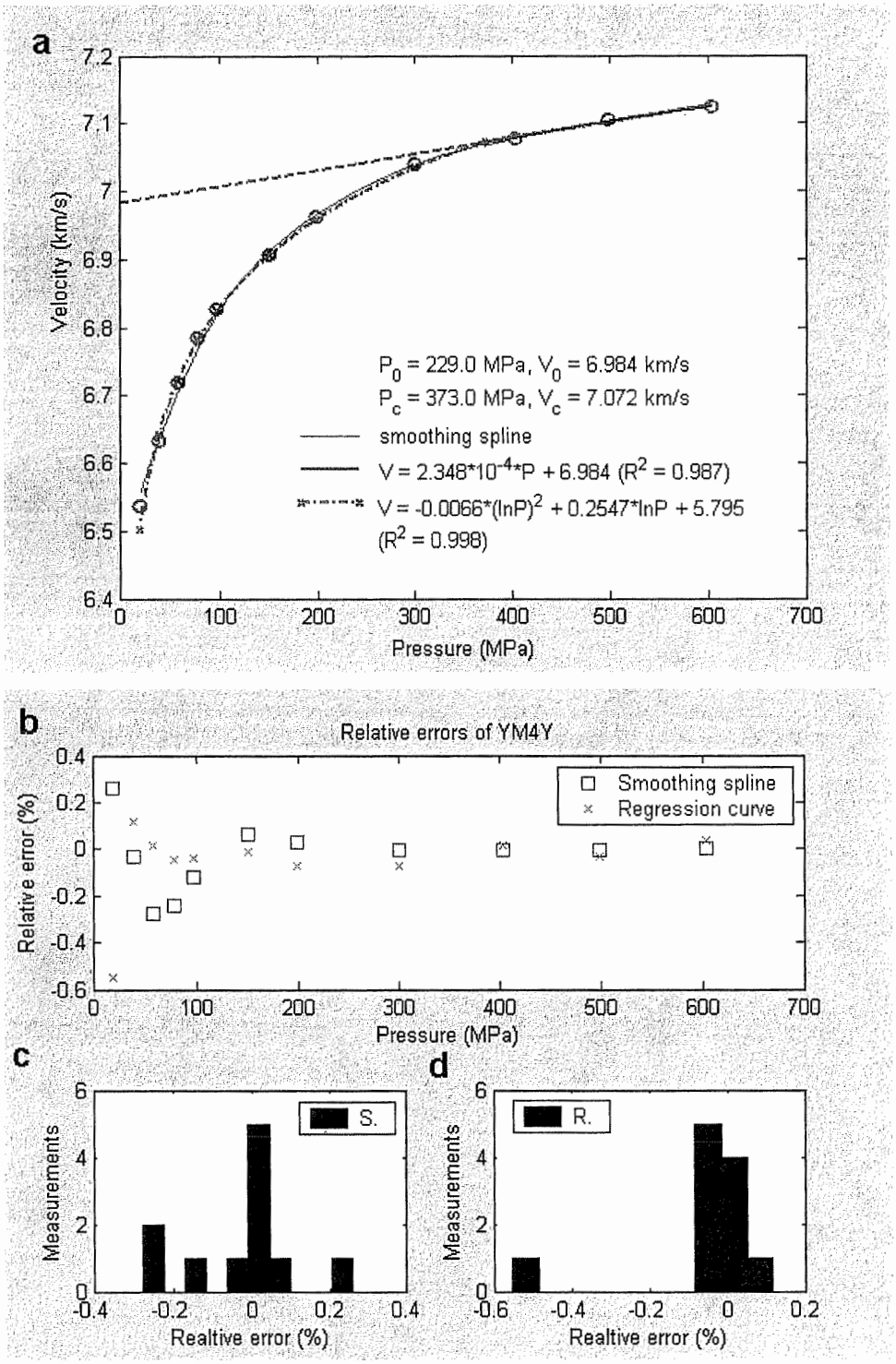


Figure A3.1 Regression results of experimental data points of amphibolite YM4Y (a) Regression equations of YM4Y. (b) Distribution of relative errors versus pressure; (c) Histogram of relative errors of spline interpolation; (d) Histogram of relative errors of regression results.

ÉCOLE POLYTECHNIQUE DE MONTRÉAL
3 9334 00314336 7